Numerical Study of Flow Structure and Pedestrian Level Wind Comfort Inside Urban Street Canyons

A thesis submitted in partial fulfillment of the requirements for the Degree of
Doctor of Philosophy in Mathematics

By
Purvi Paritosh Pancholy

under the supervision of
Dr. Phillip L Wilson, Dr. Miguel Moyers Gonzalez, Prof. Mark Jermy, Dr. Patrick Geoghegan, and Dr. Kevin Clemens

School of Mathematics and Statistics
UNIVERSITY OF CANTERBURY

August 13, 2018

Abstract

The air flow around an individual building or between buildings or groups of buildings is complex. This can introduce high wind speeds at a pedestrian level causing discomfort or even injuries. However, the effect of wind environment around buildings varies from site to site, depending on many factors such as the wind speed, wind direction, height and shape of a building, the neighbouring urban environment and so on. Sometimes a building will create a better urban wind environment and sometimes it may worsen it. When two or more buildings are considered, a recirculating flow can occur in the "street canyon" between them. These urban flows can impact pedestrians in the building wake or in the recirculating flow in the street canyon.

A three-dimensional numerical study using the steady Reynolds Averaged Navier-Stokes (RANS) of Computational Fluid Dynamics (CFD) has been performed to analyse the flow pattern and pedestrian comfort inside urban street canyons for medium rise buildings inside a thick atmospheric boundary layer. The wind direction considered was perpendicular to the street canyon. CFD validation for a single building has been performed by comparison with previous wind tunnel measurements for two reduced scale models. The near-wall modelling approach with the no-slip boundary condition has been used to model the wall roughness effect.

We initialized our study by analysing the flow structure inside the uniform and non-uniform street canyons. Considered parameters in this study include: the street width, building width and building height. Pedestrian comfort was quantified as the fraction of the street area where the wind speed was about 3 m/s on the extended "Land Beaufort Scale" at 1.75 m height, was used to compare the cases. This study reveals that for the uniform street canyon cases pedestrian comfort near the downstream building decreases with increasing street width. Whereas, a decrease in the building width decreases pedestrian comfort inside the street canyon. For the non-uniform cases, a step-up street canyon increases the pedestrian comfort inside the canyon whereas a step-down street canyon decreases the pedestrian comfort.

The obtained results for the uniform and non-uniform street canyons revealed that the flow coming from the upstream building roof has an impact on the flow structure and hence on the pedestrian wind comfort inside the street canyon. Hence a study was extended to find the impact of changing roof shapes of both buildings, only the upstream building or only the downstream building on the flow structure and pedestrian comfort inside

the street canyon. The street width to the building height ratio $S/H = 1$ was considered for all studied cases. The results of this study, when compared with the flat-flat roof case, indicate that there is a strong influence of the roof shape change on the flow field and pedestrian comfort in the street canyon. For the pedestrian comfort assessment study using the different roof shapes reveals that for the considered street width, the pedestrian comfort inside the entire street is improved compared to the flat-flat case, in the case of slanted and upwind wedge roof shape of both the buildings, upwind wedge roof shape of only the upstream building and for all types of non-flat roofs on the downstream building.

Finally, finding the impact of adding a panel on the building roof on the flow structure and pedestrian comfort inside the street canyon has been performed. Key parameters considered for this study include: angle of the panel and location of the panel. The obtained results reveal that adding panel at the leading edge of the upstream building roof at an angle of 45° and at the trailing edge of the upstream building roof at angles of 45° and 60° modifies the flow structure inside the street canyon in a way that improves wind comfort at the pedestrian height.

Acknowledgements

First and foremost, I would like to thank God Almighty for giving me the patience and strength to complete this thesis.

I would then like to express my deepest gratitude to all my supervisors. This thesis would not have been achievable without the encouragement, patience and guidance I received from them, their efforts throughout this entire course has taught me a new set of skills which I never imagined I could possess. My biggest and most heartfelt thanks go to Dr Phil Wilson for being the best supervisor, teacher and mentor I could ever ask for. I am very grateful for his perpetual encouragement, effort, patience, support, and most importantly for believing in me. A huge thank you to Prof Mark Jermy, for his expertise and guidance throughout this process. Simple thanks seem inadequate for his support and encouragement during my time at the University of Canterbury. I also wish to sincerely thank Dr Miguel Moyers Gonzalez and Dr Patrick Geoghegan for agreeing to be my supervisors, supporting, giving good advice, and encouraging me to pursue a PhD study. I am extremely thankful to Dr Kevin Clemens for his help and suggestions during my PhD study.

I greatly appreciate and acknowledge the financial support I received from IBM grant number E6327. I am also thankful to Mr Robert Hamilton, Client Service Coordinator, MetService, Wellington who provided me wind data for the city New Plymouth, New Zealand for the wind data analysis.

Many thanks to all the postgraduate colleagues and staff of the School of Mathematics and Statistics at the University of Canterbury for making my time as a PhD student very enjoyable. I am grateful for all the support I received during my stay, as a postgraduate student. This includes the excellent working condition, opportunities for tutoring and teaching, and funding for my trips to conferences in Auckland and Perth, Australia. And of course, I can not forget Paul Brouwers and Steve Gourdie, who were very friendly and approachable whenever I needed their assistance with my programming and computing troubles. I also wish to thank my colleagues from Mechanical Engineering department at the University of Canterbury for their support to help me to learn ANSYS.

A special thanks go to my family. Words cannot express how grateful I am to my father Prakash Trivedi and mother Jayshree Trivedi for all of the sacrifices, unconditional love and care that they have made on my behalf. Their prayers for me were what strengthened me to this extent. The strength and support of my mother brought me to this extent to pursue a doctoral study. I look at my mum as such a brilliant, ever loving,

beautiful woman in my lifespan. I would also like to especially thank my sister Rachana, brother Pranav, and brother-in-law Jay, who showed their enthusiasm and gave me a moral support and encouragement during this research period. My heartfelt regard goes to my father in law Dr Pravin Pancholy and mother in law Bhavna Pancholy, for their love and support financially as well as morally to pursue higher study after my marriage.

I owe thanks to a very special person, my husband, Paritosh, for his continued and unfailing love, support and understanding during my pursuit of PhD degree that made the completion of thesis possible. He was always around at times I thought that it is impossible to continue, he helped me to keep things in perspective. I greatly value his contribution and deeply appreciate his belief in me. The last words for my adorable daughter, Hiya, who has been the light of my life for the last three years and who has given me the extra strength and motivation to get things done. Words would never say how grateful I am to both of you. I consider myself the luckiest in the world to have such a lovely and caring family, standing beside me with their love and unconditional support. I dedicate this thesis work to both of you.

Contents

List of Figures

List of Tables

List of Abbreviations

CFD	**C**omputational **F**luid **D**ynamics
RANS	**R**eynolds **A**veraged **N**avier **S**tokes
LES	**L**arge **E**ddy **S**imulation
SKE	**S**tandard **k-e**psilon
RNGKE	**Re-N**ormalisation **G**roup **k-e**psilon
RKE	**R**ealizable **k-e**psilon
RSM	**R**eynolds **S**tress **M**odel
ABL	**A**tmospheric **B**oundary **L**ayer
ELBS	**E**xtended **L**and **B**eaufort **S**cale

List of Symbols

t	time	seconds (s)
X	streamwise position co-ordinate	
Y	vertical or trasverse position co-ordinate	
Z	horizontal or spanwise position co-ordinate	
H	height of the building or the Silsoe cube	meter (m)
W	width of the building in spanwise direction	m
L	length of the building in streamwise direction	m
U	mean velocity in the X-direction	m/s
V	mean velocity in the Y-direction	m/s
W	mean velocity in the Z-direction	m/s
$u^{'}$	turbulence velocity fluctuation in X-direction	m/s
$v^{'}$	turbulence velocity fluctuation in Y-direction	m/s
$w^{'}$	turbulence velocity fluctuation in Z-direction	m/s
ρ	density of the air ($= 1.225$)	kg/m^3
μ	kinematic viscosity of the air ($= 1.7894 \times 10^{-5}$)	kg/m-s
δ	boundary layer thickness	m
D	drag on the body	$kg - m/s^2$
y_{ref}	building eave height as the reference height	m
y_0	aerodynamic roughness length	m
y^+	non-dimensional wall unit	
$\triangle y$	first cell height from the wall	m
P_{ref}	mean reference static pressure in the upstream flow	Pa
U_{ref}	free stream velocity at the building height y_{ref}	m
C_P	pressure co-efficient ($= (P - P_{ref})/(\frac{1}{2}\rho U_{ref}^2)$)	
k	turbulent kinetic energy	joules
ε	turbulent dissipation rate	m^2/s^3
ω	specific dissipation rate	m^2/s^3
C_μ	empirical constant specified in the turbulent mode (0.09)	
l	turbulent integral length scale	m
U^*_{ABL}	atmospheric boundary layer frictional velocity	m/s
Re	Reynolds number ($= \frac{\rho U_{ref} H}{\mu}$)	
κ	von Kármán constant ($= 0.42$)	

Chapter 1

Introduction

1.1 Motivation

Most of the fluid flows occurring in the Atmospheric Boundary Layer (ABL) are turbulent in nature. Turbulent flow is defined as a fluid flow in which the fluid undergoes irregular fluctuations, or mixing. The velocity of the fluid at a point is continuously undergoing changes in magnitude and direction, which results in swirling and eddying as the bulk of the fluid moves in specific direction. The ABL is the lowest part of the atmosphere whose behaviour is directly influenced by its contact with a earth surface. The wind is retarded between the earth's surface and the top of the boundary layer due to roughness elements such as grass, trees and buildings. The ground level shear stresses increase with increasing ground roughness. The turbulence generated by the retarding effect of the ground results in a significant increase in the complexity of the wind flow and the effects on a ground based structures. Due to this fact atmospheric turbulence becomes an important factor in modelling of the wind forces on structures and losses they produce in extreme wind events.

Wind flow around a single building forms a complex three-dimensional flow structure. Detailed wind flow patterns and characteristics over the building surfaces are discussed in Chapter 2. When two or more buildings are aligned along two sides of a street, they create a "street canyon" between them, whose vertical bounds are the ground surface and the roof level, and the roof level is lower than the ABL height. Urban areas can be characterized as a group of such street canyons. Pedestrian comfort and pollutant dispersion depend on the wind structure at this level and can be viewed as wind engineering problems. A large number of authors has emphasized the importance of a comfortable and safe environment in such building domains as reviewed below.

Wind comfort and wind safety for pedestrians are essential to consider when designing buildings in the city. Poor building designs create bad situations and even a dangerous pedestrian level. There are a number of cases around the world for wind accidents in which people sustained serious injury or were killed. In May of 1972 in Portsmouth, England, an elderly lady died after her skull was fractured in a fall caused by a gust of wind at the corner of a 16 storey building (Aynsley, 1989). In June of the same year in Birmingham, England, another elderly woman was lifted off her feet by a

gust of wind near a tall block of apartments and died of head injuries as a result of her fall (Penwarden, 1973). In 1982 in the United States, a woman was blown to the ground by a gust of wind seriously injuring her shoulder near one of New York's tallest buildings. As a consequence of being injured, she sued the building's owners, manager, design engineer, architect as well as New York City for 6.5 million (Aynsley, 1989). In December of the same year in Canada, a family of four were seriously injured when they were blown off a jogging track on the podium roof of the Toronto City Hall (Aynsley, 1989). Therefore, it is necessary to focus on the problems and identify the possibilities of the pedestrian wind problems. The majority of such studies in the past have been conducted using wind tunnel. Computational Wind Engineering (CWE) is a new branch of wind engineering in which Computational Fluid Dynamics (CFD) methods are used to compute the detailed flow patterns around buildings and analysing pedestrian level wind comfort.

Whereby there is large literature available analysing the wind speed conditions in such urban street canyons using wind tunnel and CFD for generic building structures focusing on pedestrian level winds for discrete points, a limited range of street widths and for a wind direction parallel to the street canon, there are very few studies on aerodynamic analysis related to wind flow coming perpendicular to such street canyons at high Re. Generally, Re of wind flow around low-rise and high-rise building complexes are in the range $10^5 - 10^7$. The aim of this thesis is fourfold: it is an attempt using the steady RANS approach of CFD (1) to parametrise the generic building models, and analyse the flow structure and pedestrian comfort by changing building dimensions and street width, (2) to analyse a near-wall modelling approach to model the wall roughness effect, with a corresponding validation study for the high Reynolds number, (3) to assess the impact of varying building roof shapes on the flow structure and pedestrian comfort, and (4) to assess the impact of adding roof panels to improve pedestrian comfort. The approaching wind direction considered for all these studied cases is perpendicular to the street canyon.

1.2 History

Wind engineering flow structures are complicated firstly by virtue of the turbulent ABL and secondly due to the fact that the objects of study are mainly non-aerodynamic or bluff bodies.

The branch of Wind Engineering which deals with analysing the wind flow in the vicinity of buildings and to the resulting wind loads on buildings and structures as well as to study the wind comfort and pollutant dispersion in urban areas is called *Building Aerodynamics*. The testing of scale building models in a wind tunnel has, since 1960s, been shown to be a very effective method of predicting the flow around such buildings in urban areas (ASCE, 2003). Wind tunnel modelling had been practised in the aeronautic field, before being applied in building aerodynamics. "The wind tunnels used were specifically designed for aircraft studies, with a uniform wind speed across the tunnel section and with low turbulence" (Blocken et al., 2004). The first attempts to model building aerodynamics were made using these aircraft tunnels. However, "it was recognized at that time that

such wind tunnel results are not representative of full-scale flow around buildings" (Blocken et al. (2004)). It appeared that modelling of the mean wind speed variation with height, as present in the ABL, is essential for reliable results to be obtained. As a result, "new wind tunnels were constructed that specifically take into account the increase of wind speed with height" (Blocken et al., 2004). Such wind tunnels were called boundary layer wind tunnels. The increase in velocity with height was represented by a logarithmic function (Equation 1.1) or by a power law function (Equation 1.2), in such wind tunnels.

$$U(y) = \frac{U^*_{ABL}}{\kappa} \ln\left(\frac{y + y_0}{y_0}\right); \tag{1.1}$$

$$\frac{U(y)}{U_{ref}} = \left(\frac{y}{y_{ref}}\right)^{\alpha}; \tag{1.2}$$

where $U(y)$ is the horizontal mean wind speed at height y, U^*_{ABL} is the frictional velocity, κ is the von Kármán constant, y_0 is the aerodynamic roughness length (Wieringa, 1992), U_{ref} is the reference wind speed at reference height y_0, and α is the power law exponent.

The earlier studies of building aerodynamics in such boundary layer wind tunnels were mainly focused on finding wind loads and dynamic effects of wind on buildings (Blocken et al., 2004). Attention on analysing wind flow around buildings and pedestrian wind comfort was begun in the 1960s. Wise (1970) reported about 200 inquiries concerning the wind environment in pedestrian wind comfort around a group of tall buildings were brought to the Building Research Station (BRS) in 1960s. A number of these have been studied in detail in the BRS wind tunnel (Blocken et al., 2004). Also, wind tunnel studies of airflow around idealized model buildings were also conducted at the BRS (Wise (1970); Wise et al. (1965)). Further wind tunnel studies analysing pedestrian wind comfort around buildings for generic building configurations have been performed by Gandemer (1975), Wiren (1975), Lawson et al. (1975), Penwarden et al. (1975), Kenworthy (1985) and Stathopoulos et al. (1986). These studies provided a basis from which general guidelines, rules of thumbs and empirical formulae were established (Stathopoulos et al. (1995); Blocken et al. (2004)). Wind tunnel studies analysing the flow structure around the complex building structures have been carried out: for example, by Isyumov et al. (1975a), Isyumov et al. (1975b), Lohmeyer et al. (1988), Williams et al. (1992), Richards et al. (2002) and Ferreira et al. (2002).

Numerical modelling using CFD can provide an alternative to the wind tunnel studies. It has an advantage of being less time consuming and less expensive than wind tunnel studies and it can provide detailed wind flow information at each and every location around a considered structure. However, the major drawback of CFD is that it needs model validation either using wind tunnel studies or using full-scale measurements in order to be used with confidence.

"CFD simulations of building aerodynamics with focus on the wind flow structure around buildings were carried out by Paterson et al. (1986), Murakami et al. (1987), Murakami et al. (1988), Baskaran et al. (1989), Stathopoulos et al. (1990) and Baskaran et al. (1992)" (Blocken et al., 2004).

CFD modelling of pedestrian level wind comfort was started in early 1990s. One of the first CFD studies for the pedestrian wind assessment was carried out by Bottema et al. (1992). He studied the flow structure around a single, wide block and in a group of blocks and compared obtained results with wind tunnel measurements. Baskaran et al. (1996) studied the flow around a single building, between two parallel buildings, and around multiple building configurations. For the latter two simulations, they conducted a model validation using the available wind tunnel results of Stathopoulos et al. (1986), Wiren (1975) and Ishizaki et al. (1971). They found good agreement for the parallel buildings when compared with the wind tunnel study. Whereas, for the multiple-building configuration, an agreement was less good. "Richards et al. (2002) built a large numerical model to simulate the pedestrian level wind speed in downtown Auckland. The obtained numerical results were compared with the wind tunnel study results using a scour erosion technique" (Blocken et al., 2004). They found noticeable discrepancies in compared results.

From the literature review above, it can be concluded that some good efforts for validating CFD results for the pedestrian level wind have been conducted, but a systematic validation for a large number of buildings and building groups in different configurations have yet to be reported in the literature.

1.3 Background

1.3.1 Basic definitions

Viscosity

The viscosity of a fluid is a measure of its resistance to gradual deformation by shear stress or tensile stress. Viscosity is due to the friction between neighbouring particles in a fluid that are moving at different velocities. By using Newton's law of friction

$$\tau = \mu \frac{du}{dy},$$

where the proportionality constant μ is the viscosity of fluid.

Reynolds number

Reynolds number is defined as the ratio of inertial forces to friction forces. It is a dimensionless quantity denoted by Re.

$$Re = \frac{\text{inertial force}}{\text{friction force}} = \frac{\rho U d}{\mu} = \frac{U d}{\nu},$$

where U = characteristic free stream velocity, d = characteristic length dimension of the body (e.g. diameter of sphere or height of a square block).

Incompressible flow

In fluid flow, incompressible flow refers to a flow in which the density is constant within a fluid parcel (i.e. very small amount of fluid).

Turbulent flow

Most flows occurring in nature and industrial applications are turbulent. The parameter that determines the turbulence is the Reynolds number. The tendency to instability increases with increasing Reynolds number. For sufficiently large perturbations, the flow becomes unstable as soon as the Reynolds number exceeds a critical value. The flow then enters a transition regime in which irregular bursts of turbulence alternate with laminar flow. As the Reynolds number is further increased, turbulence becomes less periodic and eventually occurs continuously, yielding the fully developed turbulent regime (Mathieu et al., 2000).

Boundary layer

A boundary layer is the layer of fluid in the immediate vicinity of a bounding surface where the effects of viscosity are significant. The boundary layer flow can be laminar or turbulent.

Laminar boundary layers are found only when the Reynolds numbers are small. In a laminar boundary layer flow takes place in layers, i.e., each layer slides past the adjacent layers. In laminar boundary layer exchange of mass and momentum takes place between adjacent layers on a microscopic scale and therefore molecular viscosity μ determines the associated shear stress.

The boundary layer thickness δ of a laminar boundary layer for a flat plate with uniform approaching flow is given by,

$$\delta = \frac{5.0 \cdot x}{\sqrt{Re}},$$

where Re is the Reynolds number based on the length of the plate.

A turbulent boundary layer forms only at larger Reynolds numbers. A turbulent boundary layer is notable by mixing across several layers of it. In turbulent flow exchange of mass, momentum and energy occurs on a much bigger scale compared to a laminar boundary layer. The scale of mixing is not determined by molecular viscosity alone.

For a turbulent flow boundary layer thickness δ for a flat plate with uniform approaching flow is described by correlations of the general form,

$$\frac{\delta}{x} = \frac{const}{Re^n},$$

Separation of the boundary layer

For bluff bodies for which the flow streamlines do not follow the surface of the body, but rather detach from it, creating regions of so-called separated flow and to downstream of the bluff body, region known as the wake (Cook, 1985), separation occurs in places where the pressure increases.

The limit between the forward and reverse flow in the layer very near to the wall is called the *Separation Point*.

$$(\frac{\partial u}{\partial y})_{y=0} = 0$$

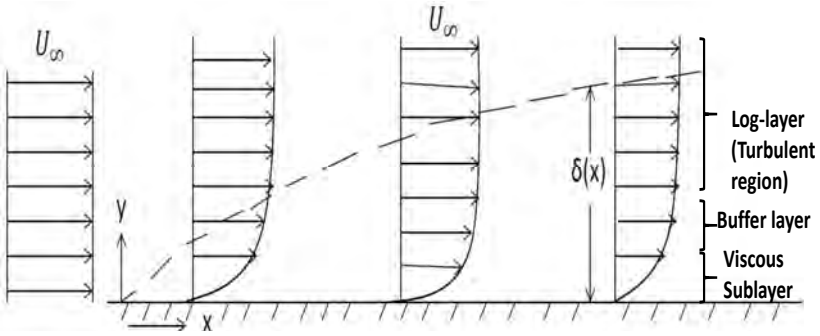

FIGURE 1.1: Boundary layer at a flat plate at zero incidence.

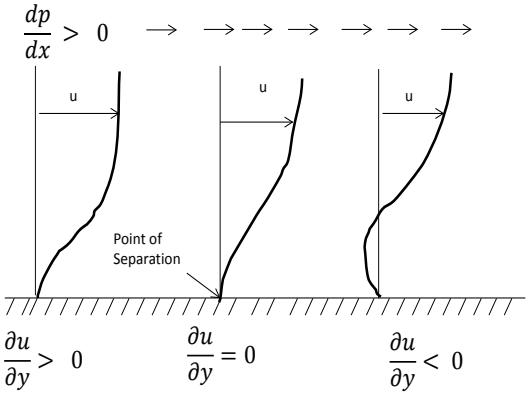

FIGURE 1.2: Adverse pressure gradient at separation.

Flow over a flat plate

Consider the flow over a flat plate (Figure 1.1). When the uniform velocity fluid approaches towards the leading edge of the flat plate, a laminar boundary layer begins to develop. The flow in this region is very predictable. After some distance, small chaotic oscillations begin to develop in the fluid field, and the flow begins to transition to turbulence, eventually becoming fully turbulent. The transition between these three regions can be defined based on a Re in which the length scale is the distance along the plate from the leading edge.

Law of the wall

The flow regimes near a flat wall can be divided into four parts. At the wall, the fluid velocity is zero. For a thin layer close to the wall, the flow velocity is linear with distance from the wall. This region is called the *viscous sublayer*, or *laminar sublayer*. Further away from the wall is a region called the *buffer layer*. In the buffer region, the flow begins to transition to turbulence, and it eventually transitions to a region where the flow is fully turbulent and the average flow velocity is related to the log of the distance to the wall. This is known as the *log-law region*. Even further away from the wall, the flow transitions to the *free-stream region* (or outer layer). Note that

the division of the flow into different regions is based on distance perpendicular to the plate. Figure 1.1 shows subdivisions of the near-wall region on the flat plate.

Pressure coefficient

The outer region of the flow around a flat plate and a bluff body (cube or a building in our case), are regions of inviscid (as if zero viscosity) and irrotational (zero vorticity) flow, and the pressure p and velocity V, in the fluid are related to Bernoulli's equation:

$$p + \frac{1}{2}(\rho V^2) = a\,constant; \tag{1.3}$$

If we denote the pressure and velocity in the region outside the influence of the body by p_0 and V_0 respectively, we have:

$$p + \frac{1}{2}(\rho V^2) = p_0 + \frac{1}{2}(\rho V_0^2); \tag{1.4}$$

$$p - p_0 = \frac{1}{2}\rho(V_0^2 - V^2); \tag{1.5}$$

The surface pressure on the body is expressed in the form of a non-dimensional pressure coefficient (C_p):

$$C_p = \frac{p - p_0}{\frac{1}{2}\rho V_0^2}; \tag{1.6}$$

In the region in which Bernoulli's equation holds:

$$C_p = \frac{V_0^2 - V^2}{V_0^2}; \tag{1.7}$$

Therefore,

$$C_p = 1 - \left(\frac{V}{V_0}\right)^2 \tag{1.8}$$

At the stagnation point, where V is zero, Equation 1.8 gives a pressure coefficient of one. This is the value measured by a total pressure pointing into a flow direction. The pressure $\frac{1}{2}\rho V_0^2$ is called the dynamic pressure.

In a region where the flow velocity is greater than V_0, the pressure coefficient is negative. Bernoulli's equation is not valid in the separated flow regions, but a reasonably good prediction of C_p can be obtained from Equation 1.8, by taking the velocity, V as that just outside the shear layers and wake region (Holmes, 2015).

Force coefficients

Force coefficients are defined in a similar non-dimensional way to pressure co-efficient:

$$C_F = \frac{F}{\frac{1}{2}\rho V_0^2 A}; \tag{1.9}$$

where F is the total aerodynamic force, and A is a reference area which is also called a projected frontal area.

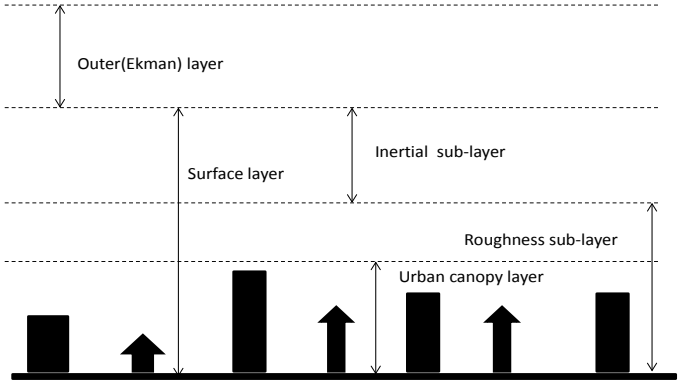

FIGURE 1.3: Schematic of atmospheric boundary layer (ABL) structure.

Aerodynamic forces are conventionally resolved into two orthogonal directions (Holmes, 2015). These may be parallel and perpendicular to the wind direction (or mean wind direction in the case of turbulent flow), in which case, the axes are referred to a *wind axes*, or are parallel and perpendicular to a direction related to the geometry of the body (body axes). The term "lift" and "drag" are commonly used in wind engineering for cross-wind and along-wind force components, respectively. Substituting L and D for F in Equation 1.9 gives the definition of *lift* and *drag* coefficients.

1.3.2 Atmospheric boundary layer (ABL)

"The lower part of the atmosphere where the circulation of air around the Earth's surface creates frictional forces are important and also where transport process at the boundary between the earth's surface and the atmosphere modifies the lowest 100 to 3000 m of the atmosphere creating a layer of micro-scales called the boundary layer" (Azad, 1993). The thickness of the ABL is determined by the gradient height at which surface friction of the ground no longer affects the general flow of the wind. In the ABL in addition to friction, has a force of buoyancy resulting from the thermal condition of the atmosphere and the influence of a Coriolis force due to the Earth's rotation. The transport of heat, momentum and pollutants are influenced by turbulence. Thus ABL is a turbulent boundary layer in rotating heavily stratified fluid. The ABL is divided into a surface (or inner) layer and outer (Ekman) layer (as shown in Figure 1.3).

Structure of atmospheric boundary layer (ABL)

Surface layer

The lower part of the ABL, in which only slight changes with height are observed in the components of vertical momentum flux is called the *surface layer*. The surface layer is further divided in to roughness sublayer and inertial sublayer. The outer layer continues from the surface layer to the top of the boundary layer (Figure 1.3).

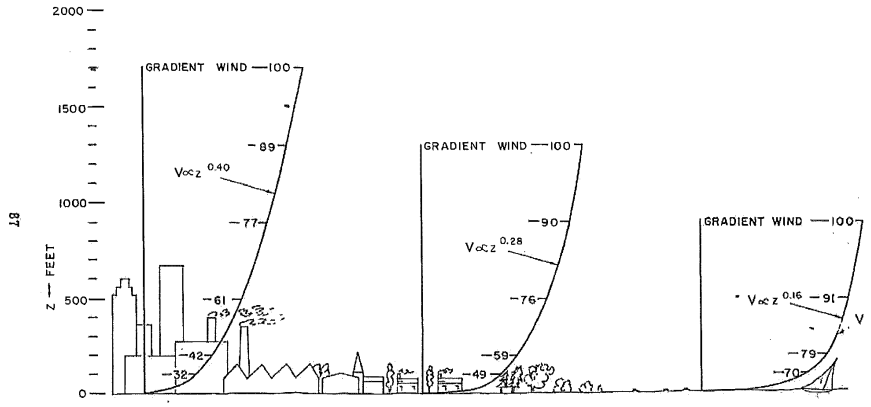

FIGURE 1.4: Profiles of mean wind speed over level terrains of different roughness. From Davenport (1965).

Roughness sublayer

The roughness sublayer is a region in which the underlying buildings, fences, trees, etc. lead to a spatial horizontal inhomogeneity of the flow. The average wind speed increases with the height above the ground, while the intensity of the turbulence or gustiness decreases. The difference in terrain conditions directly affects the magnitude of the frictional force and also causes the mean wind speed variations, which is as shown in Figure 1.4.

The roughness sublayer extends up to approximately twice the average building height. The roughness sublayer may be further divided into viscous layer and urban canopy layer.

Urban canopy layer in roughness sublayer

The assemblage of buildings, trees, and other objects composing a town or city and the spaces between them together with the air layer beneath rooftop and treetop level, forms the urban canopy layer. The logarithmic law representing the variation of the mean wind speed with height above the ground surface can be expressed by Equation 1.1.

Ekman layer

In the outer region (Ekman layer) the airflow shows little dependence on the nature of the surface, and the Coriolis force due to the Earth's rotation becomes important. The increase of the height leads to the Coriolis force and the reduction of the shear stress. This region is referred to as the Ekman layer in honour of Ekman (1905) who first dealt with the effects of rotation on boundary-layer flow in the ocean. An empirical power law representation of the mean velocity profile in the outer layer is given by Equation 1.2.

According to above understanding of the ABL, it is clear that most of the flow past obstacles in the atmosphere occurs in the surface layer, so the work in this thesis is concerned with the flow in the roughness sublayer of the surface layer.

1.3.3 Wind comfort assessment at pedestrian level

"Wind comfort assessment studies at the pedestrian level consist of combining **statistical meteorological data** with **aerodynamic information** and **comfort criteria** which focus only on the mechanical effects of wind on people" (Blocken et al., 2004), (Blocken et al., 2008b), (Blocken et al., 2009b), (Blocken et al., 2012) and (Janssen et al., 2013)). "Mechanical effects on people range from the feeling of a light breeze on the skin to being blown over by a strong gale" (Lawson et al., 1975).

Statistical meteorological data

"Generally, data are selected from a nearby meteorological station at which the wind climate is considered representative for the building site. The data should cover a period of several decades and should be exposure corrected. That data should be in hourly mean values of potential wind speed (U_{pot}) and wind direction"(Blocken et al., 2009b).

U_{pot} is the wind speed at 10 m height at an ideal meteorological station with an aerodynamic roughness length $z_0 = 0.03$ m.

Aerodynamic information

"Aerodynamic information is needed to transform the statistical meteorological data from weather stations to the location of interest at the building site, after which it is combined with a comfort criterion to judge local wind comfort" (Blocken et al., 2004), (Blocken et al., 2008b). The aerodynamic information usually consists of two parts:

- The terrain-related contribution (TRC).

  The TRC represents the change in wind statistics from the meteorological site to a reference location near the building site (U_{pot} to U_{ref}).

  Different transformation procedures exist to determine the TRC. They often employ a simplified model of the ABL such as the logarithmic mean wind speed profile or power-law profile as specified in Equation 1.1 and 1.2.

- The design-related contribution (DRC).

  The DRC represents the change in wind statistics due to the local urban design i.e., the building configuration (U_{ref} to U).

  The DRC is usually obtained by wind tunnel test or CFD.

The ratio of the local pedestrian level mean wind speed U at the location of interest (when the buildings were present) to U_{pot} is given by the total wind speed amplification factor γ,

$$\gamma = \frac{U}{U_{pot}} = \frac{U}{U_{ref}} \cdot \frac{U_{ref}}{U_{pot}},$$

which can be split into contributions from different spatial scales: The DRC (U/U_{ref}), and the TRC (U_{ref}/U_{pot}).

Where, U_{ref} = reference wind speed, it will be taken at some height near the building site (for general CFD and wind tunnel studies it is also referred

to as the wind speed value that would occur at the location of interest at a pedestrian height if the buildings were absent. In some studies it is denoted by U_0).

Comfort criteria

Types of wind and wind assessment studies

People do not only respond to the mean wind speed, but also to the random fluctuations in speed caused by turbulence. Bottema (2000) investigated the mechanical wind effects caused by three types of wind: Steady wind; non-uniform wind; and gust wind. According to wind effect study by Hunt et al. (1976), people are more affected by spatially non-uniform winds and by wind gusts, than by uniform winds. Wind gusts can be specified by a gust speed U_g; and a gust duration t_g.

Therefore, the wind force assessment studies so far are based on mean and gust wind speeds. In several publications, an effective or equivalent wind speed U_e which integrates both mean and gust speed is used, which can be defined as:

$$U_e = U + k\sigma_u$$

Where U is the mean wind speed at for example 1.75 m height (Human comfort with respect to wind is most sensitively judged at the head height ($Y \simeq 1.75\,m$) (Gandemer, 1981)), k the peak factor, and σ_u the standard deviation. If the gust duration t_g, the total averaging time T_{av}, and the probability density function (p.d.f.) of wind speed are known, k can be evaluated. Different authors have proposed different values of k between 0 (Isyumov et al., 1975b) and 4 (Hunt et al., 1972).

Pedestrian discomfort and danger thresholds

According to Bottema (2000) pedestrian discomfort can be defined as : "Pedestrian discomfort occurs when wind effects become so strong, and occur so frequently (say on time scales up to 1 h) that people experiencing those wind effects will start to feel annoyed, and eventually will act to avoid these effects", and he defined wind discomfort threshold as "the threshold where wind effects start to occur is a lower bound for discomfort". For wind danger threshold, according to him within for example an hour, any gust or equivalent wind speed exceeding a danger threshold level will be unacceptable.

Early wind tunnel study by Hunt et al. (1976) for turbulent wind speed, presented some thresholds as a function of the following effective wind speed (Bottema, 2000):

$$U_e = U + 3q;\; q = \sqrt{\sigma_u^2 + \sigma_v^2}$$

According to them wind effects become noticeable in the test results for $U_e > 6\,m/s$, but most performance is reported to remain unaffected for $U_e < 9\,m/s$. Their recommended peak factor k of 3 is valid for outdoor conditions (Bottema, 2000).

Wind discomfort or danger thresholds (U_{THR}) at pedestrian height are generally specified by the following equation (Blocken et al., 2004):

$$U_e = U + k \cdot \sigma_u > U_{THR}$$

According to Bottema (2000), in the absence of universally accepted thresholds for wind discomfort and danger, could lead to differing judgements of an architectural design, which is undesirable. As a consequence, we need general consensus on the thresholds to be used. In the absence of such a consensus, we can use the following working thresholds:

- Discomfort: $U_e = U + \sigma_u > 6\, m/s$
- Danger: $U_e = U + 3\,\sigma_u > 20\, m/s$

Classification of pedestrian areas, activities

Most of the discomfort and danger wind speed thresholds are varied depending on the human activities at a particular location. Hours of the day during which pedestrians are active for various pedestrian use areas within the city are the factor which influences the criteria of comfort. Williams et al. (1990) divided pedestrian areas into two groups: Optional use and Required use. According to them, Optional use can be defined as the areas that pedestrians have the option of using depending on the weather. Whereas Required use can be defined as areas that people are required to use. They suggested that the acceptability of the wind conditions occur for a majority of the time differently depending on the above defined two groups. In some cases, the comfort criteria consider two main aspects: Safety and Levels of comfort for various pedestrians activities such as walking, sitting or standing.

The pedestrian level wind is regarded as the important part involved in the building design. Therefore it is important to evaluate the effect of any new building on the pedestrian level wind. Stathopoulos (2006) described pedestrian-level winds in terms of velocities in the presence and absence of a new building within a specific urban environment. Penwarden (1973) found that substantial complaints occurred when the limit of comfortable wind speed was exceeded for more than 10% of the time. Therefore, all places in or near the area where pedestrian activities are involved have to estimate the probability of occurrence in order to make sure the probability is within the acceptable range.

Discomfort and danger probability

Discomfort and danger probability are defined as the percentage of hours in which the discomfort and danger thresholds are exceeded. For evaluating these probabilities the long-term wind statistics (climate data) are needed. In order to make this long-term statistics data of a meteorological station relevant to the building location, local mean wind speeds and turbulence conditions must be linked to those at the measuring station. Mean wind speed can be linked by using a wind amplification factor $\gamma = \frac{U(1.75\,m)}{U_{pot}} = \frac{U}{U_{pot}}$.

Wind speed statistics are described by cumulative Weibull distributions. The percentage P of hours with uncomfortable or dangerous conditions is given by:

$$P_{\Theta}\left(U_{pot} > U_{THR,pot}\right) = 100 \cdot A(\Theta) \cdot exp\left[-\frac{U_{THR,pot}}{c(\Theta)}\right]^{k(\Theta)} \tag{1.10}$$

Where, $U_{THR,pot}$ = given threshold for the potential wind speed,

$P_{\Theta}\left(U_{pot} > U_{THR,pot}\right)$ = probability of exceeding of $U_{THR,pot}$ by U_{pot} during wind direction Θ,

$A(\Theta)$ = probability for wind direction Θ,

$c(\Theta)$ = velocity scale for wind direction Θ (m/s) (Weibull parameter),

$k(\Theta)$ = shape parameter for the wind direction Θ (Weibull parameter).

The Weibull distribution is well suitable for $4 < U_{pot} < 16\,m/s$ (obtained from Bottema (2000)) which covers most wind speeds of interest for wind discomfort.

Note: Measured wind speed data are commonly available in the time-series format, in which each data point represents either an instantaneous sample wind speed or an average wind speed over some time period. In some instances, wind speed data may instead be available in frequency distribution format (Seguro et al., 2000).

Comfort criteria measurement by different approaches

According to our review of research into wind comfort assessment studies, a wide range of different wind comfort criteria exists which generally focus only on the mechanical effects of wind on people. Based on this review a suitable wind comfort criterion may consist of a discomfort threshold and an exceedance probability of the threshold. Many criteria also distinguish between various activities, such as sitting, strolling, walking fast etc. In that case, either different values for threshold wind speed, or different maximum exceedance probabilities, or both, are imposed for these different activities. It is unfair to judge the different approaches whether right or wrong, good or bad.

Penwarden (1973) defined comfort criteria based on mean speed for three main parameters namely: onset of discomfort, definitely unpleasant and dangerous. There is no probability of occurrence involved in this approach. The minimum mean speed allowed according to this criteria is 5m/s and the maximum speed is 20m/s.

Hunt et al. (1976) looked at comfort based on two basic categories of activities namely: safe, sure walking, and tolerance conditions and unaffected performance. They offered criteria based on wind tunnel tests on human subjects. These criteria are based on mean and gust speeds and the probability of occurrence. According to their study, the gust wind speed is higher than the mean wind speed when comparing the same activity at one time. An equivalent steady wind speed defined by them is $U_e = U + 3q$; $q = \sqrt{\sigma_u^2 + \sigma_v^2}$. They also proposed new criteria for acceptable wind conditions based on (i) comparison with a local reference point, such as an airport and (ii) probabilistic arguments, i.e. how many times a year certain comfort, performance or safety criteria should be exceeded.

A thorough study of comparison of existing wind comfort criteria was performed by Bottema (2000). "He compared most of the existing criteria based on a theoretical method, in which each criterion was converted to a maximum allowed wind amplification factor U/U_{pot} (where U is the local hourly wind speed and U_{pot} is the so-called potential wind speed" (Janssen et al., 2013). The potential wind speed is the hourly wind speed at an ideal meteorological station, at $10\,m$ height over uniformly rough terrain with an aerodynamic roughness length $z_0 = 0.03\,m$). Based on this comparison, he concluded that considerable differences exist between the different criteria. According to a study by Janssen et al. (2013), Bottema's approach provides a very valuable and systematic way of comparing different criteria, it also has some limitations. The wind amplification factor was assumed to be wind-direction independent, and the practical consequences of differences between criteria were rather difficult to interpret, visualize and communicate. In this respect, analysis of differences between criteria by means of illustrative case studies would be beneficial.

Janssen et al. (2013) compared four different existing wind comfort criteria (i.e. those by (1) Isyumov et al. (1975b), (2) Lawson (1978), (3) Melbourne (1978) and (4) the Dutch nuisance standard NEN 8100 (Janssen et al., 2013) based on a case study. They selected these criteria in their study because they are considered as "complete" criteria, as they address a wide range of activities, including "sitting/standing long", "sitting short", and "strolling". These all criteria consist of a threshold value of the wind speed and a maximum allowed exceedance probability of this threshold value. From their comparison study, they concluded that the Dutch nuisance criterion is the best pedestrian wind acceptability criterion currently available in published form. However, according to our best knowledge, its main drawback is that up to the present date all considered case studies using this criterion are based in the Netherlands. So, for this criterion to be accepted internationally it could be validated using case studies in other countries too.

According to a study by Koss (2006), the comparison of comfort criteria based on gust wind speeds shows a fundamental difficulty in the consideration of local turbulence. **Therefore, the local condition for the area of interest has to be considered and involved in the comfort criteria**.

City rules

As discussed in the previous subsection, the local wind condition is one of the key factors of the pedestrian comfort level. Different city authorities have to analyse the wind data first, then set the regulations or rules to evaluate pedestrian comfort (Aynsley, 1989). City planners can then ensure that new developments do not worsen the condition and become uncomfortable or dangerous for pedestrians.

In Bristol (Penwarden et al., 1975), there are 6 standard categories for use areas for assessing the acceptability of comfort criteria. It accounts the probability of occurrence according to the Beaufort scale. For any sitting area, if wind speed exceeds Beaufort scale 4 for 6 % of the time, the area is unacceptable.

TABLE 1.1: Definition of Auckland city wind categories (Auckland City (1997); Richards et al. (2002); Flay (1989)).

Category	Description
A	Areas of pedestrian use containing significant formal elements and features intended to encourage longer term recreational or relaxation use, i.e. major and minor public squares, parks and other public open spaces - e.g. Aotea Square, Queen Elizabeth Square, Albert Park, Myers Park, St Patricks Square, Freyberg Place.
B	Areas of pedestrian use containing minor elements and features intended to encourage short term recreation or relaxation, i.e. minor pedestrian open spaces, pleasance areas in road reserves, streets with significant groupings of landscaped seating features e.g. Khartoum Place, Mayoral Drive Pleasance areas, Queen Street.
C	Areas of formed footpath or open spaces pedestrian linkages, used primarily for pedestrian transit and devoid of significant or repeated recreational or relaxational features, such as footpaths where not covered in Categories A - B above.
D	Areas of road, carriage way, or vehicular routes, used primarily for vehicular transit and open storage, such as roads generally when devoid of any feature or form which would include the spaces in Categories A - C above.
E	Category E represents conditions which are dangerous to the elderly and infants and of considerable cumulative discomfort to others. Category E conditions are unacceptable and are not allocated to any physically defined areas of the city.

In Boston (Aynsley, 1989), an effective gust wind speed of $13.8\,m/s$ with an occurrence rate of $1\,\%$ of time is the maximum acceptable pedestrian level wind caused by new buildings.

In North America (ASCE, 2003), the criteria for three levels of activity is based on a probability of exceedance on 20%. Any speed above $5.4\,m/s$ in terms of mean speed and gust equivalent mean speed is classified as uncomfortable for any activity.

In London for example on the Canary Warf development (ASCE, 2003), the comfort level is based on 5% probability of exceedance. A wind speed above $10\,m/s$ exceeds 10% of the time is recognised as uncomfortable in this case. The approximate speed ranges corresponding to 20% probability are listed as well.

In Wellington in city of New Zealand (Council, 2000), according to the city council's wind regulation, an effective gust speed of $18\,m/s$ is the maximum acceptable speed for new buildings in the central area, and if the wind speeds in a proposed development exceed this wind condition, the developer has to take some actions to reduce the wind speeds.

In Auckland in city of New Zealand, pedestrian level winds are regulated by the requirements of the District plan (Auckland City (1997); Richards et al. (2002); Flay (1989)). This document defines the acceptable wind conditions according to the purpose intended for each area. The associated categories, which are listed in Table 1.1 range from Category A, which includes public squares, to Category D for road carriageways. There is also a Category E but this wind condition is considered dangerous and is generally undesirable (Richards et al., 2002). The associated wind statistics are as shown in Figure 1.5. These wind categories are specified in terms of the probability of exceeding certain hourly mean speeds (Flay, 1989). In order to be classified as Category A the hourly mean wind speed of the area must be less than 4.3 m/s for 99% of the time, whereas to be classified Category D the hourly mean wind speed needs to be less than 10.3 m/s for 99% of the time.

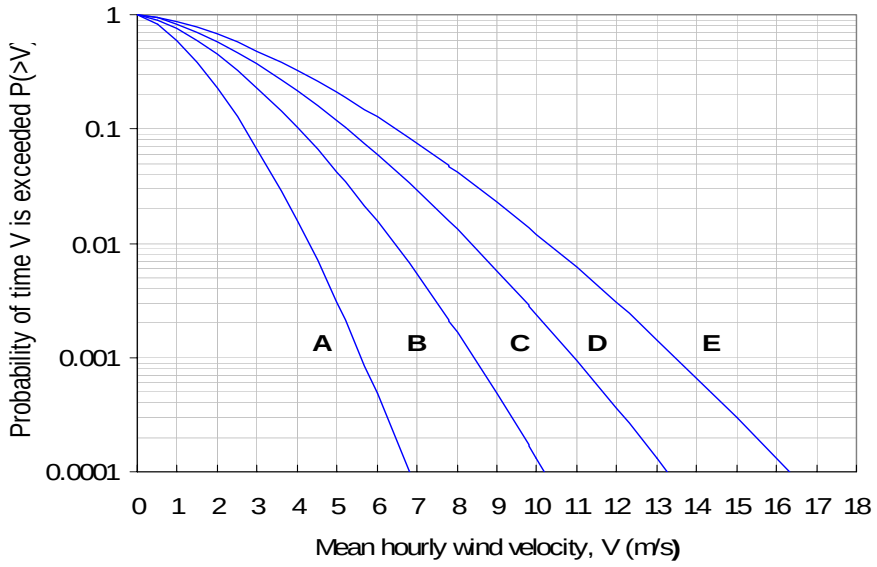

FIGURE 1.5: Wind Statistics for Auckland city wind Category. From Flay (1989).

This study concerns terrain of the type commonly found in Australia and New Zealand. These countries use Land Beaufort Scale for wind speed measurement at the ground level. Originally designed for use at sea, it has since been extended and revised for estimating wind speeds on land and to a pedestrian level height. The Land Beaufort Scale (LBS) showing wind speed at 10 m height over open terrain with an aerodynamic roughness length y_0 of 0.03 m is as given by Penwarden (1973) (as shown in Table 1.2 and copied from (Penwarden, 1973)). The Extended Land Beaufort Scale is the translation of the wind speed from 10 m height to a pedestrian level (1.75 m) height given by Lawson et al. (1975), which is as tabulated in Table 1.3 and has been used as the standard measure for the wind speed in the later chapters in this thesis.

1.3.4 Principles of CFD

Overview

A CFD code works by dividing the region of interest into a large number of cell or control volumes (the mesh or grid). In each of these cells, the partial differential equations describing the fluid flow (the Navier-Stokes equations) are replaced by algebraic approximations that relate the pressure, velocity and other variables, to the values in the neighbouring cells. These equations are then solved numerically yielding a complete flow profile to the grid resolution.

At the first stage, a computational domain is created to represent the geometry of the model. Then the mesh divides the computational domain into a finite number of cells. This is followed by the definition of the fluid properties and specifying boundary conditions. The numerical solver than solves the equations for each cell until an acceptable convergence is achieved. Finally, at the post-processing stage, the modelled results are analysed both numerically and graphically.

TABLE 1.2: Land Beaufort Scale (LBS) showing wind effects on people (Penwarden, 1973).

Beaufort Number	**Description**	**Wind speed at 10 m height (m/s)**	**Effect**
0	Calm	$0.0 - 0.2$	
1	Light air	$0.3 - 1.5$	No noticeable wind
2	Light breeze	$1.6 - 3.3$	Wind felt on face
3	Gentle breeze	$3.4 - 5.4$	Hair disturbed, clothing flaps, newspaper difficult to read
4	Moderate breeze	$5.5 - 7.9$	Raises dust and loose paper, hair disarranged
5	Fresh breeze	$8.0 - 10.7$	Force of wind felt on body, danger of stumbling when entering a windy zone
6	Strong breeze	$10.8 - 13.8$	Umbrellas used with difficulty, hair blown straight, difficult to walk steadily, sideways wind force about equal to forwards walking force, wind noise on ears unpleasant
7	Near gale	$13.9 - 17.1$	Inconvenience felt when walking
8	Gale	$17.2 - 20.7$	Generally impedes progress, great difficulty with balance in gusts
9	Strong gale	$20.8 - 24.4$	People blown over

TABLE 1.3: Extended Land Beaufort Scale (ELBS) showing wind effects on people (Lawson et al., 1975).

Beaufort Number	**Description**	**Wind speed at 1.75 m height (m/s)**	**Effect**
0	Calm	$0.0 - 0.1$	
1	Light air	$0.2 - 1.0$	No noticeable wind
2	Light breeze	$1.1 - 2.3$	Wind felt on face
3	Gentle breeze	$2.4 - 3.8$	Hair disturbed, clothing flaps, newspaper difficult to read
4	Moderate breeze	$3.9 - 5.5$	Raises dust and loose paper, hair disarranged
5	Fresh breeze	$5.6 - 7.5$	Force of wind felt on body, danger of stumbling when entering a windy zone
6	Strong breeze	$7.6 - 9.7$	Umbrellas used with difficulty, hair blown straight, difficult to walk steadily, sideways wind force about equal to forwards walking force, wind noise on ears unpleasant
7	Near gale	$9.8 - 12.0$	Inconvenience felt when walking
8	Gale	$12.1 - 14.5$	Generally impedes progress, great difficulty with balance in gusts
9	Strong gale	$14.6 - 17.1$	People blown over

Navier-Stokes equations

The Navier-Stokes equations are derived from consideration of conservation of mass, momentum and energy. Since no thermal effects will be considered in this study, the only conservation laws that are required are those that ensure mass and momentum are conserved.

Using the Finite volume method, the equation for the conservation of mass (i.e. continuity equation) is discretised by means of a mass balance for each finite volume. Thus for a steady incompressible fluid with uniform temperature, the incoming mass flow is equal to the outgoing mass flow (Versteeg et al., 2007).

"By applying Newton's Second Law of Motion, the relationship between the forces on a control volume of fluid and acceleration of the fluid gives an expression of the conservation of momentum" (Versteeg et al., 2007).

These fundamental principles can be expressed in terms of a set of partial differential equations and in solving these equations the velocity and pressure are predicted throughout the flow field.

Conservation of mass

Here we assume the fluid is incompressible, so the conservation of mass can be expressed by:

$$\boldsymbol{\nabla} \cdot (\rho \vec{u}) = \frac{\partial u}{\partial X} + \frac{\partial v}{\partial Y} + \frac{\partial w}{\partial Z} = 0 \tag{1.11}$$

where ρ is the density of the fluid, u, v and w are the velocity components in the X, Y and Z direction respectively such that, $\vec{u} = u\hat{i} + v\hat{j} + w\hat{k}$

Conservation of momentum

The conservation of momentum equations for the X , Y and Z - directions are given by:

$$\frac{\partial(\rho u)}{\partial t} + \boldsymbol{\nabla} \cdot (\rho u \vec{u}) = \frac{\partial p}{\partial X} + \boldsymbol{\nabla} \cdot (\mu \nabla u) \tag{1.12}$$

$$\frac{\partial(\rho v)}{\partial t} + \boldsymbol{\nabla} \cdot (\rho v \vec{u}) = \frac{\partial p}{\partial Y} + \boldsymbol{\nabla} \cdot (\mu \nabla v) \tag{1.13}$$

$$\frac{\partial(\rho w)}{\partial t} + \boldsymbol{\nabla} \cdot (\rho w \vec{u}) = \frac{\partial p}{\partial Z} + \boldsymbol{\nabla} \cdot (\mu \nabla w) \tag{1.14}$$

These three momentum equations, along with the continuity equation described in Equation 1.11 are called the Navier-Stokes equations.

The study of turbulent flow at high Re is facilitated by modification to the governing equations. The velocity terms in the above Navier-Stokes equations are replaced with mean and fluctuating components.

$$u = U + u' \qquad v = V + v' \qquad w = W + w' \tag{1.15}$$

In addition the pressure term is re-written as:

$$p = P + p' \tag{1.16}$$

Replacing this terms into Navier-Stokes equations and averaging them over time results in the Reynolds Averaged Navier-Stokes (RANS) equations.

Direct numerical simulation

Direct simulation allows numerical experiments to be carried out that are often difficult or impossible to realize in the laboratory and yield detailed information about the flow field in individual realizations. Unlike other simulation techniques for turbulent flows, direct numerical simulation (DNS) does not involve approximations, other than those due to discretization, which is inherent in any numerical solution of differential equations, and so provides a benchmark against which less costly simulation method may be evaluated, just as they can by using the results of physical experiments. DNS is limited to relatively low Reynolds number in practice and it is currently very expensive to conduct a DNS calculation at even moderately high Reynolds number. Thus, as has been indicated by Moin et al. (1998), DNS is a research tool, rather than an aid to engineering design.

In DNS, the steady incompressible Navier-Stokes equations may be treated numerically in various ways. At any instant of time, the flow field, characterized by $u(x,t)$ i.e. velocity as a function of space and time and $p(x,t)$ i.e. pressure as a function of space and time has, in principle, an infinite number of degrees of freedom. However, only a finite set of variables can be handled numerically and numerical schemes, therefore, involve an approximate representation of the flow in a finite number of unknowns, a procedure referred to as *spatial discretization*. For e.g., one might use the value of $u(x,t)$ and $p(x,t)$ at a discrete set of grid points to describe the flow . Spatial discretization is an approximation and, for it to be acceptable, it needs to be able to represent the real flow with reasonable accuracy. In particular, it should be capable of resolving the smallest dynamically important scales of turbulence, that is, the dissipative scale of size $O(\eta)$, where η denotes the Kolmogorov scale (Mathieu et al., 2000). As Re increases, the size of the dissipative scale decreases, and require the spatial resolution of the scheme at larger Reynolds number, for instance, the grid should be made finer in grid-based schemes. This leads to rapidly increasing memory and calculation requirements and limits the Reynolds number reachable by DNS.

Steady RANS

A common averaging method to eliminate the time dimension used in CFD is the infinite time averaging, which leads to a statistically steady description of the turbulent flow. This approach is called the steady RANS approach. "This approach as it eliminates the time dimension is very effective but questionable whether the resulting equations are still accurate to model the inherently unsteady flow behaviour" (Franke et al., 2007). However, this has been used for comparison with the "wind tunnel studies and adequately represents the wind tunnel's reality as the time-averaged approach flow conditions of the tunnel do not change" (Franke et al., 2007).

Unsteady RANS

In this approach, the basic unsteady RANS (URANS) equations are derived by applying ensemble averaging or as time averages over small (finite) time intervals. However, the turbulence models used for the steady RANS and unsteady RANS are same. "Only with ensemble averaging the resulting equations comply with the steady RANS equations now containing the partial time derivatives" (Franke et al., 2007).

Large Eddy Simulation

Large Eddy Simulation (LES) is a popular technique for simulating turbulent flows. In DNS, all the scales of the flow (i.e. injection scale to dissipative scale) are properly resolved, but the scheme is limited in Reynolds number by the available computer power. LES solves the Navier-Stokes equations, as in DNS, but for some higher Reynolds number of the flow, the spatial resolution of the scheme is insufficient to describe the smallest scales (dissipative scales). Thus, LES generates an approximation to the real flow in which scales below a certain size are missing. However, all scales of turbulence are dynamically significant and so the lack of scales below a certain size must somehow need to be corrected (Mathieu et al., 2000). This correction can be done by adding new terms into the equation of motion, which are known as *subgrid terms*, which only come into play when the smaller scales need to be resolved using LES. That is, subgrid terms are not supposed to affect the larger scales of the flow, which are handled as in DNS. The art of selecting subgrid terms, matched to the particular flow and numerical scheme used, is known as *subgrid modelling*. Such an approximation may be incapable of getting all the information about smallest scales of the real flow but allow us to achieve higher Reynolds number and/or larger computational domains compare to DNS at a given computational cost.

Numerical grid

A mesh for CFD calculation must meet several requirements. The mesh has to be designed in such a manner that it does not introduce errors that are too large. For bluff bodies like buildings, to accurately determine the flow variables such as drag, lift and pressure distribution on the building model or the wind velocity prediction on the roof or in the wake of such building model (especially regions with high turbulence level such as at the ground level or at the pedestrian height) requires a mesh on the surface of the building and in its vicinity that includes the relevant geometric details of the building model and accounts for the pressure and velocity gradients that form in the boundary layer above the surface. In the current study, meshing was performed using the functions available within ANSYS Fluent 17.0.

Meshing for analysing the flow structure around the buildings typically consists of a computational domain consisting of a velocity inlet, an outlet as outflow (the outflow boundary condition in the Fluent is a Neumann boundary condition with the derivative of all flow variables in the exit direction (perpendicular to the boundary) equal to zero Fluent (2011a)), top and sides as symmetry boundary and no-slip boundaries on the surface of

the building and on the ground. The inlet, top and side boundaries are typically about $5 - 6.5$ model heights away from the building to reduce any wall interactions, while outflow is typically set 15 or more model heights downstream to allow formation and decay of the wake region (Franke et al., 2007). A "body of influence" mesh refinement box is generally placed around the building model and often another in the building wake region to allow a greater refinement of the mesh in those regions that influence most of the flow characteristics.

Two main types of numerical grids available in CFD code are structured grids and unstructured grids.

The structured 3-dimensional mesh consists of primarily hexahedral elements which are orthogonal within an i, j, k space. This means that the grid can be indexed and the neighbours of each point can be calculated rather than looked up from pre-stored data (Sayma, 2009). Because the elements are arranged orthogonally in a structured mesh there are coding advantages that allow the mesh to contain fewer elements and be more computationally efficient. However, the generation of the domain decomposition into blocks in structured mesh requires much time and effort from the user.

The unstructured grids apply a mixture of tetrahedral, pyramidal, prismatic and hexahedral computational cells. They are easier to generate than a structured grid and better for local refinement. The disadvantage of the unstructured grids is the irregularity of the data structure, which means that the development of accurate discretisations and efficient solution methods is more difficult than for structured grids (Blazek, 2015). In this study, because of the requirement of the local refinement of the mesh on the surface of the building and in its wake to accurately predict the flow variables (especially the wind velocity), an unstructured mesh scheme was used.

A series of stacked "inflation layers" in the region of the mesh about the building surfaces and on the ground are generally used to account for the transition from the viscous sublayer through the buffer layer to the turbulent logarithmic layer and beyond of the wall boundary layer. When modelling the near-wall region the y^+ value is a critical parameter to determine the first cell of the CFD mesh resides within the viscous sublayer or the logarithmic layer region. Here, y^+ is defined as:

$$y^+ = \frac{\rho \cdot u_\tau \cdot \triangle y}{\mu}$$

where $\triangle y$ is the distance normal to the wall, and $u_\tau = \sqrt{\tau_w/\rho}$ is the shear velocity, computed from the wall shear stress τ_w.

According to the universal law of the wall, the near wall region consists of three main regions and can be represented in terms of non-dimensional variable y^+ as:

- the laminar sublayer or the viscous sublayer, where, $y^+ \leq 5$
- the buffer layer, where, $5 < y^+ < 30$ and
- the logarithmic layer can extend from $y^+ = 30$ to up to $y^+ = 500 - 1000$ (Blocken et al., 2007b)

A detailed discussion about the selection of first-cell y^+ for the turbulent model used in this study is as discussed in the subsection 2.2.3.

Turbulence modelling

"Turbulent flow contains turbulent eddies with a wide range of length scales, from the energy carrying large scales to the small dissipative scales. These spatial scales are typical 10^{-5} to 10^{-6} of the size of the computational domain in each coordinate direction" (Casey et al., 2000). By solving the complete, time-dependent Navier-Stokes equations, DNS captures the time and length scales of all the characteristic structures of the turbulent flows. However, due to the computational cost associated with the DNS for high Re flows, it has limited its application for such flows.

In most engineering applications, the emphasis is placed on the effects of the turbulence on the mean flow rather than resolving the details of the turbulent fluctuations. Thus, a turbulent flow can be described by the mean values of the flow properties and the statistical properties of their fluctuations. By performing the time-averaging operation of the momentum equations, we can obtain time-averaged momentum equations (RANS equations) and six additional unknowns, the so-called Reynolds stresses, which represent the velocity fluctuating effects of the flow. "In order to close the system of mean flow equations, assumptions are needed for the extra unknown terms generated by the averaging process. This procedure of solving the closure problems is called turbulence modelling" (Versteeg et al., 2007).

There are a variety of commercial and open source CFD programs available. Most provide several choices for modelling flow in the turbulent regions. ANSYS Fluent 17.0, for example, offers several different RANS turbulence models to solve for the flow field. However, it is unfortunate that no single turbulence model is universally accepted as being superior for all classes of problems. "The choice of a turbulence model generally depends on considerations such as the physics of the flow, the established practice for a specific class of problem, the level of accuracy required, the availability of computational resources, and the amount of time available for the simulation" (Fluent, 2013). Rather a validation strategy may be used is proposed to evaluate the performance of the different turbulence models. The validation test cases should be computed with several different turbulence models available for Reynolds stresses. A detailed discussion about the turbulence model selected for this study and validation is given in Chapter 2.

1.4 Thesis structure

This thesis is divided into six main chapters. The first chapter provides a logical introduction and motivation to the entire thesis. This also includes a brief literature review on building aerodynamics, background and some of the general techniques used in CFD to model the wind flow around buildings.

Chapter 2 compares CFD simulations developed with ANSYS Fluent to validate the CFD approach with published results for wind velocity profiles, surface pressure and turbulent kinetic energy to validate the prediction of the flow structure around a single building configuration.

Chapter 3 is a parametric study to analyse the flow structure and pedestrian comfort inside uniform and non-uniform street canyons for medium

rise buildings inside a thick ABL. Parameters in this study include; the street width, building width and building height.

Chapter 4 extends the study to include the effect of changing roof shapes of both the upstream and downstream building, only the upstream building and only the downstream building of the street canyon on the flow structure and pedestrian level wind comfort. The different roof shapes considered in this study are vaulted, slanted, trapezoidal, upstream vaulted and downstream vaulted.

In Chapter 5, CFD results of a study in which deflector panels are added on the building roof to modify the flow structure to improve pedestrian comfort inside the street canyon are added. Key parameters considered for this study are the angle of the panel and location of the panel.

Finally, Chapter 6 summarizes the main results of the current thesis. Suggestions for future studies and investigations in these areas are provided.

Each chapter contains its own description of the numerical method details. Methods used to calculate the height of the first cell of the inflation layer, used boundary layer thickness, reference wind speed are given in Appendix A, E and F respectively. Appendix B, C, and D give details of user defined functions (UDF) used in this study. Appendix G provides Matlab code to extract wind velocity data of the simulated results from ANSYS fluent and to do the contour plot. Appendix H gives Matlab code to count colour pixels of the Fluent/Matlab contour plot. Finally, Appendix I shows example of used ANSYS Fluent Setup for this study.

Chapter 2

Validation

2.1 Introduction

Turbulent flow around a surface-mounted obstacle has long been used as a benchmark problem and studied extensively experimentally to understand the basic flow structure and dynamics of coherent vortex structures around buildings (e.g. Castro et al. (1977); Martinuzzi et al. (1993); Hussein et al. (1996); Irtaza et al. (2013); Richards et al. (2007); Sakamoto et al. (1988) Larousse et al. (1993) and Lim et al. (2007)). Among the various experiments reported in the literature, Hussein et al. (1996) performed one of the most detailed experimental measurements and flow visualizations at Re of $40,000$ based on the obstacle height (H). A number of numerical studies of the flow around a single obstacle have been reported in the literature using steady RANS, unsteady RANS, and LES turbulence models (e.g. Irtaza et al. (2013); Richards et al. (2001); Yang (2004); Rodi (1997); Shah et al. (1997) and Yoshie et al. (2007)).

For the general flow features around a surface mounted obstacle as described by Cook (1985), when an atmospheric boundary layer (ABL) wind profile approaches normal to the span-wise direction of the obstacle, the wind speed increases with the height above the ground. The flow at about two-thirds of the obstacle height comes to rest to form the front stagnation point. From this point, the flow deviates into four main streams. In one of these above the stagnation point, the flow goes up and over the top of the obstacle. Below this point, the flow goes down until it reaches the ground where it has more kinetic energy than the incident wind at this level. It is, therefore, able to move upstream against the wind, losing energy until it comes to rest at a separation point on the ground. The flow rolls up into a horizontal standing vortex next to the ground upstream of the windward face of the obstacle as shown in Figure 2.1(A). According to Martinuzzi et al. (1993), the shape, location and form of the separation region over and in front of the obstacle depends on the boundary layer thickness (δ). The separation point on the ground moves closer to the obstacle with decreasing δ.

The third and fourth streams are formed by the air entering the standing vortex escaping around either side of the obstacle. When the flow next to the ground is observed, as shown in Figure 2.1(B), this vortex forms the shape from which it derives its name of the *horseshoe vortex* (Cook, 1985).

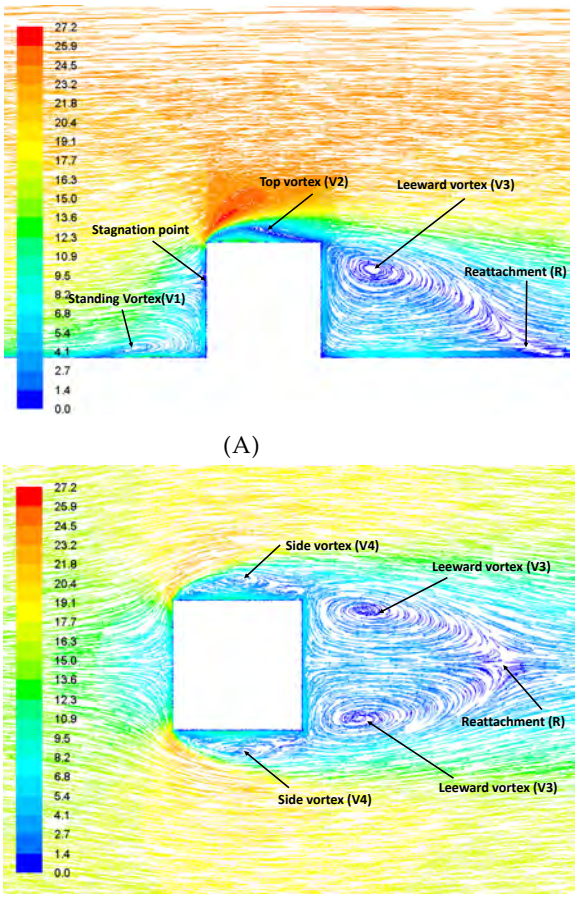

FIGURE 2.1: Velocity magnitude pathlines (A) passing through the vertical centre plane and (B) at the ground level (Obtained from this validation study results for $Re = 3.5 \times 10^5$).

The size and intensity of this horseshoe vortex scale with the thickness δ of the oncoming boundary layer (Castro et al., 1977). For thin, laminar boundary layers, (i.e. $\delta/H < 0.3$) the structure of the upstream separation is characterized by multiple secondary recirculations upstream of the horseshoe vortex (Schofield et al., 1990). Whereas for thicker, turbulent boundary layers (i.e. $\delta/H > 0.7$), the structure of the upstream separation is characterized by a bimodal behaviour of the pressure and velocity fields: i.e. the flow in the region between the primary separation and the horseshoe vortex is unstable and fluid in this region is intermittently convected down to the horseshoe vortex (Larousse et al. (1993), Martinuzzi et al. (1993)).

The three streams which separate from the front stagnation point deviate towards the three upstream sharp edges of the obstacle, where they again separate, resulting in strong shear layers, in which turbulence production terms are large (Martinuzzi et al., 2000). This high turbulence level increases diffusion and enhances entrainment by the shear layer of low momentum reverse flow in the near wake, which strongly affects the local pressure gradient and increases mixing directly behind the obstacle (Martinuzzi

et al., 1993). The horseshoe vortex also entrains the surrounding fluid towards the axis of symmetry. After the reattachment point, an initial rapid expansion of the wake occurs which is due to the increase of the mass flux in the wake close to the ground as the shear layer reattaches and is subsequently entrained by the horseshoe vortex. The separated shear layers due to the sharp upstream edges of the obstacle may or may not reattach on the surface of the obstacle. Castro et al. (1977) investigated the influence of δ on the reattachment of these shear layers. According to their observation, if the obstacle stream-wise length-to-height ratio (L/H), is sufficiently small relative to δ, the shear layers do not reattach on the obstacle, giving rise to an extended recirculation region in the near wake. According to Castro et al. (1983), the stream-wise length of the obstacle for which reattachment occurs has been shown to be a function of δ/H.

Reattachment of these separated shear layers is of the utmost importance as it alters the wake flow periodicity which changes the pressure and velocity field near the obstacle. As shown by Castro (1981), the periodicity is a result of the coupled oscillations between the separated shear layers from the lateral sides, which for the surface mounted obstacles, is modified by the shear layer along the obstacle top, the oncoming shear gradient and the appearance of junction or horseshoe vortices. According to their studied case of a thick boundary layer of $\delta/H \approx 6.6$ for the obstacle with span-wise width-to-height ratio $W/H = 1$ and $L/H = 1$, the reattachment of shear layers was observed to occur on the obstacle surfaces and no periodicity in the wake of the obstacle was found. Whereas for the studied cases of thick boundary layers by Castro (1981) for $\delta/H \approx 1.1$ and by Sakamoto et al. (1988) for $\delta/H = 0.8$ for taller obstacles with dimension ratio $W/H = L/H = 1/6$ and $W/H = 1/3$ respectively, strong periodicity in the wake was observed.

In this chapter, CFD study was performed to understand the flow structure around a square prism-like building model at $Re = 49,000$ (based on the height of the building and the free stream velocity). Performance of different near-wall treatment based turbulence models was evaluated in this study. According to Blocken et al. (2011) the accuracy of steady or unsteady RANS models for wind environment studies can easily be compromised by the presence of numerical errors (such as discretization errors and iterative convergence errors) and physical modelling errors (such as turbulence models, incorrect boundary conditions etc.). Therefore, it is advisable to validate CFD results against previous studies. Vardoulakis et al. (2011) and Ratnam et al. (2008) reported that the most widely studied flow problem in wind engineering is a 3D cube immersed in a turbulent boundary layer due to the simplicity of the shape and the complexity of the flow around the cube. Therefore, the CFD model used in this work was validated by first simulating the wind flow around a square prism building at Re of $49,000$ (based on the height of the building and free stream velocity). Here we analyse the flow structure around the building by using steady RANS and different turbulence models and comparing obtained results with an experimental study by Yoshie et al. (2007). The aim of this analysis is to select the best performing model. The performance of the turbulence models was also evaluated by comparison with a transient flow simulation using LES.

Before applying different turbulent models to the building used in this validation study, an empty channel test and mesh independence studies

were carried out. For the empty channel test, the incident wind profiles (i.e. fully developed profiles at the location where the building would be positioned) of wind velocity (U) and turbulent kinetic energy (k) were compared with experimental profiles. For mesh independent study, incident U, k and specific dissipation rate (ω) profiles were compared for different mesh elements.

To find the best model from different turbulence models available, wind velocity along the vertical centreline at different locations in the direction of the flow; wind velocity distribution in the horizontal plane near the ground (to evaluate the performance of different models at the pedestrian level) and k at different points on the roof were compared with the experimental results of Yoshie et al. (2007). From this analysis, the transition $k-kl-\omega$ (3 equation) model was found to best predict accurate overall flow structure as well as the wind speed at the pedestrian level (with an accuracy of $\approx 85\%$) when compared with the experimental results at the given Re.

It is generally assumed that flows around surface-mounted sharp-edge bluff bodies submerged in a thick turbulent boundary layer (which is generally the case of ABL) are independent of Re, provided that this exceeds around $(2-3)\times 10^4$ (based on building height and free stream velocity)(Lim et al., 2007). However, the experimental study of Lim et al. (2007) showed that this only holds when the flow around the body does not contain a strong concentrated vortex (like the standing vortex in front of a body when the flow approaches perpendicular to the span-wise direction of the body) motion. However, in this study we consider flows approaching perpendicular to the building faces, and the resulting flow fields do contain such strong vortex motion. In such cases, Re effects are significant. Therefore it is important to study the performance of steady RANS turbulent models for the Re of interest. According to best of our knowledge, wind tunnel studies analysing the flow structure and pedestrian-level wind speed for generic building configurations have only been performed up to Re of order 10^4. Lim et al. (2007) performed an experimental study of the scaled Silsoe cube at $Re = 3.5 \times 10^5$, but wind velocity is only available above the cube and not at the pedestrian level. Therefore, before modelling actual street canyons at Re of order 10^6, the turbulence models and boundary conditions were validated by comparing against the experimental results of Lim et al. (2007).

2.2 CFD simulations: computational model and parameters

2.2.1 Model description

Model A

A square prism-like building was used as a first validation model for this CFD study. A scale model of dimension $H \times W \times L = 0.16\,(m) \times 0.08\,(m) \times 0.08\,(m)$ was used to determine the wind velocity before the building, on the roof of the building and in the wake of the building using CFD study. The computational domain covers 32 L in the X direction, 14 L in the Z direction and 4 H in the Y direction as shown in Figure 2.2. The dimensions of the building model and computational domain were chosen to compare

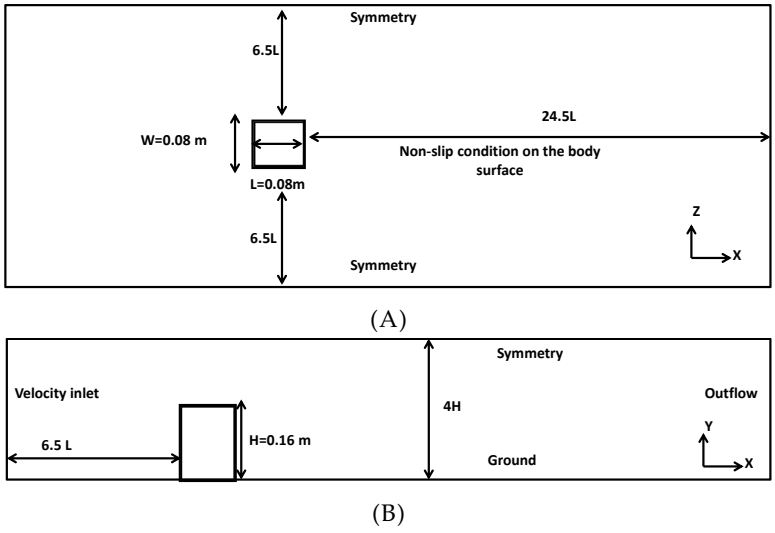

FIGURE 2.2: Computational domain and boundary conditions for the single square prism building model (A) Plan view (B) side view.

the obtained results of this study with the experimental study results of Yoshie et al. (2007). The Reynolds number was 4.9×10^4 based on the height of the building and the free stream velocity.

Model B

The full-scale Silsoe experimental building (SEB) was used as a base model for this second CFD validation study. A scale of 1:25 was used to make the model of dimension $H \times W \times L = 0.24\,(m) \times 0.24\,(m) \times 0.24\,(m)$ to study influence of higher Re on the flow quantities such as wind velocity and wind pressure. The computational domain used for this study is similar to as described above in the Figure 2.2, the cube was placed instead of rectangular building in this case. Study results were compared with the experimental results of Lim et al. (2007). The Reynolds number was 3.5×10^5 based on the height of the cube and the free stream velocity for this case.

2.2.2 Boundary conditions

Inlet boundary condition

Model A

Simulations were performed using the commercial CFD package Ansys Fluent version 17.0. The inlet boundary condition was specified according to the log-law velocity profile of the ABL suggested by Richards et al. (1993), Richards et al. (2011) and O'Sullivan et al. (2011) in which roughness was expressed as a function of y_0. This profile was introduced by using a user defined function (UDF) satisfying Equation 2.1 for $U(y)$ (see Appendix B for UDF).

$$U(y) = \frac{U^*_{ABL}}{\kappa} \ln\left(\frac{y + y_0}{y_0}\right); \tag{2.1}$$

Here, $y_0 = 1.8 \times 10^{-4}$ m was chosen according to the reference paper Yoshie et al. (2007).

The $k(y)$ profile from the experimental results was imposed at the inlet for this study case; Whereas, the $\varepsilon(y)$ and $\omega(y)$ profiles were calculated and imposed at the inlet according to Equation 2.2 and Equation 2.3 respectively:

$$\varepsilon(y) = \frac{U_{ABL}^{*3}}{\kappa(y + y_0)}; \tag{2.2}$$

$$\omega(y) = \frac{\varepsilon(y)}{C_\mu k(y)}. \tag{2.3}$$

U_{ABL}^* can be calculated by a specified velocity U_{ref} at y_{ref} as,

$$U_{ABL}^* = \frac{\kappa U_{ref}}{\ln\left(\frac{y_{ref}+y_0}{y_0}\right)}. \tag{2.4}$$

Here we take, $U_{ref} = 4.491$ m/s, at $y_{ref} = 0.16$ m taken from the wind-tunnel study result of Yoshie et al., 2007.

Model B

For the study case of the scaled Silsoe cube (Model B), two different simulations were carried out in an empty channel, using two different methods to specify inlet boundary condition:

- **Using UDF and with keeping turbulence intensity (I) constant with varying vertical height**
  In this method, the inlet boundary condition for velocity profile was specified according to the log-law profile as specified in Equation 2.1 and using a UDF; whereas the inlet $k(y)$ profile was calculated and introduced using a UDF according to the equation $k(y) = \frac{3}{2}(U_{avg} \cdot I)^2$ as given by Irtaza et al. (2013), where $U_{avg} = \sqrt{U^2 + V^2 + W^2}$ is the mean wind speed and $I = \frac{U'}{U_{avg}} = \frac{\sqrt{\frac{1}{3} \cdot (u'^2 + v'^2 + w'^2)}}{\sqrt{U^2+V^2+W^2}}$ is the turbulence intensity which was 13% at the cube eave height (obtained from Lim et al. (2007)) and was kept constant with varying vertical height. $\varepsilon(y)$ and $\omega(y)$ profiles were calculated and introduced using a UDF at the inlet according to Equation 2.2 and Equation 2.3 respectively (See Appendix C for all UDFs used for this case).

- **Profile obtained from the experimental results imposed at the inlet; where the turbulence intensity (I) was varying with vertical height**
  In this method, the velocity profile ($U(y)$) and turbulent kinetic energy ($k(y)$) profile (calculated from the given I profile) from the experimental results were imposed at the inlet using the profile method available in Fluent; Whereas, the $\varepsilon(y)$ and $\omega(y)$ profiles were calculated and imposed at the inlet according to Equation 2.2 and Equation 2.3 respectively.

In both the methods specified above, $y_0 = 3.5 \times 10^{-4}$ m was chosen according to reference paper Lim et al. (2007). U_{ABL}^* was calculated according to

Equation 2.4, by specifying velocity $U_{ref} = 21.8$ m/s at the cube reference height $y_{ref} = 0.24$ m taken from the wind-tunnel study results of Lim et al. (2007).

According to Pirooz et al. (2018), the I profile and hence the turbulent kinetic energy ($k(y)$) profile should be decreased with varying the vertical height. The reason for carrying out simulations using two different methods specified above was to find the difference in the incident wind profiles (i.e. fully developed profiles at the location where the building would be positioned) and given experimental profiles of wind velocity (U) and turbulent kinetic energy (k) for Model B; when keeping I constant versus I varied with the vertical height. Results of these simulations in the empty channel and comparison with corresponding experimental profiles for wind velocity (U) and turbulent kinetic energy (k) are as specified in subsection 2.2.4.

All the other boundary conditions were similar for both the models (A & B). The top and side boundary conditions were specified as "symmetry" which is used when expected pattern of the flow solution has mirror symmetry. The outlet boundary condition was specified as "outflow", which is used to model flow exits where the details of the flow velocity and pressure are not known prior to the solution of the flow problem. The bottom and the building or cube face boundary conditions were specified as "wall" (no-slip) to bound fluid and solid regions.

Inflation layers were generated on the ground and building or cube faces with 20 grid layers on each for Model A and 30 grid layers on each for Model B to accurately resolve the wall boundary layer and accurately predict separation and reattachment points as recommended by Fluent (2011b). It could be noted here that, the number of inflation layers was increased in the case of Model B, for an accurate prediction of the wall boundary layer as recommended by Fluent (2011b) for the unstructured mesh. The height of the first cell of the boundary layer ($\triangle$ y) was chosen to be 9.1×10^{-5} m for model A and 1.1×10^{-5} for model B (see Appendix A for the calculation) to ensure a wall unit $y^+ < 5$ to resolve the viscous sub-layer of the boundary layer, which is a requirement of the turbulent models used in this study. The geometric growth rate of 1.2 was selected to determine the adjacent inflation layer for this study. Note that, with the geometric growth rate, the prism height of a particular layer is defined by $\triangle y * r^{n-1}$, where, $r =$ height ratio and $n =$ layer number. The mesh used in this study contains tetrahedral and wedge-shaped elements.

2.2.3 Wall roughness effect

For ABL simulations using CFD, fully developed equilibrium velocity and turbulence profiles are applied at the inlet of the computational domain. These profiles must be representative of the upstream surface roughness characteristic (i.e. the terrain upstream of the inlet plane) (Blocken et al., 2007b). In more detail, the computational domain consists of three main regions namely : the central region of the domain where the buildings are modelled explicitly and both the upstream and the downstream region of the domain where actual obstacles (buildings, trees etc.) are not modelled explicitly but their effect on the flow is modelled in terms of the roughness. In the simulation of the ABL over uniformly rough terrain, horizontal homogeneity is always required in the upstream and downstream region of

the computational domain (Blocken et al., 2007b). Here, "horizontal homogeneity" as defined by Blocken et al. (2007b) refers to the absence of stream-wise gradients in the vertical profiles of the mean wind speed and turbulence quantities, i.e. the vertical velocity profile and turbulent quantities specified at the inlet should be maintained within the computational domain, until it reaches the face of the building of the study (Abdi et al., 2014). The main problem in simulating the ABL using the current batch of CFD software is maintaining the horizontal homogeneity. Richards et al. (1993) have investigated this problem thoroughly and suggested boundary conditions for the inlet that satisfy horizontal homogeneity. However, it is not enough to specify only inlet conditions to get stream-wise homogeneous flow. The near wall treatment used at the surface should be compatible with the roughness of the upstream terrain outside the computational domain (Abdi et al., 2014).

In Fluent, there are two approaches available to model the near-wall region and wall roughness effect: wall functions and low-Re modelling. These options differ in the way in which the boundary layer at the wall surface is taken into account. The boundary layer consists of an inner layer, including the viscous sublayer, the buffer layer and the logarithmic layer, and a fully developed outer layer (Wilcox, 1998). The low-Re modelling approach refers to resolving the whole boundary layer by placing grids in each part of it. Because of the thickness of the viscous sublayer decreases with increasing flow Re and the Re of wind flow around buildings are quite large ($10^5 - 10^7$), the viscous sublayer at the building surfaces can be very thin (Blocken et al., 2009a). Therefore, excessive fine near wall grid resolution is required. Because of the computational cost associated with low-Re modelling, wall functions are often used instead. They are a semi-empirical formula that bridges the region between the wall and the logarithmic layer and provide an approximation of the effect of the wall on the mean wind speed and turbulence quantities in the logarithmic layer. Therefore, much coarser grids can be used in this approach.

The grid resolution close to a wall can be characterized by a non-dimensional wall distance y^+, which is as defined in subsection 1.3.4 of Chapter 1. Appropriate grids for low-Re modelling have $y^+ < 1$ to ensure the first grid point of the wall-adjacent cell is situated in the viscous sublayer. In Fluent, $k-\epsilon$ models with the enhanced wall treatment and $k-\omega$ models are based on low-Re approach. Wall-function grids should have a y^+ between 30 and 500, to ensure the first grid point is situated in the logarithmic layer (Franke et al., 2007). In Fluent, $k-\varepsilon$ and revised $k-\varepsilon$ models with the "standard wall functions", "scalable wall functions" and "non-equilibrium wall functions" are based on the wall function approach. Previous ABL simulations using the wall function approach have addressed the problem of horizontal homogeneity associated with the use of this method. According to the detailed study by Blocken et al. (2007b), the modification of the turbulence model to account for the presence of the wall, introduces a stream-wise gradient in the vertical mean wind speed and turbulence profiles. As these profiles travel through the computational domain, the stream-wise gradients becomes more pronounced and introduce an internal boundary layer (IBL) in which the wind speed and turbulence profiles rapidly adapt the new and smaller roughness (Blocken et al., 2007a). This in turn accelerates the flow near the ground. However, they have specified that, changes in

these parameters will lead to similar observations but with different profiles. Nevertheless, probably because of the very grid resolution required for low-Re modelling, wall functions have been used so far for the pedestrian wind comfort assessment study. In the present paper, the performance of $k-\epsilon$ models with enhanced wall treatment will be evaluated by comparison with low-Re modelling results for validation study.

2.2.4 Empty channel test

As specified in subsection 2.2.3, for the walls, a low-Re modelling approach is used in this study. In Fluent version 17.0, low-Re modelling implies that the walls are smooth (roughness height is zero), which is also the case for the bottom of the domain. A smooth bottom surface can lead to a non-horizontal homogeneous ABL in the simulations (Blocken et al., 2007b), and, thus, stream-wise gradients can occur in the vertical mean wind speed and turbulence quantities. The occurrence of these gradients was tested by a simulation in a $3D$ empty channel for Model A and B. The empty channel is the computational domain without the actual building model present in it. All the simulation settings such as inlet profiles, turbulent model, boundary conditions and modelling of wall roughness in the empty channel are similar to actual flow simulation around the buildings. Incident profiles (i.e. fully developed profiles at the location where the building would be positioned) were compared with the experimental profiles in both cases. Figures 2.3 and 2.5 show the comparison of experimental wind velocity profiles with the CFD incident profiles for model A and model B and with corresponding general power law profile for Model A and log law wind profile for Model B for the specified terrain types respectively.

Following observations were noted for both studied cases:

- It can be seen from the simulated profiles of the wind speed as shown in Figure 2.3 and Figure 2.5 that the stream-wise gradients were limited for model A and model B when compared with the corresponding experimental profiles.
- For Model A, k-profile values were under-predicted as shown in Figure 2.4.
- For model B, for the considered methods as specified in subsection 2.2.2, the difference in the CFD incident k-profile values with varying intensity with vertical height was minor when compared with the experimental k-profile values. However, the difference in the incident k-profile values with using constant intensity with vertical height was large when compared with the experimental k-profile values.

This type of change in the profile of the turbulent kinetic energy (k) as observed for model A, has been reported in the past by Zhang (1994), Quinn et al. (2001) and Riddle et al. (2004). These studies used the $k-\varepsilon$ turbulence model with wall functions. Riddle et al. (2004) employed Fluent version 6.0 with the $k-\varepsilon$ model observed significant profile changes in an empty computational domain. According to Blocken et al. (2007a) the flow profile imposed at the inlet and the incident flow profiles can be considerably different in the CFD simulations. This difference depends on the equilibrium of the inlet profiles of the wind speed and the turbulence quantities,

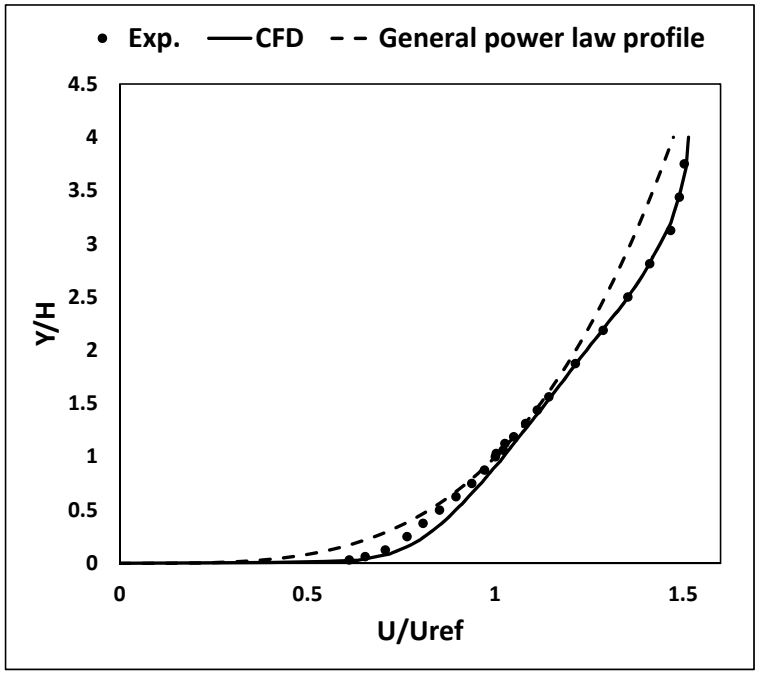

FIGURE 2.3: Comparison plot of the experimental vertical profile of mean wind speed ratio (U/U_{ref}) with the CFD incident profile for square prism building (Model A) and with corresponding general power law profile for the specified terrain type.

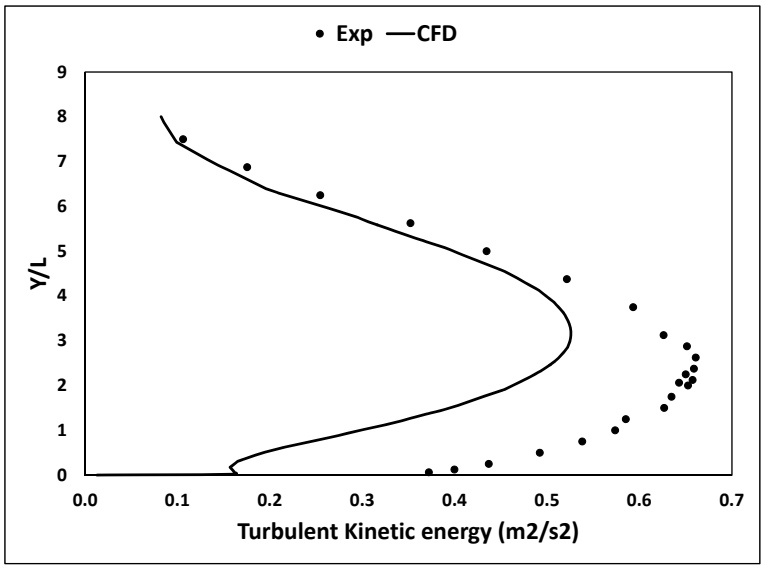

FIGURE 2.4: Comparison plot of the experimental vertical profile of the turbulent kinetic energy (k) with the CFD incident k-profile for model A.

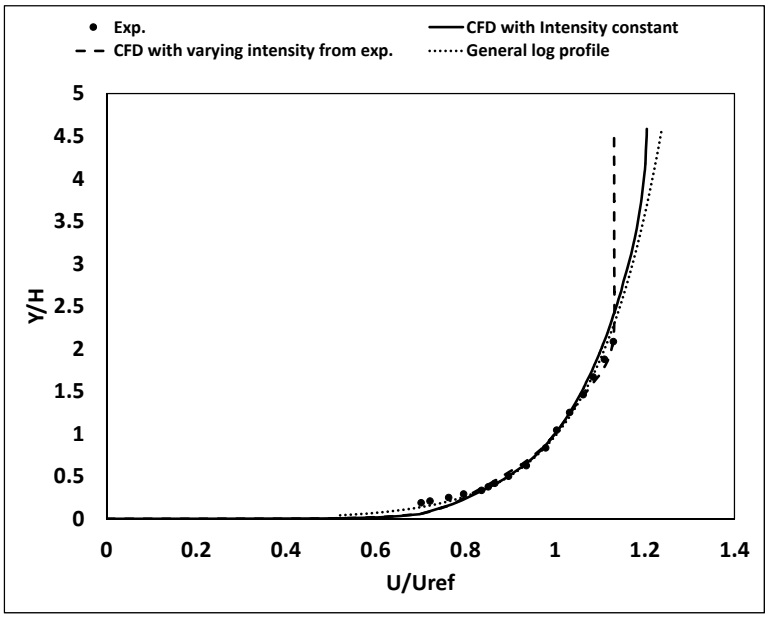

FIGURE 2.5: Comparison plot of the experimental vertical profile of mean wind speed ratio (U/U_{ref}) with the CFD incident profile for scaled Silsoe cube (Model B) and with corresponding general log law wind profile for the specified terrain type.

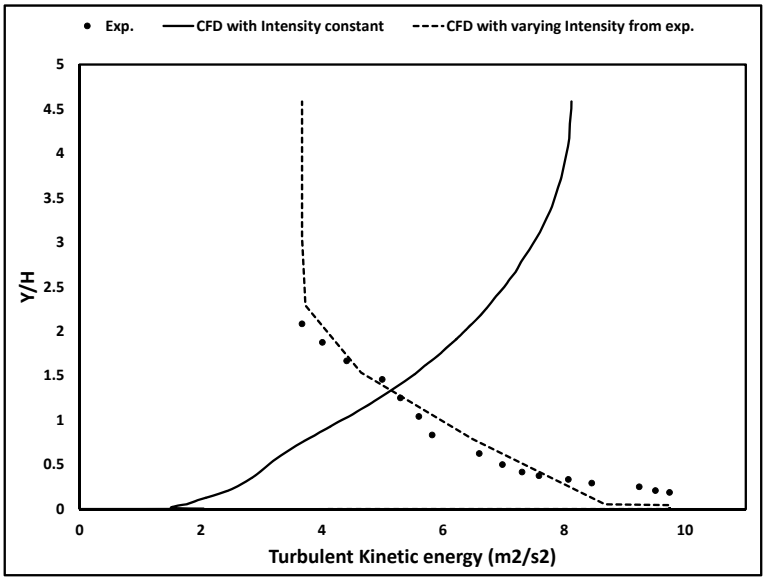

FIGURE 2.6: Comparison plot of the experimental vertical profile of the turbulent kinetic energy (k) with the CFD incident k-profiles for model B.

the turbulence model used, the grid resolution and the upstream length of the computational domain. With the used near-wall turbulence models in this study, no changes were made to improve this variation in the values of the k-profile, because this was considered as the one of the usual problem associated with the CFD simulations as discussed above.

For the k-profile comparison for model B, for the CFD incident k-profile with varying intensity with vertical height, it justifies the argument made by Pirooz et al. (2018) that k-profiles should be decreased with the vertical height and it matches reasonably well when compared with the experimental k-profile. However, for the case with keeping constant intensity (I) with height, k-profile is not decreasing with height. Note here that, this case with constant I was considered here as to find the way in the case when the actual data of the turbulence intensity (I) or turbulent kinetic energy ($k(y)$) are not available to simulate the flow profile for the given terrain type of the ABL. Specifically for the buildings and street canyon cases considered in this study from the next chapter onwards have been assumed to be belong to the city area of the country like New Zealand or Australia. Where according to our knowledge accurate experimental or full-scale data are not available for the intensity (I) or the turbulent kinetic energy ($k(y)$) profiles.

Despite the variation of the k-profile for the model B (scaled Silsoe cube) as discussed above, CFD incident profiles of the wind speed show limited stream-wise gradients when compared with the corresponding experimental profile and general log-law profile (as shown in Figure 2.5). Therefore, the method of using UDF and with keeping turbulence intensity (I) constant with vertical height has been used for this validation results discussed further in this chapter.

2.2.5 Computational mesh

An empty channel mesh independence study was carried out for both the models as specified in subsection 2.2.1 to demonstrate the independence of the flow field on the refinement of the mesh for this study.

Model A

For this model, the coarse mesh had 0.4 million cells of resolution 0.016 m throughout the computational domain. The medium mesh had 0.65 million cells with a resolution of 0.0128 m throughout the computational domain and the fine mesh had 1.4 million cells and a resolution of 0.0096 m throughout the domain. Figure 2.7 represents the incident wind profiles plot for $U(y)$, $k(y)$ and $\omega(y)$ for different mesh. These profiles for the coarse mesh were the same as for the fine mesh. Thus, it can be concluded that the coarse mesh is sufficient for running a mesh independent solution. the medium mesh with the resolution of 0.0128 m throughout the computational domain was used to simulate the flow past the building model. The mesh resolution of 0.0064 m was used on the faces of the building model A. Figure 2.8 represents the mesh arrangement on and around the building model.

Mesh independence study was also carried out with the building model included for this case and with using the transition $k-kl-\omega$ (3 equation) model; as this has been considered as the suitable model for these kinds of

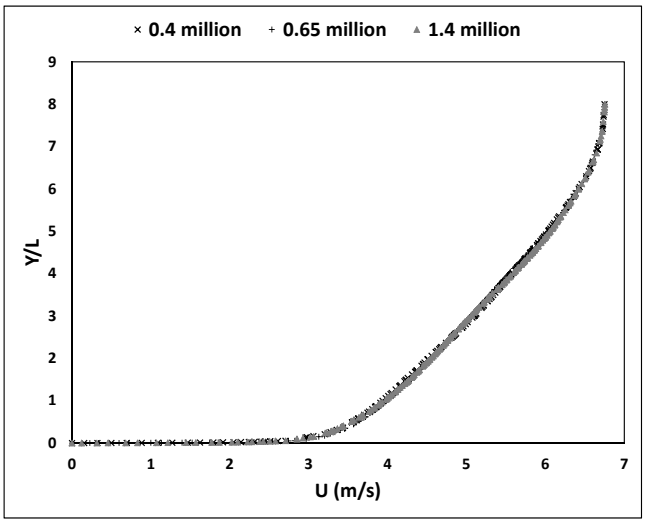

(A)

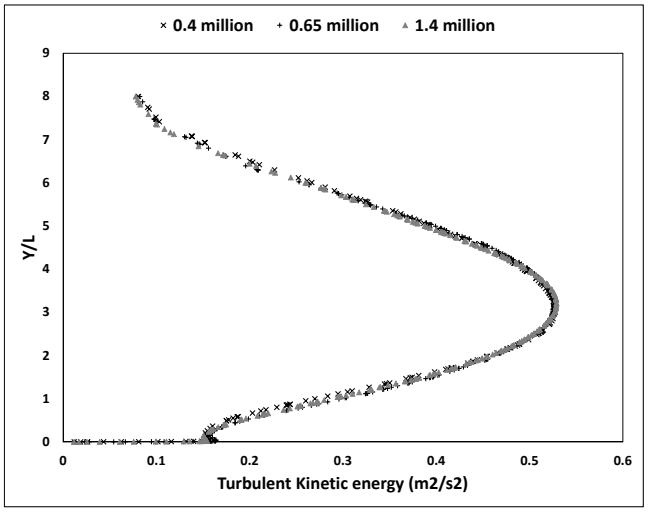

(B)

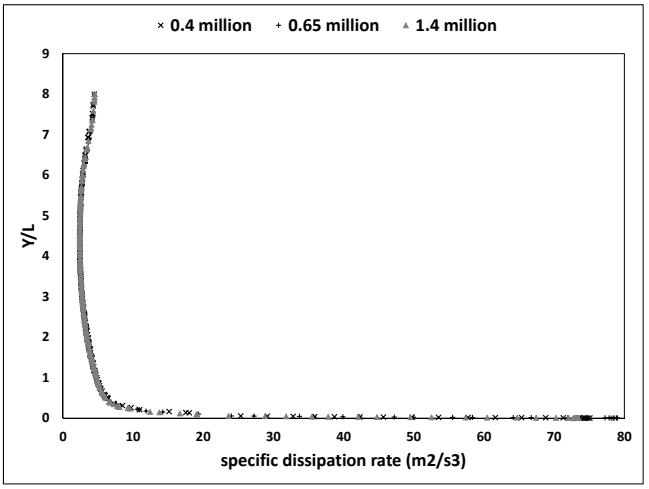

(C)

FIGURE 2.7: Mesh independence study for Model A; using different mesh elements showing incident profile of (A) $U(y)$ (B) $k(y)$ and (C) $\omega(y)$.

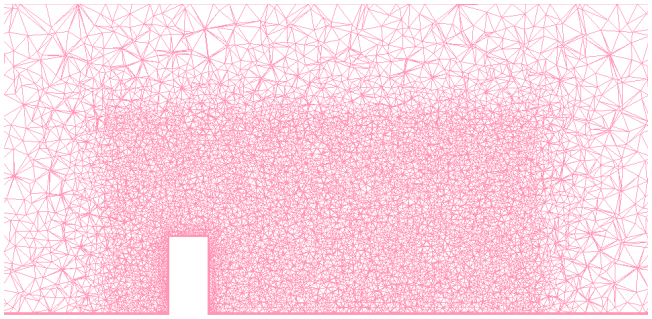

(A)

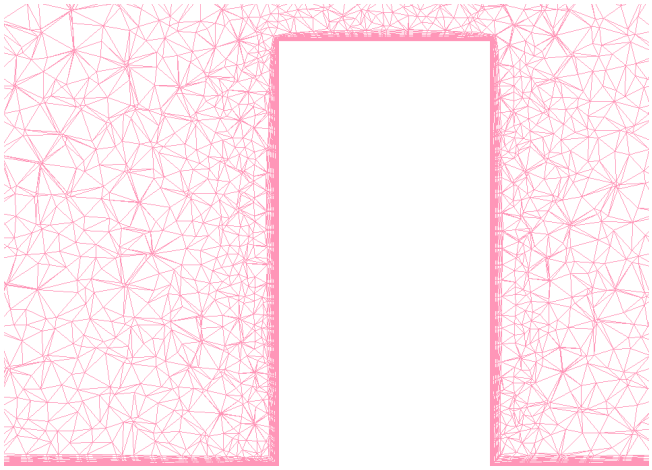

(B)

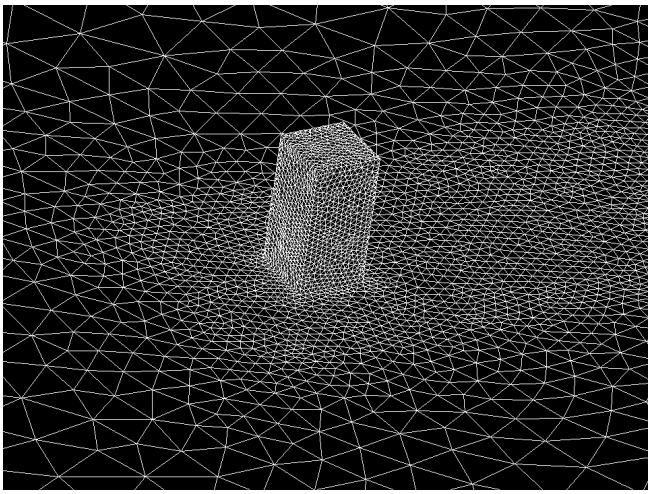

(C)

FIGURE 2.8: Typical mesh arrangement around Model A using (A) vertical section ($X - Y$) (B) zoomed view for the vertical section ($X - Y$) around building showing inflation layers on the ground and faces of the building (C) 3D view of the model.

studies (as discussed in the results section below). The medium mesh had 0.7 million cells with resolution of 0.0064 m on the faces of the building and 0.0128 m throughout the rest of the computational domain. The fine mesh had 1.5 million cells and a resolution of 0.0048 m on the faces of the building and 0.0096 m elsewhere. The distribution of U velocity on the vertical cross-section at the centre plane ($Z = 0$) of the building for the medium mesh and large mesh were compared with the experimental data available for this model as shown in Figure 2.13. Comparison results clearly indicate that the considered medium mesh for this study effectively predicts the flow structure around the model building (specifically separation and reattachment of the flow around the building).

Model B

A similar type of mesh independence study was carried out for Model B. The coarse mesh had 1.9 million cells of resolution 0.024 m throughout the computational domain whereas the medium mesh had 3.3 million cells with a resolution of 0.016 m throughout the computational domain. The fine mesh had 7 million cells with mesh resolution of 0.012 m through the domain. Figure 2.9 represents the incident flow profiles for different mesh elements. A similar conclusion as above was drawn from this study that the coarse mesh was sufficient for running the mesh independent study. However, a medium mesh with the resolution of 0.016 m throughout the computation domain was used to run the simulation when model B was placed in the computational domain. The mesh element of size 0.008 m was used on the faces of the cube for this simulation.

Note here that, the minimum mesh resolution used in both validation cases was as recommended by Franke et al. (2007) and Tominaga et al. (2008a). However, this has been recommended as an initial minimum grid resolution. Franke et al. (2007) has also recommended that the resolution of the grid should be fine enough to capture the important physical phenomena like shear layers and vortices with sufficient resolution. Therefore, even if coarse mesh refinement gives good agreement with the fine mesh for the incident wind profiles, medium mesh resolution was considered for both validation studies.

Also, note here that these mesh independence studies were carried out for the steady RANS and not for the LES. However, for the LES simulations, local grid refinement was used in the area of interest as recommended by Franke et al. (2007).

2.2.6 Turbulence model

According to the previous literature review, the choice of a turbulence model is one of the most important factors in predicting the flow around the building. Mochida et al. (2002) and Tominaga et al. (2008b), compared the performance of different $k-\varepsilon$ based turbulent models with the experimental data and with the direct numerical simulation (DNS) and LES study results for a single building model. Following observations were made:

- The reattachment length of the separated shear layer on the roof of the building varies for different turbulence models. In their study, the standard $k-\varepsilon$ model failed to reproduce the reattachment on the roof

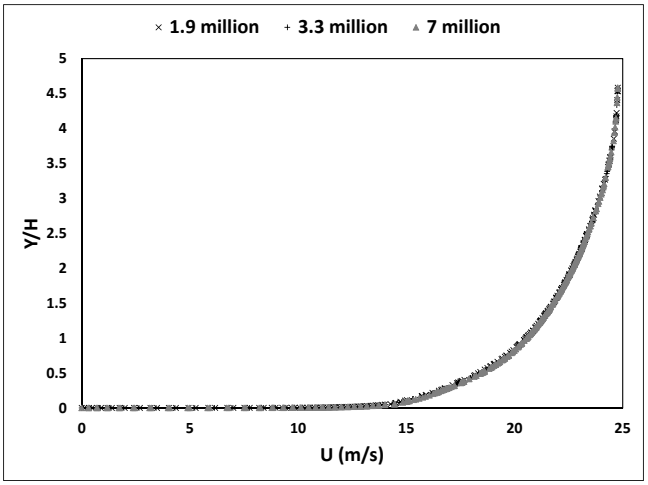

(A)

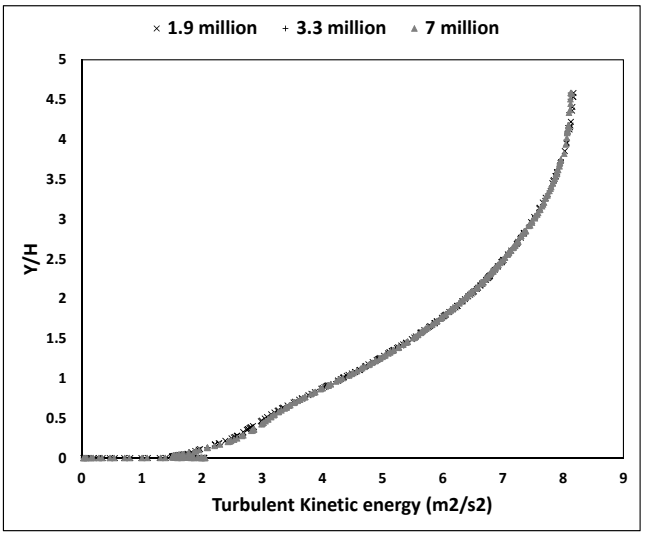

(B)

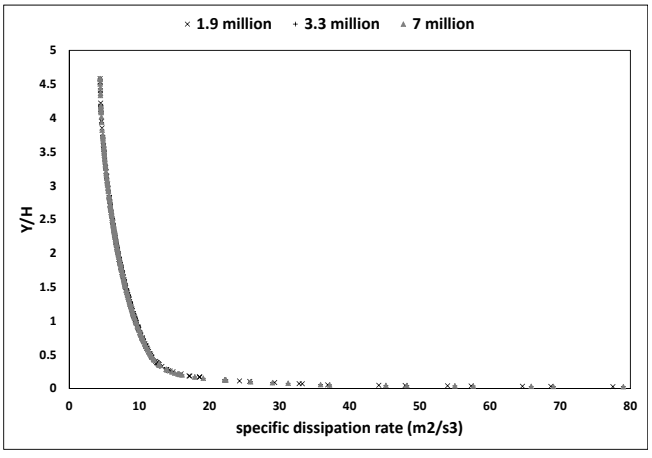

(C)

FIGURE 2.9: Mesh independence study for Model B using different mesh elements, showing incident wind profiles of (A) $U(y)$ (B) $k(y)$ and (C) $\omega(y)$.

of the building. Whereas, the revised $k-\varepsilon$ models have reproduced the reattachment and reverse flow on the roof, but the reattachment length was larger than the experimental observation

- The reattachment length behind the building was observed to be larger than the experiment for all studied turbulence models
- For the wind speed assessment at the pedestrian level, the amplification factor U/U_0 (which is the ratio of the local pedestrian level wind speed U to the wind speed U_0 that would occur at the same position without building model) was predicted well with an accuracy of $10-15\%$ with experimental results in the region where $U/U_0 > 1$ by all $k-\varepsilon$ models. However, when the results of the revised $k-\varepsilon$ models were compared with the standard $k-\varepsilon$ model, prediction accuracy of the revised $k-\varepsilon$ models was slightly higher than the $k-\varepsilon$ model in the region $U/U_0 > 1$, while it was lower for $U/U_0 < 1$.

Hence, it is important to evaluate the turbulence model prior to applying it to the building model of the study. In this study, different near-wall modelling based steady-RANS turbulent models were evaluated, with the primary objective of finding the accuracy of the particular model to analyse the flow pattern at the pedestrian level. Many of the models used in this study were already assessed by Yoshie et al. (2007), Mochida et al. (2002) and Blocken et al. (2008a) for predicting pedestrian level wind speed by comparing with the experiments. However, they have used a wall function method for their studies. With the choice of boundary conditions and unstructured mesh used in this study turbulent models evaluated in this study were a re-normalized group $k-\varepsilon$ (RNGKE) model, realizable $k-\varepsilon$ (RKE) model and transition $k-kl-\omega$ model. Enhanced wall treatment was used for the $k-\varepsilon$ based models as the value of y^+ were less than 5 (Fluent, 2011c). The performance of used turbulence models was evaluated based on a comparison of CFD results with the corresponding experimental data available.

As mentioned above from the pedestrian level wind assessment, the amplification factor (U/U_0) was well predicted when compared with the experimental results in the region when $U/U_0 > 1$ by all the steady RANS turbulence models. While it was significantly underestimated when $U/U_0 < 1$. Since area with the high amplification factor are of importance, steady RANS can be considered a suitable method for such studies.

LES is a transient approach that is particularly effective - when applied correctly - at modelling inherently unsteady features of the flow field, such as separation regions on the building faces, and the roof and the vortex shedding in the wake of the building (Murakami, 1990; Tominaga et al., 2008b). It can predict the wind speed ratio more accurately in both regions (i.e. $U/U_0 < 1$ and $U/U_0 > 1$) (Janssen et al., 2013). The disadvantage of LES is that it requires more mesh refinement and time to get accurate results. As a result even with significantly large computing capacity, LES can take many hours or days to simulate high Re flows around buildings.

To examine the accuracy of the steady-RANS models used here, LES simulations were carried out for both models A and B (as described in Subsection 2.2.1). Following the LES study example for an unstructured mesh by Irtaza et al. (2013), the Smagorinsky-Lilly model was used with

the Smagorinsky constant 0.12 (Murakami, 1993). For LES simulations, information on mean velocity and the fluctuating velocity of incident wind is required. The spectral synthesizer in the Fluent code was used to generate the fluctuating velocity component and is based on the random flow generation technique originally proposed by Kraichan and modified by Smirnov et al. (2001). In this method, fluctuating velocity components are computed by synthesizing a divergence-free velocity vector field from the summation of Fourier harmonics on the basis of the input turbulence boundary conditions. In the implementation of the Fluent code, the number of the Fourier harmonics is fixed to 100 (Fluent, 2011d).

Model A

To evaluate the performance of different steady-RANS models as mentioned above, the vertical profile of U at various X locations, horizontal profiles of U near the ground at various X-locations and the turbulent kinetic energy (k) on the top of the building model were compared with the wind tunnel study results of Yoshie et al. (2007).

The steady RANS models performance was also evaluated with the unsteady flow simulation using LES simulation. For the LES study for this model, approximately 1.4 million mesh elements were used as described in 2.2.5.

Model B

For Model B, steady-RANS simulation results were compared with the experimental study results of Lim et al. (2007) and with LES simulation, using C_P and velocity ratio U/U_{ref} on the roof of the cube at 0.01 H above the model roof. For the LES study for this model, approximately 6.7 million mesh elements were used with a more refined mesh around cube (especially on the top of the cube) as the performance of study was to get good result comparison with experimental data of Lim et al. (2007) on the top of the cube. A body of influence refinement box (a wake box) was placed on the roof of the cube to refine that area.

The results of both model comparison studies for different models with corresponding experimental data and with LES are explained in the results section of this chapter (subsection 2.3).

2.2.7 Other parameters

The Pressure-Implicit with Splitting of Operators (PISO) algorithm scheme with skewness correction was used for the pressure-velocity coupling as it has a better performance for meshes containing cells with higher than average skewness (Irtaza et al., 2013); pressure interpolation was second-order. Second-order discretization schemes were used for both convective terms and viscous terms of the governing equations. The simulations were initialized by the values of the inlet boundary conditions. All computations were performed on a cluster of 16 computers. The numerical time steps of 0.001 s was used for LES and 6500 time steps were iterated (20 iteration per time step) to compare the results with the reference paper for model A. Whereas numerical time steps of 0.0002 s was used for LES for model

B and 3000 time steps were iterated (20 iteration per time step) to compare the results with experimental data.

2.3 Results and discussion

In order to assess the accuracy of the CFD simulation results, different steady-RANS turbulent models as described in subsection 2.2.6 were studied for this validation. Obtained results were compared with the experimental results of Yoshie et al. (2007) and the LES simulation carried out in this study.

2.3.1 Model A

Velocity distribution (U velocity) along the vertical centre line ($Z = 0$) at different locations in the direction of the flow (as shown in Figure 2.10(A)), U velocity distribution in the horizontal plane ($Y = 0.125L$) near the ground (Figure 2.10(B)) and the turbulent kinetic energy (k) profiles at the location $Y = 2.125L$ on the roof (Figure 2.10(A)) were investigated for this model.

Wind velocity distribution on the vertical cross-section

The distribution of U velocity on the vertical cross-section at the centre plane ($Z = 0$) of the building is as shown in Figure 2.11. The dotted solid circles in the figure represent the experimental distribution of U velocity. The CFD results with different steady-RANS turbulent models agree considerably well with the experimental values overall. However, near the roof surface measurement line $X/L = -0.25$ (the third measuring line from the left), U was negative in the experiment and reverse flow occurs (Yoshie et al., 2007), which was only reproduced by the transition $k - kl - \omega$ model in the CFD study. For the measuring line $X/L = 2$ and $X/L = 3.25$ (the last two measuring lines from the right) the calculated U was lower than the experimental value.

The obtained CFD results of different steady-RANS models were also compared with the LES simulation performed as shown in Figure 2.12. It can also be observed from this plot that LES results give good agreement overall except in the free shear layer region above the recirculation region in the wake of the building. Note that, in this study, the Smagorinsky constant was set at 0.12. However, as discussed by Murakami (1993), the value of 0.14 is needed in this free shear layer region in the wake of the building to accurately predict the results. However, this study is mainly aimed at comparing the general flow characteristics around the building and near the ground or at the pedestrian level. The Smagorinsky constant was considered to be 0.12. As described above for the line $X/L = -0.25$, where near the roof surface U was negative and reverse flow was observed, which can also be seen with the LES calculation.

Wind velocity distribution on the horizontal cross-section near the ground

Figure 2.14 – 2.17, compares the experimental and calculated U velocity in the horizontal plane near the ground ($Y = 0.125L$), for different turbulence

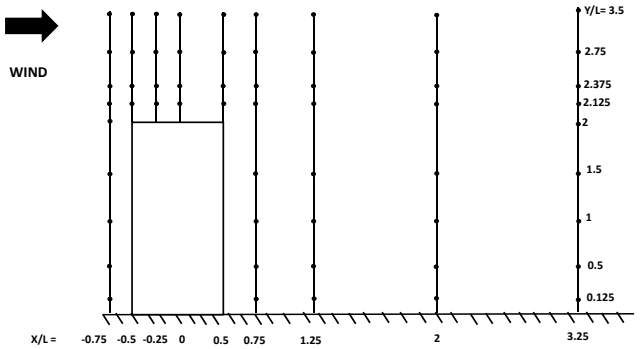

(A)

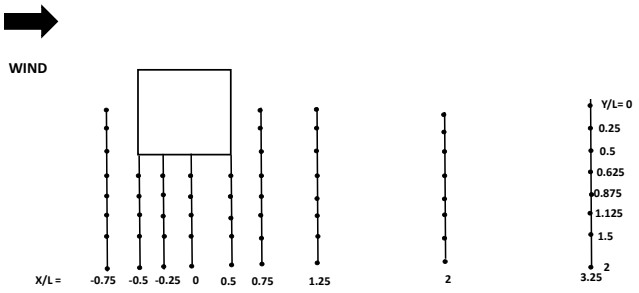

(B)

FIGURE 2.10: Wind tunnel measuring points in (A) vertical cross-section ($Z = 0$) and (B) Horizontal plane ($Y = 0.125L$) (Yoshie et al., 2007).

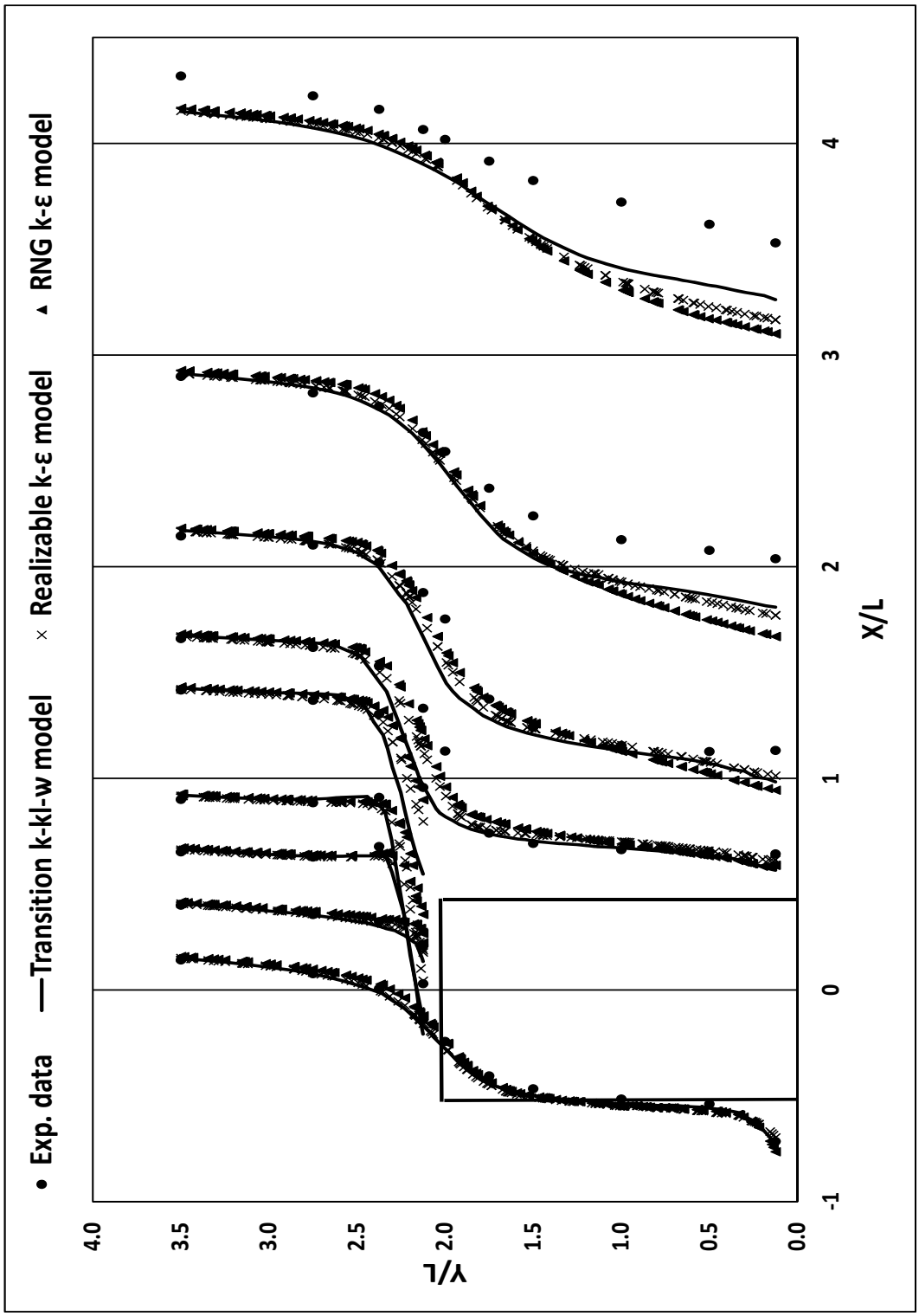

FIGURE 2.11: Vertical U profile CFD steady-RANS calculation results compared with the experimental data points (Yoshie et al., 2007).

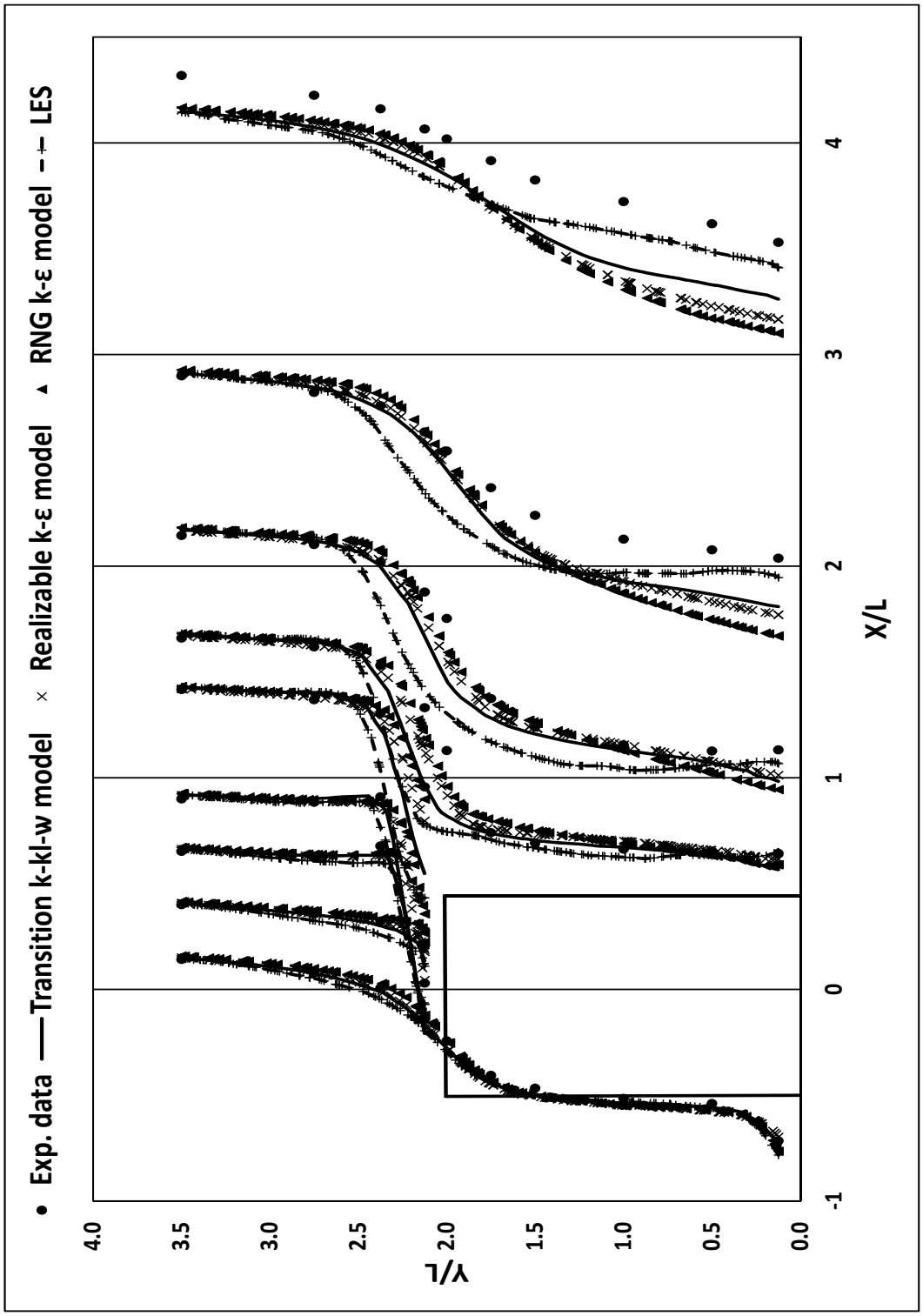

FIGURE 2.12: Vertical U profile CFD steady-RANS calculation results compared with the experimental data points (Yoshie et al., 2007) and LES results.

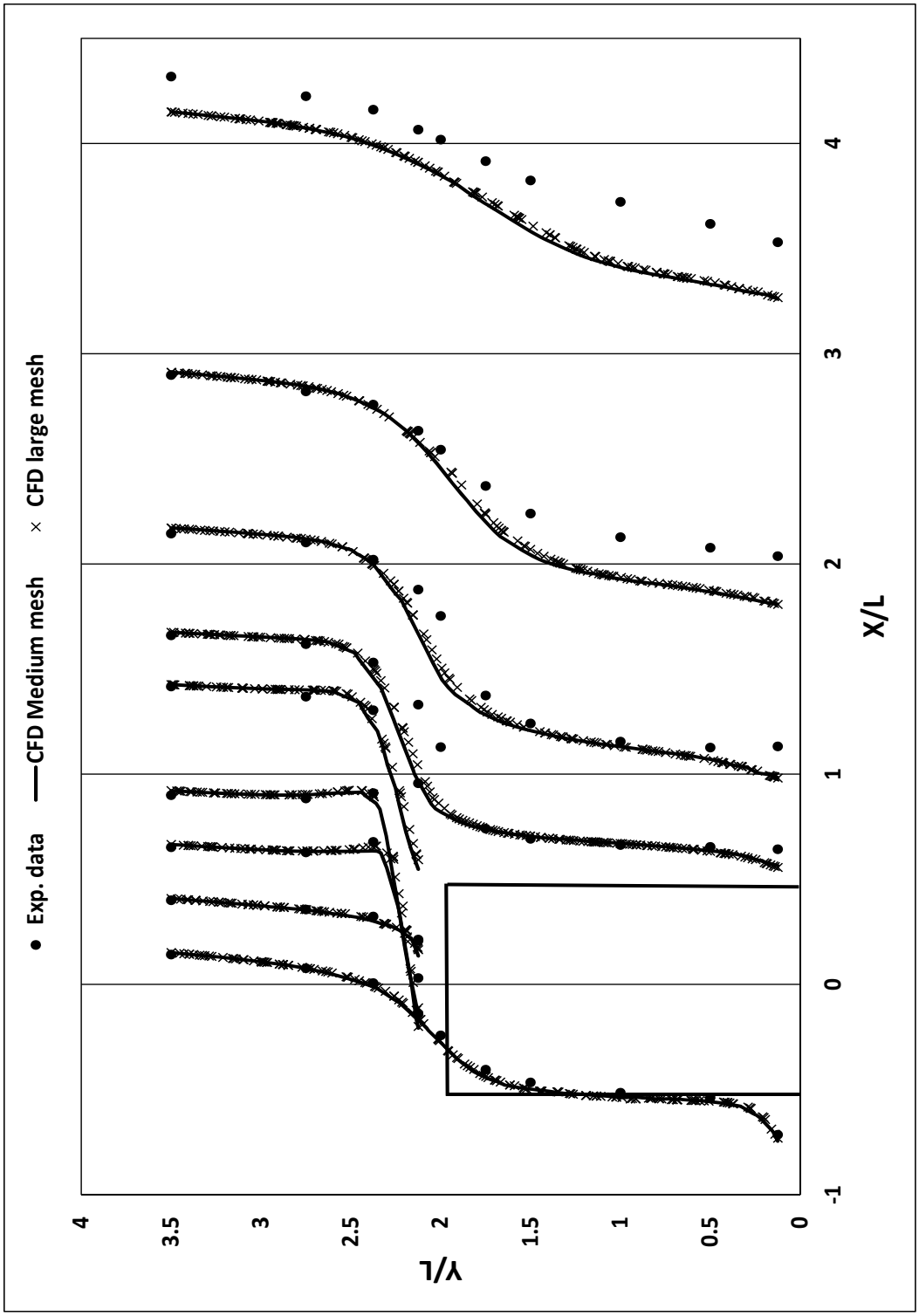

FIGURE 2.13: Vertical U profile CFD steady-RANS calculation results using transition $k-kl-\omega$ model for medium mesh and large mesh compared with the experimental data points (Yoshie et al., 2007).

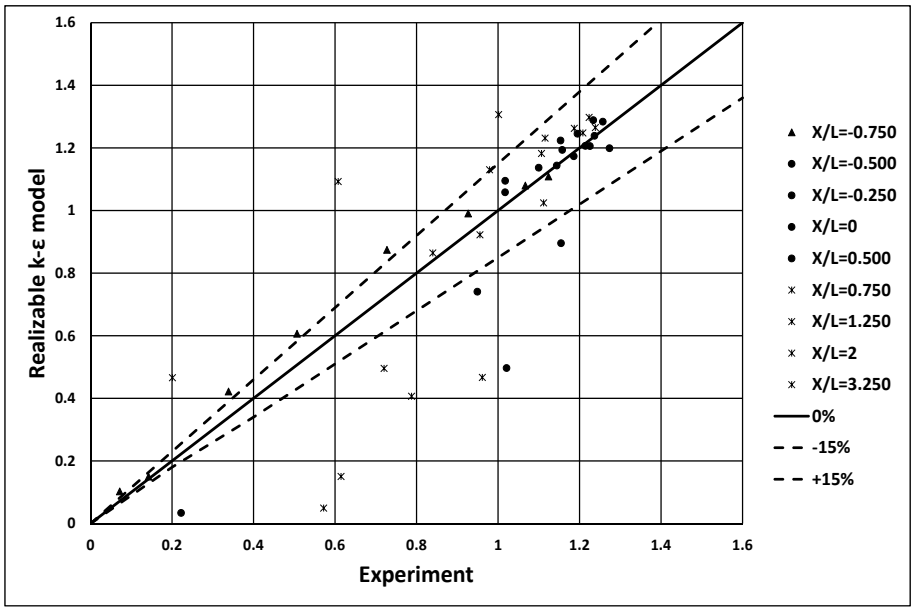

FIGURE 2.14: Pedestrian level wind comfort assessment using Realizable $k-\epsilon$ model.

models used in this validation study. The results were based on the transition $k-kl-\omega$ model, the realizable $k-\varepsilon$ (RKE) model, the re-normalized group $k-\varepsilon$ (RNGKE) model and LES study results. It can be seen that in the region where the wind speed has increased (i.e. where wind speed ratio is 1.0 or higher), which is important in the evaluation of the pedestrian wind environment study, it was predicted well within the accuracy of approximately 15%. However, in the weak wind region behind the building, the wind speed ratio was evaluated lower than in the experiment. Comparison with different model states that predicted accuracy is slightly higher using the transition $k-kl-\omega$ model and with the RNGKE model (higher than LES). Willemsen et al. (2002) reported that wind tunnel experiments can conservatively exhibit a standard error of 20% when measuring the pedestrian level wind. Therefore, it should be noted that the wind tunnel data also include uncertainties, to an extent.

Turbulent $k-$ profile on the vertical cross-section

The difference between the velocity fields for the various turbulence models is closely related to the accuracy of the turbulent energy (k) ((Tominaga et al., 2008b)). Figure 2.18 shows the distribution of the vertical k-profile on the line $Y/L = 2.125$ for the different steady-RANS turbulence models studied here. It can be observed from this plot that all the evaluated turbulence models in this study underestimate k overall. On the roof of the building realizable $k-\varepsilon$ model shows good agreement with the experiment. However, from the downwind corner of the roof and behind the building transition $k-kl-\omega$ gives closer agreement with the experimental data points.

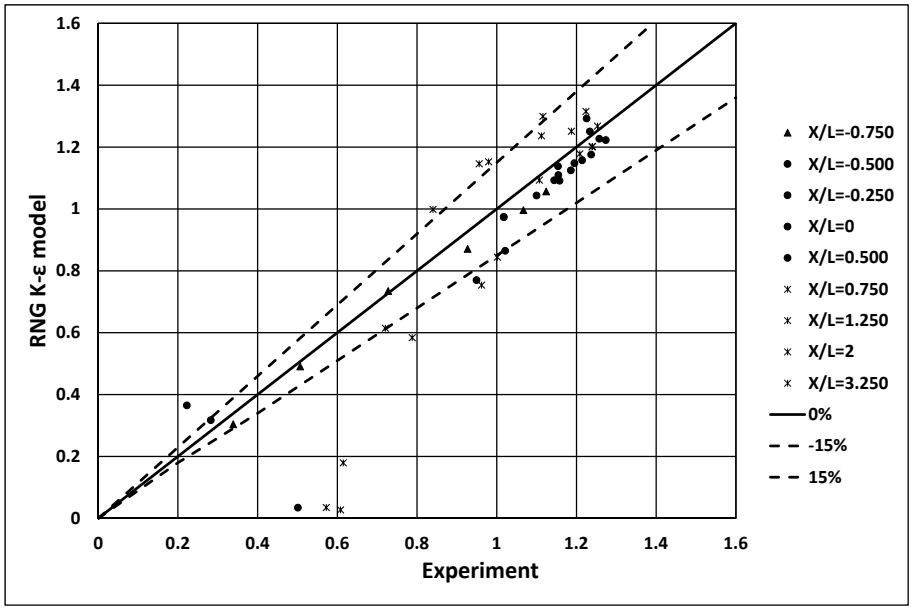

FIGURE 2.15: Pedestrian level wind comfort assessment using the re-normalized group $k - \varepsilon$ (RNGKE) model.

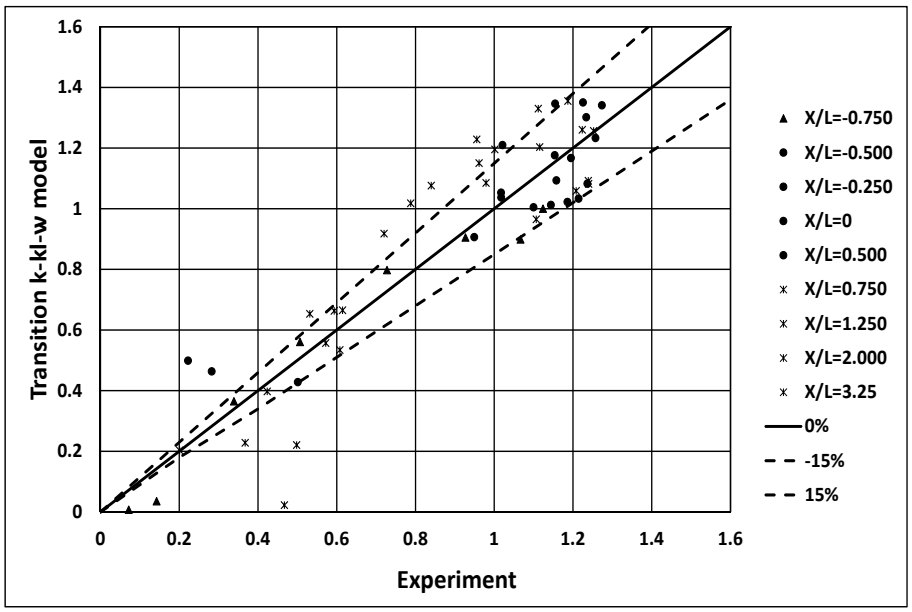

FIGURE 2.16: Pedestrian level wind comfort assessment using transition $k - kl - \omega$ model.

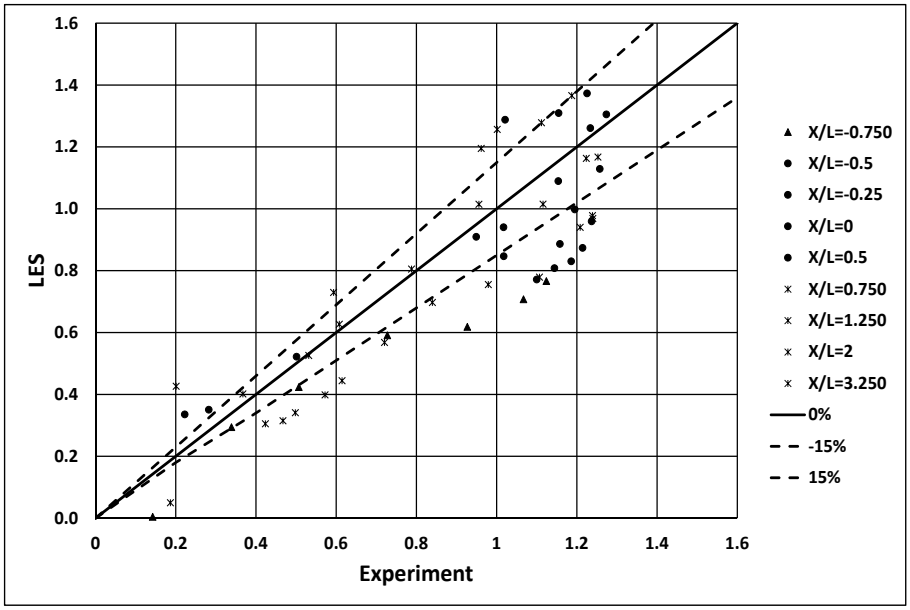

FIGURE 2.17: Pedestrian level wind comfort assessment using LES.

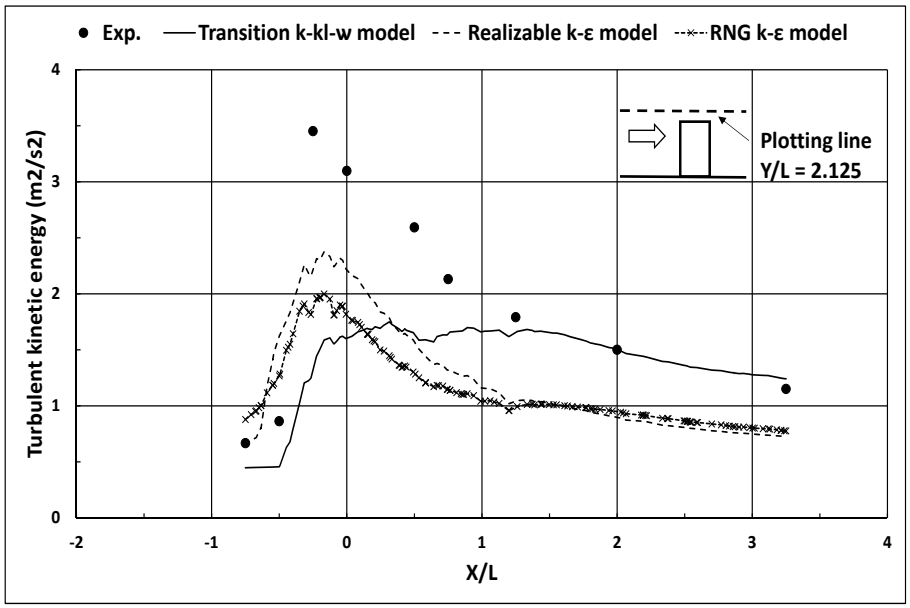

FIGURE 2.18: k-profile on the roof of the building at $Y = 2.125L$.

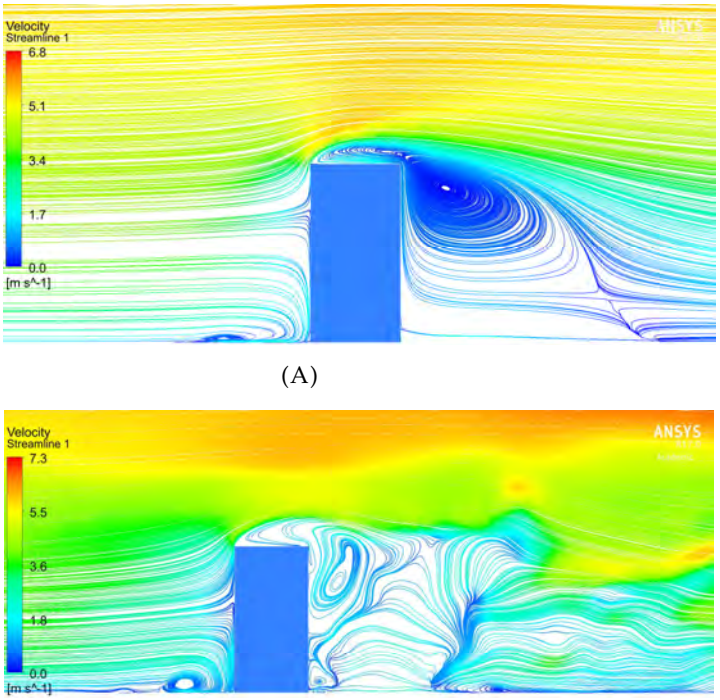

FIGURE 2.19: Comparison of velocity magnitude streamlines in the centre plane $Z = 0$ for (A) the steady RANS and (B) LES.

Flow visualization to compare results of steady RANS and LES for Model A

To compare the simulation results of steady RANS and LES, a flow visualization study was carried out for Model A. Figure 2.19 shows the velocity streamlines for the steady RANS (using $k-kl-\omega$ model) and LES results, in the vertical cross-section at the center plane $Z = 0$ for the building model. Since streamlines represent the tangent or parallel to the local velocity vector, it is generally used in Fluent to show the direction of the local velocity. From the flow visualization, it can be seen that the stagnation point on the front of the building agrees well for both steady RANS and LES. The flow separation from the upstream edge of the top of the building and the backflow from the wake of the building can clearly be seen in both the cases. In the case of LES, the separation zone in the wake of the building differs from time to time, which shows the evidence of vortex shedding.

For the comparison of the flow structure near the ground, velocity streamlines were also plotted for both steady RANS ($k-kl-\omega$) and LES as shown in Figure 2.20. Flow separation from the upstream edge of both sides of the building can be clearly observed in both the cases. However, in the wake of the building vortex shedding can clearly be observed in the case of LES which was not seen in the case of steady RANS. It should be noted that due to the wake box used to refine the mesh around the building vortex shedding can be clearly observed in the near wake region of the building in the case of LES which gets restricted far downstream due to the lower number

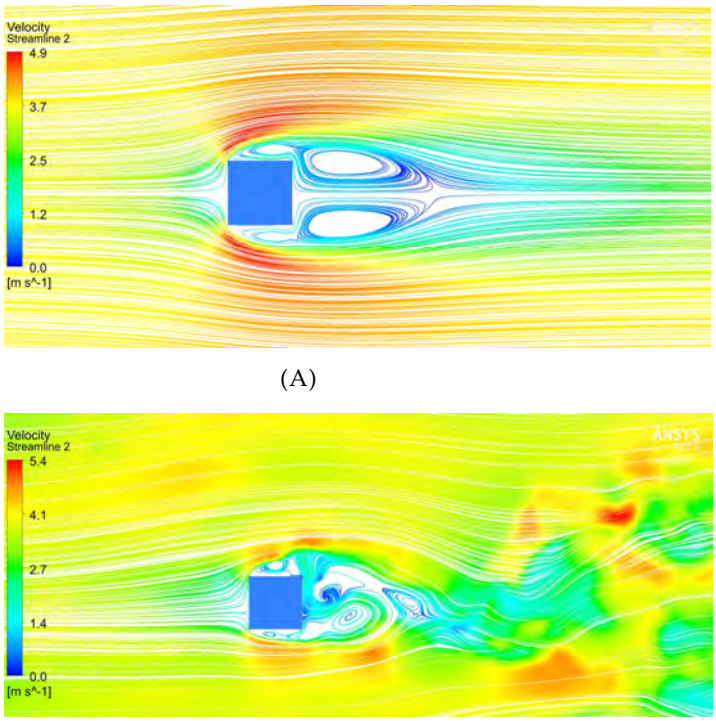

FIGURE 2.20: Comparison of velocity magnitude streamlines near the ground for the plane $Y = 0.05$ for (A) the steady RANS and (B) LES.

of mesh elements there.

In Fluent, iso-surfaces are generally used to display results on cells that have a constant value for a specified variable. In this study velocity iso-surface plots for steady-RANS and LES simulations were carried out by keeping the Z-co-ordinate of the mesh fixed in the plane $Z = 0$ as shown in Figure 2.21. This is showing further evidence of vortex shedding in the case of LES which is not observed for the steady RANS.

Summary for CFD simulation results of Model A

- Comparison of the vertical distribution of the wind velocity U for the different steady-RANS models with the experimental data and with the LES simulation gives considerably good agreement with the experimental data in the general flow region.
- On the roof of the building reverse flow occurs according to experimental study, which was reproduced only by the transition $k-kl-\omega$ and LES simulations.
- Velocity distribution near the ground was predicted slightly higher ($\approx 85\%$) using the transition $k-kl-\omega$ and RNGKE model compared to other models, even better than LES.
- Turbulent kinetic energy (k) on the line above the roof was underestimated by all the steady-RANS turbulent models overall. However,

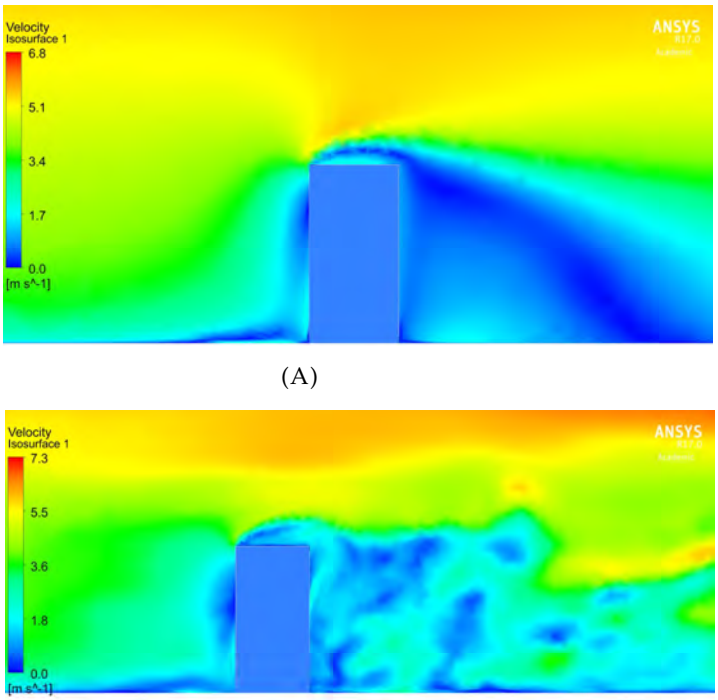

FIGURE 2.21: Comparison of velocity iso-surface contours for the centre plane $Z = 0$ for (A) the steady RANS and (B) LES.

on the roof of the building, realizable $k - \varepsilon$ gives closer agreement whereas behind the building $k - kl - \omega$ agrees well with experimental results.

- According to the flow visualization study, vortex shedding can only be observed for the transient flow simulation using LES.

2.3.2 Model B

In order to investigate the performance of different steady-RANS models at $Re = 3.5 \times 10^5$, the pressure coefficient (C_p) and wind velocity (U) on the top of the cube were evaluated. The results were compared with the available experimental study results of Lim et al. (2007) and with the LES simulation results.

Figure 2.22 shows a comparison plot of calculated C_p on the roof of the cube using different models. Comparison with experimental C_p shows that all the models give overall good agreement. However, transition $k - kl - \omega$ model and LES give high negative C_p on the first half of the top of the cube where a $k - \varepsilon$ based model shows a good match. Whereas, for the second half of the region on the top of the cube transition $k - kl - \omega$ model and LES give a comparatively good match with experimental data in contrast to the $k - \varepsilon$ based models.

Figure 2.23 shows a comparison of results of different turbulence models with the experimental data of Lim et al. (2007) on the top of the cube. The performance of different turbulence models was also compared with a

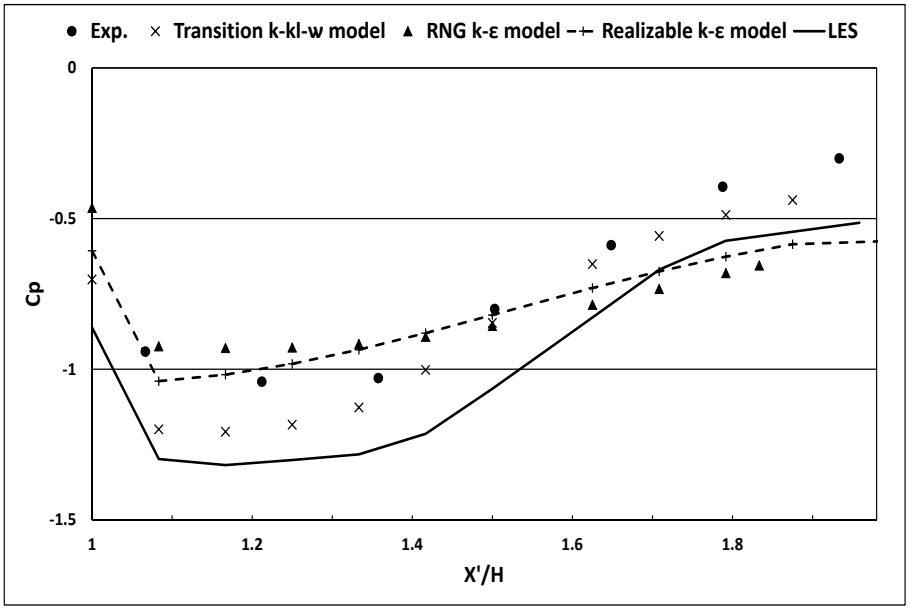

FIGURE 2.22: Pressure coefficient along the centreline ($Z = 0$) of the cube. $X^{'}$ was measured on the top of the cube.

transient LES simulation. The results show that none of the steady-RANS models accurately predict reattachment of the separated shear layer due to the sharp upwind edge of the cube, whereas LES gives good agreement with the experimental data. The performance of different $k-\varepsilon$ based models on predicting the reattachment length on the top of the building was previously evaluated by Tominaga et al. (2008b) at $Re = 2.4 \times 10^4$. According to their study, revised $k-\varepsilon$ based models (such as the realizable $k-\varepsilon$ (RKE) model and the re-normalized group $k-\varepsilon$ (RNGKE) model) could produce shear layer reattachment and reverse flow on the top of the building. However, for the high Re evaluated here and with the choice of the unstructured mesh, $k-\varepsilon$ models were unable to reproduce the reattachment of the shear layer on the top of the cube. However, it was observed that the transition $k-kl-\omega$ model shows reattachment of the flow on the top of the cube, but the reattachment location is beyond the experimentally measured point. As a result, the transition $k-kl-\omega$ model has been used for all the simulations performed in this study.

Flow visualization to compare results of steady RANS and LES for Model B

A flow visualization study similar to Model A was carried out in this case. Velocity streamlines showing the flow structure in the centre plane of the cube and ground were plotted to compare the result of steady RANS and LES.

Figure 2.24 shows the velocity streamlines in the centre plane of the cube. The flow separation on the front of the cube, the front face stagnation point, and the flow separation due to the sharp upwind edge of the top of the cube can clearly be observed for both cases. Further evidence to the velocity plot shown in Figure 2.23 the separated shear layer on the

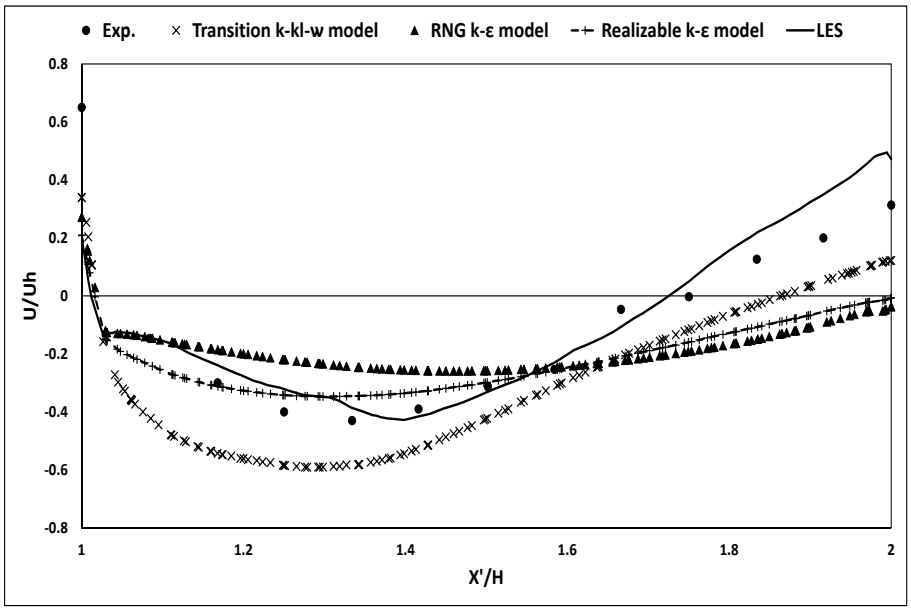

FIGURE 2.23: The axial velocity (U) along the centreline ($Z = 0$) of the cube and parallel to the top of the cube at $0.01\,H$ above it.

top of the building occurs in the case of LES at about three-quarters of the distance along the top surface which can be observed to have shifted downward near the trailing edge of the top of the cube in the case of the steady RANS.

The flow structure near the ground surface using velocity streamlines for both the steady RANS simulation (using $k - kl - \omega$) model and LES are as shown in the Figure 2.25. The flow separation due to the sharp edges of the side faces for both cases can clearly be seen in this study. As described for Model A, vortex shedding can only be seen in the LES simulation.

Further evidence of observed vortex shedding in LES which was not captured by steady RANS can be seen by the velocity iso-surface plots as shown in Figure 2.26. In this case, iso-surfaces were drawn based on fixing the Z-co-ordinate for the plane $Z = 0$. Mesh refinement using a wake box near the cube was also done for this model. Due to this reason, the vortex shedding in the far wake region looks slightly restricted.

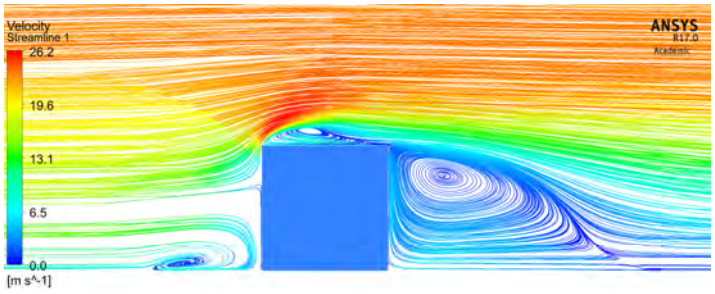

(A)

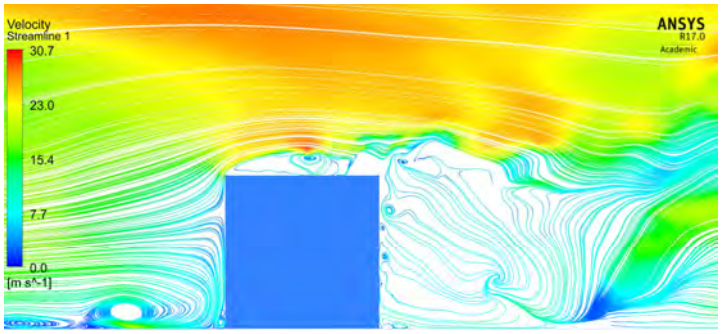

(B)

FIGURE 2.24: Comparison of velocity magnitude streamlines in the centre plane $Z = 0$ for (A) the steady RANS and (B) LES.

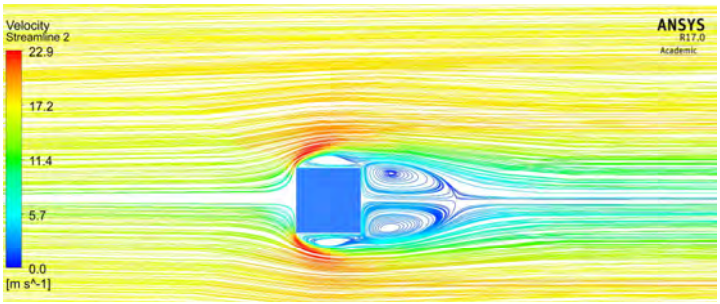

(A)

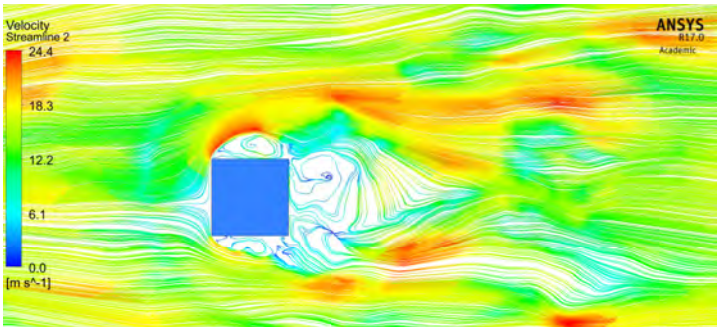

(B)

FIGURE 2.25: Comparison of velocity magnitude streamlines near the ground for the plane $Y = 0.05$ for (A) the steady RANS and (B) LES.

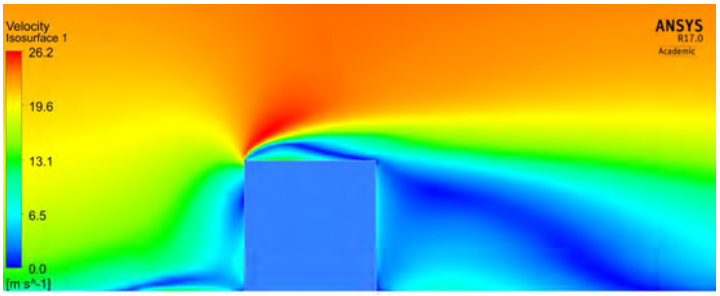

(A)

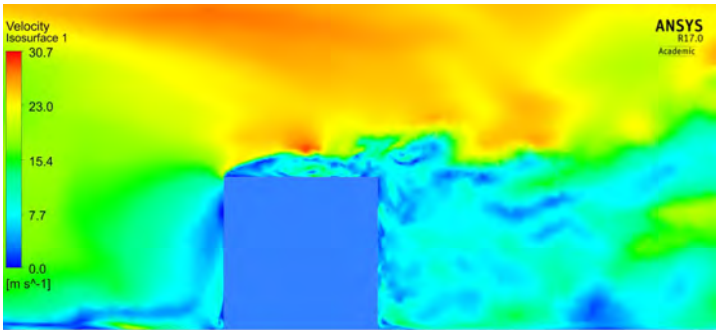

(B)

FIGURE 2.26: Comparison of velocity iso-surface contour for the centre plane $Z = 0$ for (A) the steady RANS and (B) LES.

2.4 Summary of Chapter 2

A technique and procedure for CFD have been developed and validated with published wind tunnel data that was generated for the flow past a single building and a cube. The CFD procedure was verified using wind pressure coefficient, velocity and turbulent kinetic energy distributions for two different building models with Re of order 10^4 and 10^5. The velocity distribution on and around the building model A in the vertical cross-section and near the ground calculated from CFD using the transition $k-kl-\omega$ shows a good match to those found in the reference paper. However, CFD results of the turbulence kinetic energy distribution were found to be under-predicted compared to those found in the experimental results.

The performance of different turbulence models with an increase in Re was also evaluated. The velocity and pressure coefficient distributions on the top of the model used for this study calculated from CFD and using the transition $k-kl-\omega$ model show an overall good match with the published data.

The LES modelling scheme was also examined for a single building model with an increase in Re. It was found that the LES predicts overall velocity distribution on and around the building and pressure distribution on the top of the building model comparatively well with the corresponding experimental data. However the velocity distribution near the ground when validated against the wind tunnel data gives less agreement than the RANS simulations. The vortex shedding and overall flow structure created

by LES CFD simulation were found to be a good match to the experimental data. However, the long computational time required to generate the velocity distribution needed for the parametric study for different street canyons in the following chapters was felt to be excessive.

In Chapter 2, a variety of methods of characterizing the flow structure of a single building like structure were found of value. These include:

- plotting of the pressure coefficient distribution on the top of the building
- plotting of the velocity distribution over and around the building
- plotting of the turbulent kinetic energy to examine the overall flow prediction by different turbulence models in CFD
- plotting of velocity streamlines to examine the flow paths and formation of vortex structures
- visualization of vortices through iso-surfaces

Chapter 3 will involve a parametric study to analyse the flow structure and pedestrian level wind comfort assessment study inside uniform and non-uniform street canyons using the CFD steady RANS modelling approach. Many of the methods for characterization of aerodynamic flow past a building that were validated in Chapter 2 will be used to evaluate the flow structure analysis in Chapter 3.

Chapter 3

Flow Structure and Pedestrian Level Wind Categorisation Inside Uniform and Non-uniform Street Canyons

3.1 Introduction

3.1.1 Flow structure around and in-between two buildings in tandem arrangement

High rise buildings in urban areas should be designed to ensure the comfort of their inhabitants. The construction of a building inevitably changes the outdoor environment around the building. These changes include wind speed, wind direction, air pollution, driving rain and heat radiation. The changes in these quantities depend on the shape, size and orientation of the building and on the interaction of the building with surrounding buildings (Blocken et al., 2004).

For multiple obstacle arrays, the flow field is more complex than the flow around a single obstacle due to mutual interference (Sakamoto et al., 1988). When an obstacle is placed in the wake of another obstacle in the cross-flow, the arrangement is called the *tandem arrangement*. In this case, the unsteady aerodynamics of the second obstacle becomes dependent not only on the flow characteristics of its wake, but also on the wake of the upstream obstacle. This phenomenon is called *Buffeting* (Havel et al., 2001). Depending upon the spacing between the two tandem obstacles, the flow structure can be divided into three main regimes (Oke, 1988), namely (1) Isolated roughness flow: When the spacing between the two obstacles is wide, their flow fields do not interact and the flow returns to the upwind profile before the downstream obstacle is encountered and the flow is called *isolated roughness flow*; (2) Wake interference flow: when the obstacles are more closely spaced such that the height, spacing and density of the array combine to disturb the flow structure before the upstream obstacle and inside the gap, it is called the *wake interference flow* and (3) Skimming flow: For the very small spacing between the obstacles, a stable circulatory vortex is established in the gap which is called the *skimming flow*.

Experimental studies analysing the flow structure around a pair of wall-mounted obstacles in tandem have been reported by Meinders et al. (1999) at a low Re of 3854 and for a thin boundary layer; Martinuzzi et al. (2000), Martinuzzi et al. (2004) at a moderate Re of $22,000$ and for a thin boundary layer; and Sakamoto et al. (1988) at a moderately high Re of 1.52×10^5 inside a thick boundary layer. Numerical studies on flow around an array of wall-mounted cubes include Farhadi et al. (2008) and Paik et al. (2009) at a moderate Re of $22,000$. Generally, Re of wind flow around lo-rise or high-rise building complexes are very large and could be in the range of $10^5 - 10^7$.

Sakamoto et al. (1988), have investigated the interference effects of a second obstacle situated in the wake of the first for tall, surface mounted obstacles of square cross-section and with $W/H = 1/3$. They investigated this interference effect by the reattachment of the separated shear layers from the sharp leading edges of the sides of the upstream obstacle. They identified four regimes as a function of the gap length S and W as follows (1) Stable reattachment: when the relative spacing between the obstacles is in the range of $S/W < 2$, the separated shear layers from both sides of the upstream obstacle attach to the side surfaces of the downstream obstacle and no flow periodicity is found in the wake. (2) Unstable reattachment or bistable flow: for a larger spacing for $2 < S/W < 3.5$, a part of the separated shear layers from the upstream obstacle starts to roll up intermittently in to the region between the two obstacles and periodicity is observed in the wake of both obstacles. (3) Stable synchronized: for a critical range of spacing for $3.5 \leq S/W \leq 50$ the periodically separated shear layers roll up strongly into the gap between the two obstacles without reattachment. (4) Unstable synchronized: for very large spacing of $S/W \geq 50$, both obstacles behave as isolated, and the vortex shedding downstream of the two obstacles is no longer synchronized which results in two distinct vortex streets.

Martinuzzi et al. (2000) studied the flow around two surface-mounted tandem cubes of height H, in a thin laminar boundary layer. They investigated this interference effect by the reattachment of the separated shear layer from the sharp leading edge of the upstream obstacle top. They found similar regimes as Sakamoto et al. (1988), namely (1) a bistable regime for the range $S/H < 1.4$, which is similar to the unstable reattachment regime of Sakamoto et al., 1988 described above. In this case, the shear layer separated from the leading edge of the upstream obstacle top, impinges on the top of the downstream obstacle; (2) a "lock-in" regime for the range $1.4 < S/H < 3.5$ for which case the upstream shear layer impinges on the leading face (near the leading edge) of the downstream obstacle and a strong vortex rolls in the gap and (3) quasi-isolated regime for $S/H > 3.5$, which is similar to the unstable synchronized regime of Sakamoto et al., 1988. In this case, the separated shear layer from the top of the upstream obstacle reattaches in the gap between two obstacles.

The studies of Sakamoto et al. (1988) and Martinuzzi et al. (2000) when compared as functions of obstacle separation, suggests that buffeting flows for two obstacles for thick and thin boundary layers share many qualitative similarities. However, these studies are performed at the moderate Re. Also, note that these investigations were based on the reattachment of the shear layers either from the sides or the top leading edges of the upstream obstacle. Experimental and numerical simulations to analyse the

flow structure for two tandem obstacles at high Re (for Re in the range of $10^6 - 10^7$) inside a thick boundary layer and investigating reattachment of all three separated shear layers (from the top and sides of the upstream obstacle leading edges) have yet to be reported in the literature. This type of flow study is important because generally, wind flow around buildings occurs at high Re and inside the thick atmospheric boundary layer.

In the present parametric study, which has as its aim to study the flow field between and close to two buildings, we analyse the $3D$ flow structure around and in-between two medium-rise buildings with equal height and long in span-wise length (i.e. the width of buildings) compared to building height. The parameters used for this analysis are the street width, building width and building height.

3.1.2 Pedestrian comfort inside uniform and non-uniform street canyon

A street canyon is said to be *uniform* if the adjacent building heights are equal (i.e. $H_1 = H_2$) as shown in Figure 3.1; if the adjacent building heights are unequal, it is said to be *non-uniform* (i.e. $H_1 \neq H_2$) and either step-up if $H_1 < H_2$ or step-down if $H_1 > H_2$. The dimensions of a street canyon are expressed by its aspect ratios S/H (street width to building height), and S/W (street width to building width) assuming $W_1 = W_2$. In this study the building with the greatest height is used to calculate the aspect ratio for non-uniform canyons.

Wind comfort and wind safety for pedestrians are important requirements for urban areas. According to the definition of pedestrian comfort by Bottema (2000): " Pedestrian discomfort occurs when wind effects become so strong and occur so frequently (say on time scale up to 1 h), that people experiencing those wind effects will start to feel annoyed and eventually will act in order to avoid these effects". This wind comfort and wind safety generally refer to the mechanical effects of wind on people. Mechanical effects on people range from the feeling of a light breeze on the skin to being blown over by a strong gale (Lawson et al., 1975). Lawson et al. (1975) have provided extended "Land Beaufort scale" (ELBS) of wind effects on people (Table 1.3). The tabulated wind speed refers to the value that is measured at a pedestrian height of ($Y = 1.75$ m) over open terrain with an aerodynamic roughness length y_0 of 0.03 (Wieringa, 1992). According to the ELBS, at Beaufort Number 3 (gentle breeze or wind speed of $2.4 - 3.8$ m/s) these effects include disturbed hair, clothes flapping and newspapers being difficult to read. So, if we consider a person sitting in an open cafe or standing at a bus stop in the street canyon, for example, wind can cause a disturbance. In this study, a reference wind speed of 5.9 m/s at the building eave height of 20 m was chosen to obtain a wind speed of Beaufort Number 3 at the pedestrian height of approximately 1.75 m.

According to Blocken et al. (2007a) studies focused on pedestrian-level winds are mainly classified in two categories: (1) fundamental studies, which are typically conducted for simple, generic building configurations to obtain insight into the flow behaviour, to study the influence of different building dimensions and street widths, to provide input for knowledge-based expert systems (KBES), and for model validation; (2) applied studies, which provide knowledge of the wind environment conditions in specific

and much more complex case studies. We take our study to be of a fundamental nature, aimed as it is at a parametric understanding of the $3D$ flow field in and around the street canyon and at the pedestrian level. Fundamental studies have been conducted by Ishizaki et al. (1971) and Wiren (1975), who carried out wind tunnel measurements along the street centre line in various two-building configurations. Both studies focused on the mean wind speed in the street between rectangular buildings of equal height. More detailed wind-tunnel measurements were given by To et al. (1995), who reported contours of mean wind speed and turbulence measurements at a pedestrian level in streets between two high rise buildings of equal height for parallel and perpendicular wind direction. Numerical studies for two-building models were conducted by Bottema (1992) and Baskaran et al. (1996). A very detailed numerical assessment of the influence of varying a wide range of street widths was first conducted by Blocken et al. (2007a) for parallel wind direction and with buildings of equal height.

These studies on wind speed conditions in a street canyon were mainly focused on pedestrian-level winds for discrete points, a limited range of street widths and for a wind direction parallel to the street canyon. Detailed CFD study of wind blowing perpendicular to the street canyon still requires more attention. In this study, we perform a detailed CFD simulation to provide the mean wind speed at the pedestrian level across the entire street for a perpendicular wind direction in order to assess pedestrian wind comfort inside street canyons.

Section 3.2 describes more in detail about the model of a street canyon, boundary conditions and performed mesh independence study for this analysis. Section 3.3 describes in detail about the obtained results for the flow structure and pedestrian comfort inside the uniform and non-uniform street canyon respectively. Section 3.4 presents summary of this study.

3.2 CFD simulations: computational model and parameters for uniform and non-uniform street canyon study cases

3.2.1 Model description for street canyon

The effect of changing street widths, building widths and building heights on the flow pattern and pedestrian wind comfort inside a street canyon were investigated by performing CFD simulations. The size of the computational domain was selected according to CFD best practice guidelines by Franke et al. (2007). The computational domain covers $33\,H$ in the $X-$ direction, $16\,H$ in the $Z-$ direction and $6\,H$ in the $Y-$ direction. The Reynolds number was 8.1×10^6 based on the reference height (20 m) and corresponding wind speed (5.9 m/s) as specified in the section 4.1. We considered three cases: uniform canyon with varying street width; uniform canyon with varying building width, and non-uniform street canyon.

The model geometry of the uniform street canyon as shown in Figure 3.1 with dimensions $W \times H \times L = 80\,(m) \times 20\,(m) \times 20\,(m)$ was chosen to represent common medium-rise buildings. The chosen street widths were

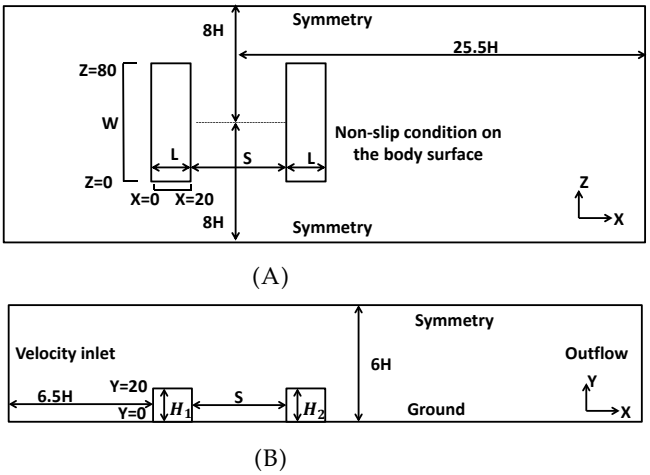

FIGURE 3.1: Computational domain and boundary conditions for the uniform street canyon (A) Plan view (B) side view.

$S = 10$, 12, 14, 16, 18, 20, 24, 30, 40 and 50 m, corresponding to narrow to regular and wide street widths for medium rise buildings.

On the other hand, when investigating the role of building width on the flow structure and pedestrian comfort the chosen building widths were $W = 20$, 40, 60, 80 and 100 m. For this case, the height and length of both buildings were kept constant at 20 m. The chosen street widths were $S/H = 20$ and 40.

Finally, in the non-uniform street canyon cases, the chosen heights of the building were $H_1 = 16$ m and $H_2 = 20$ m for the step-up street canyon, and $H_1 = 20$ m and $H_2 = 16$ m for the step-down street canyon, with street widths of $S = 20$ m and 40 m for both non-uniform cases. The width (W) of both buildings was kept constant at 80 m.

3.2.2 Boundary conditions for street canyon

Simulations were performed using the commercial CFD package Ansys Fluent version 17.0. At the inlet of the computational domain, mean wind speed and turbulence profiles were imposed using two methods similar to as described in subsection 2.2.2 i.e. using (1) UDFs and (2) using profiles imposed at the inlet. These simulations were carried out in an empty channel prior to applying a suitable profile to simulate flow around buildings and street canyon.

- **Using UDF and with keeping turbulence intensity (I) constant with varying vertical height**
  For the UDF method, the vertical profile of the mean wind speed was given by the logarithmic law satisfying Equation 2.1 as described in Chapter 2. The turbulent kinetic energy $k(y)$ at inlet was specified using equation $k(y) = \frac{3}{2}(U_{avg} \cdot I)^2$, as given by Irtaza et al. (2013), where $U_{avg} = \sqrt{U^2 + V^2 + W^2}$ is the mean wind speed and $I = \frac{U'}{U_{avg}} = \frac{\sqrt{\frac{1}{3} \cdot (u'^2 + v'^2 + w'^2)}}{\sqrt{U^2+V^2+W^2}}$ is the turbulence intensity which was specified to be 21.5% at the building height and was kept constant for

all trials. Note that, above specified turbulence intensity was obtained from AS/NZS $1170.2:2011$ (Structural Design Actions-Part 2: Wind Actions, 2011) at the building height of 20 m. Specific dissipation rate $\omega(y)$ using turbulent dissipation rate $\varepsilon(y)$ was also specified at the inlet. Equations used for turbulent dissipation rate $\varepsilon(y)$ and specific dissipation rate $\omega(y)$ were Equation 2.2 and Equation 2.3 respectively. See Appendix D for UDFs used for this study.

- **Profile obtained from the AS/NZS $1170.2:2011$ (Structural Design Actions-Part 2: Wind Actions, 2011) for the Intensity (I) imposed at the inlet; where the turbulence intensity (I) was varying with vertical height**
  In this method, the velocity profile ($U(y)$) was calculated by the logarithmic law satisfying Equation 2.1 as described in Chapter 2 and turbulent kinetic energy ($k(y)$) profile (calculated from the given I profile) from the AS/NZS $1170.2:2011$ (Structural Design Actions-Part 2: Wind Actions, 2011) were imposed at the inlet using the profile method available in Fluent; Whereas, the $\varepsilon(y)$ and $\omega(y)$ profiles were calculated and imposed at the inlet according to Equation 2.2 and Equation 2.3 respectively.

U^*_{ABL} can be calculated by a specified velocity U_{ref} at reference height y_{ref} as given by Equation Equation 2.4.

Here we take, $U_{ref} = 5.9$ m/s, the free stream wind speed at the building height $y_{ref} = 20$ m to analyse the wind speed between $2.4 - 3.8$ m/s at the pedestrian height as specified in the above section.

The top and sides of the computational domain had symmetry boundary conditions. The outlet boundary condition was specified as outflow. The bottom of the domain and that on all faces of both buildings was the no-slip boundary condition. Inflation layers were generated on the ground and both buildings faces with 40 grid layers in each to accurately resolve the boundary layer. We found that such resolution was necessary in order to accurately predict separation and reattachment points. The height of the first cell of the boundary layer was chosen to be 2.7×10^{-5} m to ensure wall unit $y^+ \approx 1$ to resolve the viscous sub-layer of the boundary layer, a requirement of the turbulent model used in this study. The non-uniform mesh contains tetrahedral and wedge-shaped elements. The boundary layer thickness based on the height of the building was $\delta/H \approx 45$, which is the expected value for roughness length $y_0 \approx 0.2$ m and corresponding power-law exponent $\alpha = 0.28$ for the real atmospheric boundary layer in which a power-law velocity profile is assumed.

Simulations were carried out in an empty channel (with roughness present but without buildings) using two different methods as specified above (using (1) UDFs and (2) profiles) prior to applying the turbulent model and boundary conditions to specified street canyon study cases. Figure 3.2 shows simulation results of the empty channel test comparing the wind speed profiles specified at the inlet and the incident profiles (i.e. fully developed profiles at the location where the buildings would be positioned). It can be seen from this plot that with the turbulent model and boundary conditions used predicts wind speed profile accurately. Figure 3.3 shows comparison of the inlet vertical profile of the turbulent kinetic energy ($k(y)$) (obtained from the AS/NZS $1170.2:2011$ (Structural Design Actions-Part 2: Wind Actions,

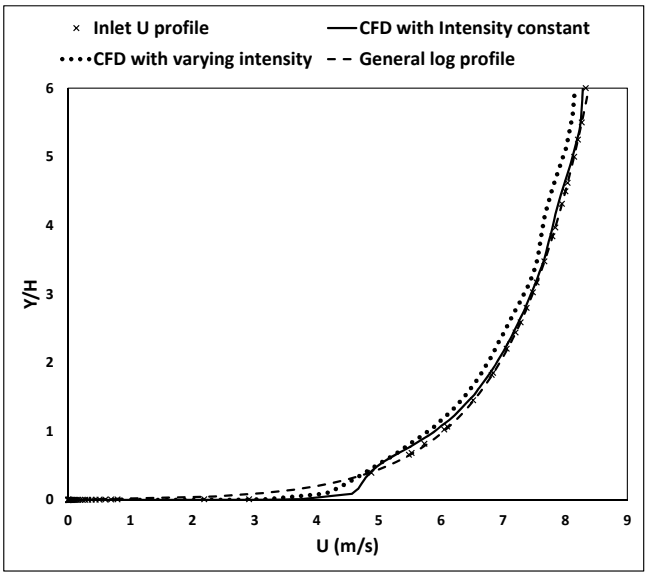

FIGURE 3.2: Comparison plot of the inlet vertical profile of wind speed with the incident wind profiles (at the location where buildings would be positioned) and with corresponding general log-law profile for the specified terrain type.

2011)) with the incident profiles for the case of constant intensity with vertical height and the case of varying intensity with vertical height. It could be seen from this comparison plot that the values of incident k-profiles were under-predicted for both the cases compared to the inlet profile. The reason for this under-prediction of k-profile is as mentioned in the subsection subsection 2.2.4. Also, it was specified in the subsection 2.2.4 and according to Pirooz et al. (2018) that k-profiles should be decreased with the vertical height, which is not the evidence in the case with either of the data obtained from the AS/NZS 1170.2 : 2011 (Structural Design Actions-Part 2: Wind Actions, 2011) or from the simulated profiles using CFD in this study. This clearly indicates the requirement of wind tunnel experiment or full-scale measurement to get exact mean wind speed and turbulence profiles for the specified terrain type and for the Re of interest. However, the observed stream-wise gradient in the incident mean wind speed profiles using these two methods was minor when compared with the inlet profile and with the general log-law profile for the specified terrain type. Hence, further simulations for the specified street canyon study cases were carried out using the UDF method for the inlet boundary condition.

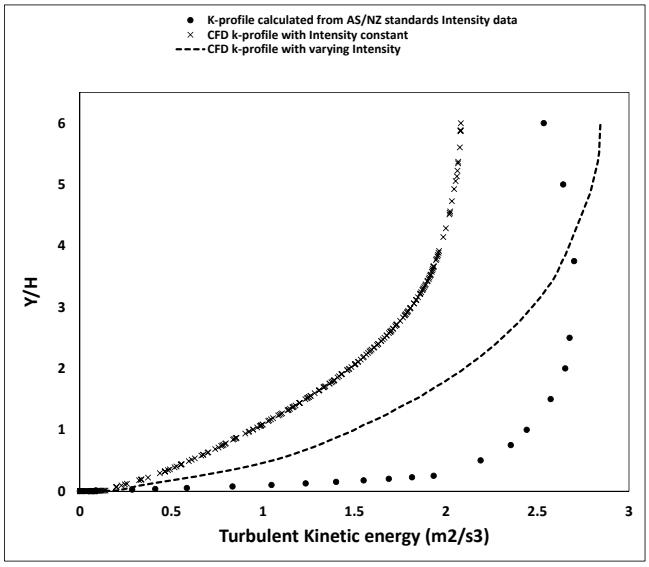

FIGURE 3.3: Comparison plot of the vertical profile of turbulent kinetic energy profile obtained from AS/NZS 1170.2 : 2011 (Structural Design Actions-Part 2: Wind Actions, 2011) with the CFD incident profiles.

3.2.3 Computational mesh for uniform and non-uniform street canyon study cases

A mesh independence study in an empty channel (with roughness elements present but without buildings) was carried out to demonstrate the independence of the flow field on the refinement of the mesh for this study. The coarse mesh had 3 million cells of resolution 2.5 m throughout the computational domain. The medium mesh had 5.5 million cells with a resolution of 2 m throughout the computational domain and the fine mesh had 9.8 million cells and a resolution of 1.6 m throughout the domain. Figure 3.4 shows results of the mesh independence study. The undisturbed vertical profiles of mean wind speed, turbulence quantities were compared for all three meshes at the location where the building would be positioned. These profiles are called "incident" profiles. These profiles for the coarse mesh are almost indistinguishable to that of the fine mesh. Thus, it could be concluded that the coarse mesh is sufficient. However medium mesh as specified above was used for all studied cases of uniform and non-uniform street canyon and mesh resolution used on the faces of buildings was 1 m. The reason for selection of the Medium mesh for this study is as specified in the subsection 2.2.5 of Chapter 2.

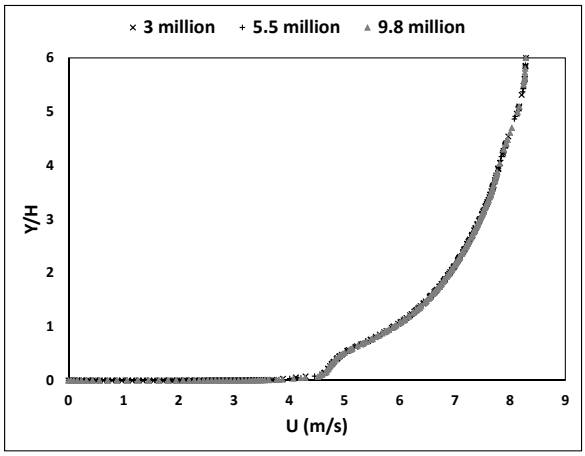

(A)

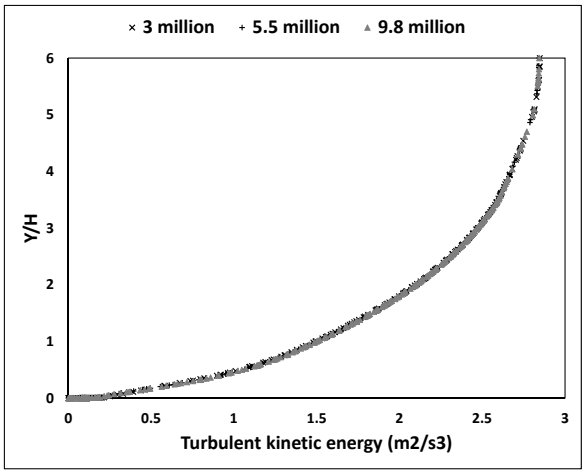

(B)

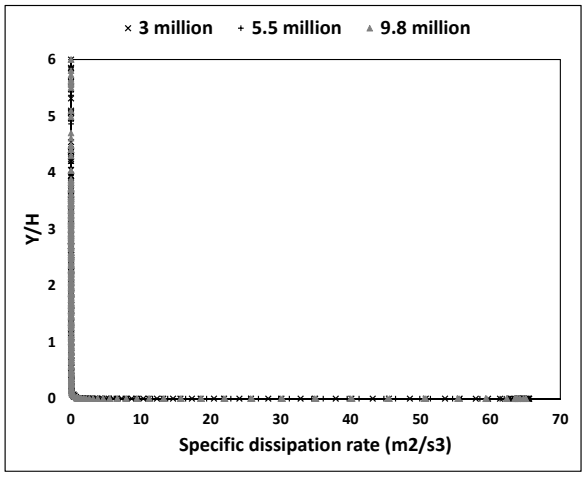

(C)

FIGURE 3.4: Mesh independence study for the street canyon in an empty channel; using different mesh elements showing incident wind profiles of (A) wind speed (B) turbulent kinetic energy and (C) specific dissipation rate.

3.2.4 Other parameters

The Pressure-Implicit with Splitting of Operators (PISO) algorithm scheme with skewness correction was used for the pressure-velocity coupling; pressure interpolation was second-order. Second-order discretization schemes were used for both convective terms and viscous terms of the governing equations. The simulations were initialized by the values of the inlet boundary conditions. Surface monitor points inside the street canyon with (X, Y, Z) coordinates $(22, 8, 40)$, $(26, 12, 30)$, $(30, 7, 20)$, $(34, 5, 70)$, and $(38, 10, 50)$ were used to measure convergence for the mean wind speed. These are the points used for $S/H = 1$ and $W/H = 4$ and were changed accordingly with a change in street aspect ratio S/H and building width to building height aspect ratio W/H. The simulations were terminated when the residuals at all specified surface monitor points reached the criteria of a difference in value between two iterations of 0.0005 for 20 consecutive iterations.

3.3 Results and discussion

In this section we studied the effect of varying the street width and building width in an uniform street canyon as follows: (a) the ratio of street width to building height is between 0.5 and 2.5 from which several examples were chosen for analysis; (b) the ratio of building width to building height is between 1 and 5 for street aspect ratio $S/H = 1$ and 2. The non-uniform street canyon cases studied here are: (a) step – up street canyon with $S/H = 1$ and 2 and (b) step – down street canyon with $S/H = 1$ and 2. Table 3.1 gives the brief description of the studied cases and corresponding figures to follow through this section.

3.3.1 Street width as an influencing parameter

Flow structure

Simulation results for $S/H = 0.5$, 0.7, 1.0, 1.2, 1.5 and 2 are presented in this section. Figure 3.5 shows the variation of C_p along the centre plane ($Z = 40$) for different uniform street canyons on the ground from the inlet of the flow up to the upstream building and comparison with the C_P on the ground for the empty channel up to the location where the building would be positioned. Figure 3.6 shows the variation of C_p on the different faces of the upstream building for different uniform street canyons cases considered here.

From Figure 3.5 it can be observed that inside the boundary layer ($\delta/H \approx 45$ in the present study) the change in far upstream values of C_p is nearly equal for the different studied cases. The pressure distribution on the ground in the case of the empty channel was approximately 0 and was unchanged with the downstream distance of the channel which clearly indicates no pressure gradients and hence no velocity gradients exist in the empty channel. The pressure minimum near the upstream building is located near the horseshoe vortex at around $0.3\,H$ upstream of the windward face. In addition, the pressure maximum at around $0.6\,H$ corresponds to the location of the upstream stagnation point which causes an increase in the surface

TABLE 3.1: Table referring to different the studied cases of uniform and non-uniform street canyon and corresponding figures.

Parametric study based on	**Building height**		**Buildings** width **(m)**	**Street width (m)**	**Results**		
	H_1 **(m)**	H_2 **(m)**			**Center plane pathlines**	**Pedestrian plane streamlines**	**Pedestrian plane wind comfort assessment**
Street width	20	20	80	10, 14, 20, 24, 30, 40	Figures 3.7 and 3.8	Figure 3.10	Figure 3.13
Building width	20	20	20, 40, 60, 80, 100	20	Figure 3.14	Figure 3.15	Figure 3.16
Case 2	20	20	20, 40, 60, 80, 100	40	Figure 3.17	Figure 3.18	Figure 3.19
Building height	20	16	80	20	Figure 3.20(A)	Figure 3.21(A)	Figure 3.22(A)
	16	20			Figure 3.20(B)	Figure 3.21(B)	Figure 3.22(B)
Case 2	20	16	80	40	Figure 3.20(C)	Figure 3.21(C)	Figure 3.22(C)
	16	20			Figure 3.20(D)	Figure 3.21(D)	Figure 3.22(D)

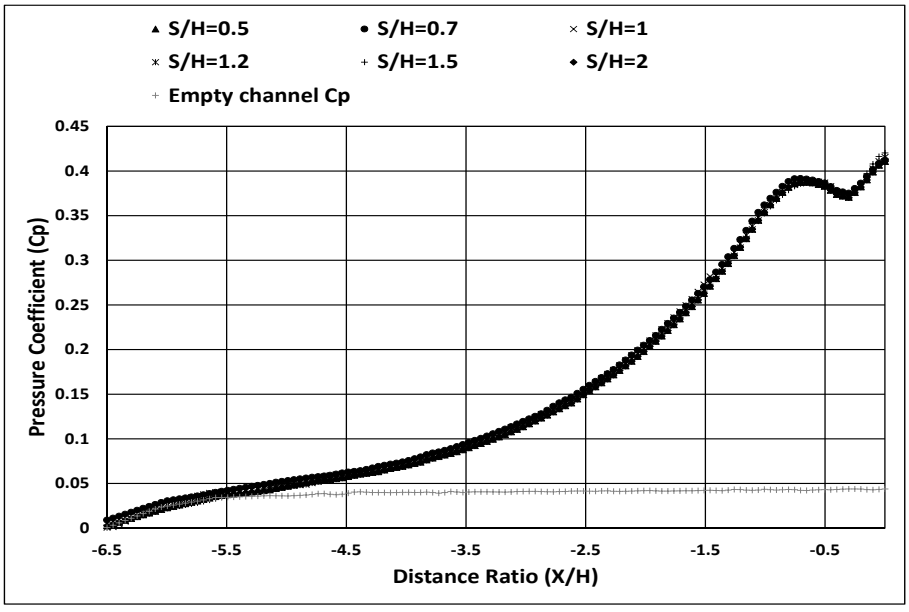

FIGURE 3.5: Comparison of the pressure distribution before the upstream building along the centre plane for the considered uniform street canyon cases and with empty channel pressure distribution on the ground.

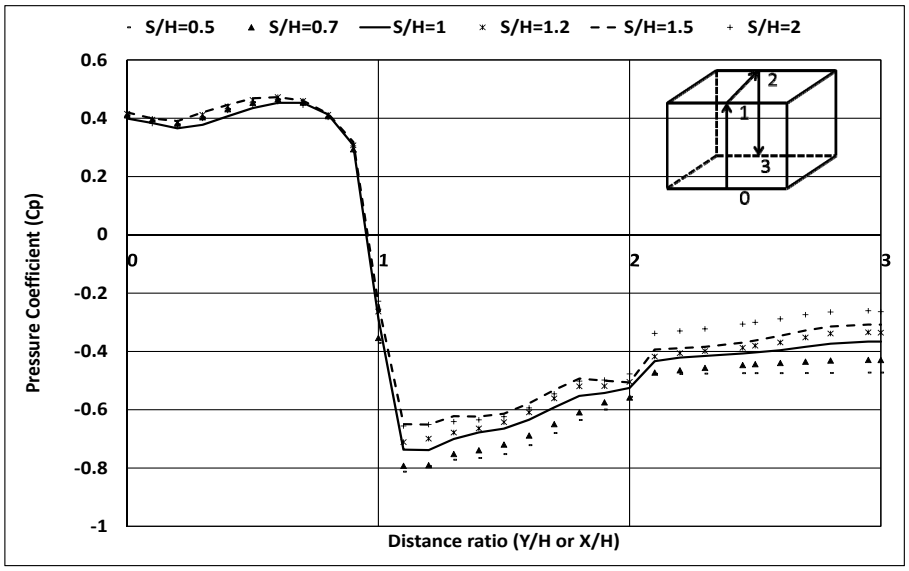

FIGURE 3.6: Pressure coefficient comparison plot along the centre plane of the upstream building for the considered uniform street canyon cases.

pressure. The locations of the horseshoe vortex and stagnation point for the different studied cases are identical.

From Figure 3.6 it is observed that the stagnation point on the front face of the upstream building occurs at about 0.6H from the ground for all studied cases. From this point the flow diverts into four different streams as described in section 2.1 of Chapter 2. The point of minimum positive C_p which is identical for all studied cases occurs on the front face at about 0.2H above the ground. The stream which deviates toward the roof again separates due to the front sharp edge and the separated shear layer reattaches on the same roof surface and bifurcates. This flow structure can be clearly observed in Figure 3.7 and detailed view of the same in Figure 3.8(B). According to Castro et al. (1977), at the leading edge of the upstream building roof, separation causes a high negative pressure which indicates the minimum C_p region. This pressure increases toward the trailing edge and recovers to nearly zero pressure which suggests that the flow may reattach on the top surface. Also, they specified from their analysis that for $\delta/H > 0.7$ the separated shear layer permanently reattaches on the top of the building which explains the reattachment of the shear layer on the same surfaces for our studied cases for $\delta/H \approx 45$. The negative pressure on the rear face of the upstream building varies due to the strong mixing of the fluid in the street canyon with that from entrainment (Sakamoto et al., 1988).

The separated flow on the roof of the upstream building gives rise to a large three-dimensional recirculation region over the roof as can be seen in Figure 3.7 and closer inspection of the same in Figure 3.8(B), in which the vortex core can be recognized at approximately $0.5\,H$ downstream of the leading edge. Most of the flow from the roof of the upstream building displaces towards the roof of the downstream building. Back-flow from

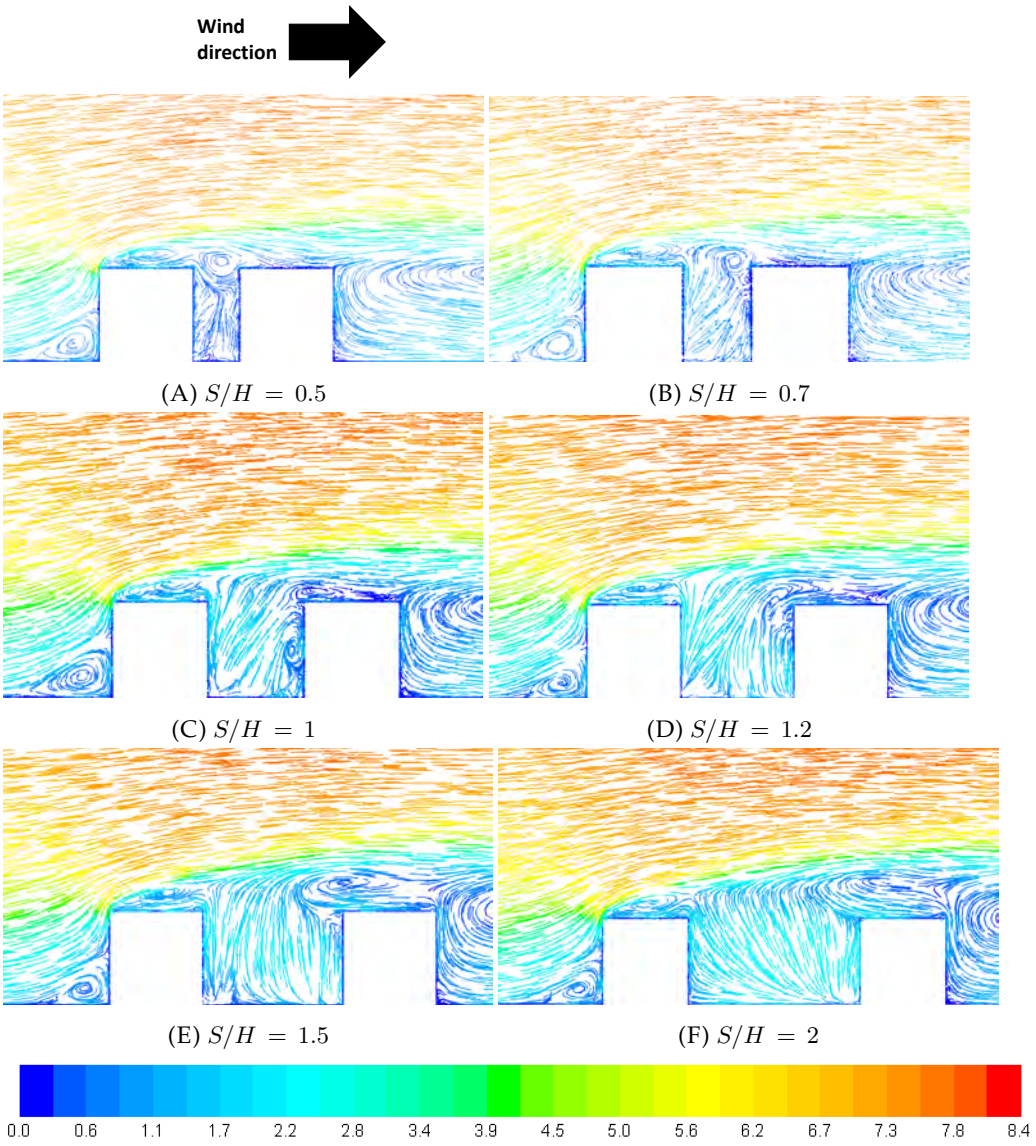

FIGURE 3.7: Velocity magnitude (m/s) pathlines in XY-plane at the centre plane ($Z = 40$) for the uniform street canyon with different street aspect ratios.

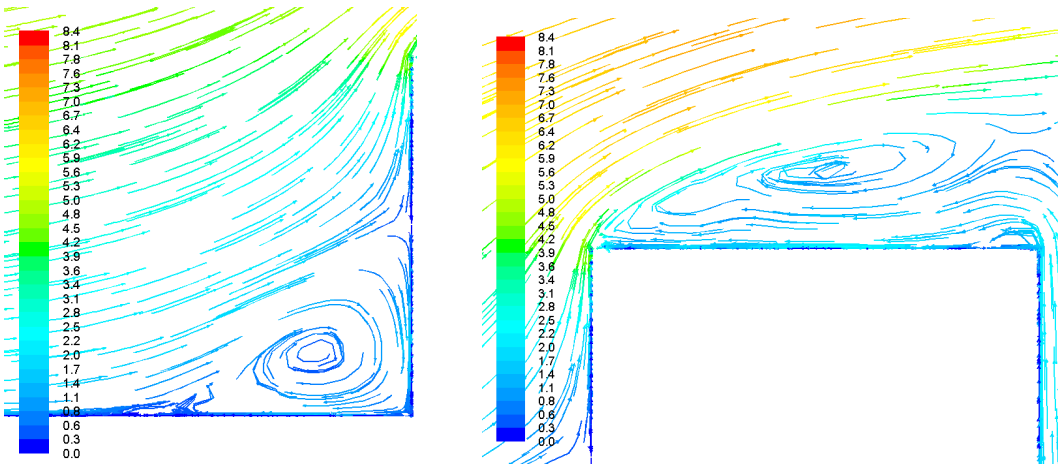

FIGURE 3.8: Detailed view of (A) the flow structure before the the upstream building and (B) the flow separation on the roof of the upstream building using velocity magnitude (m/s) pathlines in XY- plane at centre plane ($Z = 40$) for street canyon with aspect ratio $S/H = 1$.

the canyon is forced into the roof region of the upstream building. By reason of continuity along the plane of symmetry, the backflow is forced laterally to be re-entrained by the main flow (Dianat et al., 1984). The flow in the canyon for different S/H ratios can be characterized by a strong fluid stream directed upwards and towards the windward face of the downstream building. A recirculation can be observed in the case of $S/H = 0.5$ near the top corner of the windward wall of the downstream building which can be seen to move on the roof of the downstream building with an increase in aspect ratio (S/H). Backflow on the roof of the downstream building can be observed in the case of $S/H = 1.5$ and 2.

Figure 3.8(A) represents a closer view of the upstream separation region for $S/H = 1$, which reveals that the horseshoe vortex system actually consists of a complex vortex structure. The extension of the horseshoe vortex along the sides of the uniform street canyon can be seen in the velocity magnitude streamlines plot at $Y = 1.5$ m in Figure 3.10. On the side faces of the upstream building, the separated flow at the leading edges gives rise to intense corner vortices. For these separated shear layers, reattachment occurs on the sides of the downstream building in all studied cases up to $S/H = 2$. However, these periodically separated shear layers, have rolled up inside the canyon gap for the studied case of $S/H = 2.5$. Thus the horseshoe vortex tends to convect the fluid towards the buildings and into the canyon. Whereas the fluid entering into the canyon from the upstream building roof exits to the sides (Havel, 2006). This interaction confines the lateral shear layers and pushes them outward, which allows the development of the second vortex street inside the canyon.

Figure 3.9 represents the velocity magnitude streamline near the ground level at the pedestrian height of 1.5 m, for the entire plane for the uniform street canyon case of $S/H = 2$. Note that, this figure was shown here as a representative case for all street canyon cases and to show that with the

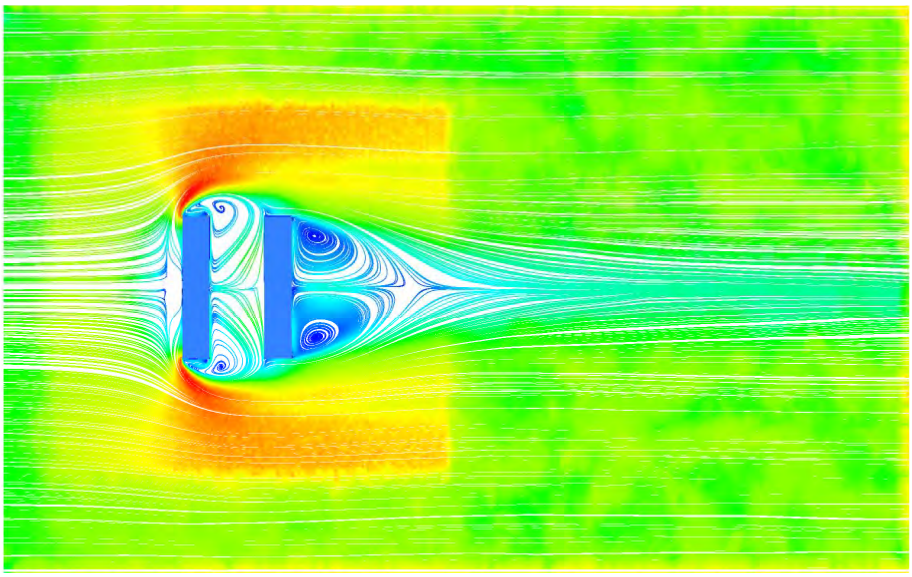

FIGURE 3.9: Velocity magnitude streamlines in XZ- plane at $Y = 1.5$ m level for the uniform street canyon case of $S/H = 2$.

used symmetry boundary condition for the sides of the computational domain shows parallel flow at the side boundaries and does not create any blockage effect. For all the similar kind of plots showing velocity magnitude streamlines hereafter and in the following chapters will only show the cut plane or zoom view near the street canyon to get the clear idea of the flow around the buildings and street canyons.

Figure 3.10 represents the velocity magnitude streamlines near the ground level at the pedestrian height of 1.5 m to show the complex flow structure at the ground level for different uniform street canyons.

From the above flow description of the flow separation from the leading edges of the upstream building, it can be generalized that the separated shear layer from the roof of the building reattaches on the same roof surface, whereas the separated shear layers from the lateral surfaces reattach either on the sides of the downstream building or rolls up inside the canyon gap. For this kind of flow behaviour three regimes analogous to Sakamoto et al. (1988) can be inferred: (1) stable reattachment for $S/H < 0.9$; (2) unstable reattachment or bistable flow for $0.9 \leq S/H \leq 2$; and (3) stable synchronized for $S/H > 2$ as shown in Figure 3.11. The explanation about these regimes is as mentioned in the Introduction.

Figure 3.12 shows the $3D$ view of the coherent vortex structure over the first building, in the gap between buildings, and over the top of the second building. The shear layer reattachment on the top of the upstream building can be clearly seen in this image.

Pedestrian comfort

Figure 3.13 shows the results of the wind categorisation, by means of contours of the Beaufort numbers from $0 - 5$ according to the ELBS of Lawson

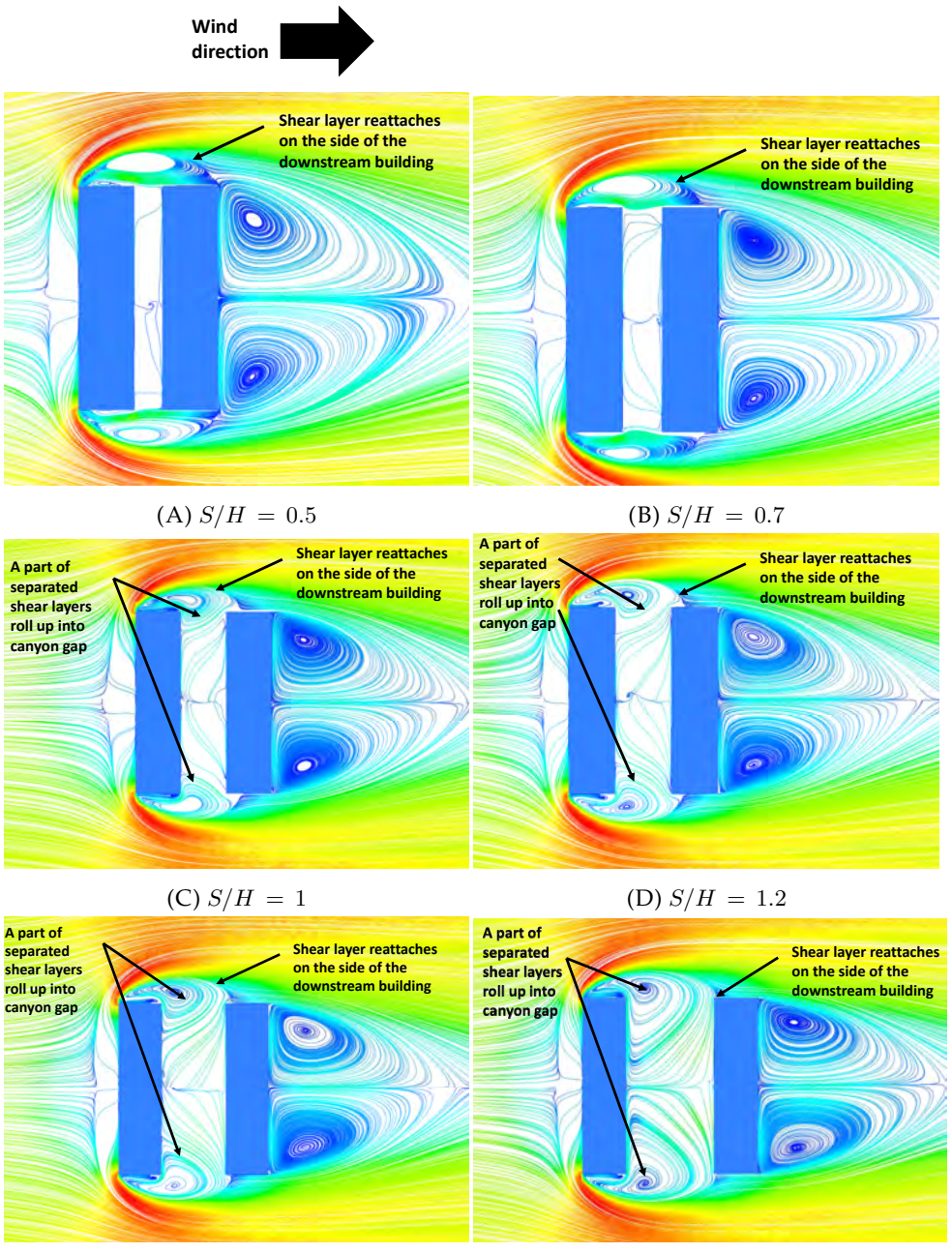

(A) $S/H = 0.5$ (B) $S/H = 0.7$

(C) $S/H = 1$ (D) $S/H = 1.2$

(E) $S/H = 1.5$ (F) $S/H = 2$

FIGURE 3.10: Velocity magnitude streamlines (cut plane to zoom near the street canyon) in XZ- plane at $Y = 1.5$ m level for the uniform street canyon with different street aspect ratio.

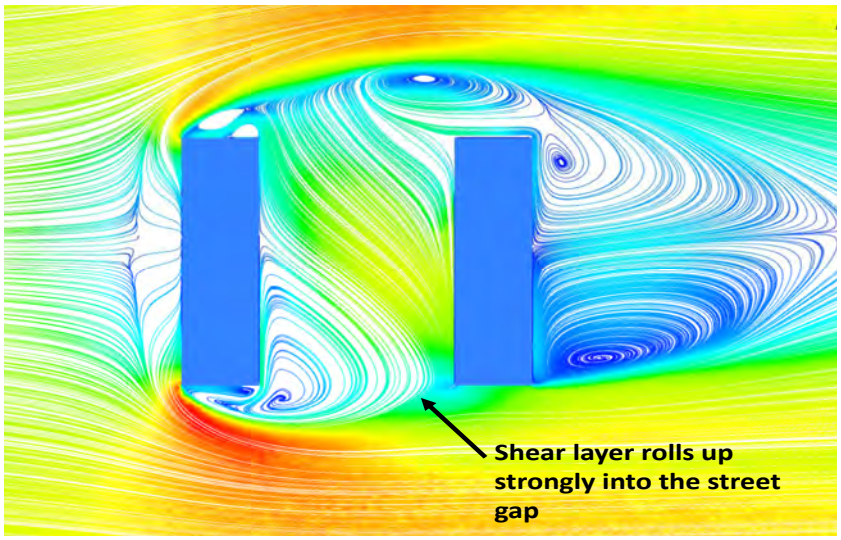

FIGURE 3.11: Velocity magnitude streamlines (cut plane to zoom near the street canyon) in XZ- plane at $Y = 1.5$ m level for the uniform street canyon case of $S/H = 2.5$ showing stable synchronized regime.

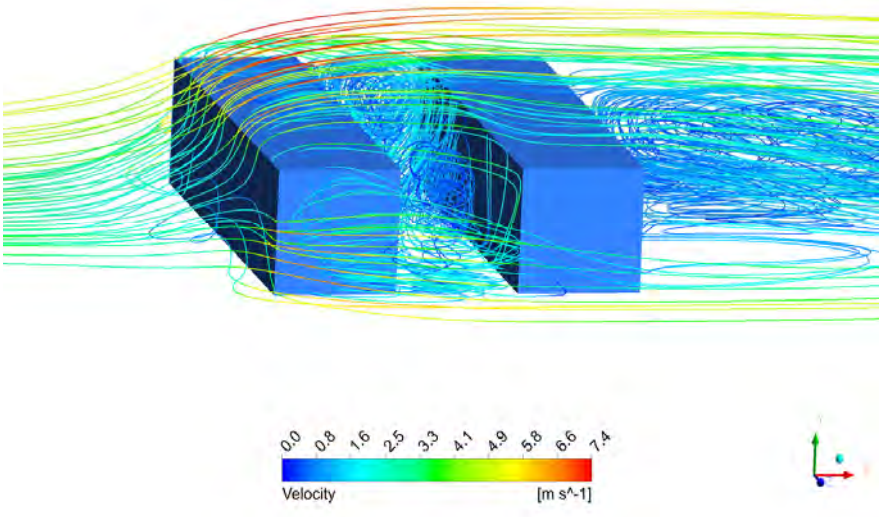

FIGURE 3.12: Isometric view of streamlines showing coherent vortex structure around and inside the uniform street canyon for $S/H = 1$.

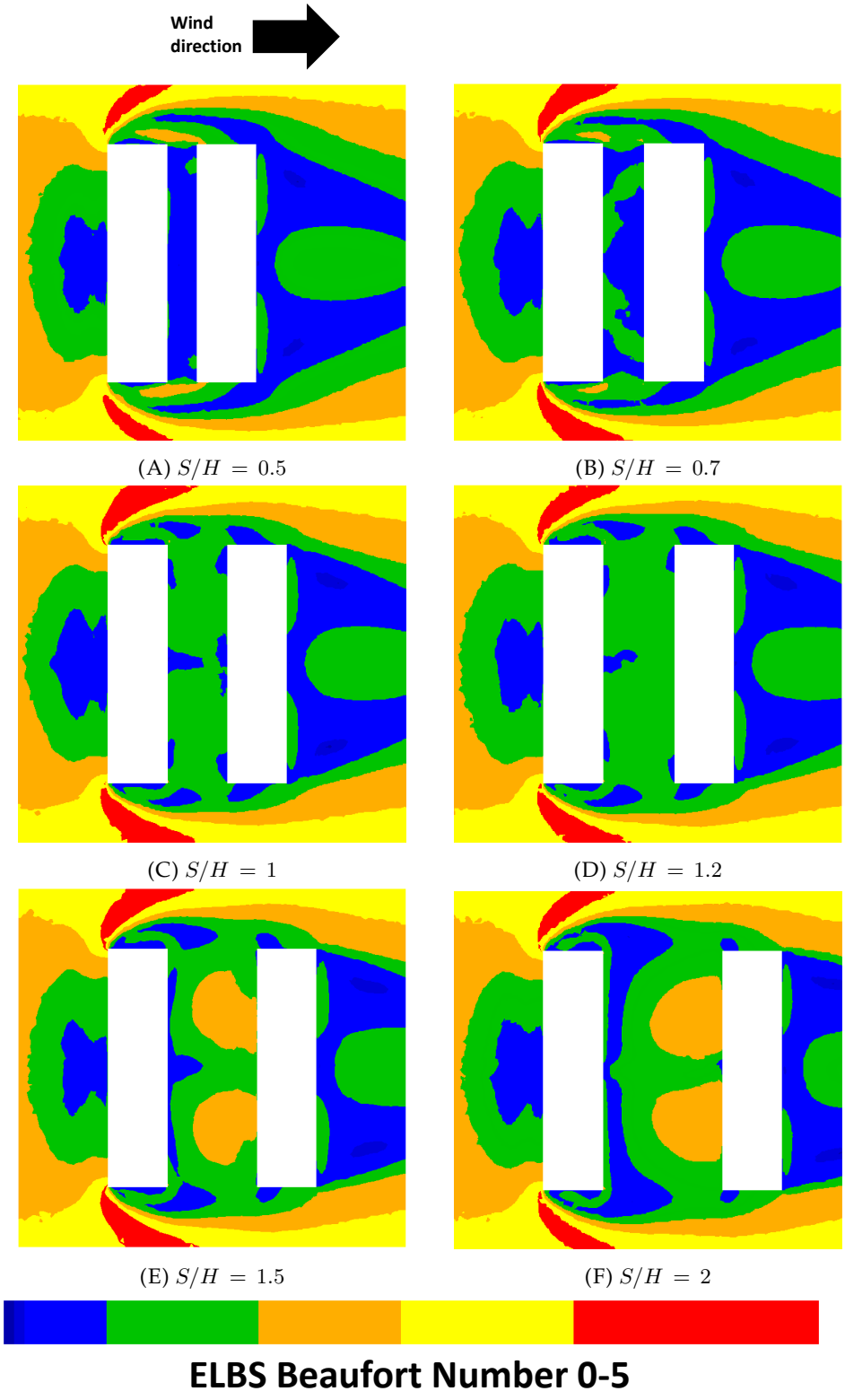

FIGURE 3.13: Wind categories at $Y = 1.5$ m in the XZ-plane for the street canyon with the different roof shapes of both buildings. Here, dark blue represents 0 to 0.1 m/s, on Beaufort Number 0 on ELBS; blue represents 0.2 to 1.0 m/s, on Beaufort Number 1on ELBS; green represents 1.1 to 2.3 m/s, on Beaufort Number 2 on ELBS; orange represents 2.4 to 3.8 m/s, on Beaufort Number 3 on ELBS; yellow represents 3.9 to 5.5 m/s, on Beaufort Number 4 on ELBS; and red represents wind speeds between 5.6 m/s to 7.5 m/s, on Beaufort Number 5 on ELBS.

et al. (1975). This assessment was carried out at a height of $Y = 1.5$ m inside the street canyon, a representative height in between head height and the sitting height for a person. Therefore, contours of wind speed in Figure 3.13 are divided into six colours according to the ELBS as follows: dark blue ($0 - 0.1$ m/s, Beaufort Number 0 on ELSBS); blue ($0.2 - 1.0$ m/s, Beaufort Number 1 on ELBS); green ($1.1 - 2.3$ m/s, Beaufort Number 2 on ELBS); orange ($2.4 - 3.8$ m/s, Beaufort Number 3 on ELBS); yellow ($3.9 - 5.5$ m/s, Beaufort Number 4 on ELBS) and red ($5.6 - 7.5$ m/s, Beaufort Number 5 on ELBS). It can be observed from Figure 3.13 that almost 100% of the area near the downwind face of the upstream building which could be in frequent use by pedestrians is in the favourable zone in all cases. Wind speed remains favourable for pedestrians on both sides of the street up to $S/H = 1.2$. Beyond this, i.e. for $S/H = 1.5$, and 2 an unfavourable zone inside the canyon increases. For the case of $S/H = 1.5$ and 2 an unfavourable zone inside the canyon particularly near the upwind face of the downstream building but extending up to the middle of the street has been found. Note here that, the pedestrian comfort inside the street canyon decreases with an increase in the street width. The reason for this could be the variation of the flow structure inside the canyon with increase in the street width. As discussed above, with the increase in the street width, the reattachment length of the separated shear layers from the sides of the upstream building decreases and it moves from the side faces of the downstream building to the front edge of the downstream building and at $S/H = 2.5$, the periodically separated shear layer rolls up strongly in to the canyon gap which allows more fluid to enter from the sides and thus increase in the wind speed.

Summary of the study using the street width as an influencing parameter

From the above study analysis for different uniform street canyons using the street width as an influencing parameter, the following general conclusions can be made:

- For all studied cases, the flow structure before the upstream building are quantitatively similar
- The location of stagnation points on the ground before the upstream building and on the front face of the upstream building remain identical for all studied cases
- The separated shear layer from the roof of the upstream building reattaches on the same roof surface for all studied cases
- Separated shear layers from the sides of the upstream building reattach on the side surfaces of the downstream building up to $S/H <= 2$ and for the case of $S/H = 2.5$ they reattach inside the canyon gap
- Overall wind velocity inside the street canyon remains favourable for pedestrians approximately up to $S/H = 1$ and then the wind speed near the downwind building up to the centre of the street increases with increase in the street width

- No significant increase in the wind speed near the downwind wall of the upstream building has been observed for the pedestrian accessible zone

3.3.2 Building width as an influencing parameter

In this subsection, we explore the effect of varying W/H while keeping S/H fixed. The two fixed ratios S/H were 1 (shown to be predominantly favourable in the previous subsection) and 2 (showing a large unfavourable zone). Results for velocity magnitude pathlines in the centre plane with different building widths and for the constant street aspect ratio $S/H = 1$ are shown in Figure 3.14.

The ratio $1 \leq W/H \leq 5$ and $1 \leq S/H \leq 2$

Flow structure for varying the building width for the case of $S/H = 1$

It can be observed that the shape of the standing vortex in front of the upstream building changes with the increase in building width. The separated shear layer due to the flow separation at the sharp leading edge of the upstream building roof reattaches on the same roof but the reattachment point moves towards the trailing edge of the roof with the increase in the building width. Reverse flow from the canyon on the roof of the upstream building cannot be observed in the case of $W/H = 1$. The core of the vortex inside the street canyon moves from the downwind wall of the upstream building to the roof of the downstream building. Note that Figure 3.14(D) is the same as Figure 3.7(C).

Figure 3.15 shows the velocity magnitude streamlines at the pedestrian height of 1.5 m. The periodically separated shear layers due to the sharp leading edges of the sides of the upstream building roll up strongly into the canyon gap without reattachment in the case of $W/H = 1$ and 2. Whereas, for the studied cases of $W/H > 2$, a part of those separated shear layers due to the sides of the upstream building starts to roll up into the canyon gap. In the studied cases two regimes analogous to Sakamoto et al. (1988) can be inferred: (1) stable synchronized up to $W/H = 2$ and (2) bistable flow for $W/H >= 3$.

Pedestrian level wind categorisation for varying the building width for the case of $S/H = 1$

Figure 3.16 shows the pedestrian wind categorisation plot for varying building width for $S/H = 1$ at the pedestrian height of 1.5 m. In the case of $W/H = 1$, the centre part of the canyon is an unfavourable zone for pedestrians. With the increase in the building width that unfavourable zone inside the canyon decreases in size. However, in the case of $W/H = 5$ approximately 5% of the region near the corners of the street forms an unfavourable zone.

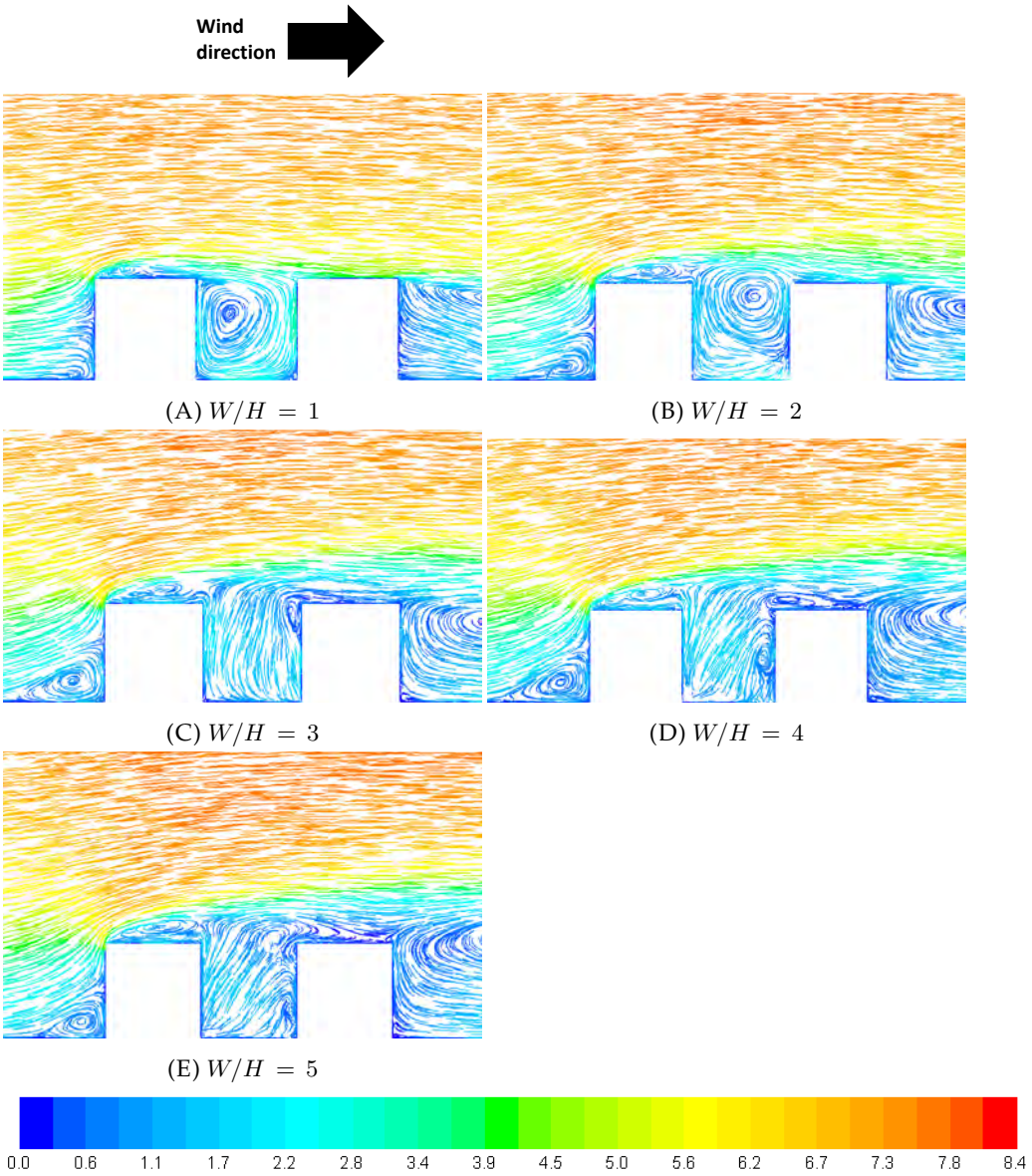

FIGURE 3.14: Velocity magnitude (m/s) pathlines in XY-plane at the centre plane ($Z = 40$) for the uniform street canyon with different building widths and for the constant street aspect ratio $S/H = 1$.

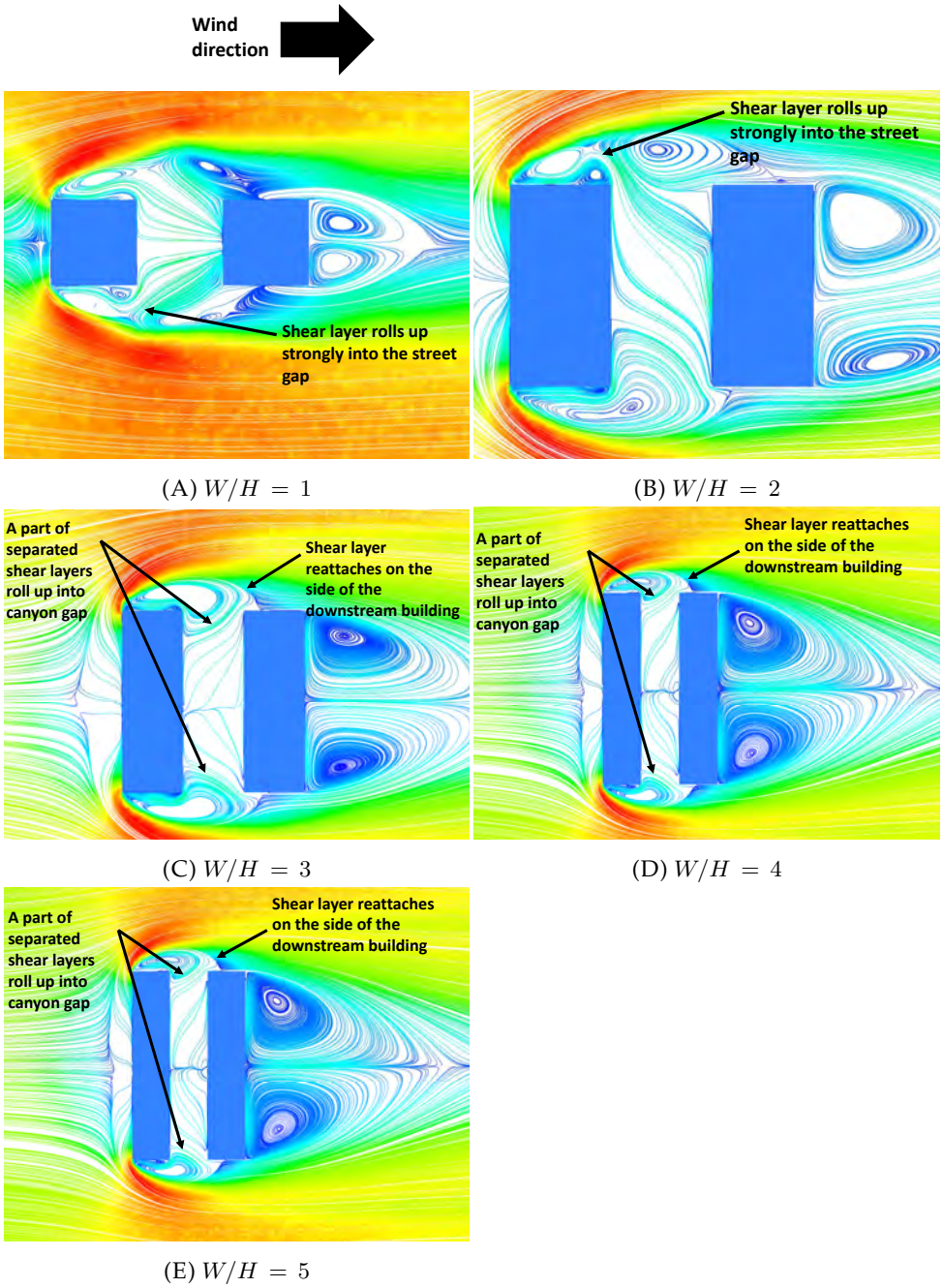

(A) $W/H = 1$ (B) $W/H = 2$

(C) $W/H = 3$ (D) $W/H = 4$

(E) $W/H = 5$

FIGURE 3.15: Velocity magnitude streamlines (cut plane to zoom near the street canyon) in XZ- plane at $Y = 1.5$ m level for the uniform street canyon with different building widths and for the constant street aspect ratio $S/H = 1$.

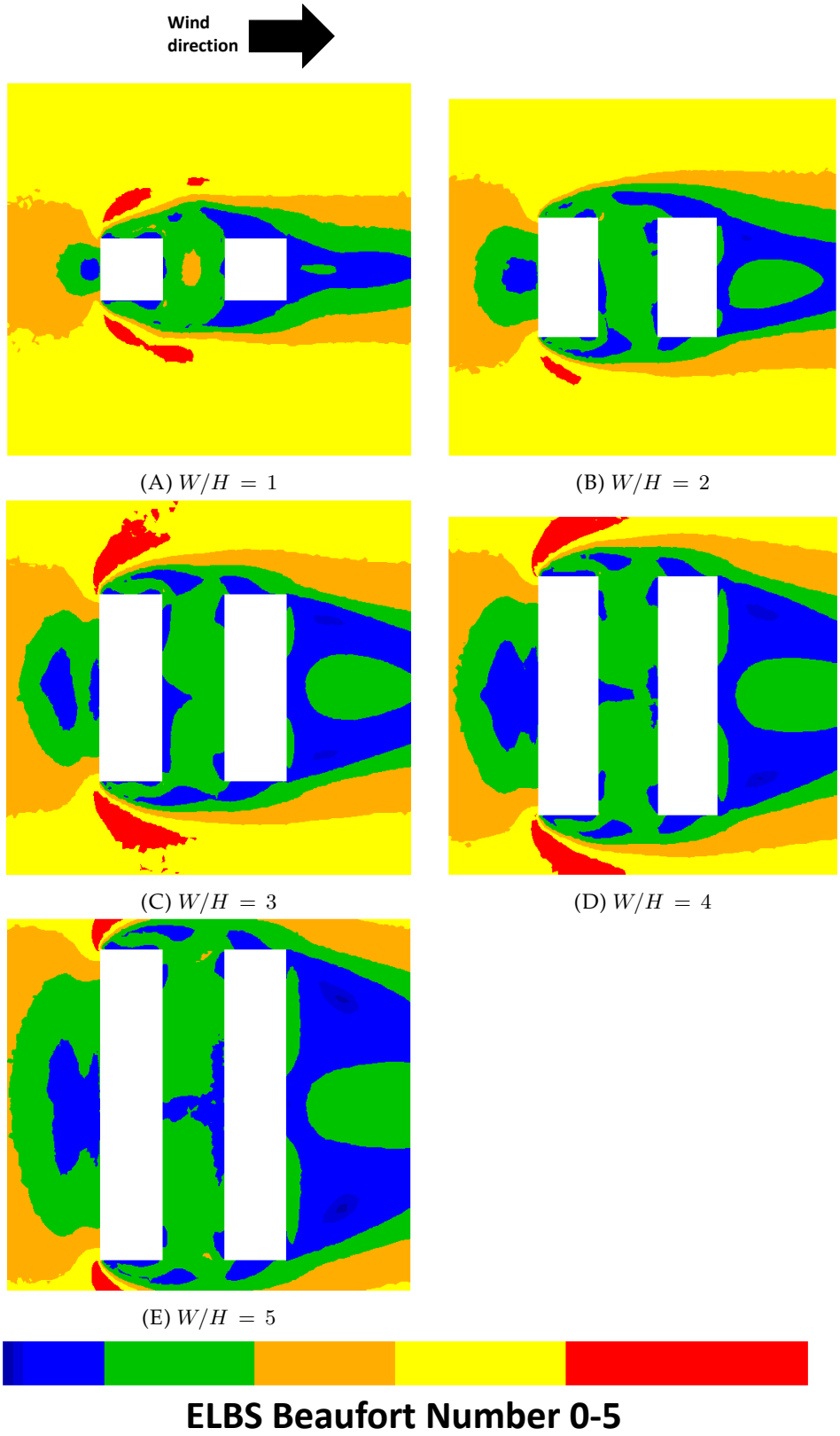

FIGURE 3.16: Wind categories at $Y = 1.5$ m in the XZ-plane for the uniform street canyon with different building widths and for the constant street aspect ratio $S/H = 1$. Colours as in Figure 3.13.

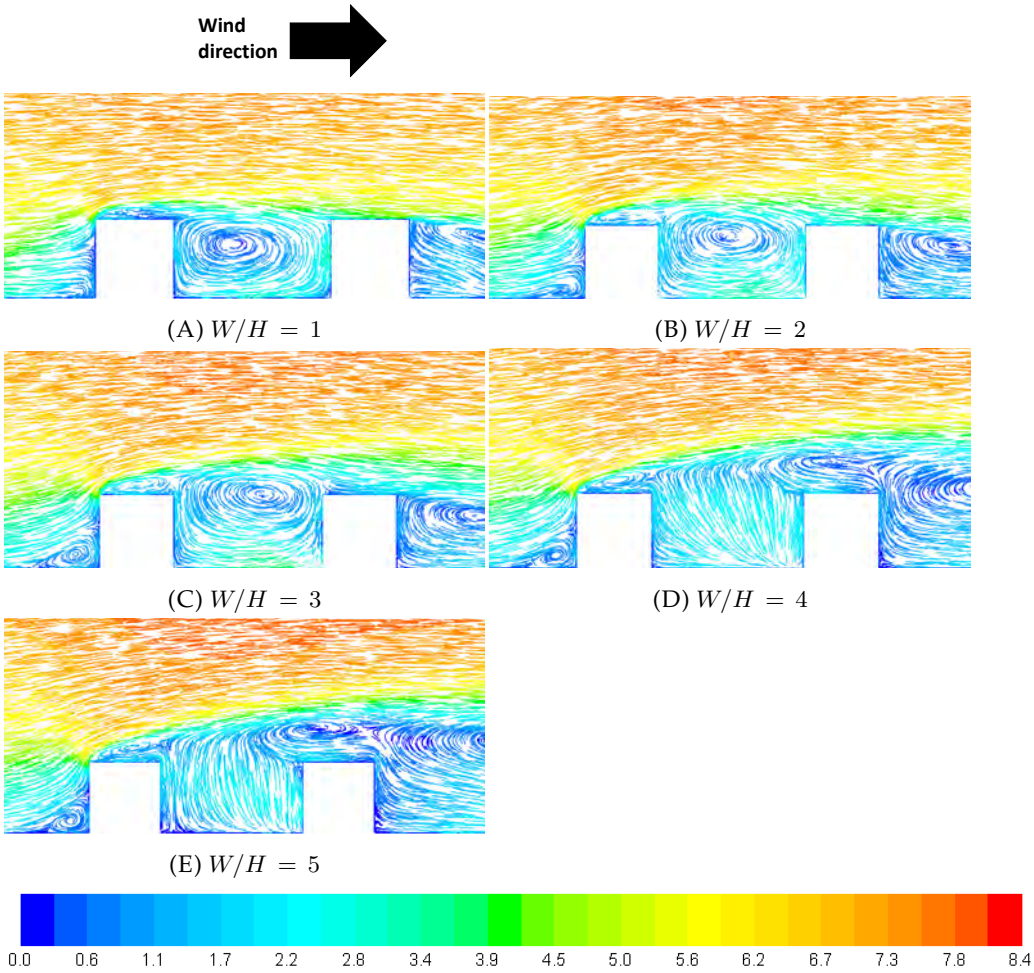

FIGURE 3.17: Velocity magnitude (m/s) pathlines in XY-plane at the centre plane ($Z = 40$) for the uniform street canyon with different building widths and for the constant street aspect ratio $S/H = 2$.

Flow structure for varying the building width for the case of $S/H = 2$

Results for velocity magnitude pathlines in the centre plane with different building widths and for the constant street aspect ratio $S/H = 2$ are shown in Figure 3.17. Note that Figure 3.17(D) is the same as Figure 3.7(F). In the case of varying the street width for the street aspect ratio $S/H = 2$, most of the flow characteristics are similar to as discussed above in the case of $S/H = 1$. These common features include a variation of the shape of the standing vortex in front of the upstream building, reattachment of the separated shear layer from the leading edge of the upstream building roof, transition of the recirculation region from the downwind wall of the upstream building towards the downstream building roof. In the current study, the backflow can be observed on the roof of the downstream building in the case of $W/H = 4$ and 5.

For the flow structure near the ground (at the pedestrian height of 1.5 m)

as shown in Figure 3.18, two regimes analogous to Sakamoto et al. (1988) can be inferred: (1) stable synchronized up to $W/H = 3$ and (2) bistable flow for $W/H > 3$.

Pedestrian level wind categorisation for varying the building width for the case of $S/H = 2$

Figure 3.19 shows the pedestrian wind categorisation plot for varying building width for $S/H = 2$ at the pedestrian height of 1.5 m. It can be observed from this figure that, with an increase in the building width the wind speed also has increased inside the canyon gap. In the case of $W/H = 3$, approximately 75% area inside the canyon gap can be seen to be in the unfavourable zone for pedestrians. However, for the case of $W/H = 4$ and 5, the zone of discomfort has been reduced comparatively.

From this parametric study for a uniform street canyon using the street width and building width as influencing parameters, it can be observed that increase in the street width introduces high wind speed at the pedestrian level. Whereas, a decrease in the building width introduces high wind speed at the pedestrian level. This high wind speed converts favourable zones into unfavourable zones inside the street canyon.

3.3.3 Building height as an influencing parameter

Flow structure inside the non-uniform street canyon

In this section, the impact of the non-uniform street canyon on the flow structure and pedestrian comfort was considered. Simulations were carried out for step-up and step-down street canyons with the ratio $W/H = 4$. The cases of $S/H = 1$ (seen to be favourable for pedestrian comfort in Section 3.3) and $S/H = 2$ (generally unfavourable) were considered for this analysis. Here, H is taken to be H_1 for the step-down case and H_2 for the step-up case.

Most of the flow characteristics are similar to those discussed in subsection 3.3.1 for the uniform street canyon. These common features include the flow separation on the ground before the upstream building, generation of the horseshoe vortex, the stagnation point on the front face of the upstream building, separation of the flow from the leading edges of the upstream building and reattachment of the separated shear layer from the roof of the upstream building on the same roof. However, there are some key differences in the flow structure which have measurable effects on pedestrian comfort.

Figure 3.20 shows results for the flow structure in the centre plane for four cases. For the step-up street canyon cases, the fluid entering the canyon from the roof of the upstream building is larger than the corresponding uniform street canyon cases, as is suggested from Figures 3.20(A) and 3.20(B) respectively by comparison with Figures 3.7(C) and 3.7(F). This is due to the fact that a decrease in height of the upstream building compared to the downstream building allows more fluid to enter into the canyon compared to the uniform street canyon.

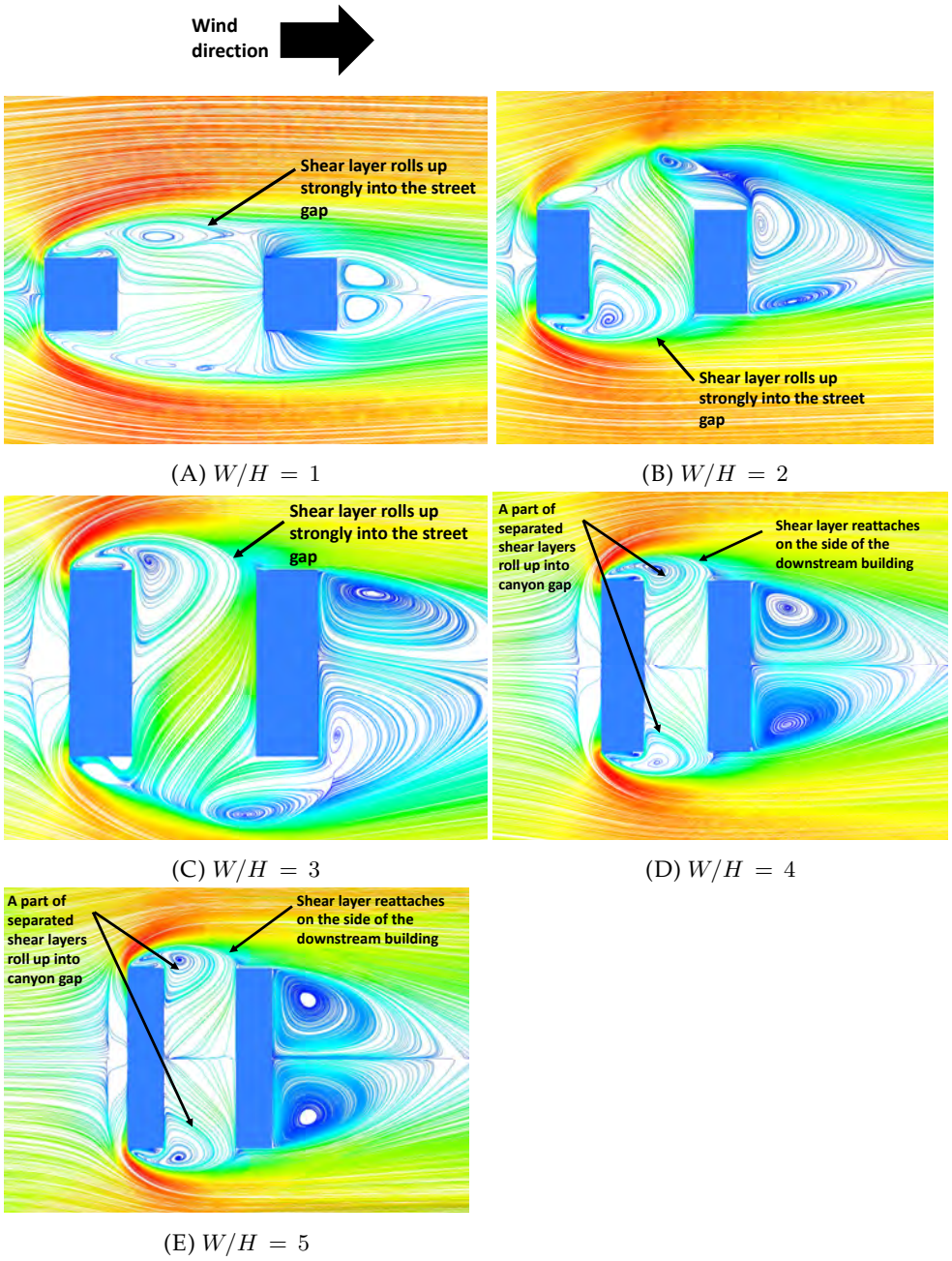

(A) $W/H = 1$ (B) $W/H = 2$

(C) $W/H = 3$ (D) $W/H = 4$

(E) $W/H = 5$

FIGURE 3.18: Velocity magnitude streamlines in XZ- plane (cut plane to zoom near the street canyon) at $Y = 1.5$ m level for the uniform street canyon with different building widths and for the constant street aspect ratio $S/H = 2$.

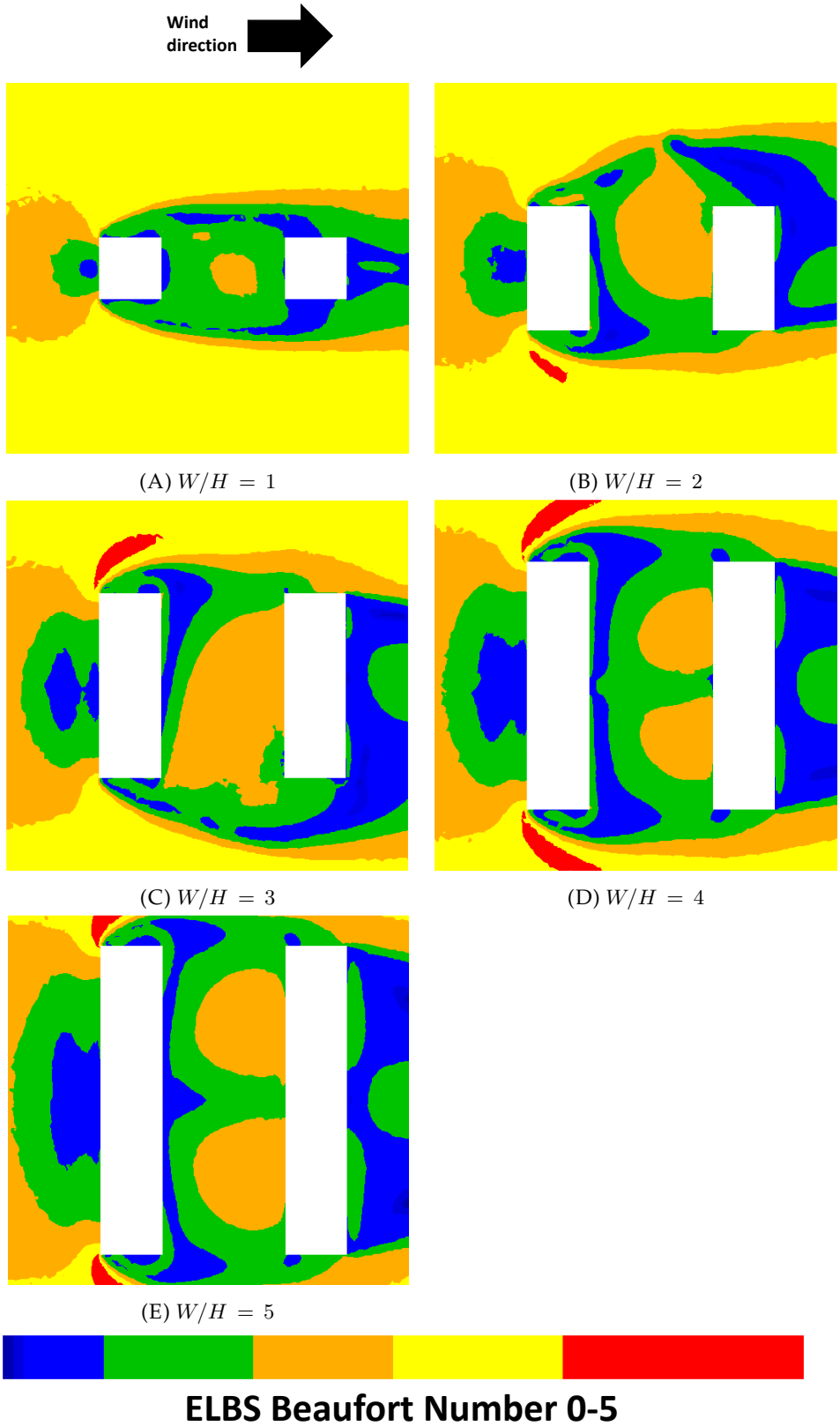

FIGURE 3.19: Wind categories at $Y = 1.5$ m in the XZ-plane for the uniform street canyon with different building width and for the constant street aspect ratio $S/H = 2$. Colours as in Figure 3.13.

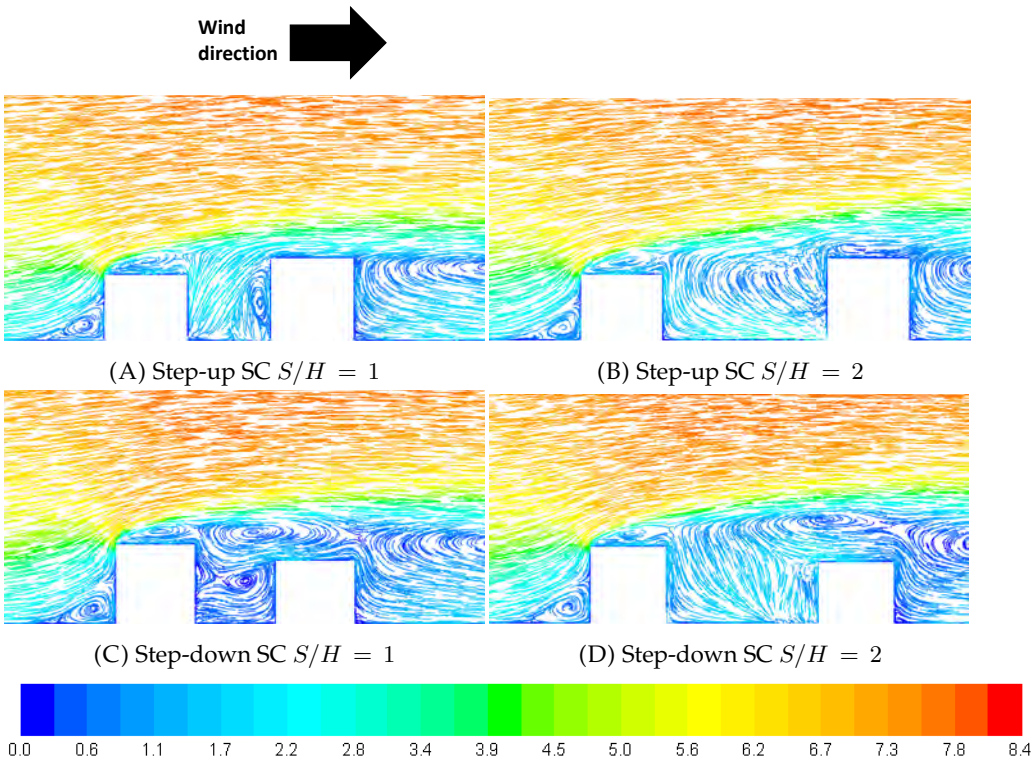

FIGURE 3.20: Velocity magnitude (m/s) pathlines in XY-plane at the centre plane ($Z = 40$) for the non-uniform street canyon cases.

For the step-down street canyon cases, a large back-flow or a secondary re-circulation region can be observed on the roof of the downstream building in Figures 3.20(C) and 3.20(D) respectively. This secondary recirculation was not seen in any other cases studied.

The observed changes in the flow structure in the plane $Y = 1.5$ m at the pedestrian height are shown in Figure 3.21. In the case of the step-up street canyon for $S/H = 1$ in Figure 3.21(A), the reattachment length of the separated shear layers has been reduced compared to the uniform street canyon for the same street width (Figure 3.10(C)). In the case of the step-up street canyon with $S/H = 2$ in Figure 3.21(B), these shear layers reattach on the front face of the downstream building instead of on the downstream building sides as they did in the uniform street canyon with the corresponding street width (Figure 3.10(F)). No drastic changes are seen for both step-down cases in Figure 3.21(C) and 3.21(D), when compared with the corresponding uniform street canyon cases (in Figure 3.10(C) and 3.10(F)).

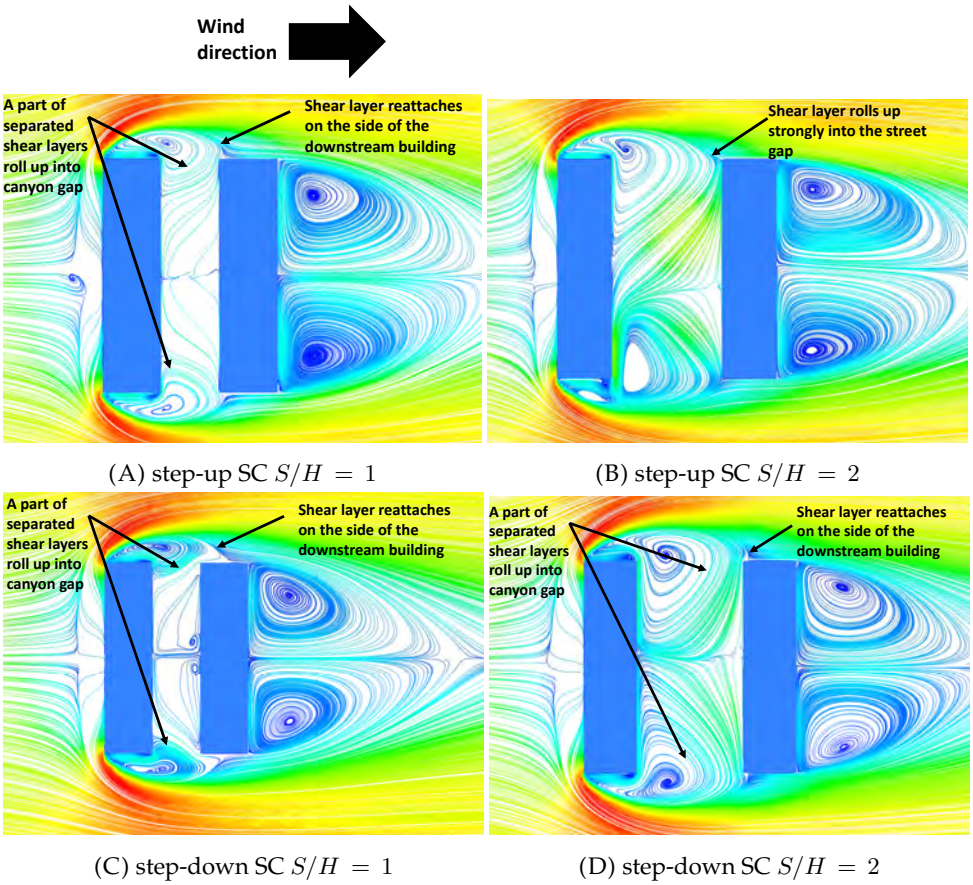

(A) step-up SC $S/H = 1$ (B) step-up SC $S/H = 2$

(C) step-down SC $S/H = 1$ (D) step-down SC $S/H = 2$

FIGURE 3.21: Velocity magnitude streamlines (cut plane to zoom near the street canyon) in XZ- plane at $Y = 1.5$ m level for the non-uniform street canyon cases.

Pedestrian level wind categorisation inside the non-uniform street canyon

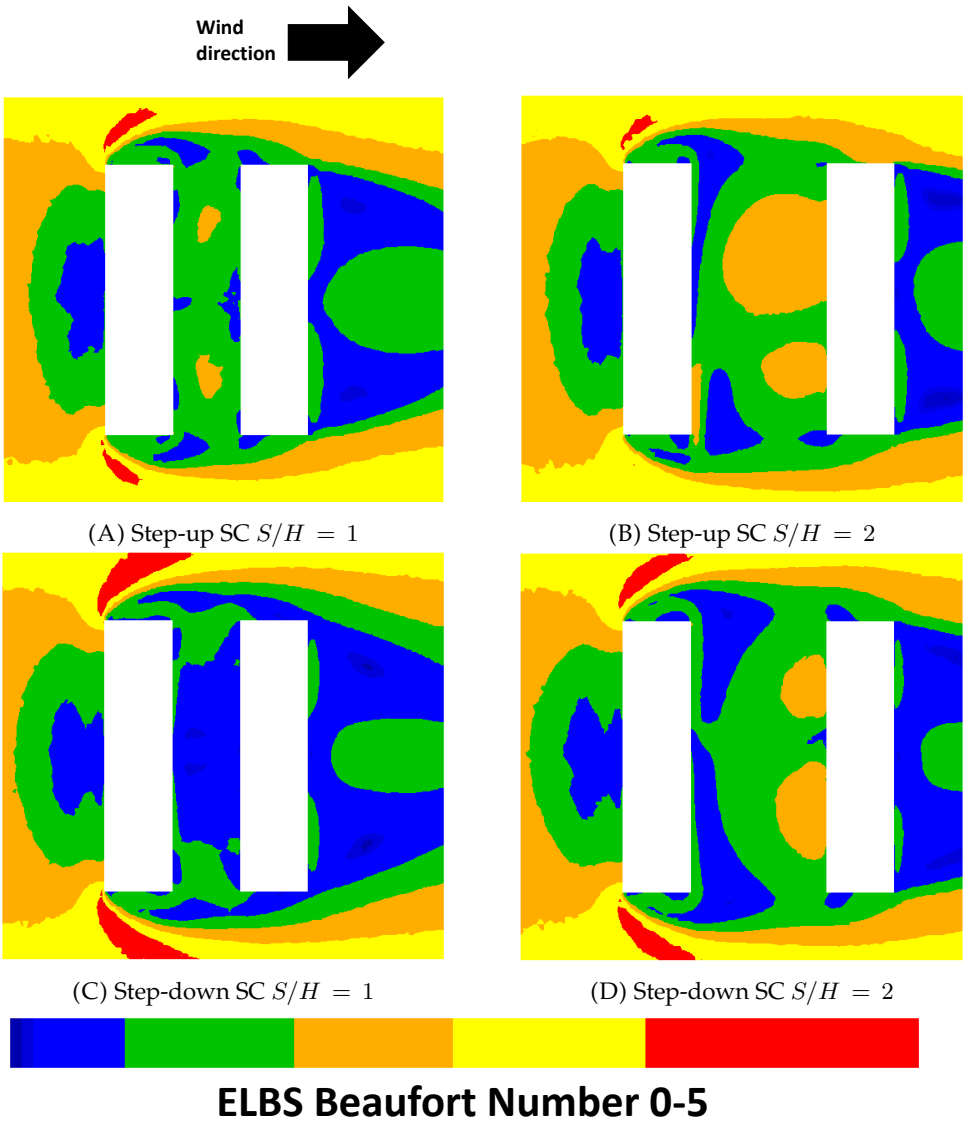

FIGURE 3.22: Wind categories at $Y = 1.5$ m in the XZ- plane for all four studied non-uniform canyon cases. Colours as in Figure 3.13.

Figure 3.22 shows contour plots of pedestrian wind comfort at a height of 1.5 m inside the street canyon for four non-uniform canyon cases. For the step-up street canyon cases Figure 3.22(A) and 3.22(B), pedestrian level wind speed has been increased compared to the respective uniform street canyon cases (Figure 3.13(C) and 3.13(F)). On the other hand, the step-down street canyon cases Figure 3.22(C) and 3.22(D), show larger favourable zone for pedestrians when compared to uniform street canyon cases (Figure 3.13(C) and 3.13(F)).

3.4 Summary of Chapter 3

In this study, different parameters defining urban street canyons, including street width, building width and building height are used to find the influence of such parameters on the flow structure and pedestrian wind comfort. The results indicated that there is a strong influence of the canyon geometry on the flow field and pedestrian comfort in the street canyon. The flow structure and hence the pedestrian comfort inside the street canyon mainly depend on the reattachment of the separated shear layers due to the sharp leading edges of the upstream building, and on the vortex structure in the canyon.

Different building and street canyon configurations were considered by varying the ratios of the street width to the building height (S/H), the ratio of the building width to the building height (W/H), and the ratio of the upstream building height to the downstream building height (H_1/H_2). Three regimes were identified depending on the reattachment of the separated shear layers due to the sharp leading edges of the sides of the upstream building. In the stable reattachment regime, the separated shear layers reattached on the sides of the downstream building, and a large area inside the canyon was found to be comfortable for pedestrians. In the bistable flow regime which is analogous to Sakamoto et al. (1988), where a part of the separated shear layers rolls up into the canyon, an increase in street width and a decrease in building width lead to a large zone of discomfort for pedestrians. For the stable synchronized regime, where separated shear layers roll up strongly into the canyon without reattachment, a large region of discomfort at pedestrian height was observed.

The pedestrian level discomfort in the street canyon is the highest for the stable synchronized regime, indicating that it is the most unfavourable configuration for pedestrian comfort. By contrast, the stable reattachment regime is the most favourable configuration for pedestrian comfort.

For the non-uniform canyon, it has been observed that the step-up configuration decreases the pedestrian comfort inside the canyon, whereas, the step-down street canyon configuration shows a decrease in wind speeds at the pedestrian level, creating favourable zones for pedestrian comfort.

In this study, only a perpendicular wind direction and buildings with flat roofs have been considered. Change in the shape of the upstream or downstream buildings or of both buildings or a change in the wind angle will cause variation in the flow structure and pedestrian comfort inside the street canyon. Also, it has been predicted in the present studied cases that vortex shedding occurs inside the canyon and in the wake of the downstream building. Transient flow simulations are required to confirm the predictions. The reason why steady RANS CFD is not capable of reproducing the vortex shedding in the wake of buildings or inside street canyons is due to the underestimation of turbulent kinetic energy in these regions (Blocken et al., 2011) and that it's a steady model of an intrinsically unsteady phenomenon. Therefore, it is desirable to use LES for highly accurate CFD analysis. However, in order to use these models for predicting wind environment around buildings, a dramatic increase in computer processing speed is needed. Further investigations are recommended to focus on these areas.

Chapter 4 will involve a parametric study to analyse the flow structure and pedestrian level wind categorisation study inside the street canyon with different roof shapes. The analysis of the flow structure and the pedestrian comfort inside the street canyon discussed in Chapter 3 will be used to evaluate the flow structure analysis in Chapter 4.

Chapter 4

The Effect of Roof Shapes

4.1 Introduction

Building geometry configurations such as building height, building width, roof height, roof shape and street width influence the flow field within an urban street canyon. A parametric study of the flow field in an urban canyon between two flat-roofed buildings with varying the street width, building width and building height has been performed in the previous chapter (Chapter 3). The results show that the flow structure around and inside the street canyon depends strongly on the reattachment of the separated shear layers due to the sharp leading edges of the upstream building. For the considered building and street configuration inside the thick atmospheric boundary layer, the separated shear layer from the upstream building roof for all the studied cases reattached on the same roof. Whereas, the separated shear layers from the sides of the upstream building reattached on the sides of the downstream building or near the leading edge or front face of the downstream building or the periodically separated shear layers were found to be rolled up strongly in the canyon. The reattachment of the side shear layers and the flow coming from the roof of the upstream building alters the flow structure inside the canyon when the street width, building width, or building height are varied.

The above study and Martinuzzi et al. (2000) suggest that changing the shape of the building roof may alter the flow structure inside the canyon. However, the flow around buildings with different roof shapes is less discussed; most such studies were used to determine the surface pressure on those buildings. Poitras et al. (2003) studied experimentally the flow structure around a single building with slanted roofs with varying slopes of the roofs. The Reynolds number (Re) based on the height of the building were $12,000$, $22,000$ and $32,000$. According to that study, upstream of the building the flow structure for the building having sloped roofs was similar to that for flat-roofed buildings apart from the horseshoe vortex. However, they found a variation of the flow structure over the different roofs, on the sides of the buildings and downstream of the buildings. They found no shear layer over the upstream edge of the sloped roofs while an arch vortex was created on the sides of the building and downstream of the building which was similar to that of a flat roof. However, in the case of the slanted roof, they reported that the upper part of the arch vortex generated behind

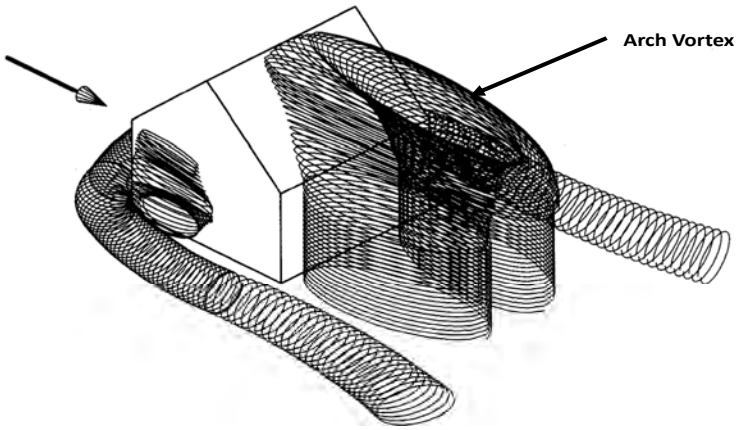

FIGURE 4.1: Schematic representation of the main structures of the flow around a sloped roof building (from Poitras et al. (2003)).

the building starts from the apex of the roof and continues downstream with an elliptical shape; this vortex increases in size with the slope of the roof (as shown in Figure 4.1).

Numerical study of a two-dimensional flow approaching perpendicular to the street canyon axis and for different roof shapes was carried out by Yassin (2011) and Huang et al. (2015) at moderate Re of $20,000$. Yassin (2011) investigated the impact of roof shape and height on the wind flow and pollutant dispersion within urban canyons. He analysed the flow field in urban canyons with three roof height (Z_H) to building height (H) ratios (Z_H/H) of 0.17, 0.33 and 0.5 and five roof shapes cases, in which both buildings have the same roof shape: flat, slanted, downwind wedge, upwind wedge, and trapezoidal (Cases: 1, 2 and $4-6$ as shown in Figure 4.2). He analysed the flow structure inside the canyon using the contours of horizontal wind velocity, and distribution of turbulent kinetic energy for different roof shapes and heights. According to his study, the wind velocity inside the street canyon increased with the flat roof, slanted roof, but decreased with the downwind and upwind wedge-shaped roofs. The wind velocity decreased as the roof height increased. They also revealed that pollutant concentration increased inside the street canyon as the roof height decreased. It also decreased with the slanted and trapezoidal roofs but increased with the flat roof, the upwind wedge roof and the downwind wedge-shaped roof.

Huang et al. (2015) performed a two-dimensional numerical simulation to investigate the impact of the roof shape and height of the upstream building roof on the flow and pollutant dispersion in an urban street canyon. The five different upstream roof shapes were: vaulted, trapezoidal, slanted, upwind wedge, and downwind wedge roofs (Cases: $7-11$ as shown in Figure 4.2) and three different Z_H/H ratios of $1/6$, $1/3$ and $1/2$. They analysed the flow structure inside the street canyon using the distribution of velocity vectors and turbulent kinetic energy. Their results revealed that under a high upstream roof height the vaulted shape of the upstream roof is beneficial for pollutant removal from the street canyon compared with

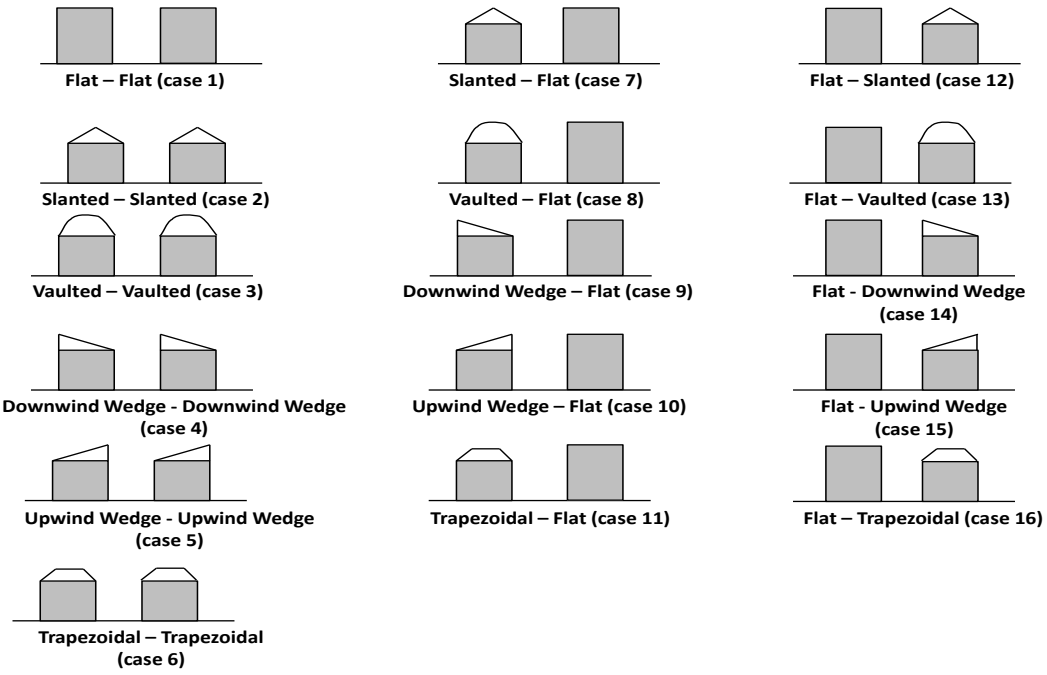

FIGURE 4.2: Computational urban street canyon configurations with different roof shapes.

the trapezoidal, slanted, and wedge-shaped roof shapes, while the highest pollution level occurs in the canyon for the upward wedge-shaped roof indicating that the upward wedge-shaped roof favours gaseous pollutant build-up in urban canyons.

From the above literature review, it can be concluded that the flow structure around two tandem buildings with flat roofs for low to high Re and the two-dimensional simulations to analyse the flow structure and pollutant dispersion inside urban street canyons with different roof shapes and roof heights have been studied extensively. However, three-dimensional study to find the impact of roof shapes and roof heights on the flow structure and pedestrian comfort inside street canyons at high Re inside a thick boundary layer has yet to be reported in the literature. This type of flow study is important because generally wind flow around buildings occurs at high Re and inside the thick atmospheric boundary layer. The present study has as its aim an examination of the flow field between and close to two buildings for different roof shapes. The impact of changing roof shapes of both buildings, only the upstream building or only the downstream building on the pedestrian comfort is analysed in section 4.3. Considered wind direction is normal to the street canyon for all studied cases. The street width to the building height ratio $S/H = 1$ was considered for all studied cases. This ratio was chosen to compare the change in the flow structure and pedestrian comfort inside the street canyon with the flat roof of Chapter 3.

Section 4.2 discuss in detail about the model of the street canyon. The impact of changing the roof of the buildings on the flow structure and pedestrian comfort is discussed in section 4.3.

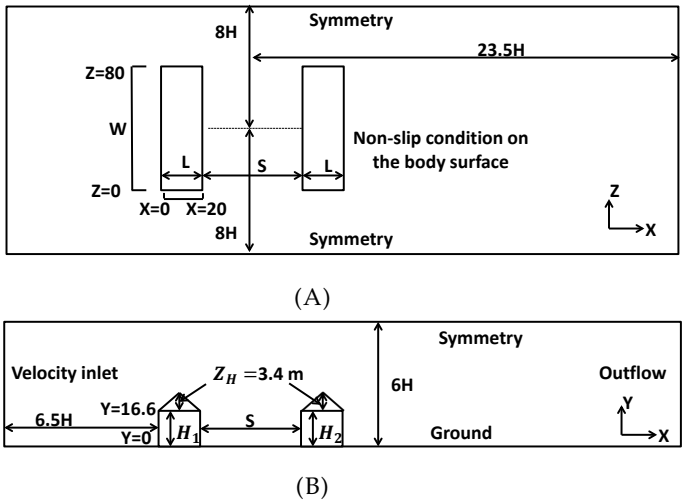

FIGURE 4.3: Computational domain and boundary conditions for slanted-slanted building configuration (case 2) (a) Plan view (b) side view.

4.2 CFD simulations: computational model and parameters for the different roof shapes

Figure 4.2 shows different street canyon configurations for all roof shapes considered in this study. Taking case 2 as an example, the model geometry of the street canyon with slanted-slanted configuration with dimensions $W \times H \times L = 80\,(m) \times 20\,(m) \times 20\,(m)$ was chosen to represent common medium-rise building structures. As shown in Figure 4.3, the chosen street width was $S = 20$ m for all studied cases. The flat roof building height was considered to be 20 m, whereas for all other roof shapes the building height (H) was 16.6 m and roof height (Z_H) was 3.4 m ensuring all cases were analysed at the same Re. The wind direction was perpendicular to the street canyon.

The effect of changing the building roof shapes on the flow pattern and pedestrian wind comfort inside a street canyon was investigated using computational fluid dynamics (CFD). The size of the computational domain was selected according to CFD best practice guidelines by Franke et al. (Franke et al., 2007). The Reynolds number (Re) was 8.1×10^6 based on the total building height $H + Z_H$ and free stream velocity.

All the other computational conditions, such as the turbulence model, boundary conditions, wall roughness effect and mesh arrangements were as described in Chapter 3.

4.3 Results and Discussion

4.3.1 Flow structure inside the street canyon

Figure 4.4 shows the variation of C_P along the centre plane ($Z = 40$) for the different faces of the upstream building for cases $1 - 6$.

From Figure 4.4 it can be observed that the stagnation point on the front face of the upstream building occurs at around $0.6\,H$ from the ground for

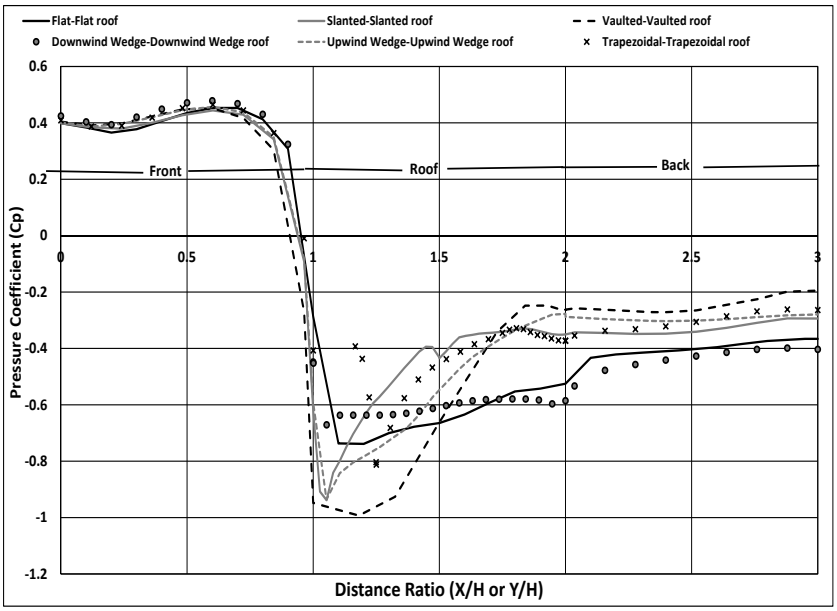

FIGURE 4.4: Pressure coefficient comparison plot along the centre plane of the upstream building for the considered roof shapes of both buildings (cases $1 - 6$).

all studied cases. The point of local minimum positive C_P which is approximately identical for all studied cases occurs on the front face at about $0.2\,H$ above the ground.

The flow structure in the case of a flat-flat roof ((Case 1)) is as described in subsection 3.3.1. These include separation of the flow due to the leading edge of the upstream building roof, reattachment of the separated shear layer on the same roof, back-flow from the canyon into the roof region of the upstream building resulting in a secondary recirculation region at the trailing edge of the upstream building, separation of the flow due to the sharp leading edges of the sides of the upstream building and reattachment of these separated shear layers on the downstream building sides.

In the slanted-slanted case ((Case 2)), the stream follows the slope of the upstream building roof while there is a recirculation zone that develops over the leeward side of the roof which can be clearly seen in Figure 4.5(B) and closer inspection of the same in Figure 4.6(B) which also shows a small recirculation near the windward sharp corner of the windward side of the roof. As shown in Figure 4.4 the negative pressure distribution is maximum at the windward corner of the roof, has a minimum of -0.9, increasing to -0.4 at the apex of the roof. The pressure remains relatively constant over the leeward side of the roof and the leeward wall of the building. Most of the flow from the roof of the upstream building diverts towards the roof of the downstream building. Backflow from the canyon is forced into the roof region of the upstream building resulting in recirculation at the leeward wall of the upstream building roof and forced laterally to be re-entrained by the main flow consistent with Dianat et al. (1984). The flow in the canyon can be characterized by a strong fluid stream directed upward towards the windward face of the downstream building.

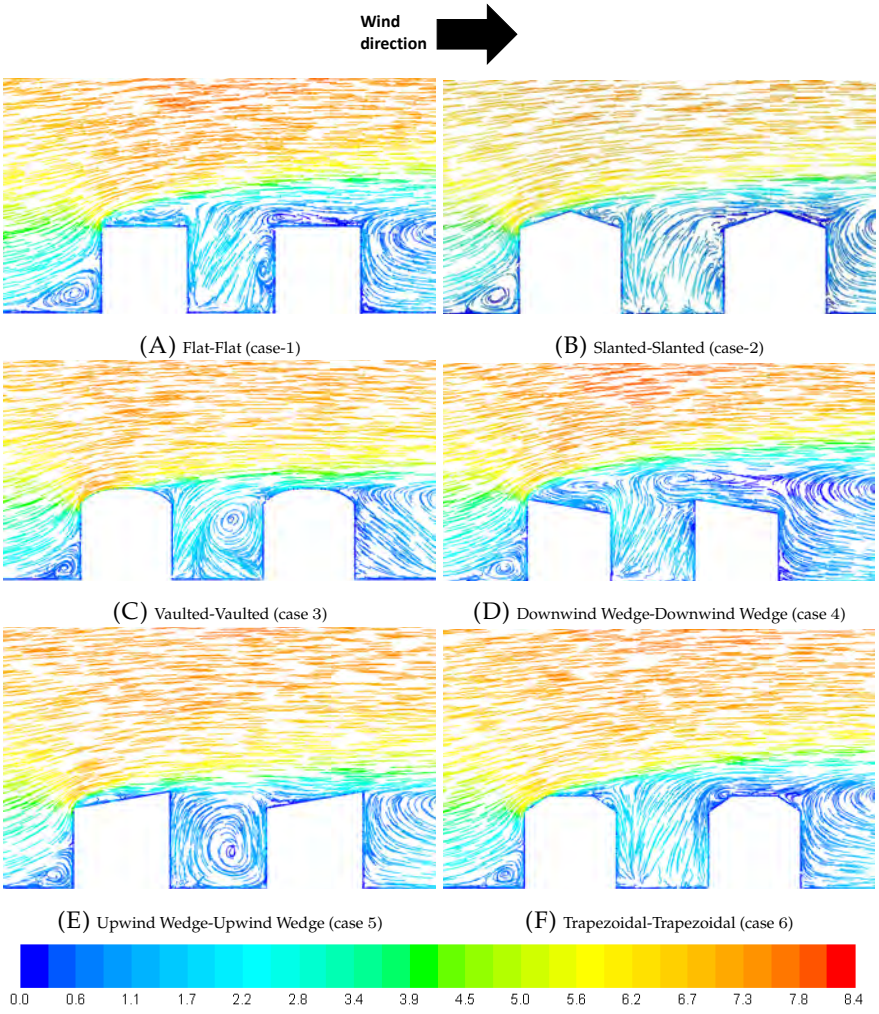

FIGURE 4.5: Velocity magnitude (m/s) pathlines in XY-plane at the centre plane ($Z = 40$) for the street canyon with different pairs of roof shapes.

For the vaulted-vaulted case ((Case 3)), the stream which deviates towards the upstream building roof does not separate from the roof and follows the shape of the roof. There is a recirculation zone that develops over the leeward side of the roof, which can be seen in Figure 4.5(C) and closer inspection of the same in Figure 4.6(C). The flow accelerates over the roof apex producing a minimum C_P of about -1.0 before the apex, according to Figure 4.4. The flow decelerates again as it descends over the leeward side of the roof, and the pressure coefficient reaches up to a value of -0.26 towards the leeward edge of the roof and on the leeward wall of the building down to the ground. Most of the flow from the roof of the upstream building diverts towards the roof of the downstream building. Backflow from the canyon is forced into the roof region of the upstream building and forced laterally to be re-entrained by the main flow consistent with Dianat et al. (1984). The flow in the canyon can be characterized by a strong fluid stream directed upward along the upstream face of the downstream building and by the presence of a coherent canyon vortex. The core of the recirculation vortex can be seen near the upwind face of the downstream building.

For the downwind wedge-downwind wedge case ((Case 4)), the flow separates from the roof due to the sharp leading edge of the upstream building roof. As shown in Figure 4.4, the negative pressure distribution has a minimum of -0.67 near the sharp leading edge where flow separates and increases to -0.58 near the leeward edge of the roof. The separated shear layer does not reattach to the same building roof giving rise to a complex separation pattern over the roof as shown in Figure 4.5(D) and closer inspection of the same in Figure 4.6(D). The separated flow due to the leading edge of the upstream building gives rise to a large three-dimensional recirculation region over the roof of the building, for which a vortex core can be recognized at approximately $0.65\,H$ downstream of the leading edge. Backflow from the canyon is forced into the roof region and forced laterally to be re-entrained by the main flow, again consistent with Dianat et al. (1984). The flow in the canyon can be characterized by a strong fluid stream directed upward towards the windward face of the downstream building. A large recirculation can be observed o the roof of the downstream building.

In the upwind wedge-upwind wedge case (Case 5), the flow separates due to the sharp leading edge of the upstream building which gives maximum negative pressure on the leading edge of the roof (Figure 4.4). The separated shear layer reattaches on the same roof. The flow in the canyon can be characterized by a strong fluid stream directed upward along the leeward wall of the upstream building and by the presence of a coherent canyon vortex. The core of the large recirculation vortex can be recognized near the upwind face of the downstream building.

For the trapezoidal-trapezoidal case (Case 6), the flow remains attached and follows the slanted shape of the windward side of the roof. Near the sharp corner of this slanted side of the roof, the flow separates and produces a minimum C_P of about -0.68 which can be clearly seen from Figure 4.4. The flow again decelerates over the flat top and towards the slanted leeward side of the roof, with C_P reaching a value of -0.35 near the downstream corner of the leeward slanted side of the roof. The pressure remains relatively constant over the leeward wall of the building. Backflow from the canyon is forced into the roof region resulting in a recirculation near the

leeward edge of the roof and forced laterally to be re-entrained by the main flow, consistent with Dianat et al. (1984). The flow pattern inside the street canyon can be observed to be similar to that of the flat-flat case.

Turning now to the flow streams which deviate towards the side faces of the upstream building, these separate due to the leading sharp edges giving rise to intense corner vortices. These separated shear layers roll up inside the canyon gap in the vaulted-vaulted case which can be clearly seen in Figure 4.7(C). In all the other cases, these separated shear layers reattach on the side faces of the downstream building. However, a part of these separated shear layers can be seen rolled up into the canyon gap.

Note that, in this study, the flow structure around and inside the street canyon is described by the velocity measurement either in the centre plane of the street (i.e. for the vertical flow structure) or using the horizontal plane at the pedestrian height of 1.5 m. In Chapter 3, by using building width as an influencing parameter and by keeping the aspect ratio $S/H = 1$ and by doing the velocity measurement, it was observed that the flow when enters into the street from sides remains symmetric when $W/H \geq 3$. Therefore, it can be concluded that for the building aspect ratio of $W/H = 4$, used in the study, the flow exhibits similar behaviour. Hence, centre plane has been used as one of the cases representing the vertical flow structure inside the canyon.

For the studied cases 7-11, in which the roof shapes of only the upstream building are changed, we observe that the flow structure on the roof and sides of the upstream building, inside the canyon, and on the top of the downstream building roof is similar to those described cases $1 - 6$. This is shown in Figure 4.8 and Figure 4.9, which show the flow structure in the centre plane and at the pedestrian height of 1.5 m, respectively. However, in the vaulted-flat case (Case-8), the reattachment of the flow due to the horseshoe vortex in the wake of the second building is different than that of the vaulted-vaulted case (Case-3) as seen by comparing Figure 4.9(C) with Figure 4.5(C).

In the case of roof shape changes for the downstream building only (cases 12-16), the flow structure on the roof and sides of the upstream building and inside the canyon is similar to that of the flat-flat roof case as can be seen in Figure 4.10. It can be observed here that in the flat-slanted, flat-vaulted, flat-upwind wedge and flat-trapezoidal cases, a large recirculation is observed on the roof of the downstream building, which was not present with the same roof shapes of the upstream building (cases 2, 3, 5, 6, 7, 8, 10 and 11). In the flat-downwind wedge, this recirculation region on the roof of the downstream building found disappeared which was present in the downwind wedge-downwind wedge (case-4) and downwind wedge-flat (case-9) cases. No drastic variation in the flow structure at the pedestrian height is observed when compared to the flat-flat roof case for all cases. This can be clearly seen in the Figure 4.11.

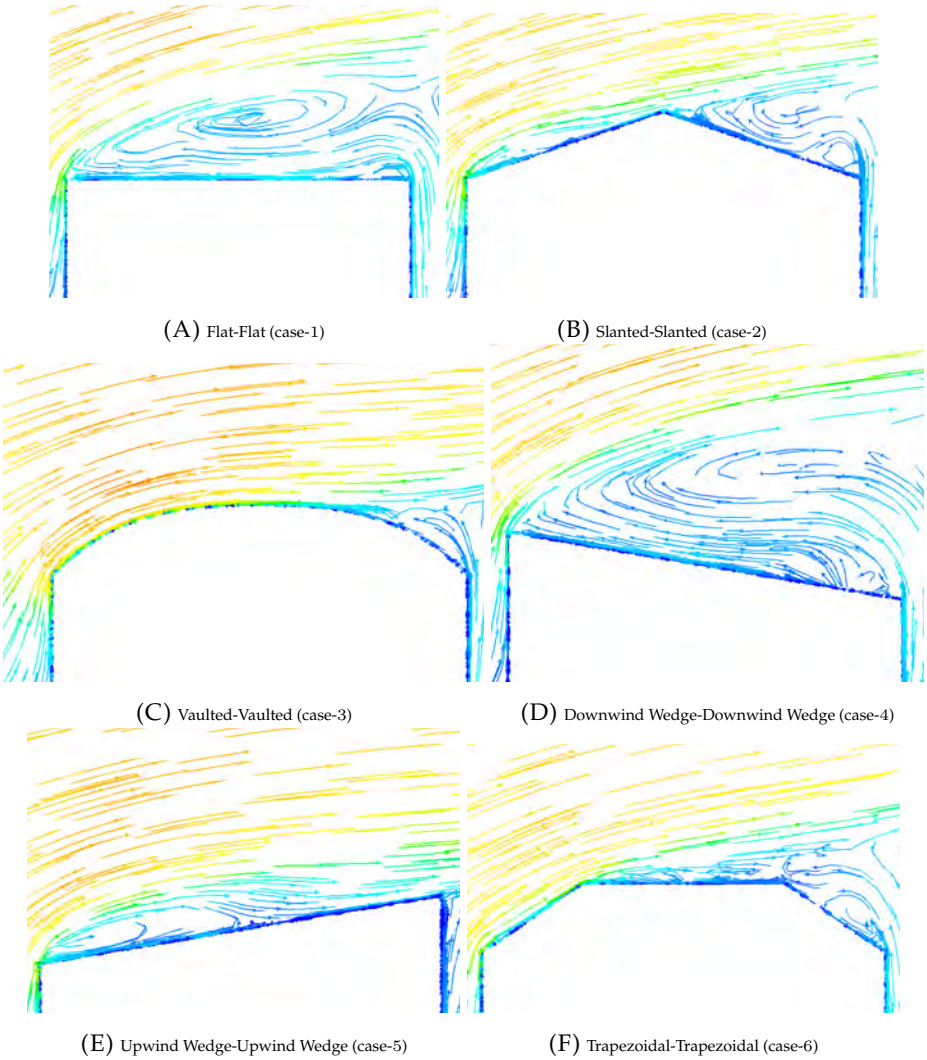

(A) Flat-Flat (case-1)

(B) Slanted-Slanted (case-2)

(C) Vaulted-Vaulted (case-3)

(D) Downwind Wedge-Downwind Wedge (case-4)

(E) Upwind Wedge-Upwind Wedge (case-5)

(F) Trapezoidal-Trapezoidal (case-6)

FIGURE 4.6: Detailed view of the flow separation on the roof of the upstream building using velocity magnitude (m/s) pathlines in XY-plane at centre plane ($Z = 40$) for different pairs of roof shapes.

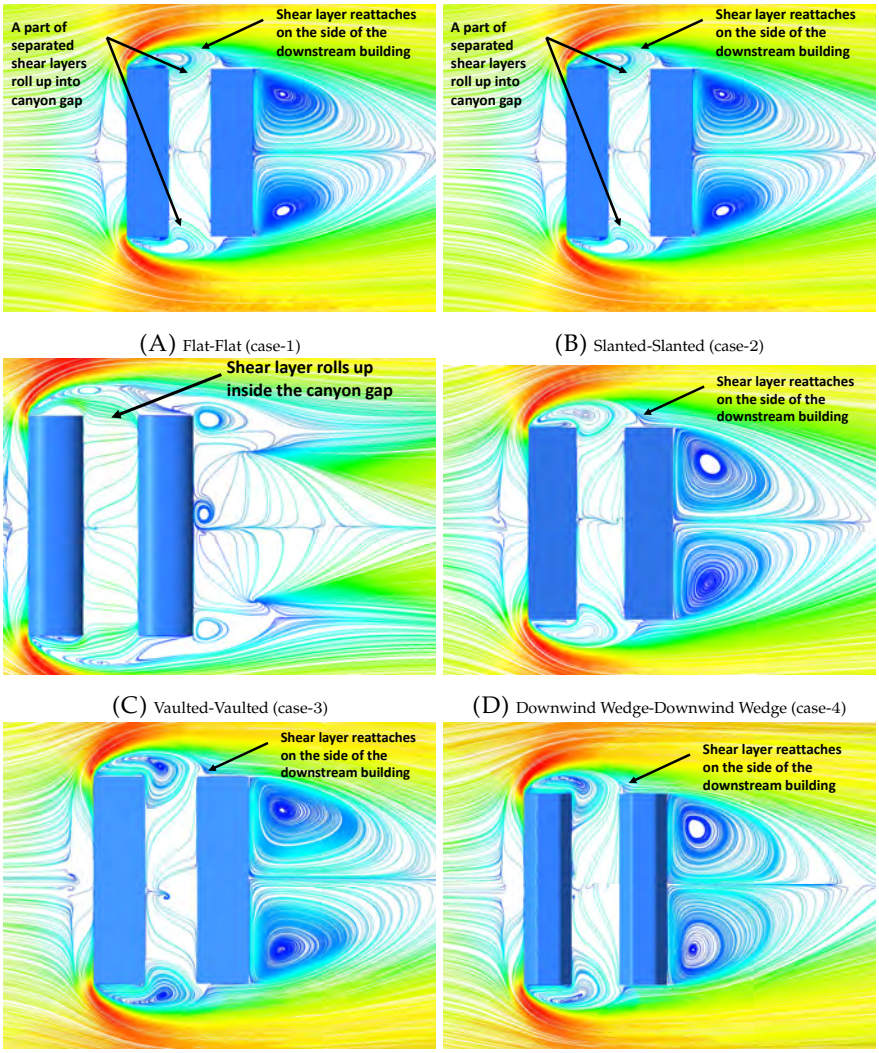

(A) Flat-Flat (case-1)

(B) Slanted-Slanted (case-2)

(C) Vaulted-Vaulted (case-3)

(D) Downwind Wedge-Downwind Wedge (case-4)

(E) Upwind Wedge-Upwind Wedge (case-5)

(F) Trapezoidal-Trapezoidal (case-6)

FIGURE 4.7: Velocity magnitude streamlines (cut plane to zoom near the street canyon) in XZ- plane at $Y = 1.5$ m level for the street canyon with different pairs of roof shapes.

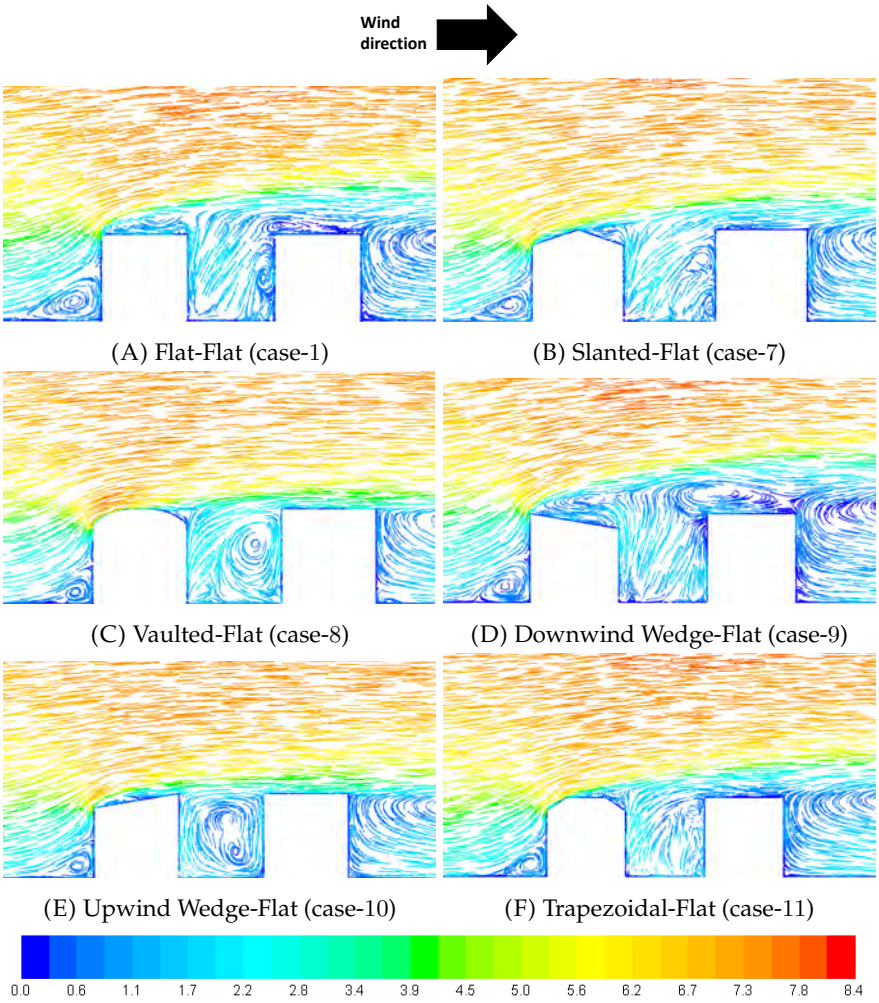

FIGURE 4.8: Velocity magnitude (m/s) pathlines in XY-plane at the centre plane ($Z = 40$) for the street canyon with different pairs of roof shapes.

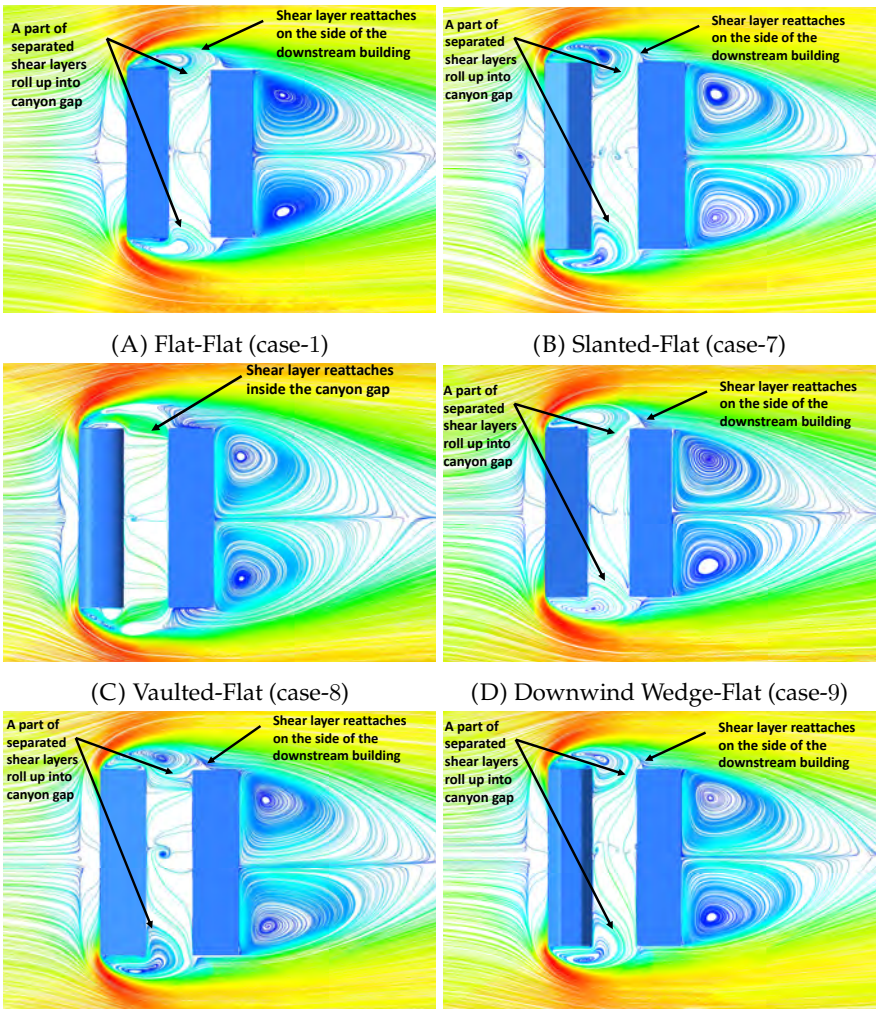

(A) Flat-Flat (case-1)

(B) Slanted-Flat (case-7)

(C) Vaulted-Flat (case-8)

(D) Downwind Wedge-Flat (case-9)

(E) Upwind Wedge-Flat (case-10)

(F) Trapezoidal-Flat (case-11)

FIGURE 4.9: Velocity magnitude streamlines (cut plane to zoom near the street canyon) in XZ- plane at $Y = 1.5$ m level for the street canyon with different pairs of roof shapes.

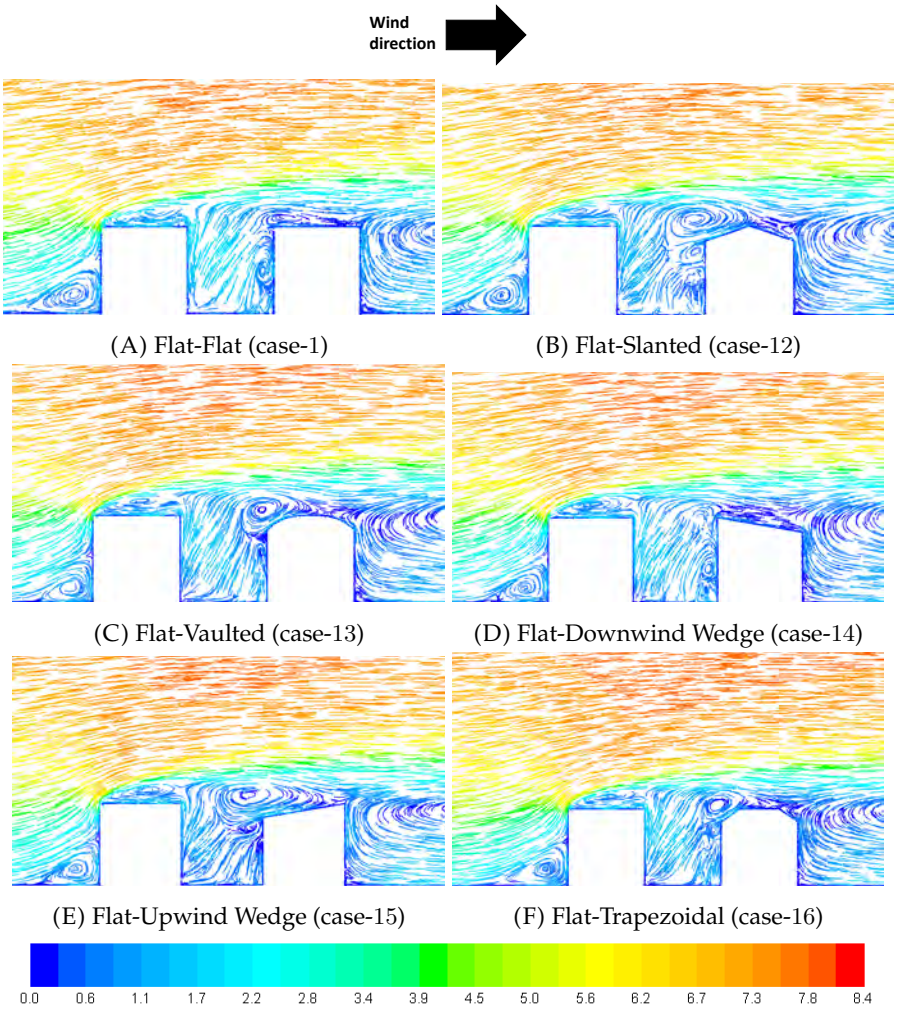

(A) Flat-Flat (case-1)

(B) Flat-Slanted (case-12)

(C) Flat-Vaulted (case-13)

(D) Flat-Downwind Wedge (case-14)

(E) Flat-Upwind Wedge (case-15)

(F) Flat-Trapezoidal (case-16)

FIGURE 4.10: Velocity magnitude (m/s) pathlines in XY-plane at the centre plane ($Z = 40$) for the street canyon with different pairs of roof shapes.

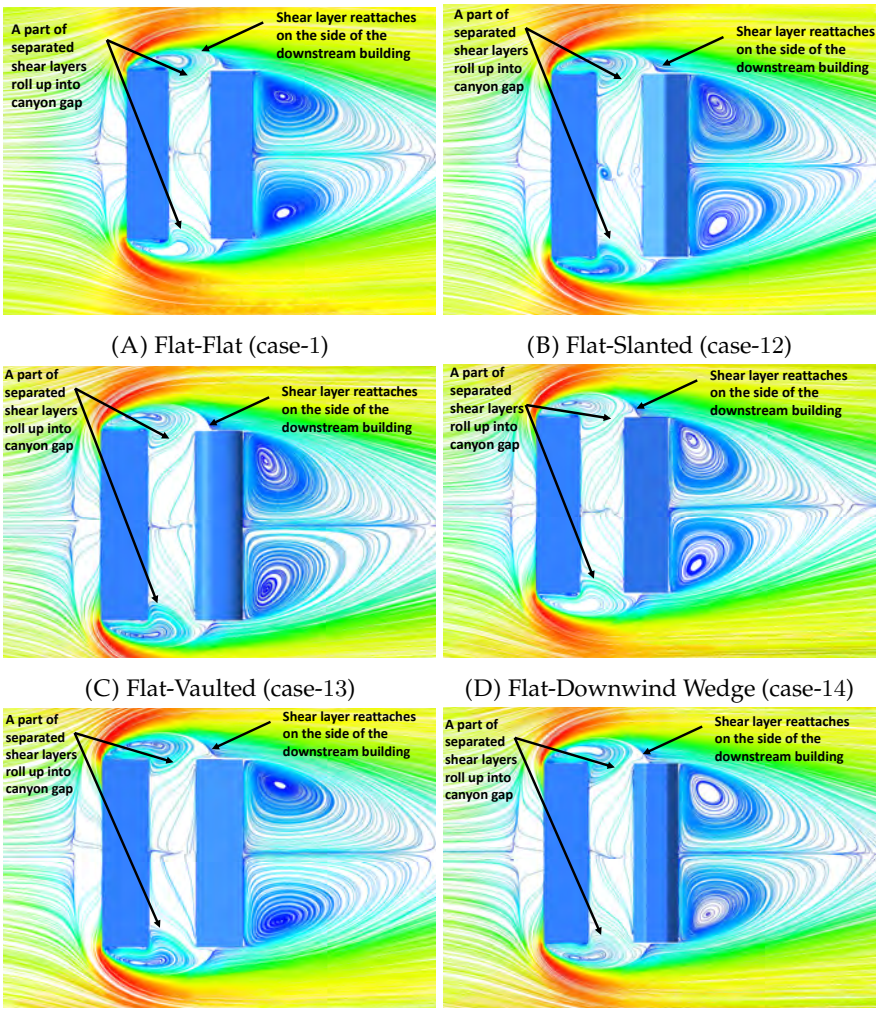

(A) Flat-Flat (case-1)

(B) Flat-Slanted (case-12)

(C) Flat-Vaulted (case-13)

(D) Flat-Downwind Wedge (case-14)

(E) Flat-Upwind Wedge (case-15)

(F) Flat-Trapezoidal (case-16)

FIGURE 4.11: Velocity magnitude streamlines (cut plane to zoom near the street canyon) in XZ- plane at $Y = 1.5$ m level for the street canyon with different pairs of roof shapes.

4.3.2 Turbulent kinetic energy field inside the street canyon

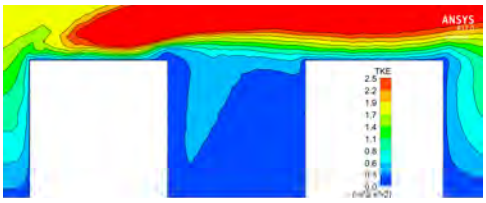

(A) Flat-Flat (case-1)

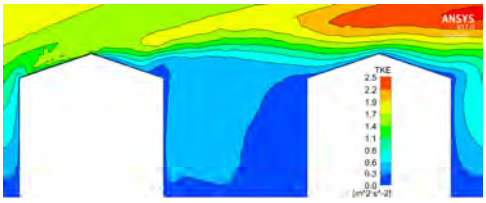

(B) Slanted-Slanted (case-2)

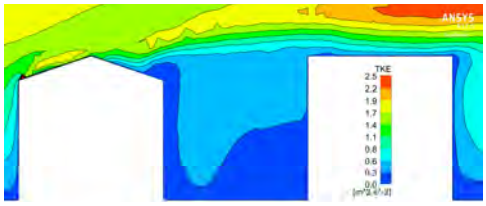

(C) Slanted-Flat (case-7)

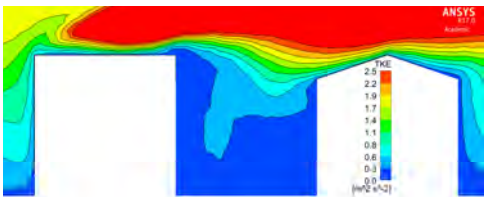

(D) Flat-Slanted (case-12)

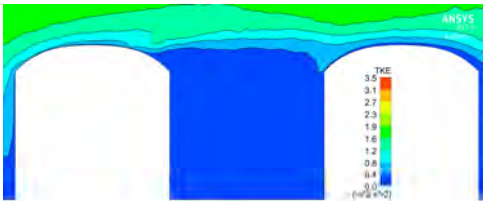

(E) Vaulted-Vaulted (case-3)

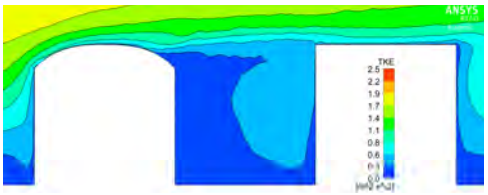

(F) Vaulted-Flat (case-8)

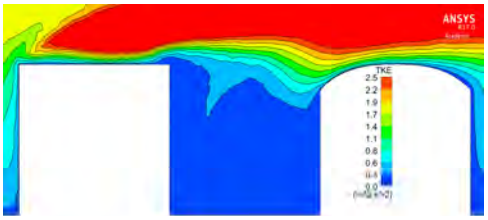

(G) Flat-Vaulted (case-13)

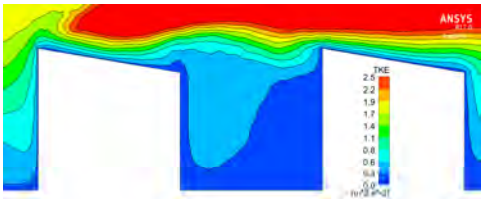

(H) Downwind wedge-Downwind wedge (case-4)

FIGURE 4.12: The distribution of the turbulent kinetic energy (k) in the centre plane ($Z = 40$) for considered roof shapes.

The turbulent kinetic energy (k) is defined by and calculated by the approximation,

$$k = \frac{1}{2}(\overline{u_x'^2} + \overline{u_y'^2} + \overline{u_z'^2})$$

and $k = \frac{3}{4}(\overline{u_x'^2} + \overline{u_z'^2})$ in XZ-plane, and $k = \frac{3}{4}(\overline{u_x'^2} + \overline{u_y'^2})$ in XY-plane, respectively. Where, $\overline{u_y'^2} = \frac{1}{2}(\overline{u_x'^2} + \overline{u_z'^2})$, and $\overline{u_z'^2} = \frac{1}{2}(\overline{u_x'^2} + \overline{u_y'^2})$ were assumed because the v and w cannot be measured on the XZ-plane, and XY-plane, respectively (Kim et al., 2003). Figures 4.12 and 4.13 represent the k-profile in the centre plane for the considered different pairs of roof shapes. Also, Figures 4.14 and 4.15 show vertical distribution of the k-profile in the $Z = 20$ plane for all cases. Note, that this plane was selected to find the difference between the k-profile in the center plane and plane at $Z = 20$. Due to the flow symmetry, similar kind of vertical k-profile can be expected in the vertical plane at $Z = 60$. Among all the studied cases, the flat-flat, vaulted-vaulted, trapezoidal-trapezoidal, slanted-flat and flat-slanted cases

were used for detail analysis. Figures 4.16, 4.18, 4.20, 4.22 and 4.24 represent horizontal distribution of the k around and inside the street canyon, at the three different planes $Y = 1.5$, 10 and 18 m, for the above mentioned cases which used for detail analysis. These horizontal planes were used as the representative cases to show the k-profile near the ground, in the center plane (horizontally) and plane parallel to the roof. Also, Figures 4.17, 4.19, 4.21, 4.23 and 4.25 show 3D isometric views of the street canyon for the cases mentioned above. Note that, these cases were selected for the detailed analysis of the k-profile due to the following reasons:

1. The flat-flat case was selected because it is the most discussed case for this study and for the uniform and non-uniform street canyon cases studied in the Chapter 3, and results for other roof shapes are compared with this case

2. In the vaulted-vaulted case, from the centre plane contour plot of the k (4.12(E)), it was observed that there is a limited exchange of the k into the street from the roof level, and hence to find the reason for it, this case was used for the further analysis

3. In the trapezoidal-trapezoidal case, from the centre plane contour plot of the k (4.13(F)), it was observed that a large portion of the k conveyed into the canyon from the roof level, and hence to find the reason for it, this case was used for the further analysis

4. The slanted-flat case was selected as one of the case representing flat roof of the downstream building and the flat-slanted case was selected because usually in the real urban areas wind can blow from any direction, and hence used to analyse the distribution of the k-profile when the upstream building is flat

From the centre plane contour plot of the k-profile (Figures 4.12 and 4.13), it can be observed that, the peak value of k occurs near the leading sharp edge of the roof, in all the cases with upstream building roof as flat, downwind wedge and upwind wedge. This is due to the fact that the production of k increases as a result of the larger velocity gradient due to the separation with sharp roof edge as discussed in subsection 4.3.1. These high turbulence levels increase convection and enhance entrainment by a shear layer of low momentum reverse flow in the canyon from the roof level, which strongly affects the local pressure gradients and hence allowing mixing of the fluid from the roof level into the canyon. This can be clearly seen from the centre plane plot of the flat-flat, downwind wedge-downwind edge, upwind edge-upwind edge, and all the cases with the upstream building roof flat, downwind edge, and upwind edge. In the flat-flat and upwind wedge-upwind wedge cases, the separated shear layer from the upstream building roof reattaches on the same surface and hence contains the low k when it reaches the trailing edge of the roof and hence conveys a smaller portion of k (hence less momentum transfer) into the street canyon. Whereas, in the downwind wedge-downwind wedge case flow does not reattach on the same roof surface and hence conveys a larger portion of k (and hence large momentum transfer) into the canyon from the roof level compared to the flat-flat and upwind wedge-upwind wedge cases.

In the cases with the slanted roof for the upstream building (case-2 and 7), as discussed above (in subsection 4.3.1), the flow separates and reattaches on the windward side of the wall which increases k and spreading of its intensity which allows fluid to travel upward towards the rooftop (apex). At this point, the flow separates again which increases k at this point and increases convection and allows large momentum exchange from the roof level into the canyon.

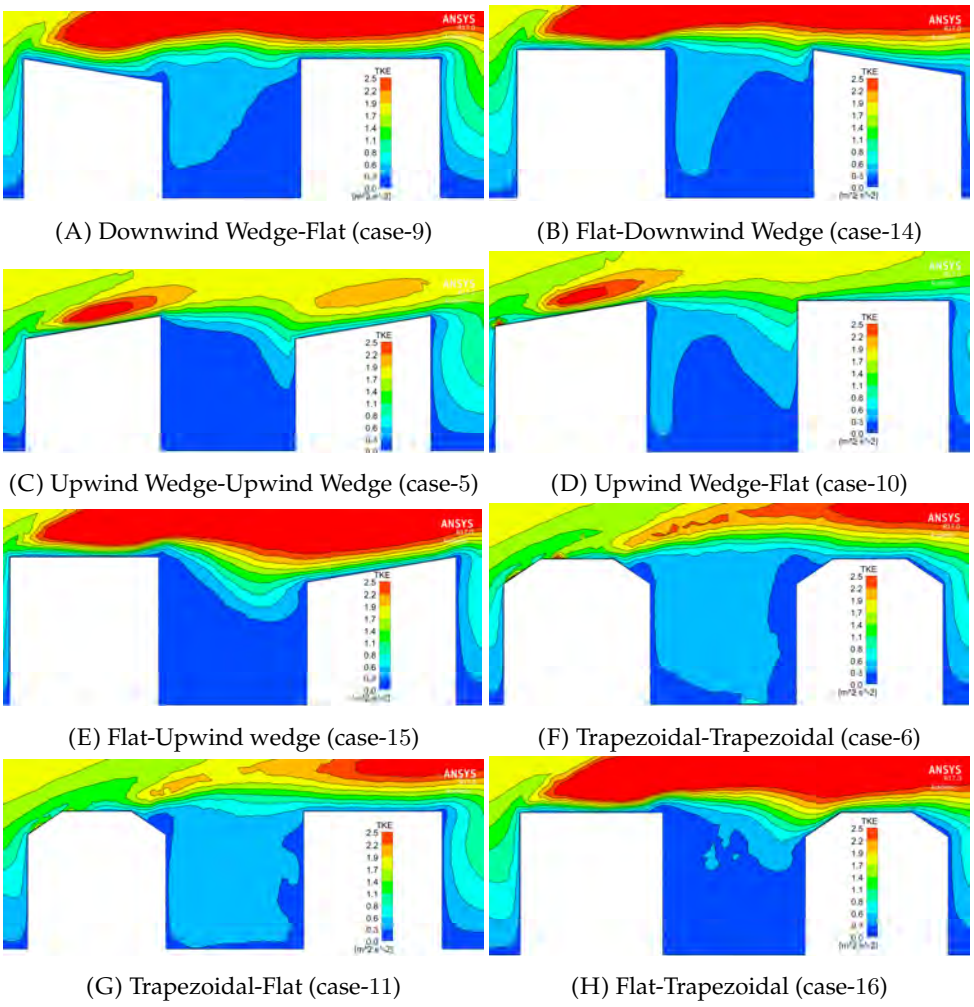

(A) Downwind Wedge-Flat (case-9)

(B) Flat-Downwind Wedge (case-14)

(C) Upwind Wedge-Upwind Wedge (case-5)

(D) Upwind Wedge-Flat (case-10)

(E) Flat-Upwind wedge (case-15)

(F) Trapezoidal-Trapezoidal (case-6)

(G) Trapezoidal-Flat (case-11)

(H) Flat-Trapezoidal (case-16)

FIGURE 4.13: The distribution of the turbulent kinetic energy (k) in the centre plane ($Z = 40$) for considered roof shapes.

In the cases with the vaulted roof for the upstream building (cases-3 and 8), as discussed in subsection 4.3.1, the flow does not separate on the roof and follows the shape of the roof. The development of recirculation zone over the leeward side of the roof results in an increase of turbulent kinetic energy at this point. However, in the case of vaulted-vaulted roof limited momentum exchange into the canyon from the roof level has been observed.

For the cases with the trapezoidal roof of the upstream building (cases-6 and 11), the separation of the flow occurs at the sharp corner of the slanted windward side of the roof. The separation of the flow at this point results

in an increase in k and hence increase in convection of the flow and hence increase in the momentum exchange from the roof level into the canyon. In all the cases with trapezoidal roof shape of the upstream building, largest momentum exchange from the roof into the canyon has been seen when compared to all other roof cases.

The flow entering into the canyon from the roof level contains high turbulent kinetic energy, and moves downward towards the ground and hence loses energy when it reaches near the ground level and recirculation occurs inside the canyon.

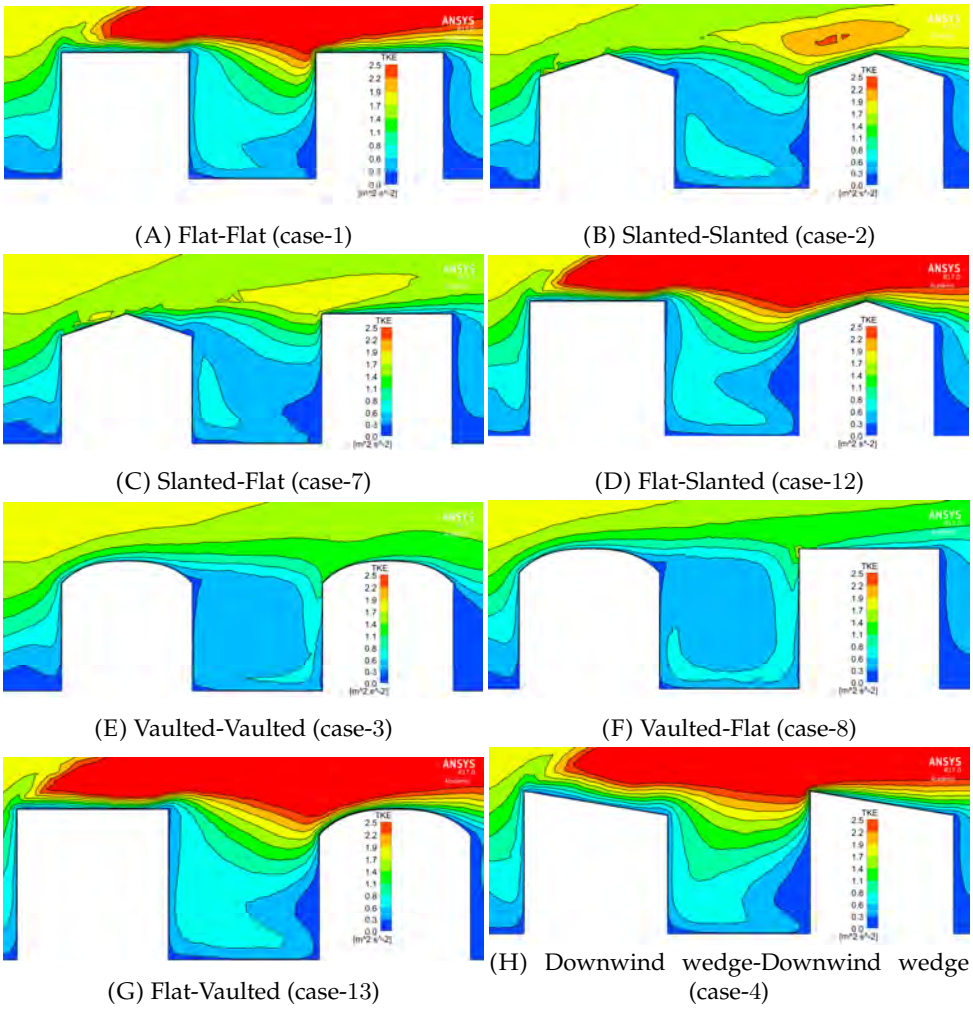

(A) Flat-Flat (case-1)

(B) Slanted-Slanted (case-2)

(C) Slanted-Flat (case-7)

(D) Flat-Slanted (case-12)

(E) Vaulted-Vaulted (case-3)

(F) Vaulted-Flat (case-8)

(G) Flat-Vaulted (case-13)

(H) Downwind wedge-Downwind wedge (case-4)

FIGURE 4.14: The distribution of the turbulent kinetic energy (k) in the vertical plane at $Z = 20$ for considered roof shapes.

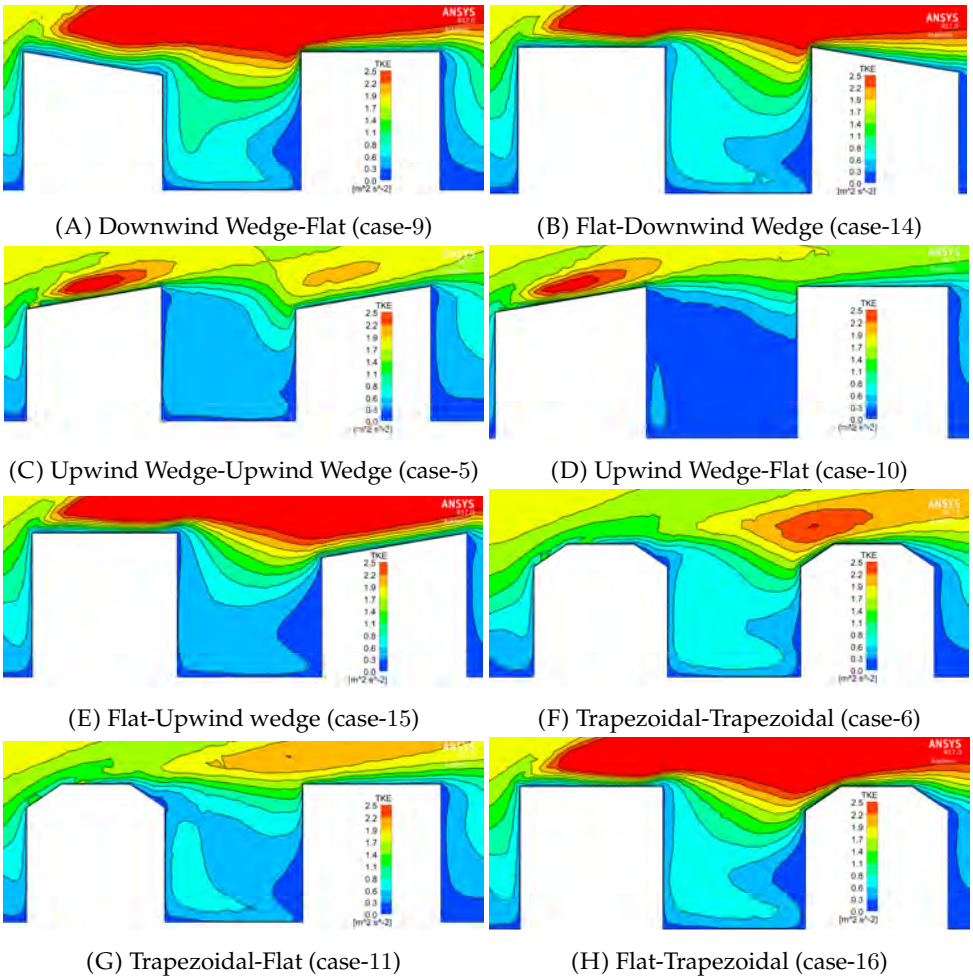

(A) Downwind Wedge-Flat (case-9)

(B) Flat-Downwind Wedge (case-14)

(C) Upwind Wedge-Upwind Wedge (case-5)

(D) Upwind Wedge-Flat (case-10)

(E) Flat-Upwind wedge (case-15)

(F) Trapezoidal-Trapezoidal (case-6)

(G) Trapezoidal-Flat (case-11)

(H) Flat-Trapezoidal (case-16)

FIGURE 4.15: The distribution of the turbulent kinetic energy (k) in the vertical plane at $Z = 20$ for considered roof shapes.

Comparing the k-profile for the cases considered with the upstream building roof as flat, downwind wedge, upwind edge, slanted, and trapezoidal it can be seen that delay in the flow separation from the rooftop in the case of slanted and trapezoidal roof delays increase in k and hence it's convection downstream. In the case of flat, downwind edge and upwind edge roof shape of the upstream building, the highest turbulent kinetic energy generated near the leading edge appears dispersed and its intensity is spreaded as the flow goes downstream, whereas in the case of the slanted and trapezoidal shape of the upstream building roof, delay in the separation delays spreading of it's intensity and hence there is more entrainment of the fluid into the canyon compared to other roof cases. This can be clearly seen from the centre plane contour plots as shown in Figures 4.12 and 4.13 and detailed analysis of the same from the horizontal contour plots and Isometric view.

While comparing the k-profile in the centre plane and plane at $Z = 20$, it can be observed that transfer of k (and hence momentum) from the roof level in $Z = 20$ plane is larger than the centre plane in all the cases.

From the horizontal representation of the turbulent kinetic energy for

the mentioned roof cases, for $Y = 1.5$, 10 and 18 it can be seen that the separation of the flow due to the sharp leading edges of the sides of the building causes an increase in the k. The reattachment of these shear layers on the sides of the downstream building also causes an increase in the turbulent kinetic energy. Due to increase in the k, the flow enters into the canyon from the sides having more turbulent kinetic energy and hence high wind speed near the downstream building and loses energy when approaches to the centre of the canyon and hence there is a reduction of the wind velocity in the centre of the canyon.

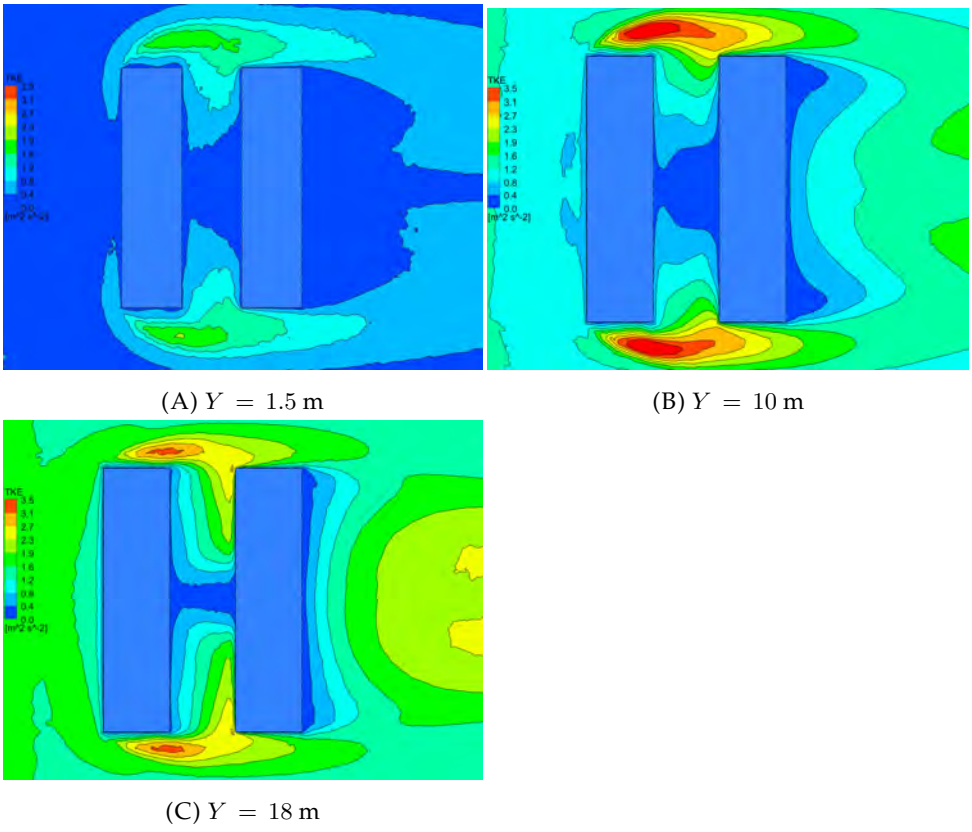

(A) $Y = 1.5$ m (B) $Y = 10$ m

(C) $Y = 18$ m

FIGURE 4.16: The distribution of the turbulent kinetic energy (k) in different horizontal planes for the flat-flat case.

Increase in the turbulent kinetic energy has also been observed, with an increase in the height from $Y = 1.5$ to 18. This is related to the fact that, the approaching flow has more kinetic energy at the roof level compared to the ground level.

Comparing all the studied cases, it can be clearly seen that the turbulent kinetic energy (k) in the outer flow increases significantly with the flat and downwind wedge shape roof of the upstream building.

From the 3D view of the turbulent kinetic energy for the different roof shapes considered for the detailed analysis, it can be clearly seen that the flow entering into the street from the roof level has more turbulent kinetic energy. It loses turbulent kinetic energy when it moves downward towards the ground and recirculation can be observed inside the street canyon.

From the above analysis of the flow structure and k-profile in the vertical and horizontal plane, it can be generalized that the flow structure and

increase or decrease in the wind velocity at any height inside the street canyon is the combined effect of the flow coming from the roof and the sides of the upstream building.

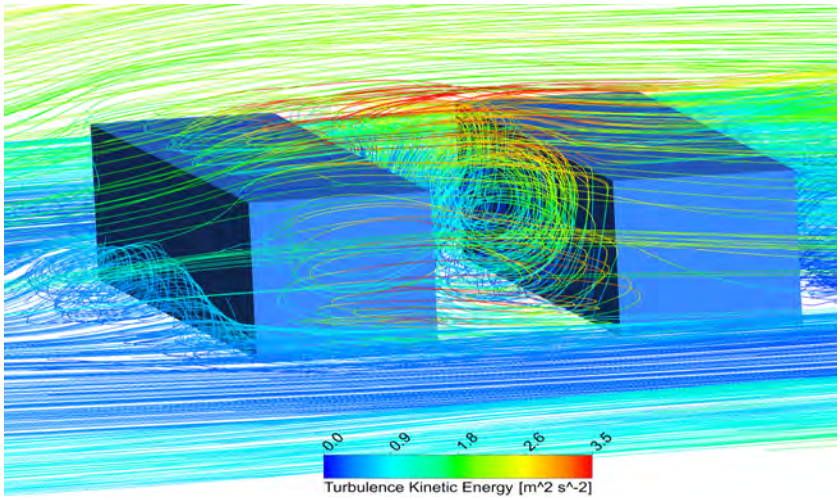

FIGURE 4.17: Isometric view of streamlines showing the turbulent kinetic energy (k) around and inside the street canyon for the flat-flat case.

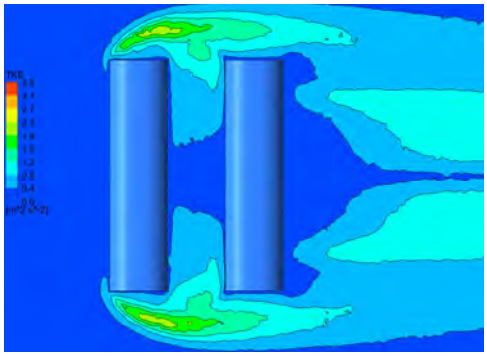

(A) $Y = 1.5$ m

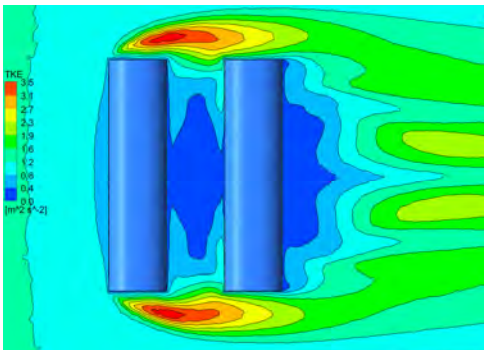

(B) $Y = 10$ m

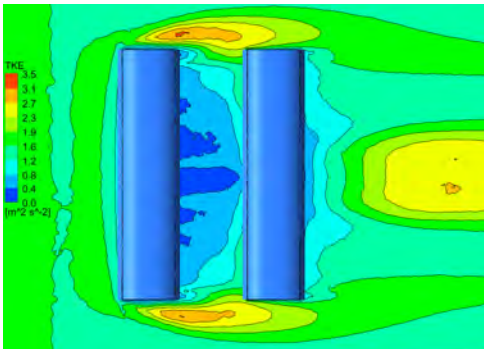

(C) $Y = 18$ m

FIGURE 4.18: The distribution of the turbulent kinetic energy (k) in different horizontal planes for the vaulted-vaulted case.

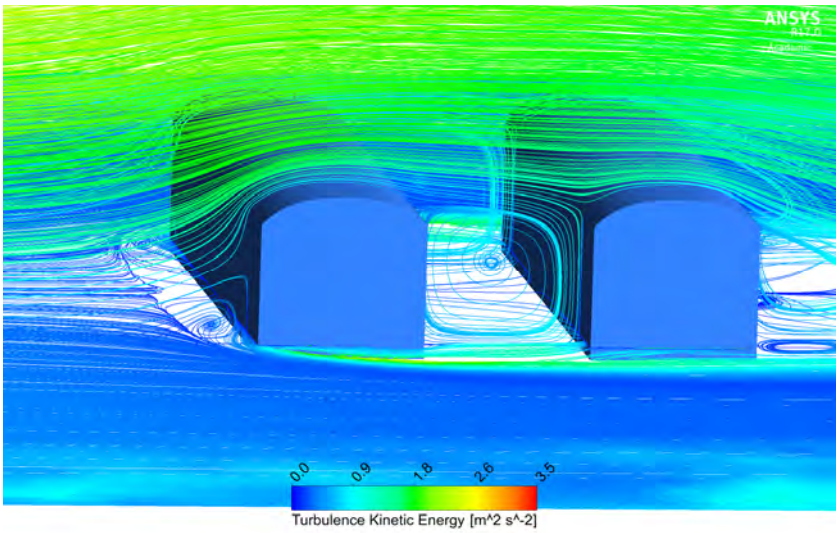

FIGURE 4.19: Isometric view of streamlines showing the turbulent kinetic energy (k) around and inside the street canyon for the vaulted-vaulted case.

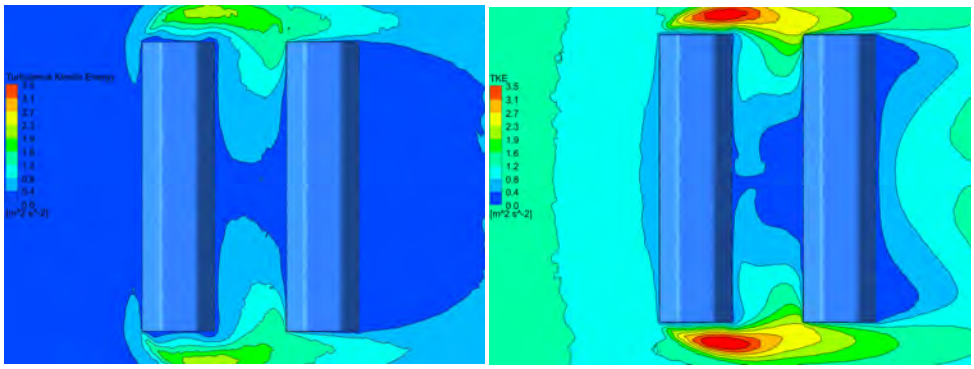

(A) $Y = 1.5$ m

(B) $Y = 10$ m

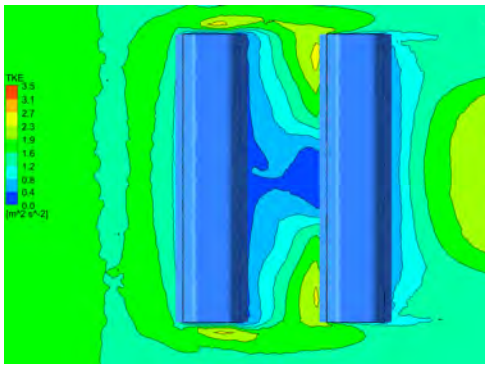

(C) $Y = 18$ m

FIGURE 4.20: The distribution of turbulent kinetic energy (k) in different horizontal planes for the trapezoidal-trapezoidal case.

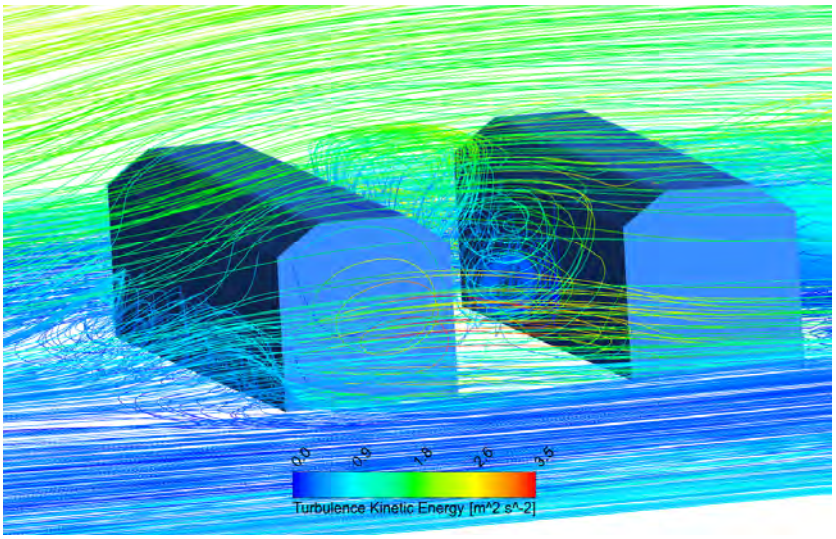

FIGURE 4.21: Isometric view of streamlines showing the turbulent kinetic energy (k) around and inside the street canyon for the trapezoidal-trapezoidal case.

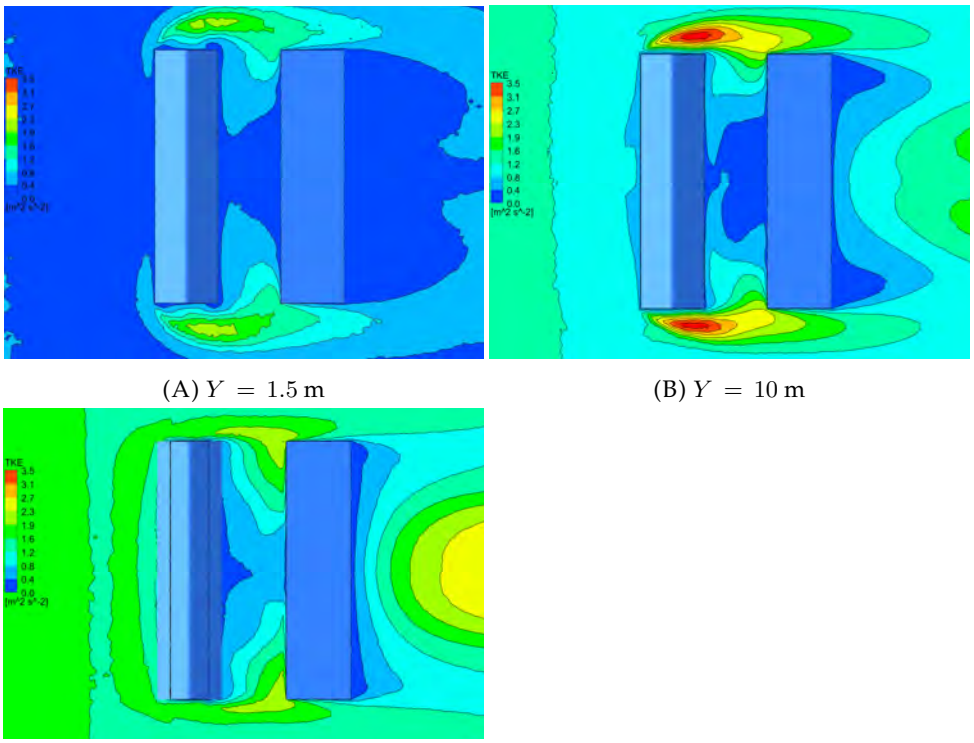

(A) $Y = 1.5$ m

(B) $Y = 10$ m

(C) $Y = 18$ m

FIGURE 4.22: The distribution of turbulent kinetic energy (TKE) in different horizontal planes for the slanted-flat case.

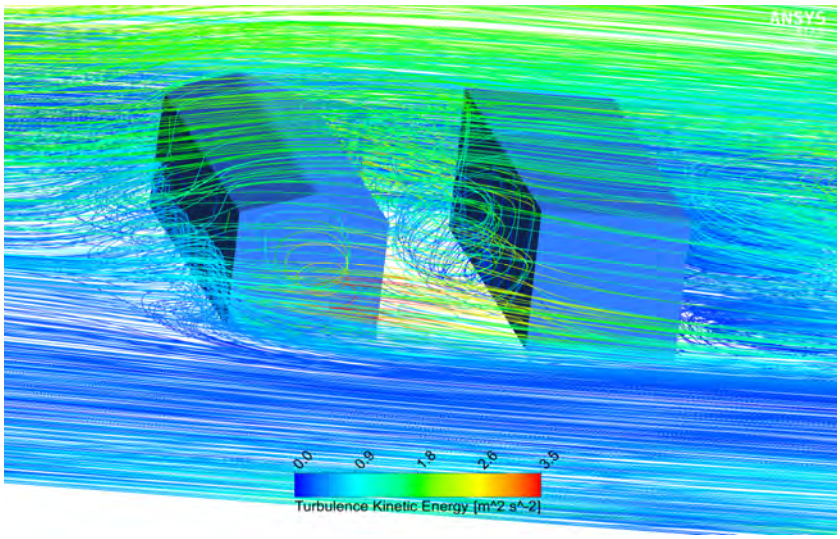

FIGURE 4.23: Isometric view of streamlines showing the turbulent kinetic energy around and inside the canyon for the slanted-flat case.

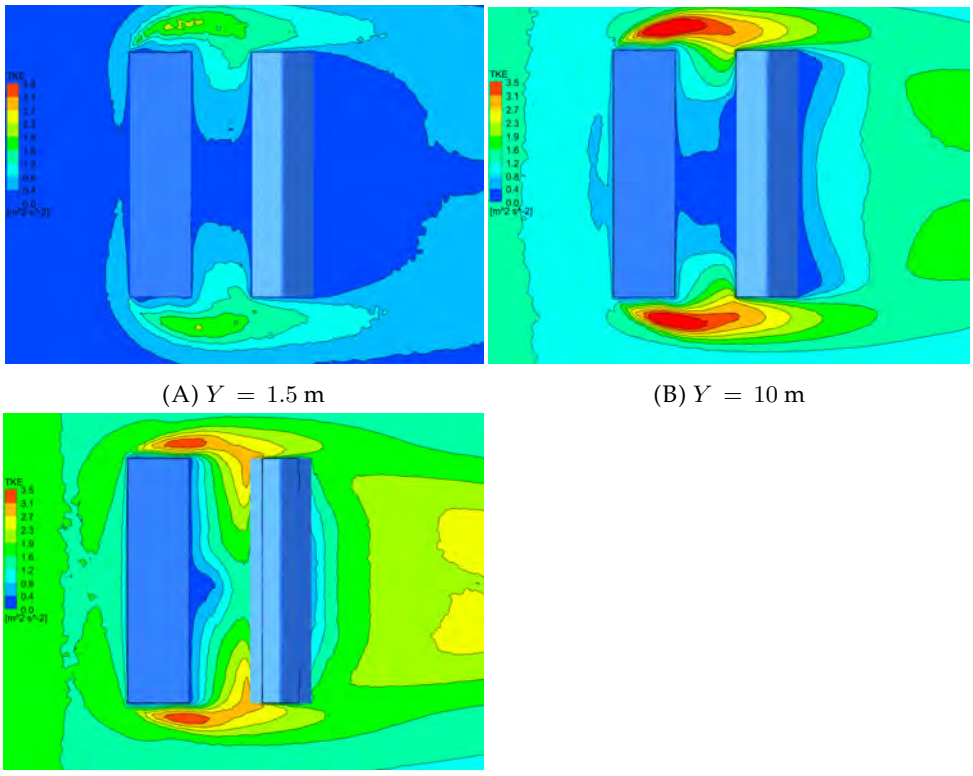

(A) $Y = 1.5$ m

(B) $Y = 10$ m

(C) $Y = 18$ m

FIGURE 4.24: The distribution of turbulent kinetic energy (TKE) in different horizontal planes for the flat-slanted case.

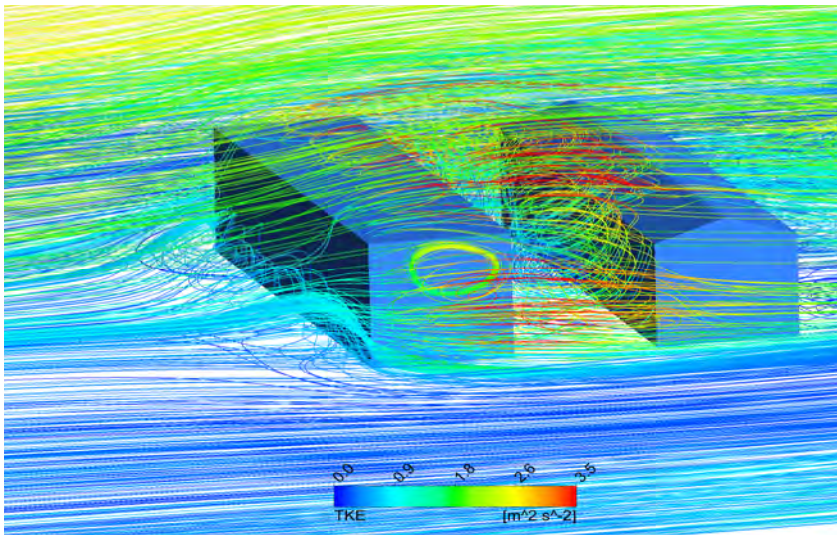

FIGURE 4.25: Isometric view of streamlines showing the turbulent kinetic energy (k) around and inside the canyon for the flat-slanted case.

4.3.3 Pedestrian level wind categorisation for different roof shapes

To assess the pedestrian comfort, Figures 4.26-4.28 show contour plots of ELBS Beaufort number at a height of 1.5 m around and inside the street canyon for various roof shapes. Results were compared with that of the flat-flat case. The height of 1.5 m was chosen as a representative height in between the standing and seated head height for a person, as mentioned in Chapter 3. We showed in Chapter 3 inside both the uniform and non-uniform street canyon with the flat-flat roof shape that as the width of the street increases, the area which complies with the comfort criterion decreases. However, when $S/H = 1$ for the flat-flat case, almost the entire region inside the street canyon was observed to be in the comfortable zone. In more detail, approximately 14% of the entire region inside the street canyon and almost 39% of the region near the downstream building had a wind speed between of 0.2 to 1.0 m/s (Beaufort Number 1). The remaining 86% of the street canyon and 61% near the downstream building had a wind speed between of 1.1 and 2.3 m/s (Beaufort Number 2). We assess the impact of roof shape on pedestrian comfort by comparing the results below with this flat-flat case for which almost the entire street canyon is in the comfortable zone.

For the different pairs of roof shapes (case-1-6) (contours as shown in Figure 4.26), overall wind speed for the entire street canyon is increased in the vaulted-vaulted, downwind wedge-downwind wedge and trapezoidal-trapezoidal cases compared to the flat-flat case. An overall decrease in the wind speed for the entire street canyon is observed in the upwind wedge-upwind wedge and slanted-slanted cases compared to the flat-flat case. The wind speed near the upstream building inside the street canyon increases in the vaulted-vaulted and downwind wedge-downwind wedge cases compared to the flat-flat case. However, a decrease in the wind speed near the upstream building is observed in the slanted-slanted, upwind wedge-upwind wedge and trapezoidal-trapezoidal cases compared to the flat-flat

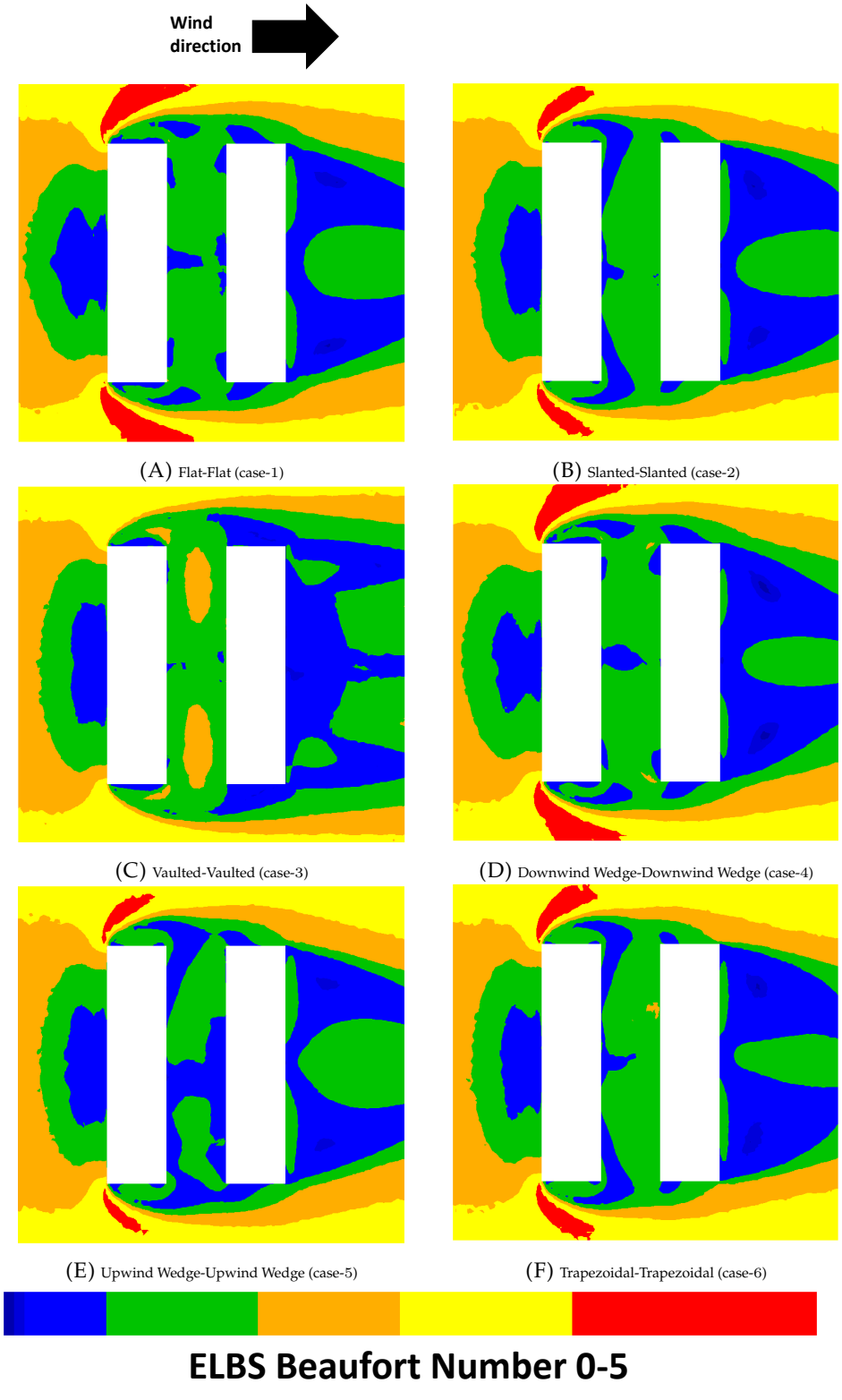

FIGURE 4.26: Wind categories at $Y = 1.5$ m in the XZ-plane for the street canyon with the different pairs of roof shapes. Here, dark blue represents 0 to 0.1 m/s, on Beaufort Number 0 on ELBS; blue represents 0.2 to 1.0 m/s, on Beaufort Number 1on ELBS; green represents 1.1 to 2.3 m/s, on Beaufort Number 2 on ELBS; orange represents 2.4 to 3.8 m/s, on Beaufort Number 3 on ELBS; yellow represents 3.9 to 5.5 m/s, on Beaufort Number 4 on ELBS; and red represents wind speeds between 5.6 m/s to 7.5 m/s, on Beaufort Number 5 on ELBS.

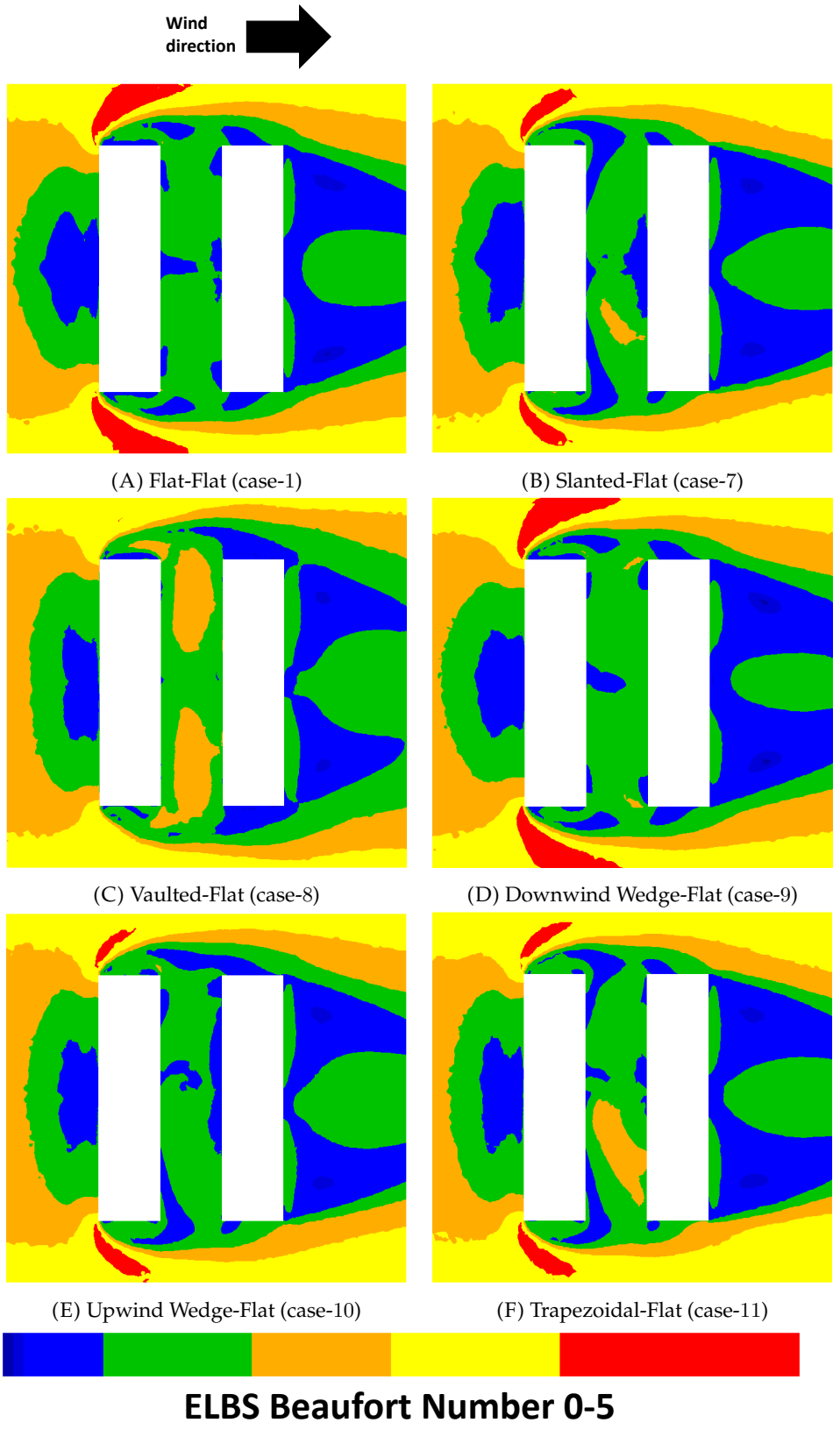

FIGURE 4.27: Wind categories at $Y = 1.5$ m in the XZ-plane for the street canyon with the different roof shapes of only the upstream building. Colours as in Figure 4.26.

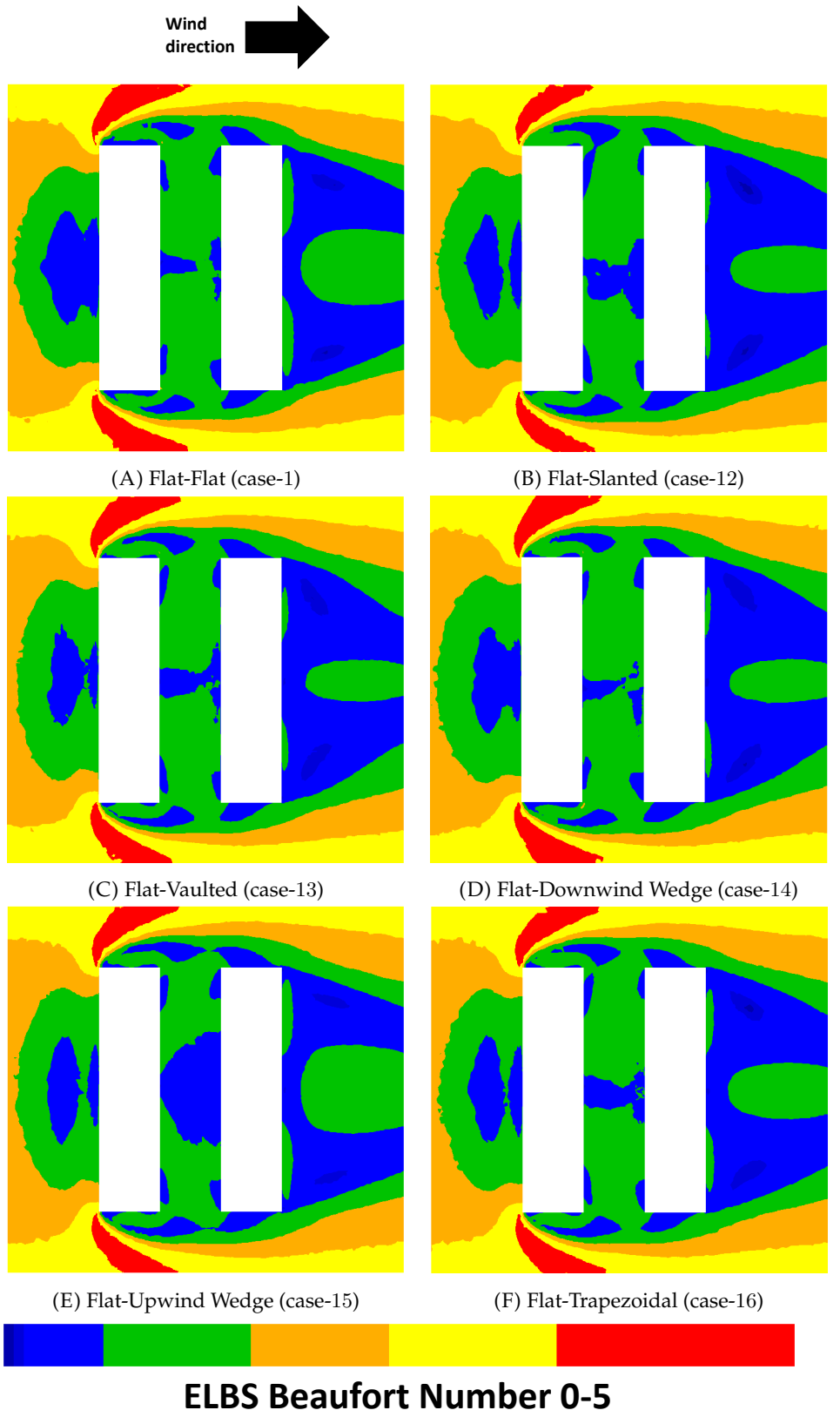

FIGURE 4.28: Wind categories at $Y = 1.5$ m in the XZ-plane for the street canyon with the different roof shapes of only the downstream building. Colours as in Figure 4.26.

case. The wind speed near the downstream building inside the street canyon increases in the slanted-slanted, vaulted-vaulted, downwind wedge-downwind wedge, and trapezoidal-trapezoidal cases when compared to the flat-flat case. Whereas, the wind speed near the downstream building decreases in the upwind wedge-upwind wedge case compared to the flat-flat case. It can also be seen that in the vaulted-vaulted case, the total region of discomfort in the centre part of the street increases compared to the flat-flat case. From this study, it can be revealed that, among the considered roof shapes of both buildings, an upwind wedge roof shape decreases the wind speed in the street canyon and vaulted roof shape increases overall wind speed in the street canyon, and can be considered to be good and bad cases for the pedestrian wind comfort.

As shown in Figure 4.27 for cases 7-11, in which roof shapes of only the upstream building is changed, it can be observed that the wind speed inside the entire street canyon increases compared to the flat-flat case in the vaulted-flat, downwind wedge-flat, trapezoidal-flat, and slanted-flat cases, and is worst in the vaulted-flat case. It also increases near the upstream building inside the canyon in the vaulted - flat case compared to the flat-flat case. An overall decrease in the wind speed near the upstream building can be seen in the upwind wedge-flat, trapezoidal-flat, and slanted-flat cases when compared to the flat-flat case. For the area near the downstream building, the wind speed increases in the vaulted-flat, downwind wedge-flat, and trapezoidal flat cases and is worst in the vaulted-flat, and trapezoidal-flat cases when compared to the flat-flat case. Of the considered roof shapes, the upwind wedge roof shape can be considered to be the best case to decrease the overall wind speed and the vaulted and trapezoidal roof shapes can be considered as the worst shapes for the pedestrian wind comfort, when in tandem with a downstream flat roof.

The contour plots in Figure 4.28 show an overall decrease in the wind speed inside the entire street canyon as well as near the upstream and downstream buildings in all the studied cases (case 12-16) when compared to the flat-flat case. As discussed in the flow structure analysis of these cases, with the flat roof shape of the upstream building allows limited momentum exchange from the upstream building into the canyon as well as the large recirculation region on the roof of the downstream building which has been observed in the flat-slanted, flat-vaulted, flat-upwind wedge and flat-trapezoidal cases, which allows limited fluid to come out of the canyon. This could probably cause the corresponding reduction in the wind speed at the pedestrian level.

As specified above from the detail analysis of the flow structure in subsections 4.3.1 and 4.3.2, overall increase or decrease in the wind speed at any height in the street canyon is the combined effect of the flow coming from the roof level and from the sides of the upstream building. Therefore, it is hard to generalize from one or two vertical planes to find the cause of an overall increase or decrease in the wind speed at the pedestrian level.

Fluent Contour plot colour sensitivity analysis

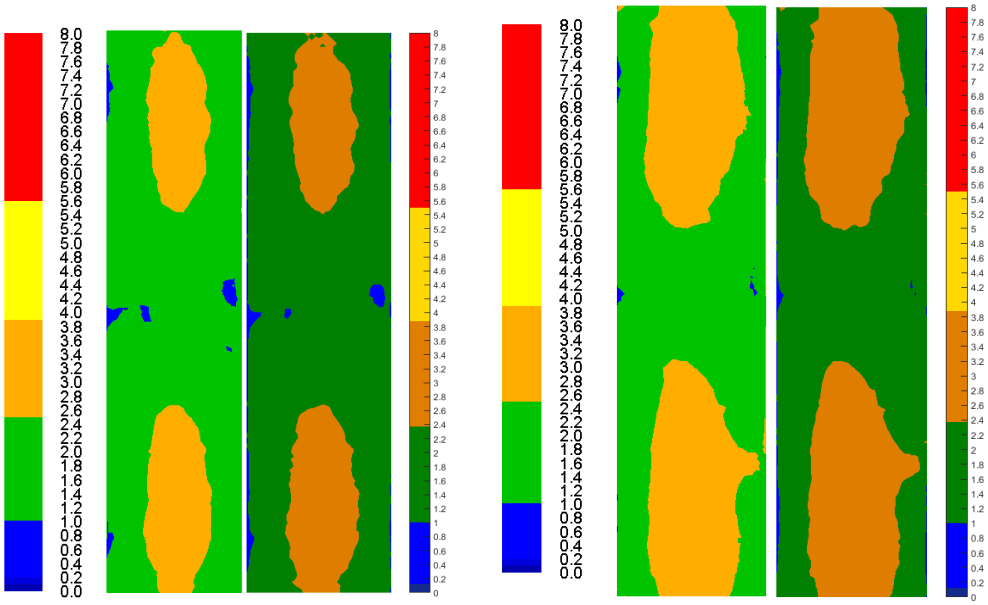

(A) Vaulted-Vaulted (case-3)

(B) Vaulted-Flat (case-8)

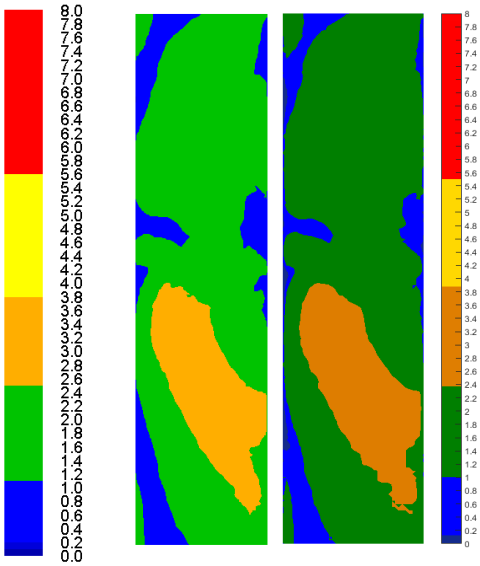

(C) Trapezoidal-Flat (case-11)

FIGURE 4.29: Fluent contour plot colour sensitivity analysis for street canyon for (A) Vaulted-Vaulted (B) Vaulted-Flat and (C) Trapezoidal-Flat cases. The left-hand side of each figure: Fluent post-processing. Right-hand side: Matlab.

While doing the pedestrian level wind categorisation using contour plots, it is important to check the sensitivity of each colour-bar representing the wind velocity accurately. Slightly variation in this may cause variation of the scale representing particular wind velocity zone. For example, in this study, we have used ELBS with different Beaufort numbers representing different levels of wind speed. Not accurately representing wind velocity can change the Beaufort scale from comfortable to discomfort zone or vice

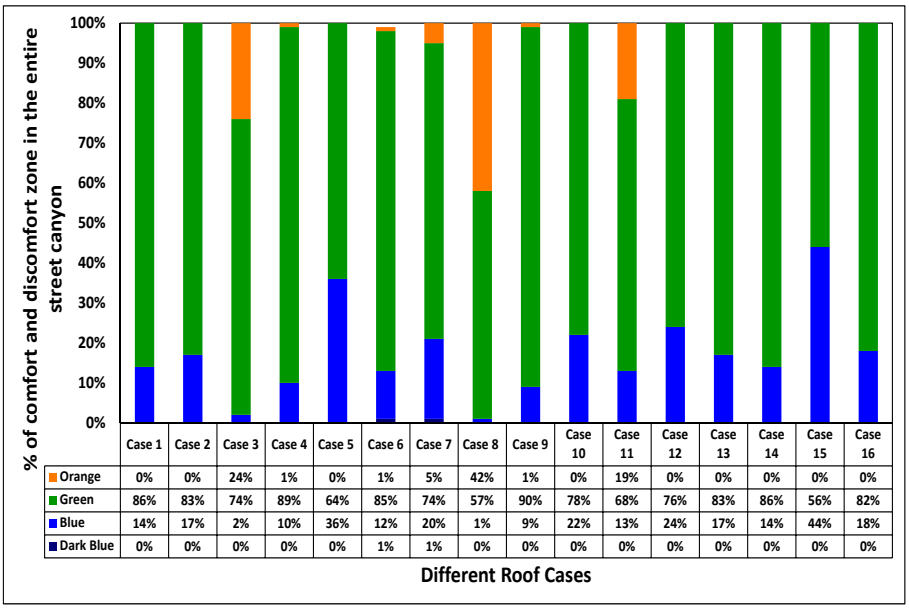

	Case 1	Case 2	Case 3	Case 4	Case 5	Case 6	Case 7	Case 8	Case 9	Case 10	Case 11	Case 12	Case 13	Case 14	Case 15	Case 16
Orange	0%	0%	24%	1%	0%	1%	5%	42%	1%	0%	19%	0%	0%	0%	0%	0%
Green	86%	83%	74%	89%	64%	85%	74%	57%	90%	78%	68%	76%	83%	86%	56%	82%
Blue	14%	17%	2%	10%	36%	12%	20%	1%	9%	22%	13%	24%	17%	14%	44%	18%
Dark Blue	0%	0%	0%	0%	0%	1%	1%	0%	0%	0%	0%	0%	0%	0%	0%	0%

FIGURE 4.30: Comparison of increase or decrease of comfort and discomfort zone for different roof shapes compared to the flat-flat roof (Case-1) inside the entire street canyon. Colours as in Figure 4.26.

versa. In all the studied cases of different roof shapes in this Chapter and in Chapter 3, the contour plots for pedestrian wind categorisation were made with Fluent's post-processing tool. In order to check the sensitivity of each colour-bar representing wind velocity accurately or not, similar kind of contour plots were prepared using Matlab. For both programs, same contour values have been considered. Cases of vaulted-vaulted roof shape, vaulted-flat roof shape and trapezoidal-flat roof shape were chosen for this analysis, as they can be seen to be the cases showing high wind speed variation inside the canyon (Figures 4.26(C), 4.27(C), and 4.28(C)). Wind velocity data from the Fluent simulation results were imported into Matlab and then the code was written to do the contour plots. (The code for the contour plot in Matlab is shown in Appendix G.

It can be clearly seen in Figure 4.29 that the contour plots generated using Fluent and those generated using Matlab match closely. Therefore, representation of pedestrian wind comfort contour plots were continued using Fluent post-processing tool.

Comparison of the wind speed

Figure 4.30 shows a stack plot representation and data table for the percentage of the entire canyon taken up by different Beaufort Number zones at a height of 1.5 m. This plot also represents the percentage of increase or decrease in the particular zone inside the entire street canyon with respect to the flat-flat case. Compared cases are as specified in Figure 4.2. The data clearly indicates that at the height of 1.5 m the wind speed inside the entire street canyon decreases in the case of slanted and upwind wedge roof shape

of both buildings (case 2 and 5), upwind wedge roof shape of only the upstream building (case 10) and all the roof shapes for only the downstream building (cases $12-16$). An increase in the discomfort zone and overall increase in the wind speed compared to the flat-flat roof has been observed in the case of vaulted, downwind wedge and trapezoidal roof shape of both the buildings (case 3, 4 and 6) and except upwind wedge roof shape roof when only the upstream building roof shape change (case $7-9$ and 11).

For the wind speed assessment area near the upstream building as shown in Figure 4.31, it can be seen that an overall reduction in the wind speed compared to the flat-flat roof case can be seen for the upwind wedge and trapezoidal roof shape of both the buildings (case 5 and 6), slanted, upwind wedge and trapezoidal roof shape of only the upstream building (case 7, 10 and 11) and all the roof shapes for only the downstream building (cases $12-16$). Vaulted and downwind wedge roof shape of both the buildings (case 3 and 4) and only the upstream building (case 8 and 9) increases the overall wind speed near the upstream building.

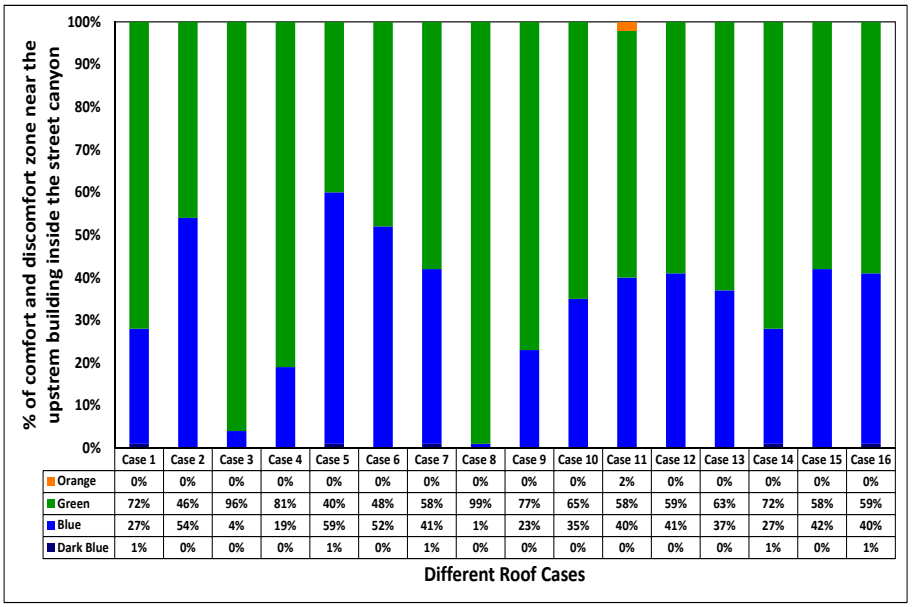

	Case 1	Case 2	Case 3	Case 4	Case 5	Case 6	Case 7	Case 8	Case 9	Case 10	Case 11	Case 12	Case 13	Case 14	Case 15	Case 16
Orange	0%	0%	0%	0%	0%	0%	0%	0%	0%	0%	2%	0%	0%	0%	0%	0%
Green	72%	46%	96%	81%	40%	48%	58%	99%	77%	65%	58%	59%	63%	72%	58%	59%
Blue	27%	54%	4%	19%	59%	52%	41%	1%	23%	35%	40%	41%	37%	27%	42%	40%
Dark Blue	1%	0%	0%	0%	1%	0%	1%	0%	0%	0%	0%	0%	0%	1%	0%	1%

FIGURE 4.31: Comparison of increase or decrease of comfort and discomfort zone for different roof shapes compared to the flat-flat roof (Case-1) near the upstream building for 3 m distance in the X-direction and 80 m distance in the Z-direction at $Y = 1.5$ m height. Colours as in Figure 4.26.

Figure 4.32 shows the data table and wind speed assessment stack chart near the downstream building and comparison of the obtained results with the flat-flat roof shape. Overall improvement in the wind speed can be seen in the case of the upwind wedge-upwind wedge (case 5), upwind wedge-flat (case 10) and considered all cases with flat roof shape of the upstream building except flat-downwind wedge (case $12-13$, 15 and 16). Vaulted-vaulted (case 3), downwind wedge-downwind wedge (case 4), trapezoidal-trapezoidal (case 6), vaulted-flat (case 8), downwind wedge -flat (case 9) and trapezoidal flat (case 11) can be considered as the worst cases for pedestrian comfort near the downstream building.

From the above detailed analysis of the pedestrian comfort for the considered S/H shows that changing the roof shape of only the downstream building improves pedestrian comfort inside the entire street compared to that of the flat-flat roof. It can also be revealed that the upwind wedge roof shape is the best to improve the pedestrian comfort inside the entire street canyon and near the upstream or downstream building when it is considered for both the buildings or only upstream building or only the downstream building. Vaulted and downwind wedge roof shapes are worst cases for the pedestrian comfort when considered for both building or only the upstream building.

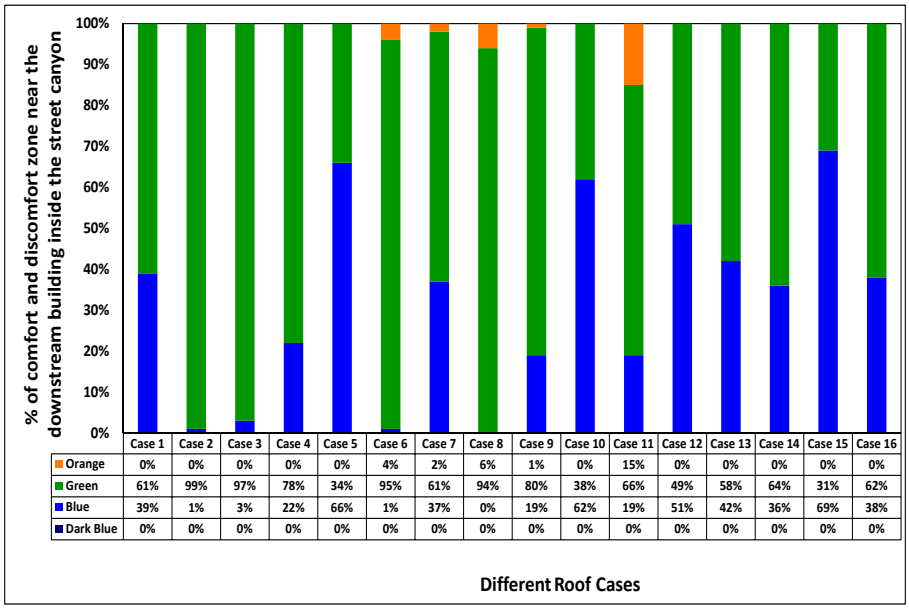

	Case 1	Case 2	Case 3	Case 4	Case 5	Case 6	Case 7	Case 8	Case 9	Case 10	Case 11	Case 12	Case 13	Case 14	Case 15	Case 16
Orange	0%	0%	0%	0%	0%	4%	2%	6%	1%	0%	15%	0%	0%	0%	0%	0%
Green	61%	99%	97%	78%	34%	95%	61%	94%	80%	38%	66%	49%	58%	64%	31%	62%
Blue	39%	1%	3%	22%	66%	1%	37%	0%	19%	62%	19%	51%	42%	36%	69%	38%
Dark Blue	0%	0%	0%	0%	0%	0%	0%	0%	0%	0%	0%	0%	0%	0%	0%	0%

FIGURE 4.32: Comparison of increase or decrease of comfort and discomfort zone for different roof shapes compared to the flat-flat roof (Case-1) near the downstream building for 3 m distance in the X-direction and 80 m distance in the Z-direction at $Y = 1.5$ m height. Colours as in Figure 4.26.

An analysis of the overall increase or decrease in the average and maximum wind speed at the pedestrian height was also carried out for the different roof shapes. The obtained data for the different roof shapes were normalized with the average and maximum wind speed for the flat-flat case as shown in Figures 4.33 and 4.34, respectively. The obtained results show that an overall increase in average wind speed compared to the flat-flat case has been occurred for all the roof shapes change of both building except upwind wedge-upwind wedge (case-5), all the roof shapes change for only the upstream building except upwind wedge-flat (case-10), and for the flat-downwind wedge cases. Whereas, an overall increase in the maximum wind speed compared to the flat-flat case has been observed in the vaulted-vaulted, vaulted-flat and trapezoidal-flat cases.

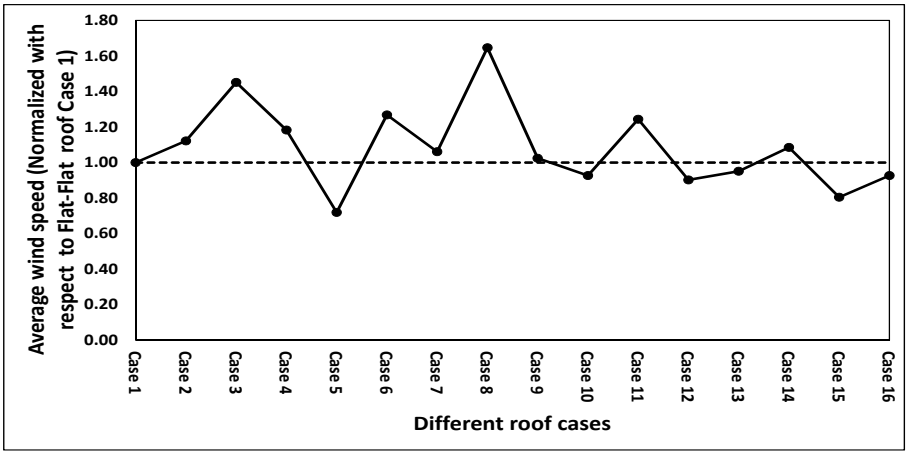

FIGURE 4.33: A ratio of the average wind speed for the different pairs of roof shape to the average wind speed for the flat-flat roof at the pedestrian height of 1.5 m.

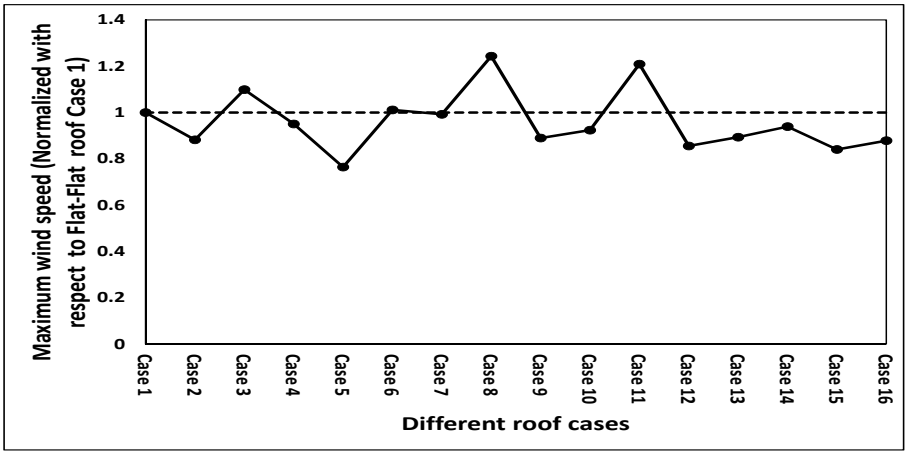

FIGURE 4.34: A ratio of the maximum wind speed for the different pairs of roof shape to the maximum wind speed for the flat-flat roof at the pedestrian height of 1.5 m.

4.4 Summary of Chapter 4

In this study, different roof shapes of both the buildings, only the upstream building and only the downstream building generating the street canyon are used to find the influence of those roof shapes change on the flow structure and pedestrian comfort. Considered wind direction was normal to the street canyon. The results of this study, when compared with the flat-flat roof case, indicate that there is an influence of the roof shape change on the flow field and pedestrian comfort in the street canyon.

For the roof shape change for both buildings and roof shape change for only the upstream building, the flow diverted towards the roof of the upstream building separates due to the leading edge of the building roof in the case of flat, slanted, downwind wedge and upwind wedge. Whereas, it remains attached in the case of vaulted and trapezoidal roof shape. For

the flow structure at the ground level, the separated shear layers due to the sharp leading edge of the sides of the upstream building reattaches on the downstream building in all these cases except for the vaulted-vaulted and vaulted-flat cases. In those cases, the separated shear layers have been observed to be rolled up inside the canyon gap. For the roof shape change for only the downstream building, overall flow structure remains similar to the flat-flat roof. However, in the flat-slanted, flat-vaulted, flat-upwind wedge and flat-trapezoidal cases, a large recirculation was observed on the roof of the downstream building which was not present with the cases with the same roof shapes of the upstream building.

From the analysis of the turbulent kinetic energy using the different vertical and horizontal planes, it was observed that in the cases with flat, downstream wedge and upstream wedge roof shape of the upstream building, due to earlier separation of the flow from the leading sharp edge, generated high turbulent kinetic energy at the leading edge appears dispersed and spreading of it's intensity as the flow goes downstream towards trailing edge of the roof. Hence, in these cases, less entrainment of the fluid occurs into the canyon from the roof level. Whereas, in the case with slanted and trapezoidal roof shapes of the upstream building, delay in the flow separation from the roof, entrains more fluid into the canyon from the roof level. In the case with the vaulted roof of the upstream building, the flow does not separate from the roof and allows less fluid to enter into the street from the roof level compared to the other cases. In the horizontal plane, it was observed that the turbulent kinetic energy was larger at the roof level than near the ground. It was also observed that the separated shear layers due to the sharp leading edges of the sides of the upstream building, reattach on the sides of the downstream building and hence generating more turbulent kinetic energy there, which allows the entrainment of the fluid into the canyon. Hence, inside the canyon, high wind speed regions can be seen near the downstream building.

From the pedestrian comfort assessment study using the different roof shapes, it can be concluded that the pedestrian comfort inside the entire street has been improved compared to the flat-flat case, in the case of slanted and upwind wedge roof shape of both the buildings, upwind wedge roof shape of only the upstream building and for all the cases with roof shapes change for only the downstream building. Pedestrian comfort near the upstream building inside the canyon was improved compared to the flat-flat case, in the cases with an upwind wedge and trapezoidal roof of both the buildings, slanted, upwind wedge and trapezoidal roof of only the upstream building and all the cases with roof shapes change for only the downstream building. Near the downstream building inside the canyon, the pedestrian comfort has been improved compared to the flat-flat case with the upwind wedge-upwind wedge, upwind wedge-flat cases and considered all the cases with the flat roof shape of the upstream building except the flat-downwind wedge case. The best roof shape to improve the overall pedestrian comfort inside the street canyon is the upwind wedge shape when it is used for both buildings or only the upstream building or only the downstream building. The worst roof shapes from this analysis are the vaulted roof shape and downwind wedge roof shape when they are used for both buildings or only the upstream building.

In this study, only the case of street width to building height $S/H = 1$

has been considered. However, in the Chapter 3, it was concluded that building width, street width and building height have a strong influence on the flow structure and pedestrian comfort inside the street canyon. In this study, the roof height was fixed to be 3.4 m for all cases of the different roof shapes. From the literature review, it was observed that changing the roof height also influence the flow structure inside the street canyon and may cause a change in the wind speed at the pedestrian level. Further investigations are expected to focus on these areas. Also, in this study, an upwind wedge roof shape is favourable but only works for one wind direction. A future study should consider the best shape for any wind direction.

It can be concluded from this study that the flow coming into the street canyon from the roof level has a strong influence on the pedestrian comfort. Roof shapes of the building can be altered only in the cases when the buildings are at the construction stage. However, for the already built up buildings, alternative ways need to be found to improve the pedestrian comfort inside such street canyons. In such cases, adding panels on the roof of the upstream building or the downstream building or both may improve the pedestrian comfort.

Chapter 5 describes an in-detail parametric study to analyse the flow structure and pedestrian comfort inside the street canyon with added panels on the roof. Wind analysis of the flow structure and pedestrian comfort inside the street canyon discussed in Chapter 3 and Chapter 4 will be used to evaluate the flow structure in Chapter 5.

Chapter 5

Modifying Flow Structure with Panels

5.1 Introduction

Following significant understanding of the flow structure and pedestrian level wind comfort for the uniform and non-uniform street canyons, and for the street canyons with different pairs of roof shapes, it was decided to expand this study to modify the flow structure by adding panels on the roof (for example, as shown in Figure 5.1) in an attempt to improve the pedestrian level wind comfort. The idea for adding such panels on the building was for modifying the pedestrian comfort by correcting bad wind flow after a building has been built. This is also important, if, for example, a new building makes the flow around an old building suddenly bad. Instead of adding street-level windbreaks, which are always there even when they are not needed, having roof level panels which could be adjusted dynamically in response to the weather conditions.

It was revealed in Chapter 3 using street width as an influencing parameter that, for the uniform street canyon with the flat roof buildings, the pedestrian comfort inside the entire street canon and near the downstream building decreases with increase in the street width. Therefore, before initializing this study, simulations were carried out to find

1. The minimum street width when the pedestrian discomfort inside the street canyon becomes noticeable, and

2. The wind speed at which the pedestrian discomfort inside the street canyon becomes noticeable

After finding the optimum street width with a larger area of pedestrian level wind discomfort, a parametric study was performed to identify the best location of adding the panel on the roof of the building and an angle at which panel should be added. Results analysing the modified flow structure and pedestrian comfort with such panels are as discussed in Section 5.3.

With adding panels on the roof, it is important to measure the drag force on the panels, so that such panels can withstand storm force winds. The drag on the body (panel in our case) is generally measured in the form of a

non-dimensional drag coefficient C_D defined by,

$$C_D = \frac{D}{(1/2)\,\rho\,U^2\,A}$$

where D =drag force, ρ = air density, U = free stream velocity and A = projected frontal area of the body in a plane perpendicular to the wind direction.

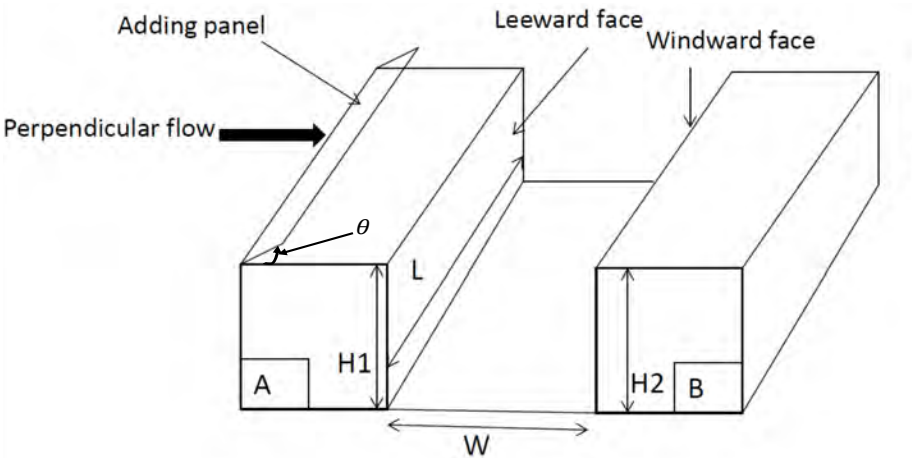

FIGURE 5.1: Panel at the leading edge of the upstream building roof at different angles. Where A in the figure denotes the upstream building and B denotes the downstream building.

No CFD study for finding drag and analysing the flow structure and pedestrian comfort by adding panel on the roof of the buildings, and for a wind direction perpendicular to the street canyon for high Reynolds number (Re) (for Re in the range of $10^6 - 10^7$) has yet been reported in the literature.

5.2 CFD simulations: computational model and parameters for the panel on the roof

The model geometry of the street canyon with adding a panel on the roof of the downstream building as an example, and with dimensions $W \times H \times L = 80\,(m) \times 20\,(m) \times 20\,(m)$ was chosen to represent common medium-rise building structures as shown in Figure 5.2. This also shows the chosen street width $S = 26$ m and the angle, θ of the panel with the roof. Chosen dimensions of the panel were: 80 m long in the Z-direction, 4 m tall in the Y-direction, and 0.2 m thick in the X-direction. Note that, the panel runs along the whole length of the roof (in Z-direction), and there is no gap between the panel and roof. The size of the computational domain was selected according to CFD best practice guidelines by Franke et al. (Franke et al., 2007).

The effect of changing in the angle and location of the panel on the flow pattern and pedestrian comfort inside a street canyon was investigated by performing CFD simulations. Different panel angles considered in this

study were $0°$, $15°$, $30°$, $45°$, $60°$, and $75°$. Note that, open panels were used in the case of $\theta \geq 45°$, whereas, solid panels were used in the case of smaller θ of $15°$ and $30°$, because at these smaller angles inflation layers create highly skewed mesh elements, which require so much of accuracy to resolve. In this study, the solid panel was generated by adding a perpendicular wall from the tip of the panel to the roof of the building, whereas, in the case of open panel no such wall was added. However, before studying these cases for smaller angles with solid panels, the flow study analysis for the solid and open panel at an angle of $45°$ on the leading edge of the upstream building was performed. Comparison for the pressure coefficient (C_p) along the vertical centreline of the windward (front) face, the front face of the panel, the roof of the building, and the leeward (back) face was performed for both studied cases as shown in Figure 5.3. Agreement of approximately 90% in the values of C_p assured the consideration of solid panels at the smaller angles. The Reynolds number (Re) was 1.1×10^7 based on the building height (height of the upstream building $=$ height of the downstream building $=$ building height) and free stream velocity. In this study, a reference wind speed of 8.1 m/s at the building eave height of 20 m was chosen to obtain a wind speed of approximately 4 m/s at a pedestrian height of approximately 1.75 m. The wind direction was perpendicular to the street canyon. The reason for selecting this specific street width and reference wind speed is as discussed in the section 5.3.

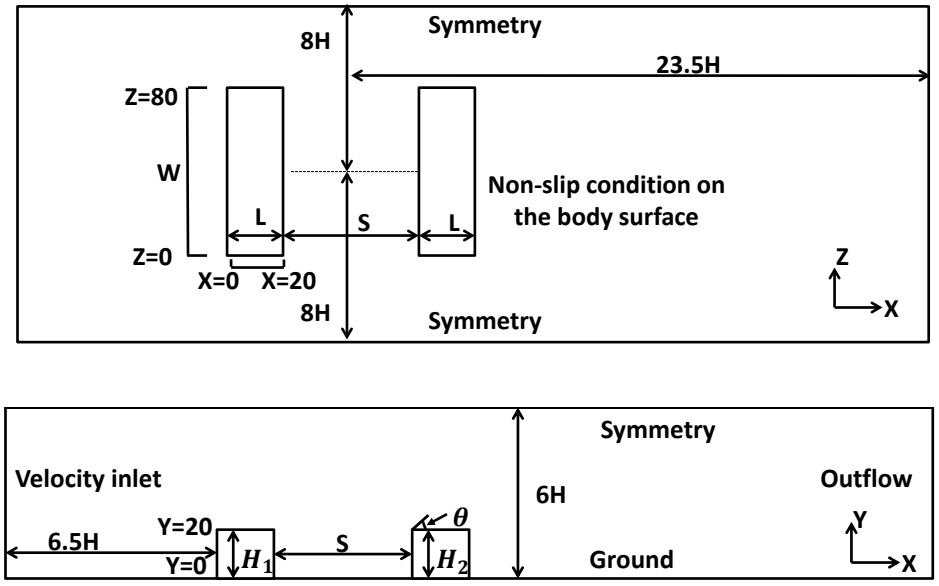

FIGURE 5.2: Computational domain and boundary conditions for adding a panel on the roof of the building (A) plan view (B) Side view.

All the other computational conditions, such as the turbulence model, boundary conditions, wall roughness effect and mesh arrangements were as described in Chapter 3. Due to the increase in the Re in this study compared to the previous Chapters, the height of the first cell of the boundary layer was changed to be 2×10^{-5} m to ensure wall unit $y^+ \approx 1$, to resolve the viscous sublayer of the boundary layer.

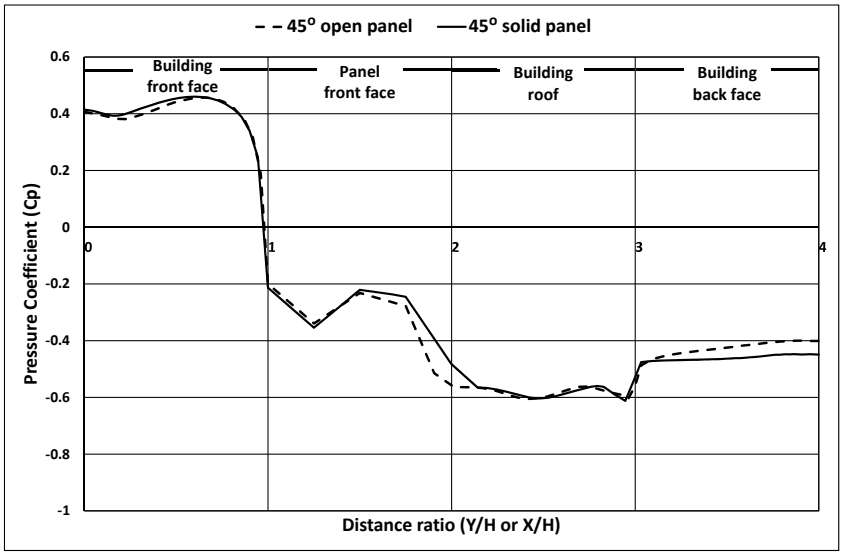

FIGURE 5.3: Pressure coefficient comparison plot for the panel at the leading edge of the upstream building at an angle of 45° for open and solid panels, along with the centre plane of the upstream building.

In this study, to find the drag on the panel, the projected frontal area that the wind sees, was calculated by the following equation and entered as the reference value while running the simulations.

Projected area $=$ height of the panel $(4\,m)$ $\times$lenght of the panel $(80\,m)$ $\times$ sin(θ)

5.3 Results and discussion

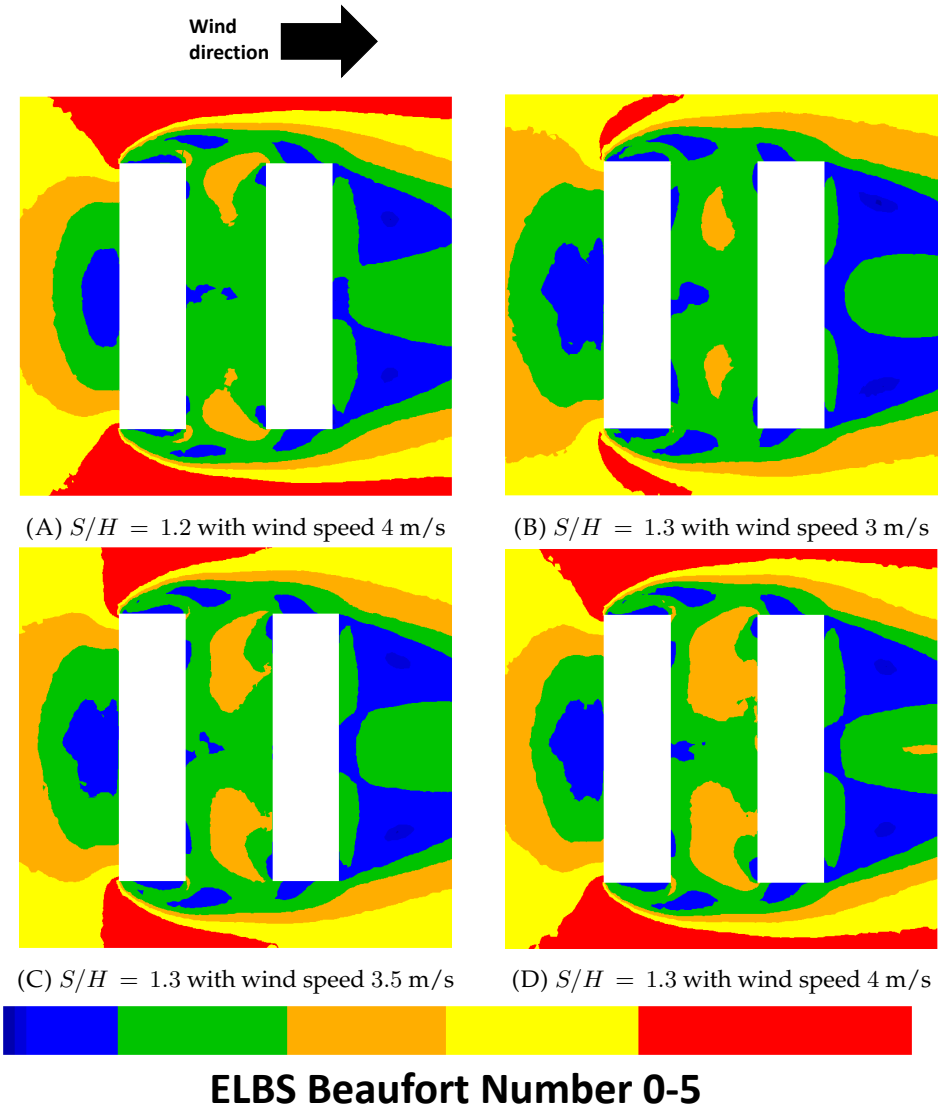

FIGURE 5.4: Wind categories at $Y = 1.5$ m in the XZ- plane for the street canyon for the uniform street canyons with a flat-flat roof (without adding panels) and varying street widths and wind speeds. Here, dark blue represents 0 to 0.1 m/s, on Beaufort Number 0 on ELBS; blue represents 0.2 to 1.0 m/s, on Beaufort Number 1on ELBS; green represents 1.1 to 2.3 m/s, on Beaufort Number 2 on ELBS; orange represents 2.4 to 3.8 m/s, on Beaufort Number 3 on ELBS; yellow represents 3.9 to 5.5 m/s, on Beaufort Number 4 on ELBS; and red represents wind speeds between 5.6 m/s to 7.5 m/s, on Beaufort Number 5 on ELBS.

As specified in the introduction section of this chapter, this study is mainly focused on adding the panel on the roof of the buildings with the flat-flat case to improve the pedestrian level wind comfort (i.e. at the height of $Y = 1.5$ m) inside the street canyon. Therefore, the initial requirement

of this study was to identify the optimum street width when pedestrian discomfort inside the canyon becomes noticeable (specifically the area near the upstream and downstream buildings inside the canyon which would be in frequent use by pedestrians). In Chapter 3, for the selected wind speed of approximately 3 m/s at the pedestrian height, the street width when unfavourable zone for the pedestrians observed noticeable was at $S/H = 1.5$. Such a wide street width could create a large boulevard and existence of such a large street width in cities, specifically in the countries like New Zealand and Australia (terrain type considered for this study) is very rare.

Therefore, a study was initialized by applying different wind speeds in the range of Beaufort Number 3 at the pedestrian height to find the minimum street width when pedestrian discomfort becomes noticeable in the canyon. Simulation results showing wind categories at the height of $Y = 1.5$ m for $S/H = 1.2$ for wind speed of 4 m/s, and for $S/H = 1.3$ for wind speed of 3, 3.5 and 4 m/s are as shown in Figure 5.4. It can be clearly seen from this contour plot that with the wind speed of 4 m/s at a pedestrian height of approximately 1.75 m and for $S/H = 1.3$, about 50% area inside the canyon gap can be seen to be in the unfavourable zone for pedestrians. Hence this case was used for the further investigation of adding a panel at different locations on the roof of the upstream building and on the leading edge of the downstream building.

5.3.1 Panel on the front edge of the upstream building roof

Flow structure

TABLE 5.1: Comparison of the drag coefficient (C_D) for the panel at the leading edge of the upstream building roof at different angles with the C_D of an isolated inclined flat plate .

angles	C_D	C_D on inclined flat plate
15° solid	−0.17	0.33
30° solid	−0.13	0.64
45° solid	0.35	0.90
45° open	0.32	0.90
60° open	0.66	1.11
75° open	0.72	1.24

In this subsection, the effect of adding a panel at the leading edge of the upstream building roof as shown in Figure 5.1 has been analysed. Considered panel angles for this analysis were 15°, 30°, 45°, 60°, and 75°. Results for the measured drag coefficient (C_D) for the panel on the roof of the upstream building at different angles and their comparison with an isolated inclined flat plate at the corresponding angle are as shown in Table 5.1 and Figure 5.5, respectively. It can be seen from the C_p contour plot for flat roof case and with the panel at angles of 15° and 30° that, the separation of the flow at the leading edge of the upstream building causes a high negative pressure which shows as a minimum C_p region. An added panel at such small angles has no effect on the flow separation at the leading edge of the

roof. The pressure increases towards the trailing edge of the roof and recovers to nearly zero pressure which suggests the flow may reattach on the top surface. At the small angles, up to 30° no drastic variation in the C_p has been observed. As specified in Holmes (2015), the drag force on the body is the combined effect of the average pressure on the front (windward) and rear (leeward) faces and the shear stress (which is minor compared to the pressure drag for a bluff body like these panels). This in our case will be the combined effect of the average pressure on the windward and leeward face of the panel. From the C_p plot, it can be observed that the windward wall pressure and hence C_p varies considerably with the position on the front face for the angles $> 30^\circ$. The leeward pressure, however, is nearly uniform over the whole rear face, as this region is totally exposed to the wake region, with relatively slow moving air. For this larger angles ($\theta > 30^\circ$), minimum C_p occurs near the top corner of the panel, which indicates separation at this point. For all studied cases, the high pressure on the windward face compared to the leeward face of the panel was observed. This variation in the C_p also causes an increase in the C_D, which can be clearly observed from Table 5.1. No drastic difference in the value of C_D was observed in the case with the open and solid panel at an angle of 45°.

Note here that, the aerodynamic forces on such panels are similar to thin, flat plate. For a thin flat plate at a low angle of attack the drag coefficient, C_D is equal to 1.28 times the trigonometric $\sin$ of the angle θ ($C_D = 1.28 \times \sin(\theta)$) (From theory used in aeronautics). Calculations for the C_D for the considered angle of attack using this formula for a flat plate has been done and tabulated in column three of Table 5.1. It can be seen that these calculated values of C_D for the thin flat plate using above-specified formula is higher in magnitude. This may be due to the fact that, this formula is based on the theoretical assumption for the isolated flat plate. In this study, panels are attached at the leading edge of the upstream building roof. So, the drag force on such panels is the combined effect of the drag on the building front face and drag on the panel. For the attached panels at the smaller angles on the roof, as specified above the stream which deviates towards the roof of the building separates at the leading edge of the roof creating high negative pressure and hence the C_D for the panels inclined at the smaller angles ($\theta \leq 30$) on the roof is negative. For the higher angles, the flow stream deviated towards the roof of the upstream building separates near the top of the panel front face which creates negative pressure on the panel front and hence for the panels at higher inclination angles ($\theta \geq 45$) the drag coefficient is low compared to the measured value for the isolated flat plate.

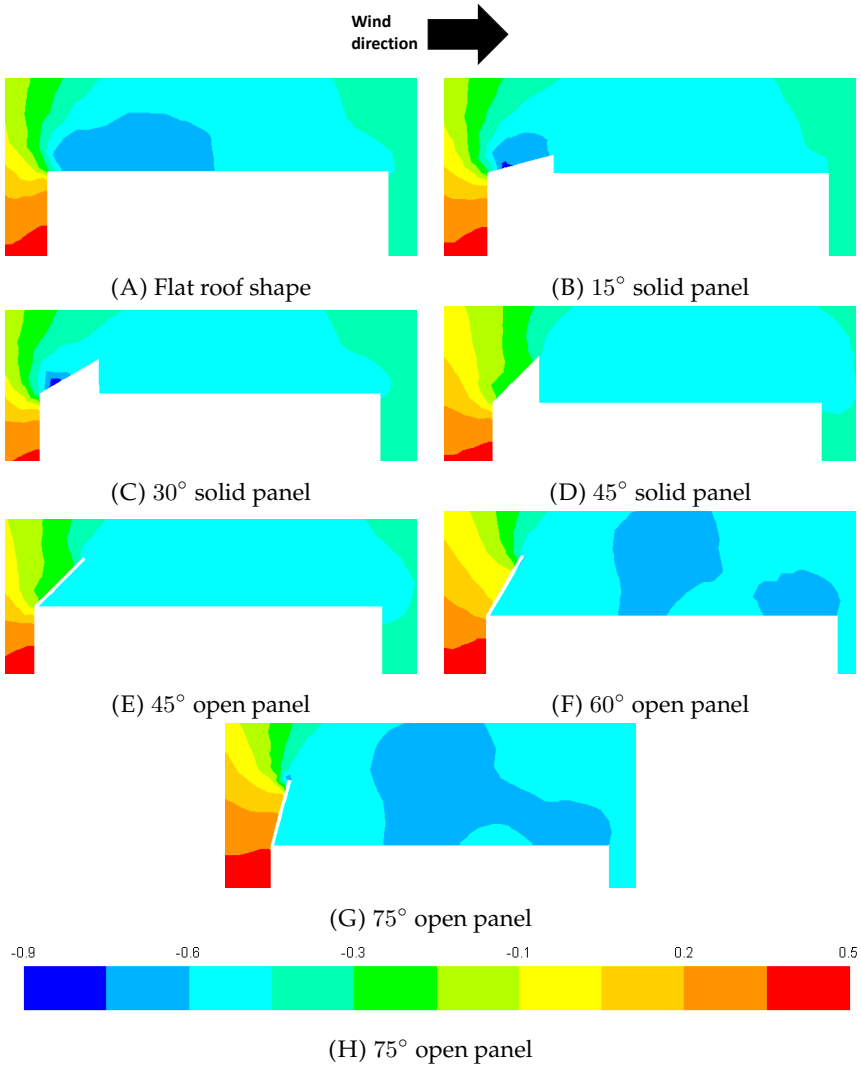

FIGURE 5.5: C_p on the roof of the upstream building in theXY- plane at the centre plane ($Z = 40$) for the street canyon with panel at the leading edge of the upstream building roof.

Figure 5.6 shows velocity magnitude pathlines in the centre plane for the considered cases in this subsection. The flow structure in the case of the flat-flat roof and with $S/H = 1.3$ is similar to as described in subsection 3.3.1 of Chapter 3. These include separation of the flow due to the leading edge of the upstream building roof, reattachment of the separated shear layer on the same roof, back-flow from the canyon into the roof region of the upstream building resulting in a secondary recirculation region at the trailing edge of the upstream building roof, separation of the flow due to the sharp leading edge of the sides of the upstream building and reattachment of these shear layers on the downstream building sides (Figures 5.10(A)). The flow in the canyon can be characterized by a strong fluid stream directed upward and towards the windward face of the downstream building. An isometric view of the streamlines coloured by the magnitude of turbulent kinetic energy (k) for the case of the flat-flat roof for $S/H = 1.3$, as shown in Figure 5.7, clearly shows above described flow structure in the

different vertical plane.

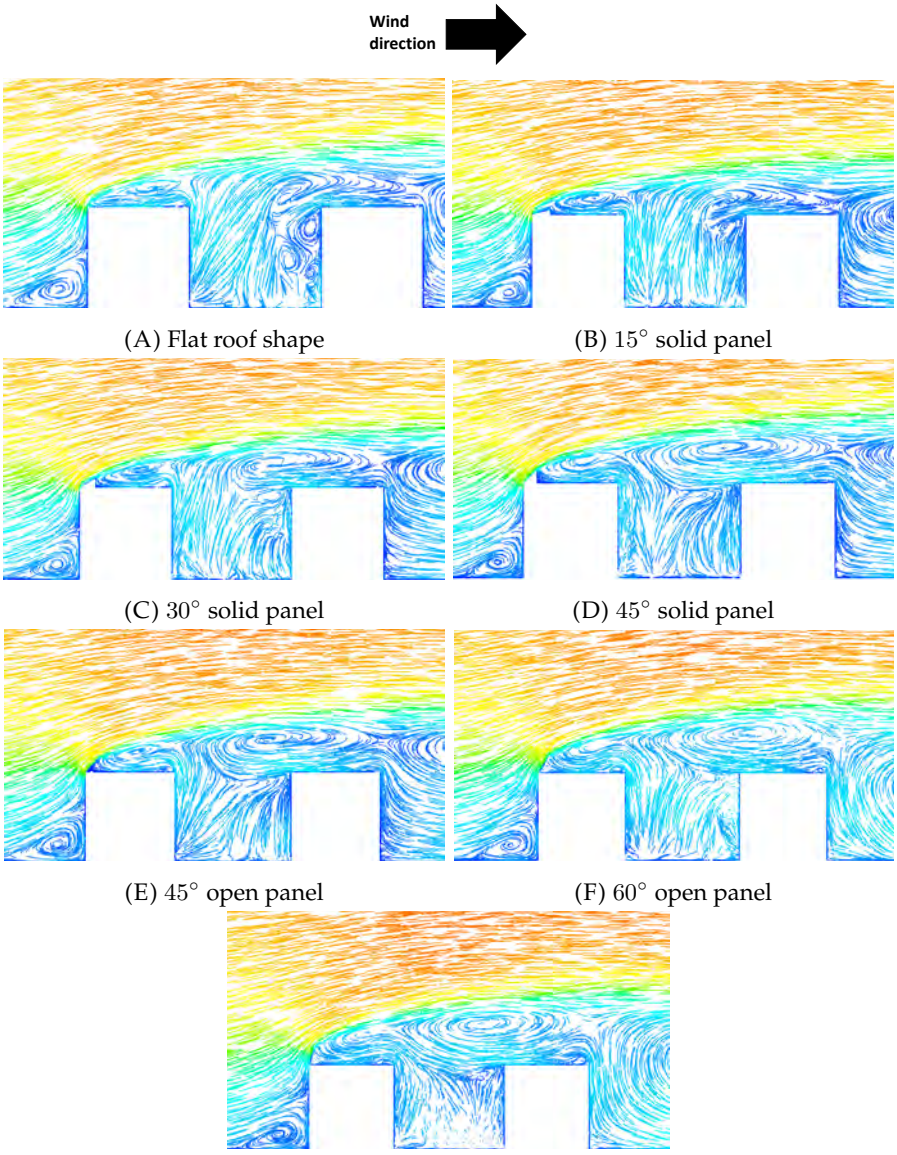

(A) Flat roof shape (B) 15° solid panel

(C) 30° solid panel (D) 45° solid panel

(E) 45° open panel (F) 60° open panel

(G) 75° open panel

FIGURE 5.6: Velocity magnitude pathlines in XY- plane at the centre plane ($Z = 40$) for the street canyon with a panel at the leading edge of the upstream building roof.

For the cases when the panel was added at angles of 15° and 30°, the observed flow patterns before the upstream building, on the roof of the upstream building, on the sides of the upstream building, and inside the street canyon were almost identical to the flat-flat case. However, in the case of a panel at an angle of 30° in the vertical centre plane (Figure 5.6(C)), a large recirculation can be observed on the roof of the downstream building, which was not present in the flat-flat case and with a panel at an angle of 15°.

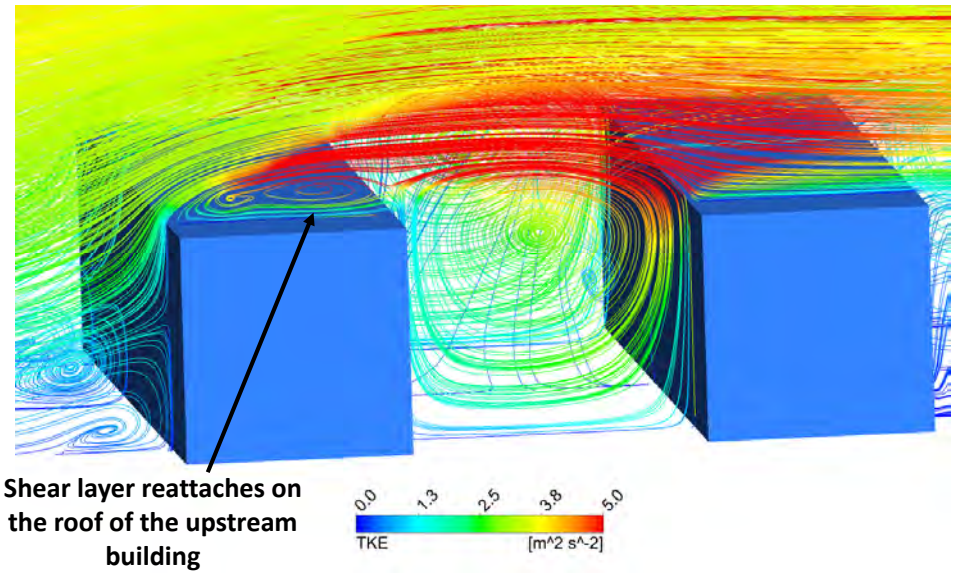

FIGURE 5.7: Isometric view of the streamlines coloured by the magnitude of turbulent kinetic energy (k) around and inside the street canyon with the flat-flat roof buildings and with the street aspect ratio $S/H = 1.3$.

However, for the cases, when the panel was added at angles $> 30°$, it was observed that the shear layer separated from the roof of the upstream building impinges on the downstream building roof near the leading edge. This can be clearly seen from the isometric view of the streamlines coloured by the magnitude of turbulent kinetic energy (k) for the panel at angles of $45°$ and $75°$ as shown in Figure 5.8 and 5.9, respectively. This kind of flow behaviour is analogous to the bistable regime as described by Martinuzzi et al. (2000) in the introduction section of Chapter 3. In centre plane, a large recirculation over the roof of the downstream building extending towards the upstream building can be observed for all the cases with panel angles $> 30°$ (Figures 5.6(D)-5.6(G)). Most of the flow from the roof of the upstream building moves towards the roof of the downstream building in these cases. This is the clear evidence of the fact that, in the flat-flat case and with the panel added at angles of $15°$ and $30°$, the flow entering into the canyon from the roof level has more kinetic energy and larger wind speed compared to the panel at angles $> 30°$. Therefore, the flow entering into the canyon from the roof reaches up to the ground level, where it loses turbulent kinetic energy and then recirculates. Whereas, in the cases with panels at angles, $> 30°$, the flow entering from the roof level has low turbulent kinetic energy (k) and low wind speed compared to smaller angles, and it does not reach down to the ground level and recirculates at about roof level in the canyon. This flow characteristic in the canyon can be clearly observed from the isometric views of the k-profiles, Figures 5.7, 5.8 and 5.9 for the flat-flat case, and panel at angles of $45°$ and $75°$ respectively.

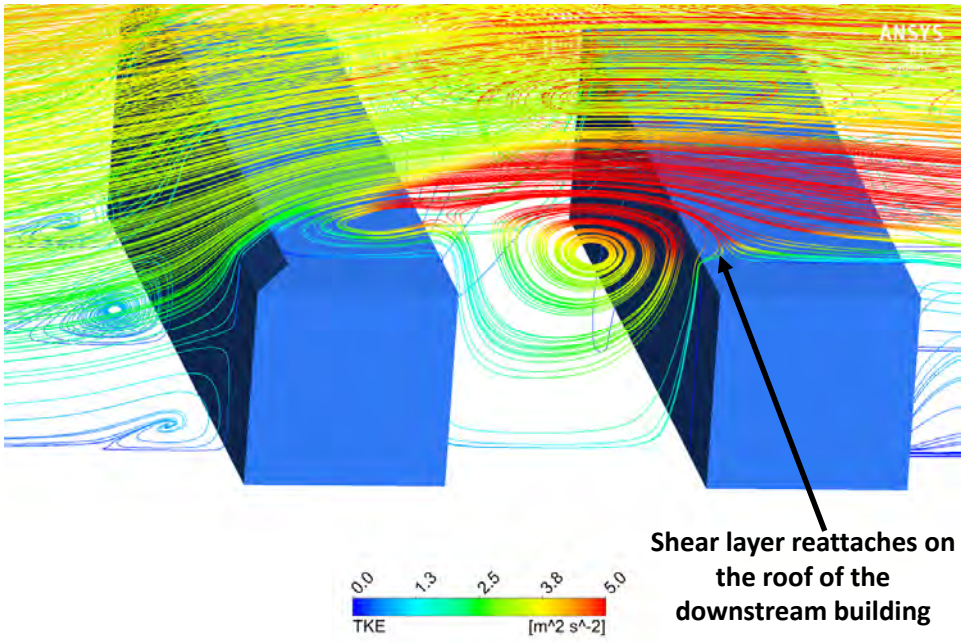

FIGURE 5.8: Isometric view of the streamlines coloured by the magnitude of turbulent kinetic energy (k) around and inside the street canyon with a panel at the leading edge of the upstream building roof at an angle of $45°$.

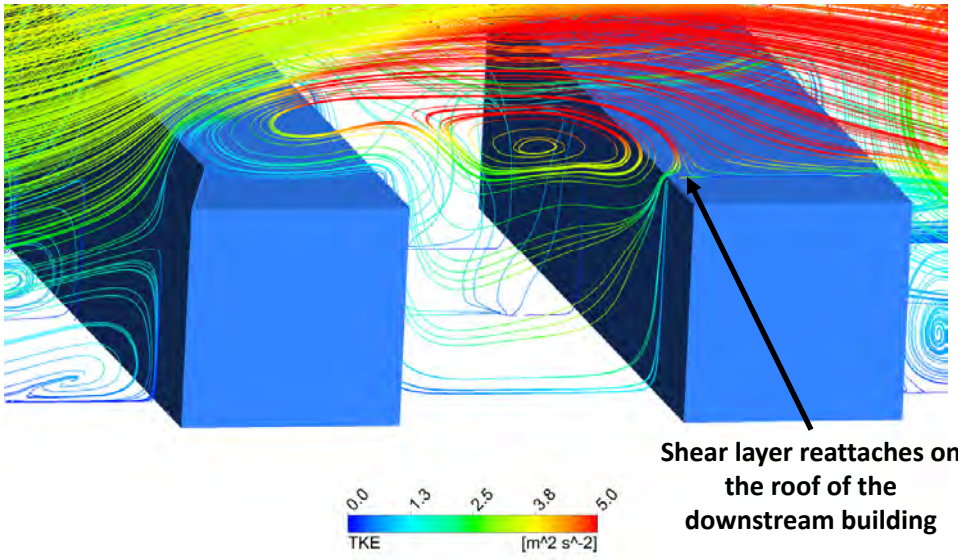

FIGURE 5.9: Isometric view of the streamlines coloured by the magnitude of turbulent kinetic energy (k) around and inside the street canyon with a panel at the leading edge of the upstream building roof at an angle of $75°$.

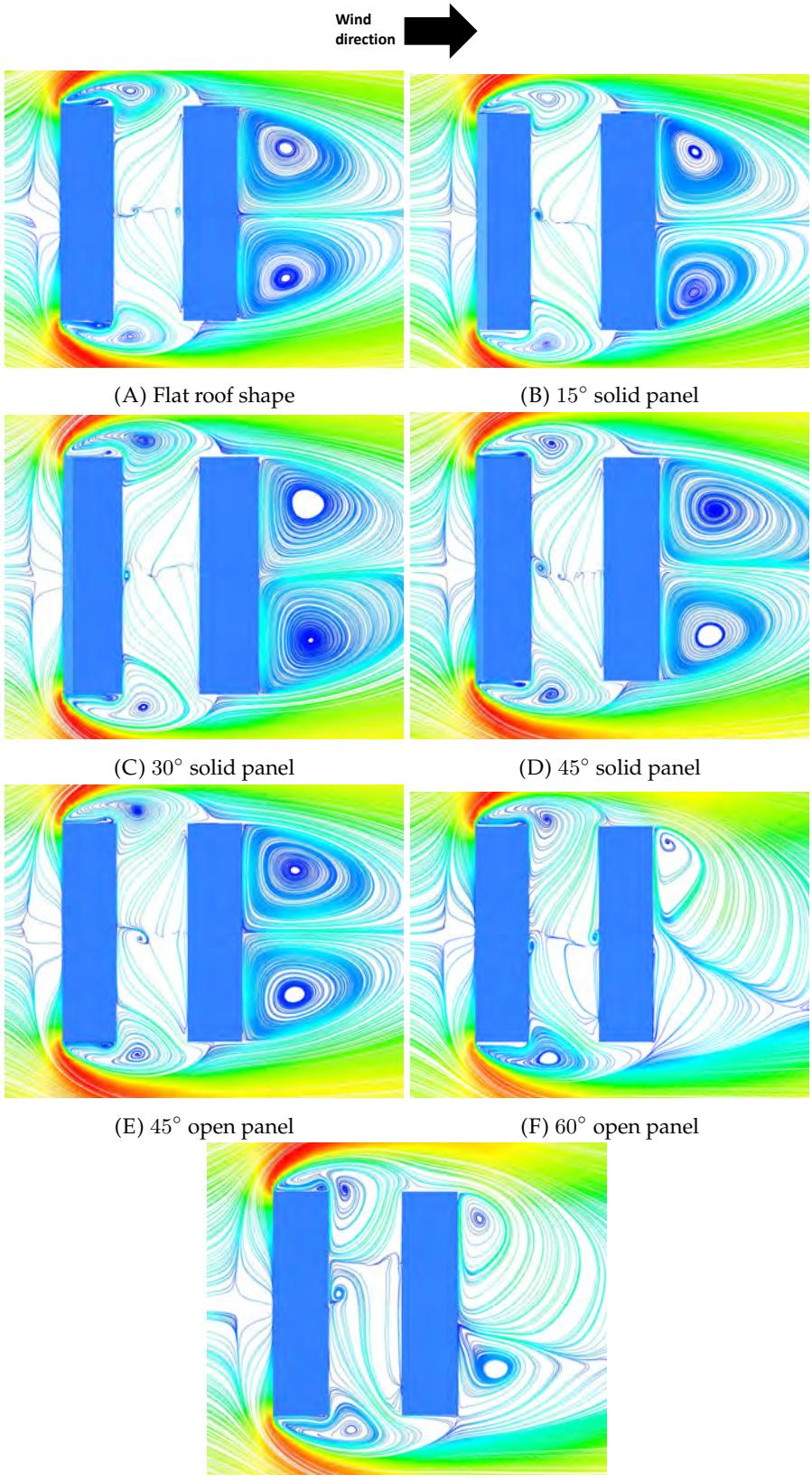

(A) Flat roof shape

(B) 15° solid panel

(C) 30° solid panel

(D) 45° solid panel

(E) 45° open panel

(F) 60° open panel

(G) 75° open panel

FIGURE 5.10: Velocity magnitude streamlines (cut plane to zoom near the street canyon) in the XZ- plane at $Y = 1.5$ m level for the street canyon with a panel at the leading edge of the upstream building roof. For all these cases separated shear layers from the sides of the upstream building reattach on the sides of the downstream building.

Turning now to the flow streams which deviates towards the side faces of the upstream building in the cases with a panel at angles $> 30^{\circ}$ (Figure 5.10), these separate due to the leading sharp edges giving rise to intense corner vortices. These separated shear layers reattaches on the sides of the downstream building for all these cases. However, in the cases with a panel at angles of 60° and 75°, the vortex structure behind the second building is different then all the other cases compared here. The vortices in the wake of the downstream building for these higher angles are unsynchronized. An experimental study by Martinuzzi et al. (2000), who analysed the flow structure around two surface mounted cubes observed such unsynchronized region behind the wake of the second building when the reattachment of the separated shear layer from the top of the upstream cube occurred on the top of the downstream building. They revealed the reason for that unsynchronized vortices is due to the vortex shedding in the wake of the downstream building. A detailed discussion about their results is as specified in the introduction section of Chapter 3. For the flat-flat case and with panels at lower angles studied here, this separated shear layer from the roof of the upstream building reattaches on the same surface and hence it would be expected to see vortex shedding inside the canyon gap as well as in the wake of the downstream building. Hence the combined effect of in-canyon vortices and those after the downstream building is completely synchronized for the lower angles (Martinuzzi et al., 2000). Whereas, for the panels at the larger angles, the reattachment of that separated shear layer from the roof of the upstream building on the roof of the downstream building could be the reason for the vortex shedding behind the downstream building. However, transient simulations are required to prove this periodicity of the flow in these cases.

Pedestrian level wind categorisation

For the pedestrian level wind categorisation, Figures 5.11 and 5.12 show contour plots of ELBS Beaufort Number at a height of 1.5 m around and inside the street canyon for the studied cases in this subsection. The height of 1.5 m was chosen as a representative height in between the standing and seated head height of a person, as mentioned in the earlier chapters. For the flat-flat case with $S/H = 1.3$, as shown in Figure 5.11(A), approximately 50% of the entire region inside the street canyon and about 35% of the region near the downstream building have wind speed between 2.4 to 3.8 m/s (Beaufort Number 3). This high wind speed can cause discomfort for pedestrians in this region, specifically the region near the downstream building which would be in frequent use by pedestrians. We assess the impact of adding panels on the leading edge of the upstream building at different angles, on the pedestrian comfort by comparing the results below with this flat-flat case, for which a large area of discomfort has been observed.

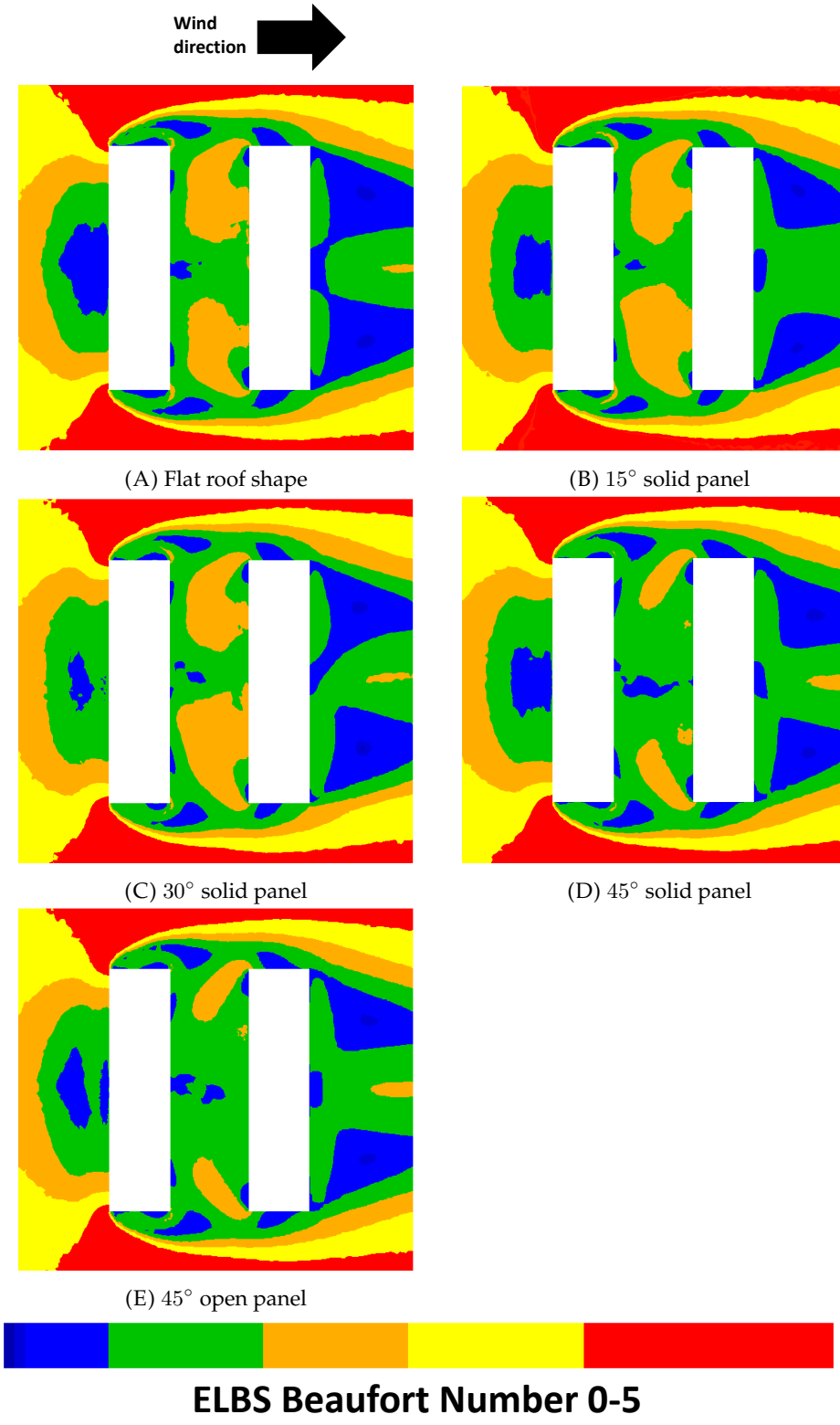

FIGURE 5.11: Wind categories at $Y = 1.5$ m in the XZ-plane for the street canyon with a panel at the leading edge of the upstream building roof. Colours as in Figure 5.4.

For the cases with a panel at angles of 15° and 30°, the observed wind

speed contours are similar to that of the flat-flat case. This is probably due to the fact that, the flow structure in these cases remains similar to the flat-flat case as discussed in the above flow description. An overall decrease in the wind speed for the entire street canyon and near the downstream building is observed in the case with panel added at an angle of $45°$, compared to the flat-flat case. No drastic change in the wind speed contour has been observed for the cases with the solid panel and open panel at $45°$. For the panels at larger angles ($60°$ and $75°$), an overall decrease in the wind speed has been observed compared to the flat-flat case. However, for such larger angles, high wind speed regions can be seen in the wake of the downstream building.

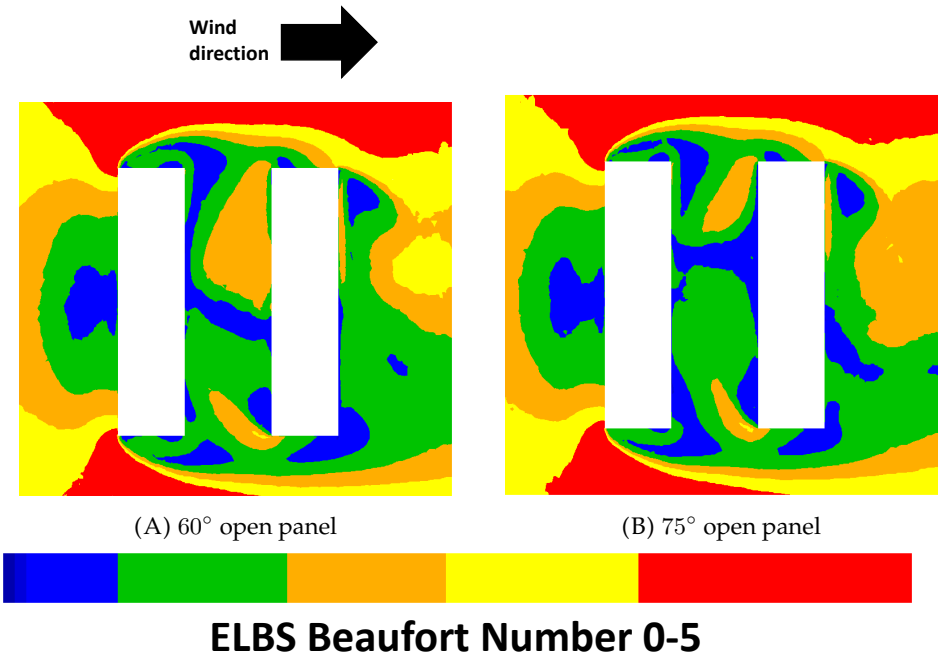

(A) $60°$ open panel (B) $75°$ open panel

FIGURE 5.12: Wind categories at $Y = 1.5$ m in the XZ-plane for the street canyon with a panel at the leading edge of the upstream building roof. Colours as in Figure 5.4.

In general, for adding a panel on the leading edge of the upstream building, for the angles, $\geq 45°$, the wind speed inside the entire street canyon is less compared to that of the flat-flat case and those with smaller angles ($< 45°$). The reason for this is, as specified in the above discussion of the flow structure, that for the larger angles, most of the flow from the roof of the upstream building moves on the roof of the downstream building. Hence the flow entering into the canyon in these cases has low turbulent kinetic energy and hence lower wind speed compared to the flat-flat case and those with smaller angles.

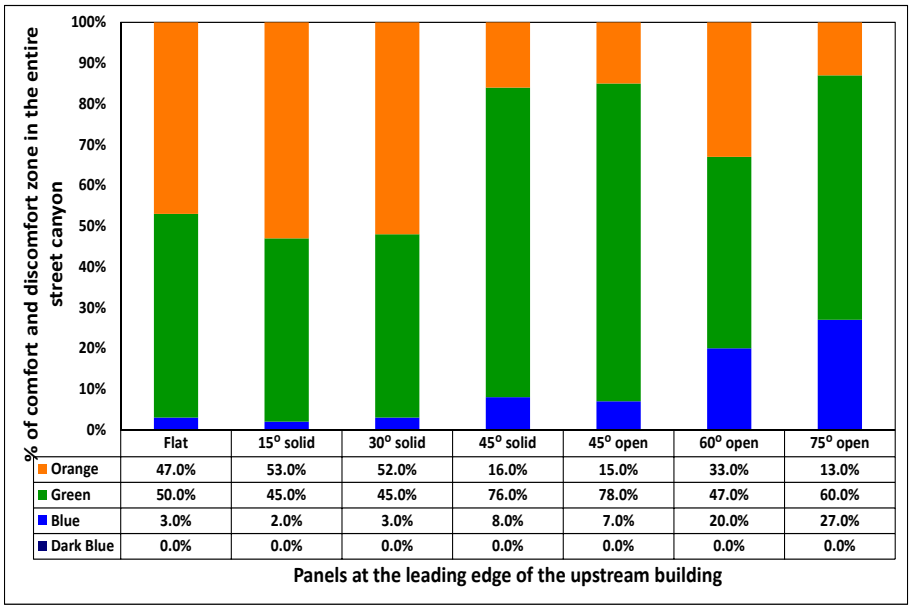

	Flat	15° solid	30° solid	45° solid	45° open	60° open	75° open
Orange	47.0%	53.0%	52.0%	16.0%	15.0%	33.0%	13.0%
Green	50.0%	45.0%	45.0%	76.0%	78.0%	47.0%	60.0%
Blue	3.0%	2.0%	3.0%	8.0%	7.0%	20.0%	27.0%
Dark Blue	0.0%	0.0%	0.0%	0.0%	0.0%	0.0%	0.0%

FIGURE 5.13: Comparison of the increase or decrease of comfort and discomfort zone with panels at the leading edge of the upstream building roof compared to the flat-flat case inside the entire street canyon using the percentage stack chart. Colours as in Figure 5.4.

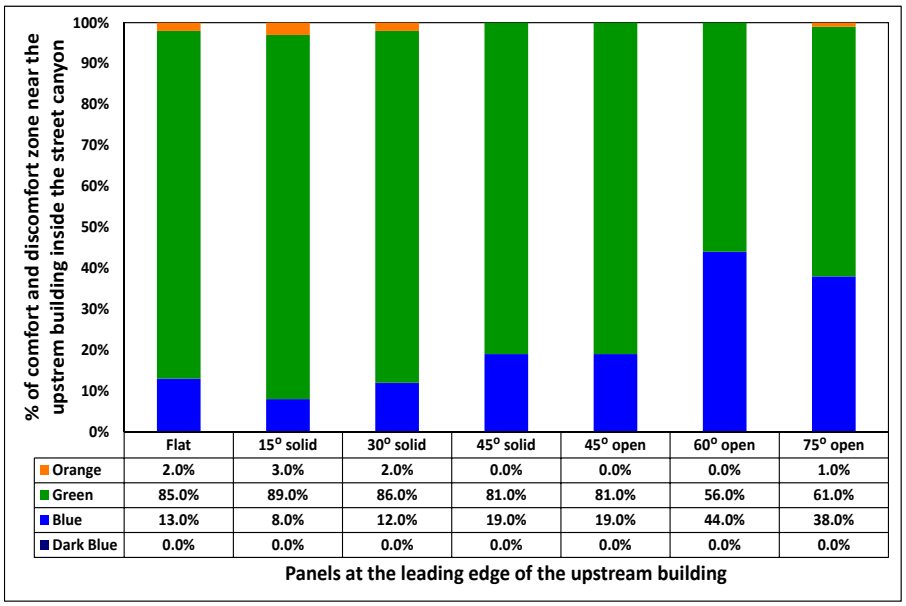

	Flat	15° solid	30° solid	45° solid	45° open	60° open	75° open
Orange	2.0%	3.0%	2.0%	0.0%	0.0%	0.0%	1.0%
Green	85.0%	89.0%	86.0%	81.0%	81.0%	56.0%	61.0%
Blue	13.0%	8.0%	12.0%	19.0%	19.0%	44.0%	38.0%
Dark Blue	0.0%	0.0%	0.0%	0.0%	0.0%	0.0%	0.0%

FIGURE 5.14: Comparison of the increase or decrease of comfort and discomfort zone with panels at the leading edge of the upstream building roof compared to the flat-flat case near the upstream building for 3 m distance in the X-direction and 80 m distance in the Z-direction at $Y = 1.5$ m height using the percentage stack chart. Colours as in Figure 5.4.

Analysis of the percentage of different pedestrian wind comfort zones

(similar to Chapter 4) according to ELBS and the percentage of increase or decrease in particular zone compared to the flat-flat case for the entire street canyon, is as shown in **??**. Pedestrian wind categorisation was also carried for the distance of 3 m in the X-direction and a distance of 80 m in the Z-direction adjacent to the upstream building (the "upstream pavement", as shown in **??**) and to the downstream building (the "downstream pavement", as shown in **??**).

Figure 5.13 shows a stack plot representation and data table for the percentage of the entire canyon taken up by different Beaufort Number zones at a height of 1.5 m. This plot also represents the percentage of increase or decrease in a particular zone inside the entire street canyon with respect to the flat-flat case. The data clearly indicates that at the height of 1.5 m the wind speed inside the entire street canyon decreases in the case with adding a panel at angles $\geq 45°$.

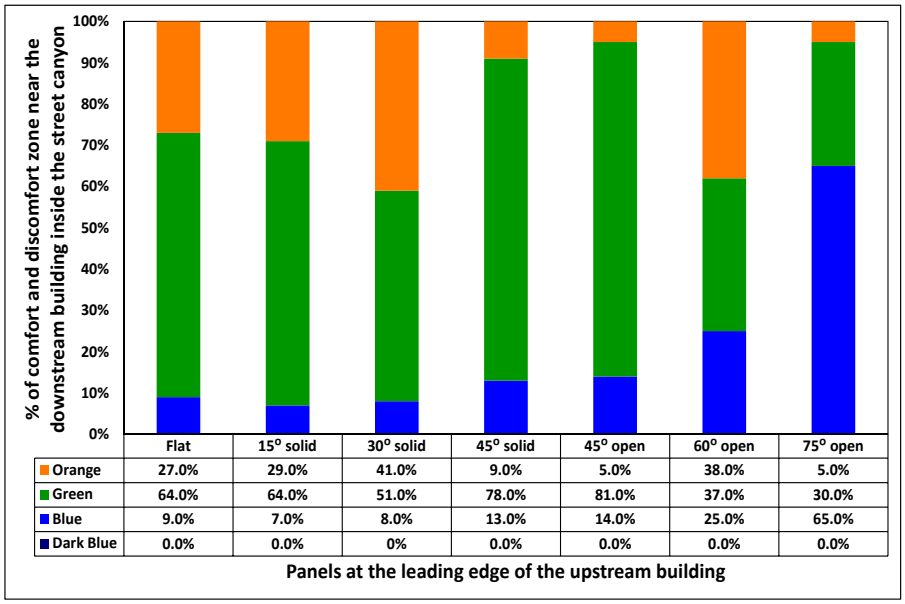

	Flat	15° solid	30° solid	45° solid	45° open	60° open	75° open
Orange	27.0%	29.0%	41.0%	9.0%	5.0%	38.0%	5.0%
Green	64.0%	64.0%	51.0%	78.0%	81.0%	37.0%	30.0%
Blue	9.0%	7.0%	8.0%	13.0%	14.0%	25.0%	65.0%
Dark Blue	0.0%	0.0%	0%	0.0%	0.0%	0.0%	0.0%

FIGURE 5.15: Comparison of the increase or decrease of comfort and discomfort zone with panels at the leading edge of the upstream building roof compared to the flat-flat case near the downstream building for 3 m distance in the X-direction and 80 m distance in the Z-direction at $Y = 1.5$ m height using the percentage stack chart. Colours as in Figure 5.4.

For the wind speed assessment area near the upstream building as shown in Figure 5.14, it can be seen that an overall reduction in the wind speed compared to the flat-flat case can be seen for all the cases with adding a panel at angles $\geq 45°$.

Figure 5.15 shows the data table and wind speed assessment stack chart near the downstream building and comparison of the obtained results with the flat-flat case. Overall improvement in the wind speed can be seen in the cases with panels at an angle of $45°$, $60°$, and $75°$. However, the discomfort zone has observed to increase in case of $60°$ compared to that of the flat-flat

case. A large area of discomfort can also be observed in case of the panel at an angle of 30° compared to that of the flat-flat case.

From the above-detailed analysis of the pedestrian comfort for the considered cases of adding a panel on the leading edge of the upstream building roof at different angles shows that the panel at an angle of 45° improves the pedestrian comfort inside the entire street canyon as well as near the upstream and downstream building.

5.3.2 Panel on the centre plane of the upstream building roof

Flow structure

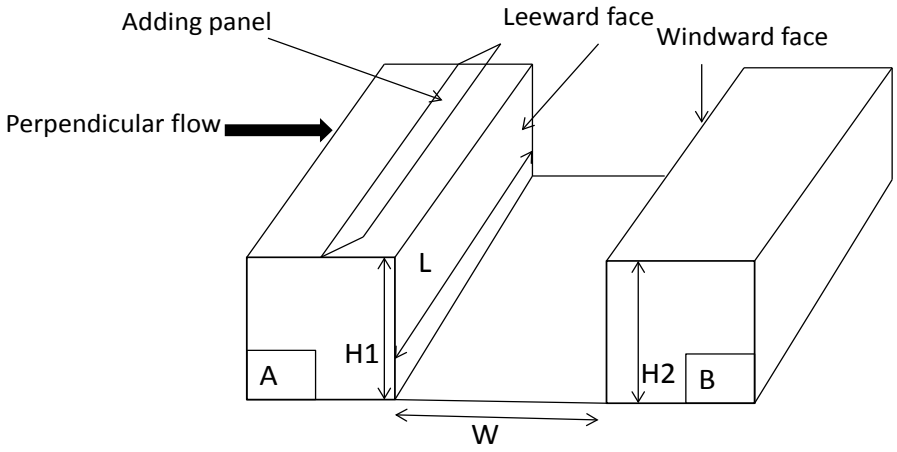

FIGURE 5.16: Panel at the centre plane of the upstream building roof at different angles. Where A in the figure denotes the upstream building and B denotes the downstream building.

TABLE 5.2: C_D for the panel at the centre plane of the upstream building roof at different angles.

angles	C_D
45° open	-0.12
60° open	-0.10

In this subsection, we explore the effect of adding a panel at the centre plane of the roof of the upstream building as shown in Figure 5.16. Considered panel angles for this study were 45° and 60°. These two angles were chosen for this analysis, because they were found to be the effective angles showing the impact on the flow structure and hence on the pedestrian wind comfort, in the previous case of the panel at the leading edge of the upstream building. Results for the measured C_D on the panel and C_p on the roof of the upstream building for the studied cases are as shown in Table 5.2 and Figure 5.17, respectively. Figure 5.18 shows the velocity magnitude pathlines in the centre plane for the considered cases. At angles of 45° and 60°, the separated shear layer from the leading edge of the upstream building

roof reattaches on the panel's windward face, as seen in Figure 5.18(B) and 5.18(C). This reattachment causes high negative pressure on the front face of the panel. This clearly indicates a minimum C_P in this region for both considered cases. As specified in above subsection, the drag force on the panel is the combined effect of average pressure on the windward and rear faces, we observed high negative pressure on the windward face compared to the leeward face of the panel for both angles. Hence the combined effect causes negative drag on the panel. This can be clearly seen from Table 5.2.

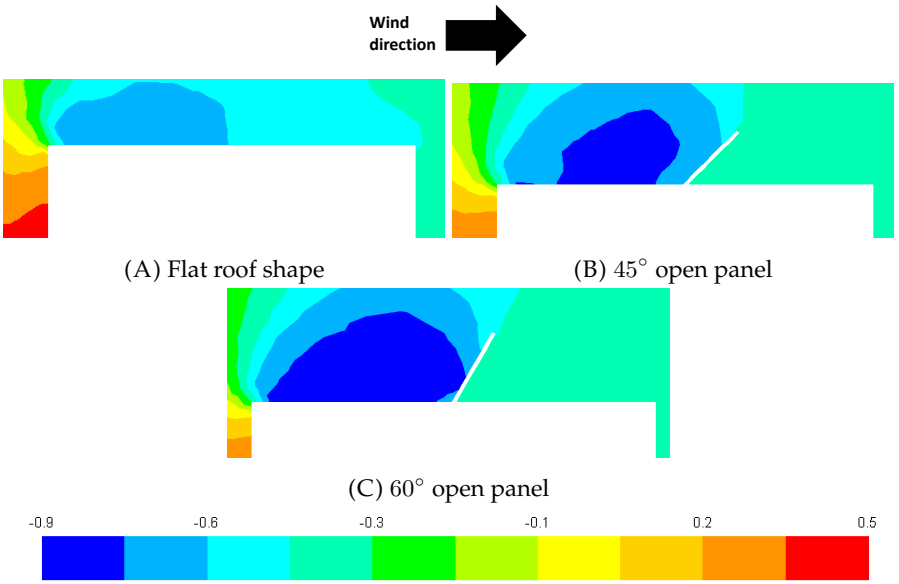

FIGURE 5.17: C_p on the roof of the upstream building in the XY- plane at the centre plane ($Z = 40$) for the street canyon with a panel at the centre of the upstream building roof.

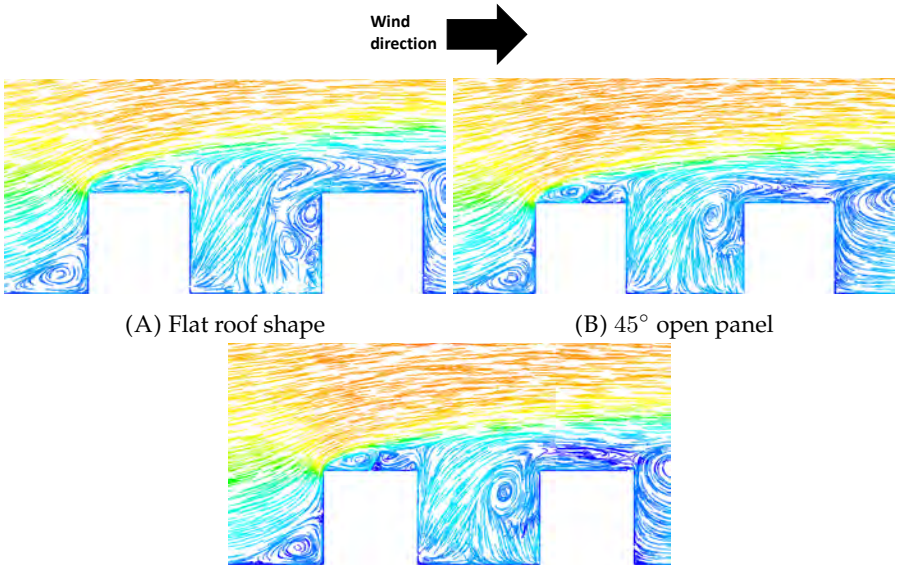

(A) Flat roof shape (B) 45° open panel

(C) 60° open panel

FIGURE 5.18: Velocity magnitude pathlines in the XY-plane at the centre plane ($Z = 40$) for the street canyon with a panel at the centre plane of the upstream building roof.

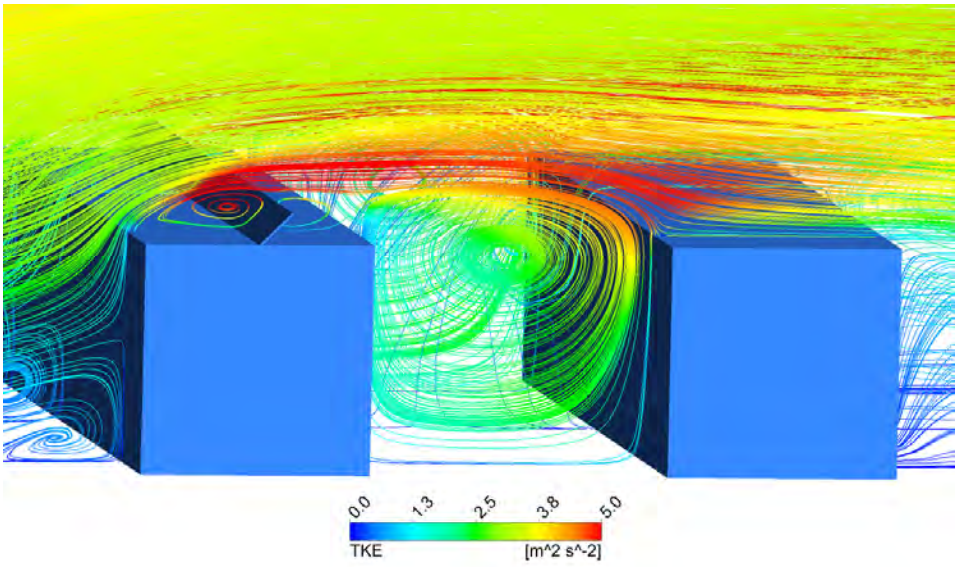

FIGURE 5.19: Isometric view of the streamlines coloured by the magnitude of turbulent kinetic energy (k) around and inside the street canyon with a panel at the centre of the upstream building roof at an angle of 45°.

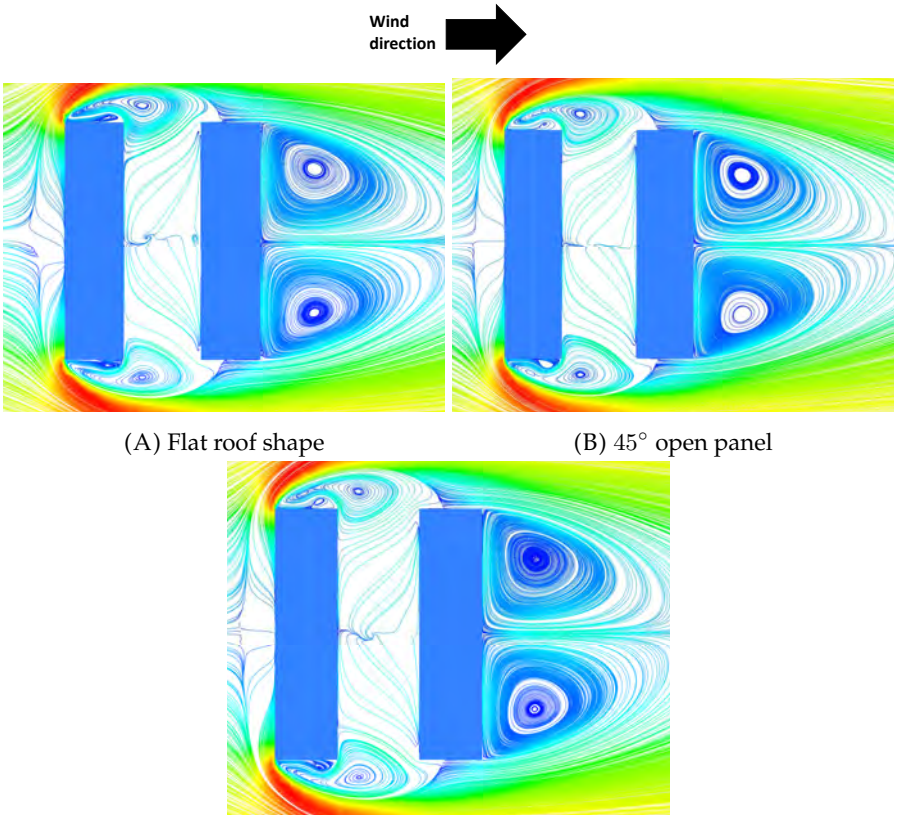

(A) Flat roof shape (B) 45° open panel

(C) 60° open panel

FIGURE 5.20: Velocity magnitude streamlines (cut plane to zoom near the street canyon) in the XZ- plane at $Y = 1.5$ m level for the street canyon with a panel at the centre plane of the upstream building roof. For all these cases separated shear layers from the sides of the upstream building reattach on the sides of the downstream building.

Figure 5.20 shows velocity magnitude streamlines at a pedestrian height of 1.5 m. No drastic change in the flow structure at this level has been observed when compared with the flat-flat case.

Variation in the flow structure inside the canyon compared to the flat-flat case has been observed for both cases. Earlier reattachment of the flow on the roof of the upstream building causes a reduction in k-profile and hence the flow entering into the canyon from the roof level has low wind speed. This can be clearly seen, when k-profile of the flat-flat roof (Figure 5.7) compared with the panel added at an angle of 45° (Figure 5.19). Due to the panel, at these higher angles, most of the flow from the roof of the upstream building displaces towards the roof of the downstream building.

Pedestrian level wind categorisation

Figure 5.21 shows pedestrian level wind categories using contour plots of ELBS Beaufort Number at a height of 1.5 m around and inside the street canyon for cases with panels at the centre plane. The obtained results for

the considered cases were compared with the flat-flat case. No drastic improvement in the wind speed and hence pedestrian comfort has been observed in the entire street for both studied cases when compared to the flat-flat case. However, the area near the downstream building inside the canyon shows a reduction of wind speed compared to the flat-flat case.

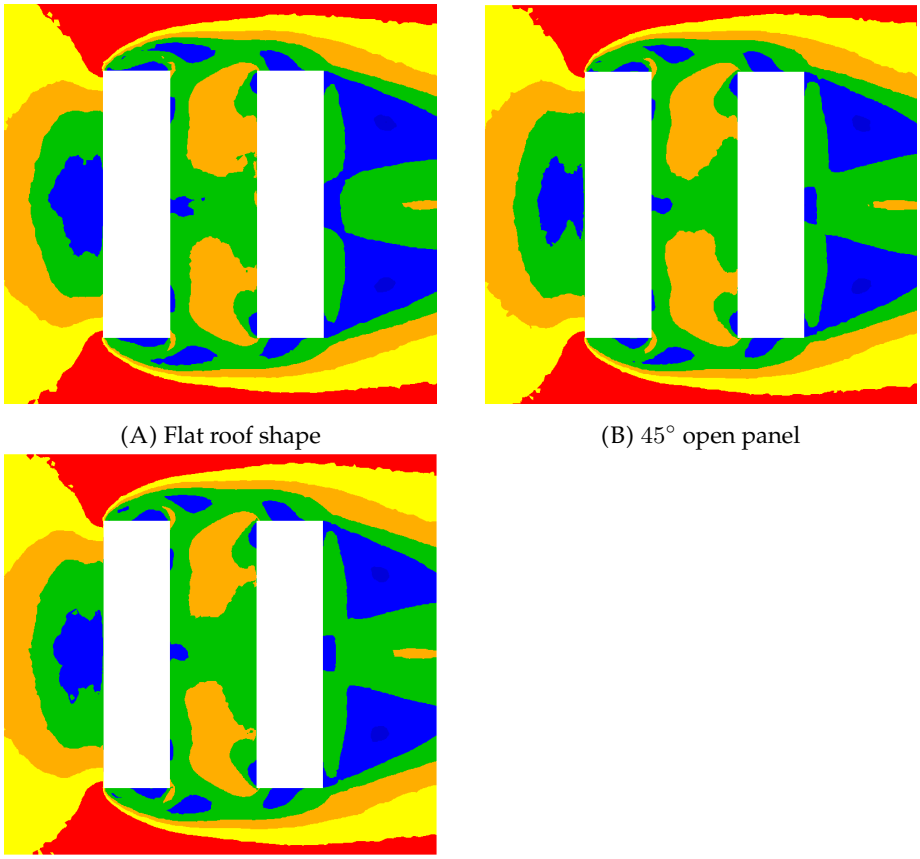

(A) Flat roof shape

(B) 45° open panel

(C) 60° open panel

FIGURE 5.21: Wind categories at $Y = 1.5$ m in the XZ-plane for the street canyon with a panel at the centre of the upstream building roof. Colours as in Figure 5.4.

5.3.3 Panel at the trailing edge of the upstream building roof

Flow structure

This subsection describes the effect of adding a panel on the trailing edge of the upstream building roof as shown in Figure 5.22. The panels were added at angles of 45° and 60° (showing large variation in the flow structure and pedestrian level wind speed when added at the leading edge of the upstream building). For the added panels at the trailing edge, no large pressure difference has been observed on the windward face and leeward face of the panel for both studied cases (as shown in Figure 5.23). Hence the combined effect shows drag on the panel (C_D) is approximately zero, which can be clearly seen in Table 5.3.

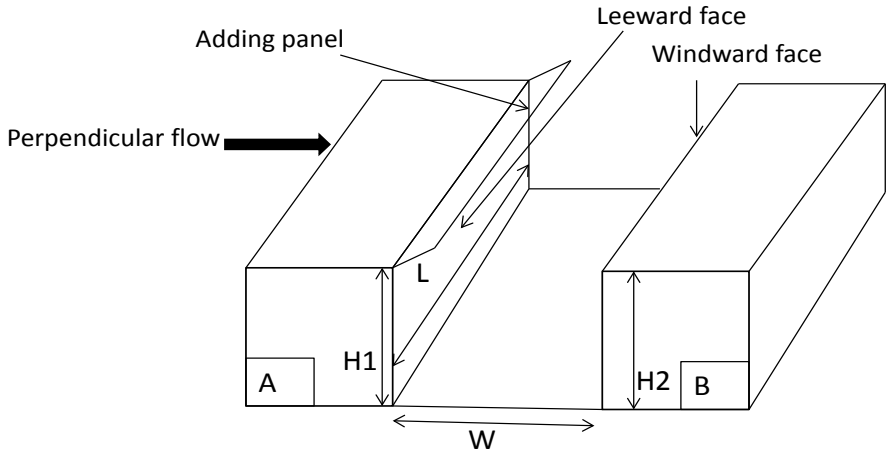

FIGURE 5.22: Panel at the trailing edge of the upstream building roof at different angles. Where A in the figure denotes the upstream building and B denotes the downstream building.

TABLE 5.3: C_D for a panel at different angles on the trailing edge of the upstream building roof.

angles	C_D
45° open	-0.001
60° open	-0.08

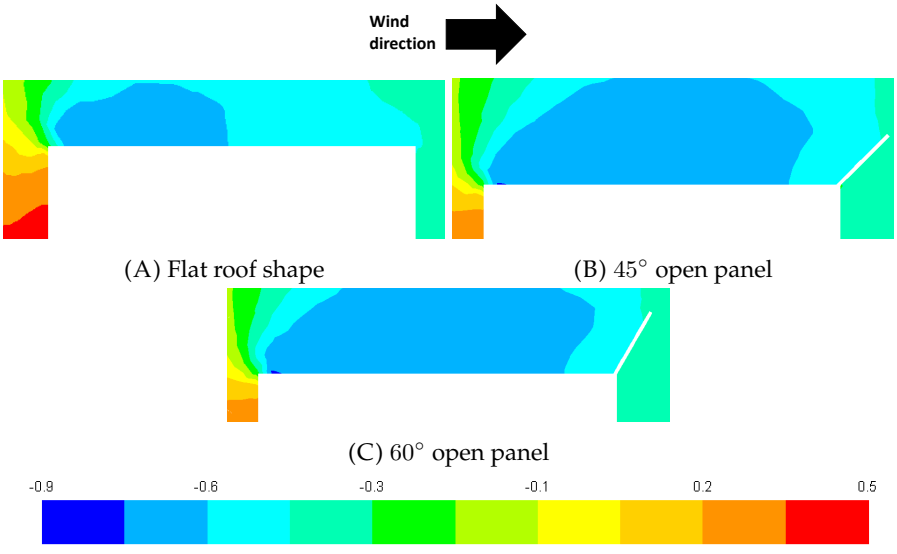

(A) Flat roof shape

(B) 45° open panel

(C) 60° open panel

FIGURE 5.23: C_p on the roof of the upstream building in theXY- plane at the centre plane ($Z = 40$) for the street canyon with a panel at the trailing edge of the upstream building roof.

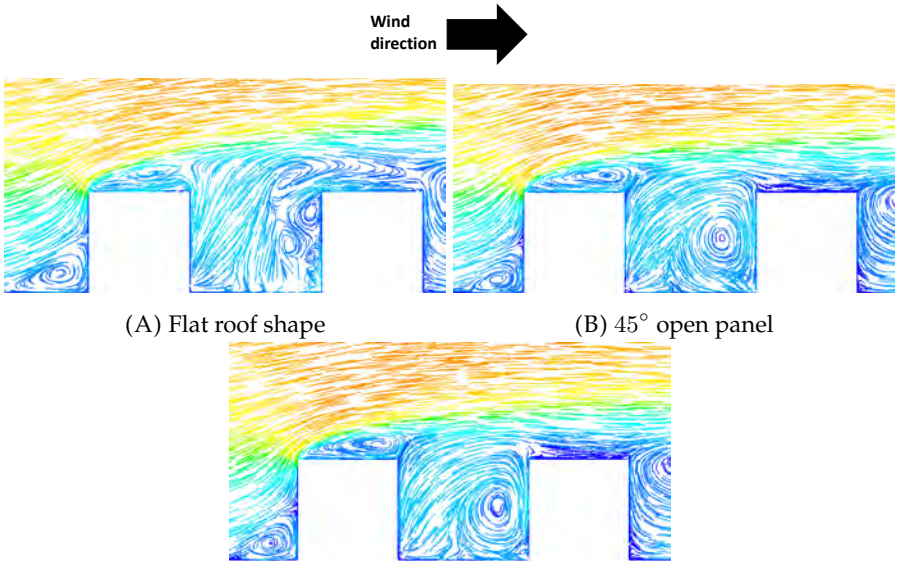

(A) Flat roof shape

(B) 45° open panel

(C) 60° open panel

FIGURE 5.24: Velocity magnitude pathlines in XY- plane at the centre plane ($Z = 40$) for the street canyon with a panel at the trailing edge of the upstream building.

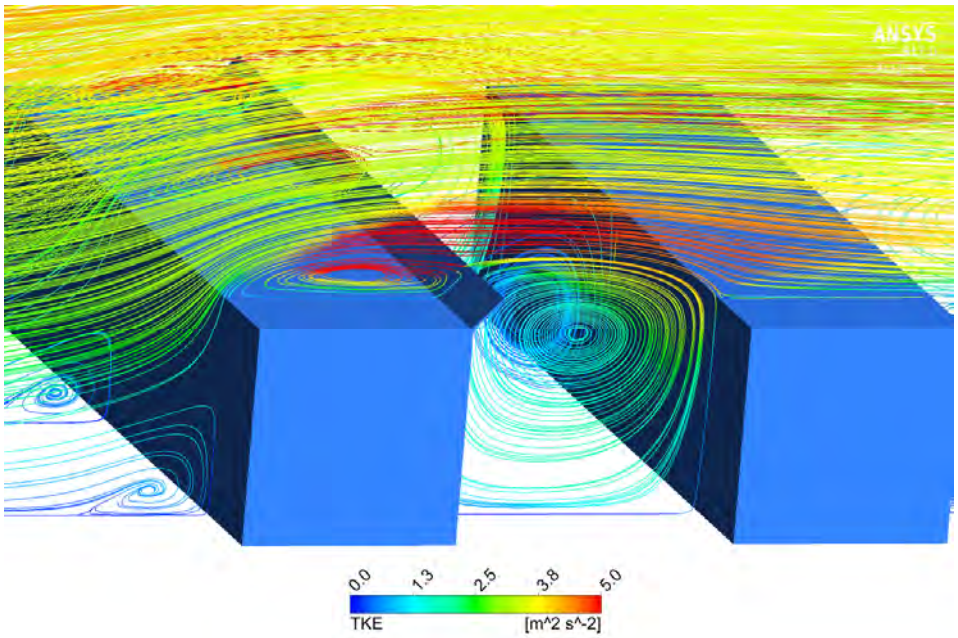

FIGURE 5.25: Isometric view of the streamlines coloured by the magnitude of turbulent kinetic energy (k) around and inside the street canyon with a panel at the trailing of the upstream building roof at an angle of 45°.

Comparison of the flow structure in the centre vertical plane shows no drastic change in the flow structure up to the roof of the upstream building when compared with the flat-flat case. However, adding the panel at the trailing edge of the upstream building blocks backflow coming from

the canyon into the roof region of the upstream building for both studied angles. The core of recirculation can also be seen moved downward (towards the ground) for both studied panel angles when compared with the flat-flat case. This can be clearly seen from the centre plane velocity magnitude pathlines Figures 5.24(B) and 5.24(C), and an isometric view of the vertical streamlines coloured by the magnitude of turbulent kinetic energy (k) for the added panel at an angle of $45°$ (Figure 5.24(C) when compared to Figure 5.7).

Figure 5.26 shows velocity magnitude streamlines at a pedestrian height of 1.5 m for the considered cases with a panel at the trailing edge. No drastic change in the flow structure at this level has been observed when compared with the flat-flat case.

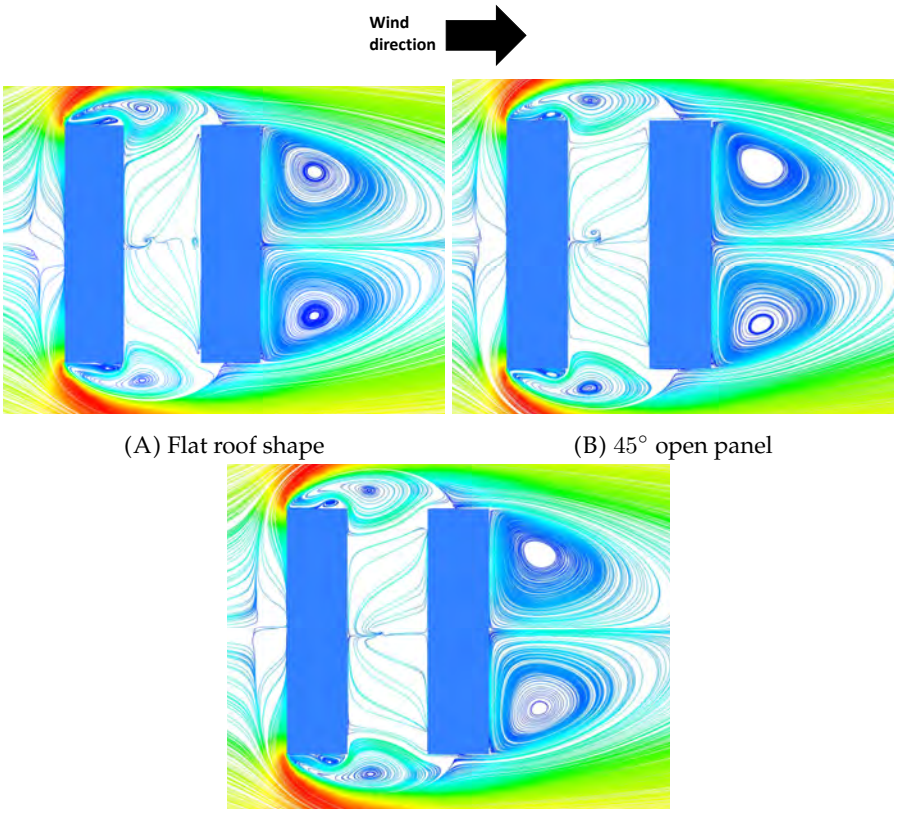

(A) Flat roof shape (B) $45°$ open panel

(C) $60°$ open panel

FIGURE 5.26: Velocity magnitude streamlines (cut plane to zoom near the street canyon) in the XZ- plane at $Y = 1.5$ m level for the street canyon with a panel at the trailing edge of the upstream building roof. For all these cases separated shear layers from the sides of the upstream building reattach on the sides of the downstream building.

Pedestrian level wind categorisation

Figure 5.27 shows pedestrian level wind categorisation using contour plots of ELBS Beaufort Number at a height of 1.5 for the considered cases of panel added at the trailing edge of the upstream building roof. The obtained

results were compared with the flat-flat case. The comparison shows improvement in the wind comfort for pedestrians near the downstream building inside the canyon. The reduction of the wind speed at this height in these cases compared to the flat-flat case is probably due to the large recirculation inside the canyon. This recirculation allows less fluid to be removed out of the canyon and hence the reduction of the wind speed inside the canyon. The core of recirculation near the downstream building inside the canyon (as can be seen in the vertical plane as shown in Figure 5.24(B) and 5.24(C)) causes reduction of the wind speed in this region.

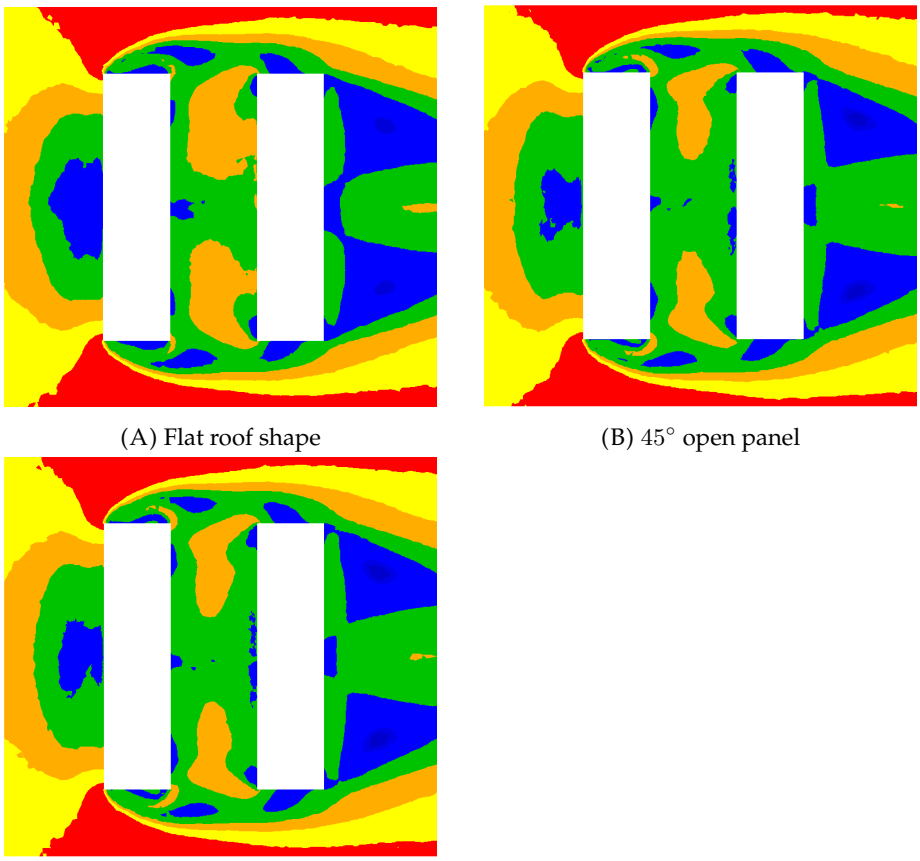

(A) Flat roof shape

(B) 45° open panel

(C) 60° open panel

FIGURE 5.27: Wind categories at $Y = 1.5$ m in the XZ-plane for the street canyon with the panel at the trailing edge of the upstream building roof. Colours as in Figure 5.4.

Analysis of the percentage of different pedestrian wind comfort zones according to ELBS and the percentage of increase or decrease in each particular zone compared to the flat-flat case was also done for the panels at the centre plane (specified cases of subsection 5.3.2), and at the trailing edge of the upstream building roof. The entire street canyon and upstream pavement and downstream pavement areas (similar to subsection 5.3.1) were considered for this analysis. Figure 5.28 shows a stack plot representation and data table for the percentage of the entire street canyon taken up by different Beaufort Number zones at a height of 1.5 m. The data clearly indicates that at this height, the wind speed inside the entire street canyon decreases in the case with adding a panel at angles of 45° and 60° at the

trailing edge of the upstream building roof when compared with the flat-flat case.

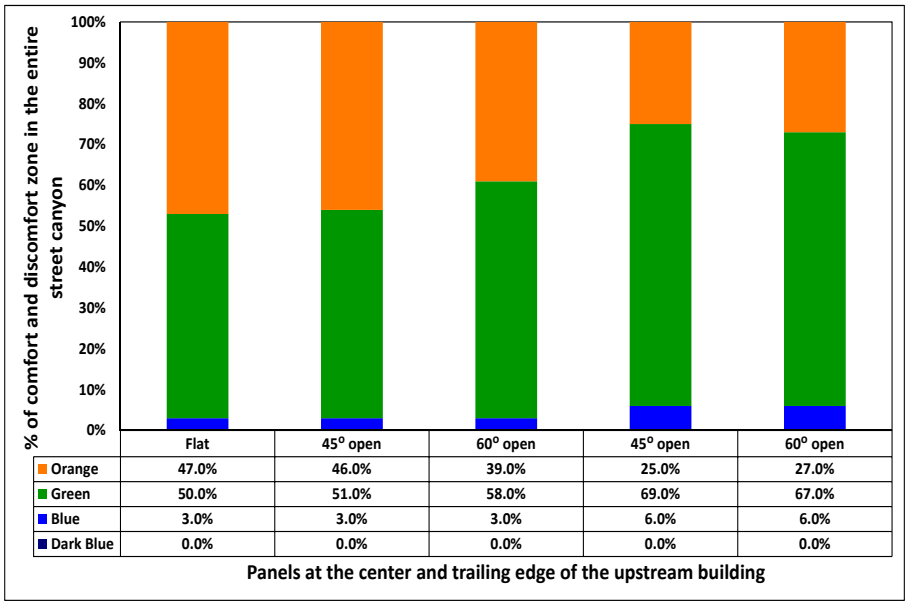

	Flat	45° open	60° open	45° open	60° open
Orange	47.0%	46.0%	39.0%	25.0%	27.0%
Green	50.0%	51.0%	58.0%	69.0%	67.0%
Blue	3.0%	3.0%	3.0%	6.0%	6.0%
Dark Blue	0.0%	0.0%	0.0%	0.0%	0.0%

FIGURE 5.28: Comparison of the increase or decrease of comfort and discomfort zone with panels at the centre plane (bar- 2 and 3) and trailing edge of the upstream building roof (bar- 4 and 5) compared to the flat-flat case inside the entire street canyon using the percentage stack chart. Colours as in Figure 5.4.

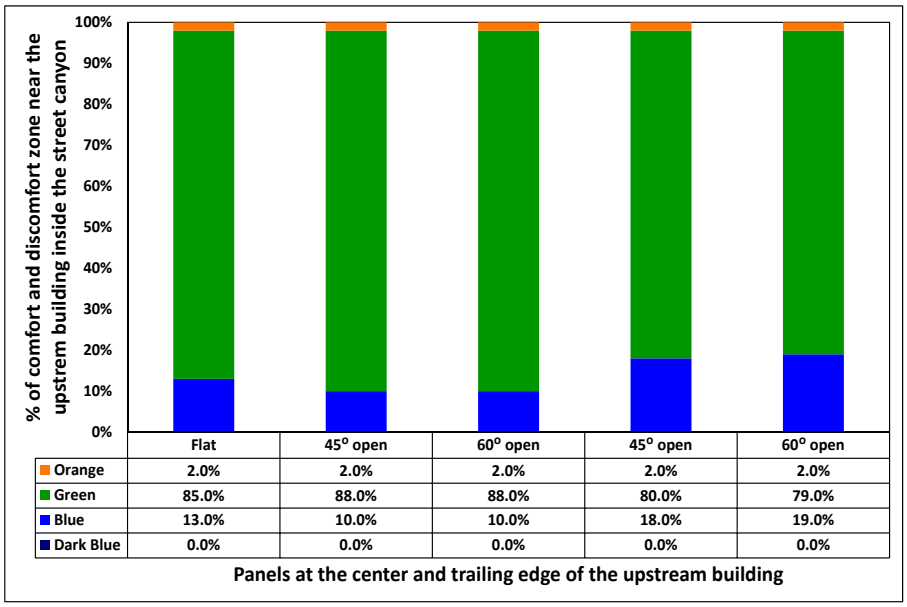

	Flat	45° open	60° open	45° open	60° open
Orange	2.0%	2.0%	2.0%	2.0%	2.0%
Green	85.0%	88.0%	88.0%	80.0%	79.0%
Blue	13.0%	10.0%	10.0%	18.0%	19.0%
Dark Blue	0.0%	0.0%	0.0%	0.0%	0.0%

FIGURE 5.29: Comparison of the increase or decrease of comfort and discomfort zone with panels at the centre plane (bar- 2 and 3) and trailing edge of the upstream building roof (bar- 4 and 5) compared to the flat-flat case near the upstream building for 3 m distance in the X-direction and 80 m distance in the Z-direction at $Y = 1.5$ m height using the percentage stack chart. Colours as in Figure 5.4.

For the wind speed assessment for the upstream pavement as shown in Figure 5.29, a slight improvement in the overall wind speed has been observed in the cases with a panel at the trailing edge of the upstream building roof.

Figure 5.30 shows the data table and wind speed assessment stack chart for the downstream pavement and comparison of the obtained results with the flat-flat case. This chart clearly indicates a reduction in the wind speed when panels were added at the trailing edge of the upstream building roof.

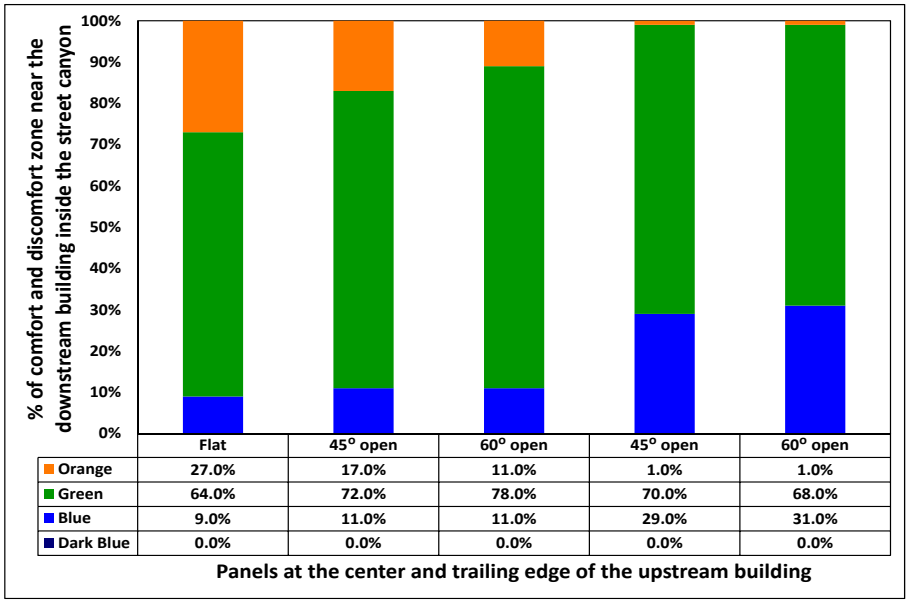

FIGURE 5.30: Comparison of the increase or decrease of comfort and discomfort zone with panels at the centre plane (bar- 2 and 3) and trailing edge of the upstream building roof (bar- 4 and 5) compared to the flat-flat case near the downstream building for 3 m distance in the X-direction and 80 m distance in the Z-direction at $Y = 1.5$ m height using the percentage stack chart. Colours as in Figure 5.4.

5.3.4 Panel on the leading edge of the downstream building roof

Flow structure

TABLE 5.4: C_D for the panel at the leading edge of the downstream building roof at different angles.

angles	C_D
15° solid	0.11
30° solid	0.13
45° open	0.18
60° open	0.19
75° open	0.20

Simulations were carried out for the panel added on the leading edge of the downstream building roof at angles of 15°, 30°, 45°, 60° and 75°as shown in Figure 5.31. The effect of adding such panels on the flow structure and on pedestrian comfort inside the street canyon is analysed in this subsection. Table 5.4 and Figure 5.32 show results of measured C_D and C_p respectively. No major difference in the value of C_p was observed when contours of different panel angle C_p compared with the flat-flat case. Also, the difference in the values of C_p on the windward face of the panel and that of the leeward face was observed to be minor for all studied angles. Therefore, the corresponding difference on the drag (C_D) for panels at different angles was minor too.

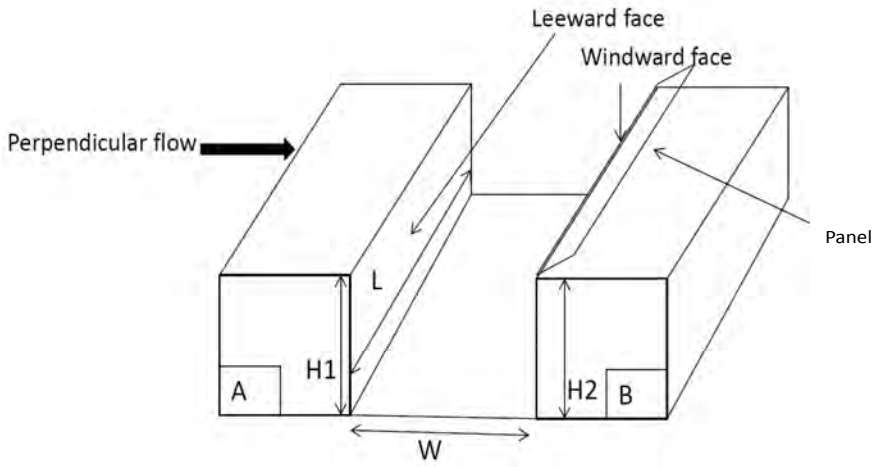

FIGURE 5.31: Panel at the leading edge of the downstream building roof at different angles. Where A in the figure denotes the upstream building and B denotes the downstream building.

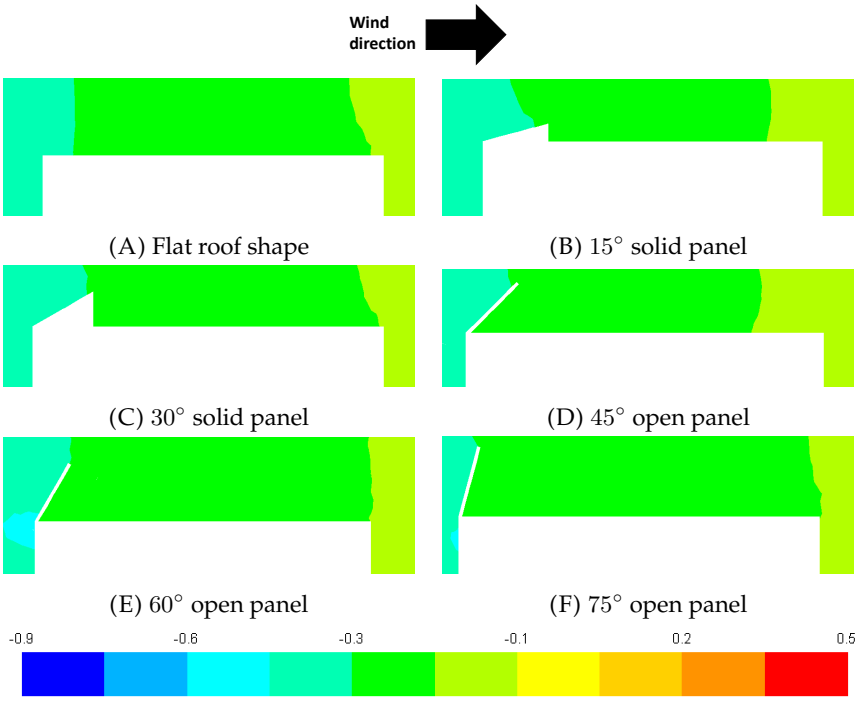

(A) Flat roof shape (B) 15° solid panel

(C) 30° solid panel (D) 45° open panel

(E) 60° open panel (F) 75° open panel

(G) 75° open panel

FIGURE 5.32: C_p on the roof of the downstream building in the XY- plane at the centre plane ($Z = 40$) for the street canyon with a panel at the leading edge of the downstream building roof.

Figure 5.33 shows velocity magnitude pathlines in the vertical centre plane for the added panels at different angles for the considered cases. It can be clearly seen from these plots that, adding a panel on the roof of the

downstream building creates no drastic change in the flow structure inside the canyon. i.e. overall flow structure in all studied cases remains identical to the flat-flat case. Figure 5.35 shows an isometric view of the streamlines coloured by the magnitude of k for the panel at an angle of 45° case. Level of turbulent kinetic energy and wind speed entering into the street from the roof levels shows similarity to that of the flat-flat case (Figure 5.7).

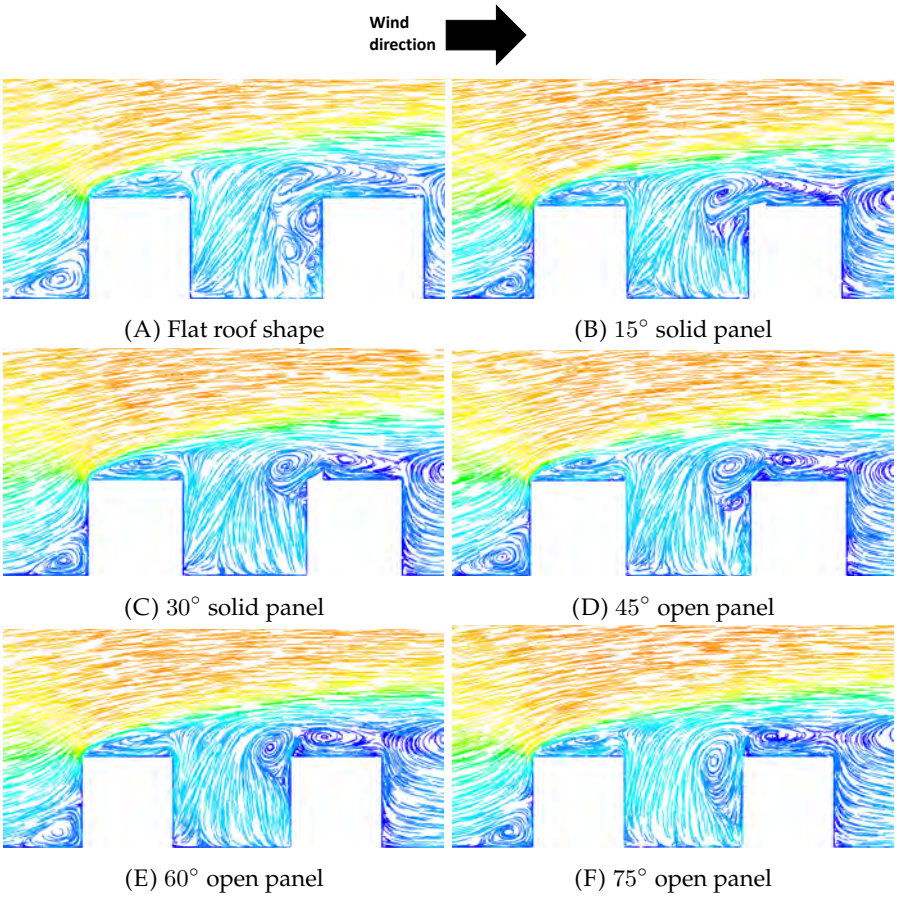

(A) Flat roof shape (B) 15° solid panel

(C) 30° solid panel (D) 45° open panel

(E) 60° open panel (F) 75° open panel

FIGURE 5.33: Velocity magnitude pathlines in the XY-plane at the centre plane ($Z = 40$) for the street canyon with a panel at the leading edge of the downstream building roof.

Figure 5.34 shows velocity magnitude streamlines at the pedestrian height of 1.5 m. No major difference in the flow structure has been noticed at this level.

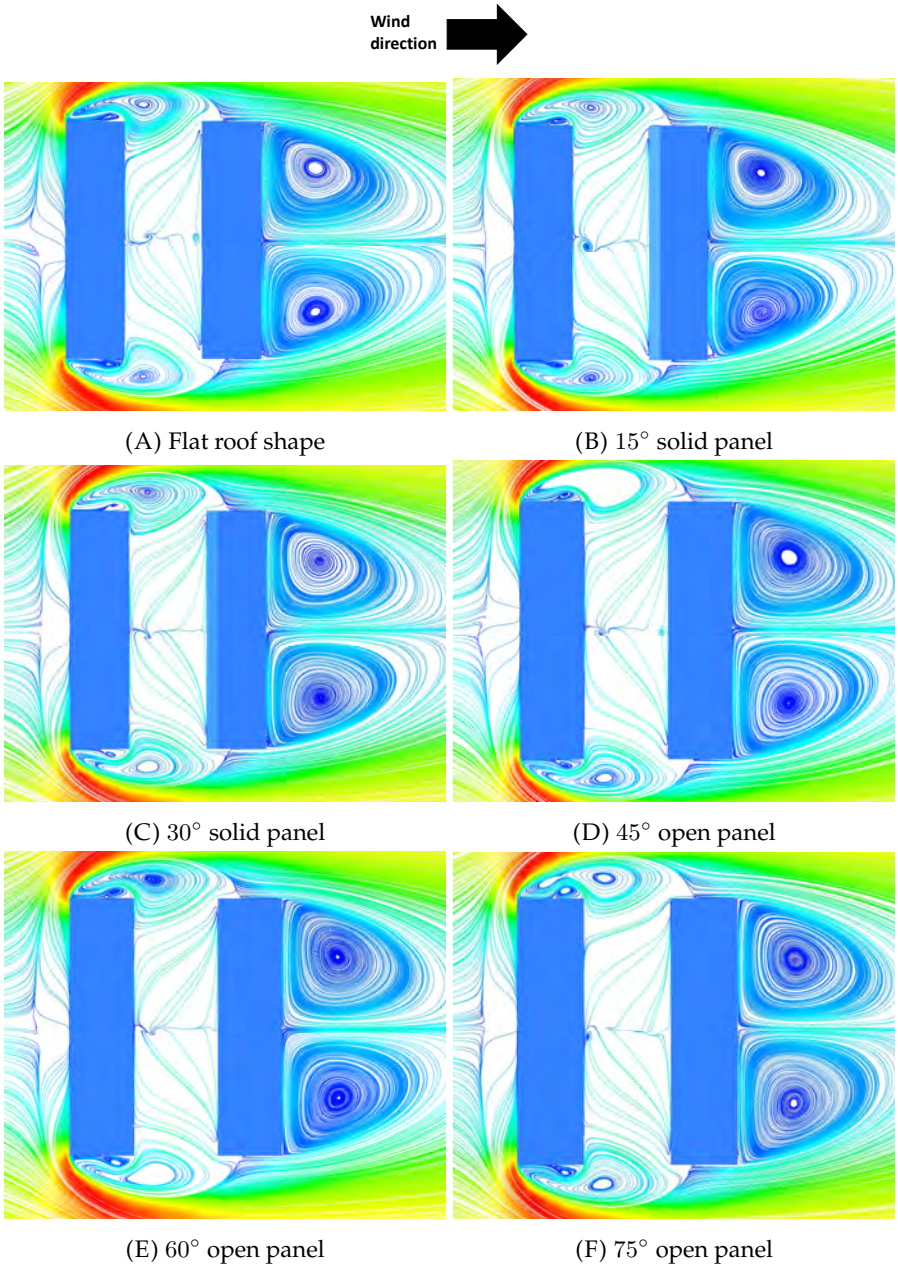

(A) Flat roof shape

(B) 15° solid panel

(C) 30° solid panel

(D) 45° open panel

(E) 60° open panel

(F) 75° open panel

FIGURE 5.34: Velocity magnitude streamlines (cut plane to zoom near the street canyon) in the XZ- plane at $Y = 1.5$ m level for the street canyon with a panel at the leading edge of the downstream building roof. For all these cases separated shear layers from the sides of the upstream building reattach on the sides of the downstream building.

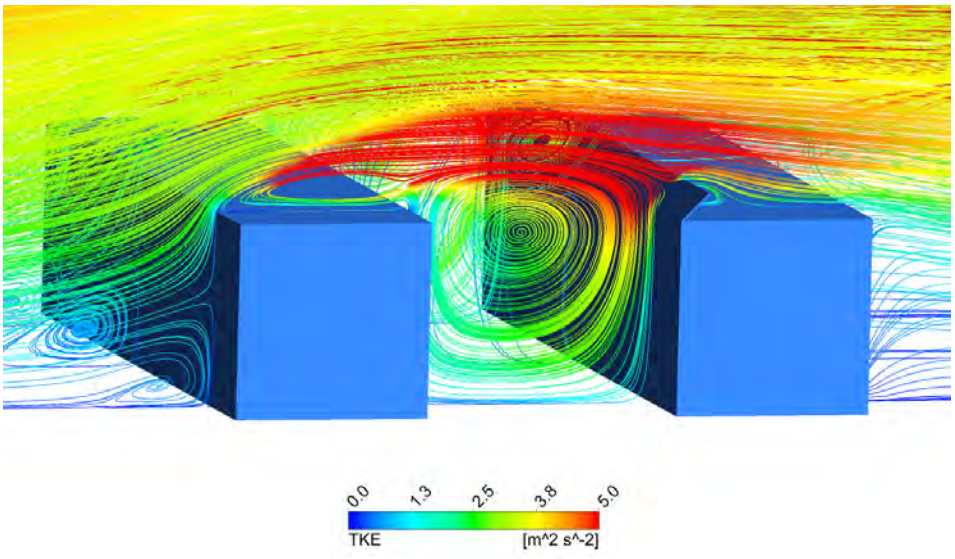

FIGURE 5.35: Isometric view of the streamlines coloured by the magnitude of turbulent kinetic energy (k) around and inside the street canyon with a panel at the leading edge of the downstream building roof at an angle of $45°$.

Pedestrian level wind categorisation

Pedestrian level wind comfort analysis with finding the percentage of difference in the wind comfort zones of ELBS Number and percentage of increase and decrease in a particular zone at a height of 1.5 m was also carried out for all cases in this subsection. Figure 5.36 shows wind categories contours for the attached panel at different angles on the downstream building roof. No major difference in different zones of wind speed contours at this height has been observed for all considered angles when compared with the flat-flat case. Figures 5.37, 5.38 and 5.39 show a stack plot representation and data table for percentage of the entire street canyon, near the upstream pavement and near the downstream pavement taken by different Beaufort Number zones at this height, respectively. The data clearly indicates no drastic change in the different wind speed zones for considered cases. In fact, this comparison shows a minor increase in the wind speed with added panels at angles of $45°$, $60°$ and $75°$ for the entire street canyon and near the downstream pavement.

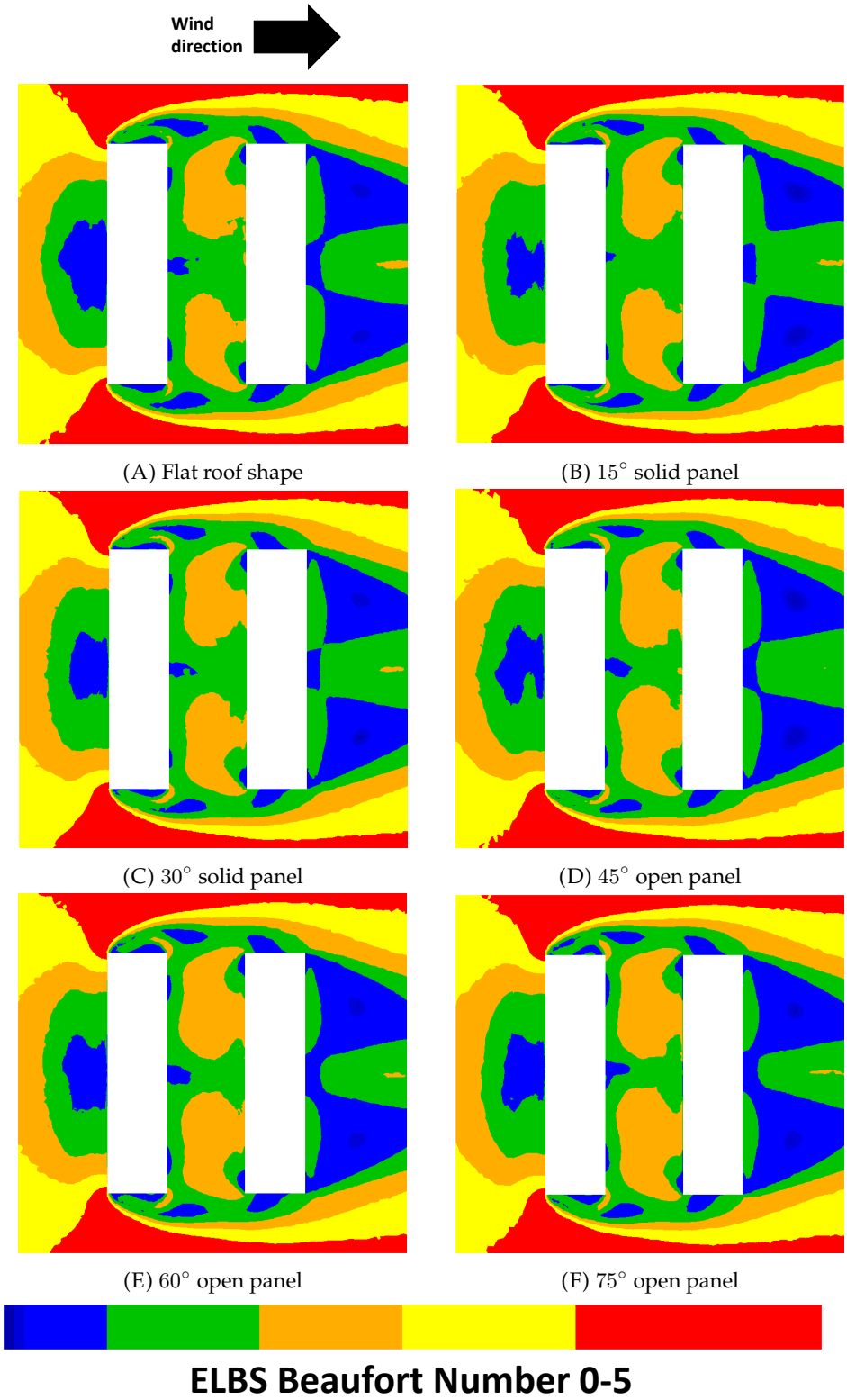

FIGURE 5.36: Wind categories at $Y = 1.5$ m in the XZ-plane for the street canyon with the panel at the leading edge of the downstream building. Colours as in Figure 5.4.

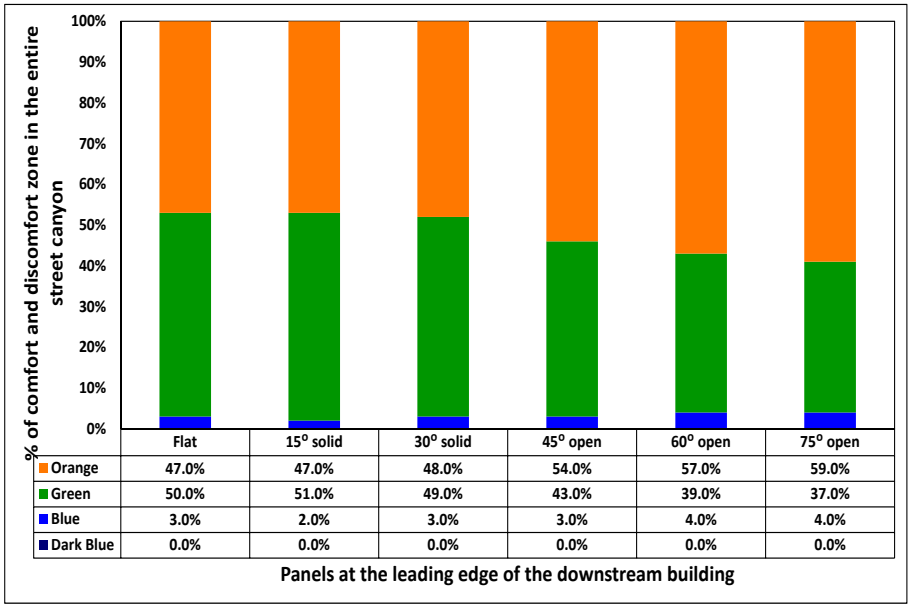

FIGURE 5.37: Comparison of the increase or decrease of comfort and discomfort zone with panels at the leading edge of the downstream building roof compared to the flat-flat case inside the entire street canyon using the percentage stack chart. Colours as in Figure 5.4.

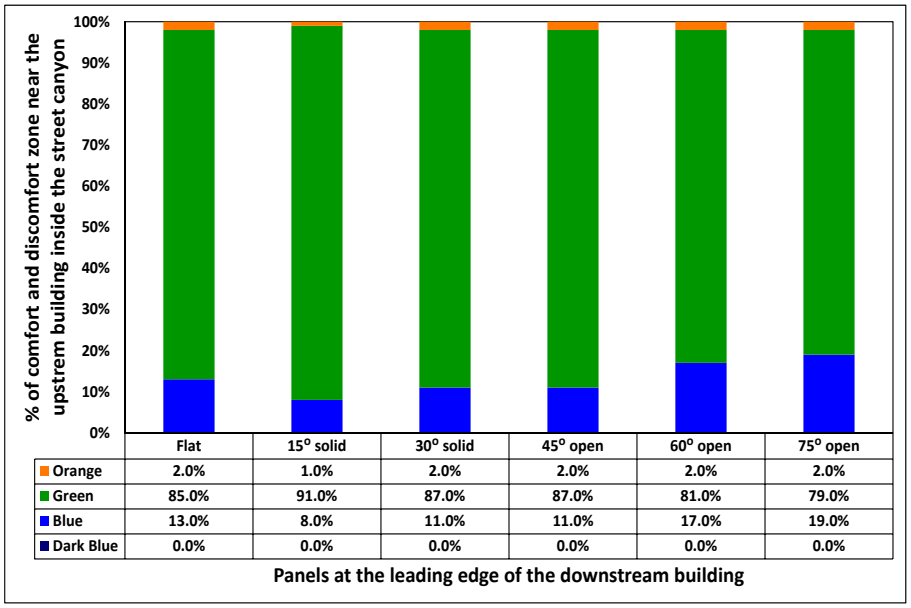

FIGURE 5.38: Comparison of the increase or decrease of comfort and discomfort zone with panels at the leading edge of the downstream building roof compared to the flat-flat case near the downstream building for 3 m distance in the X-direction and 80 m distance in the Z-direction at $Y = 1.5$ m height using the percentage stack chart. Colours as in Figure 5.4.

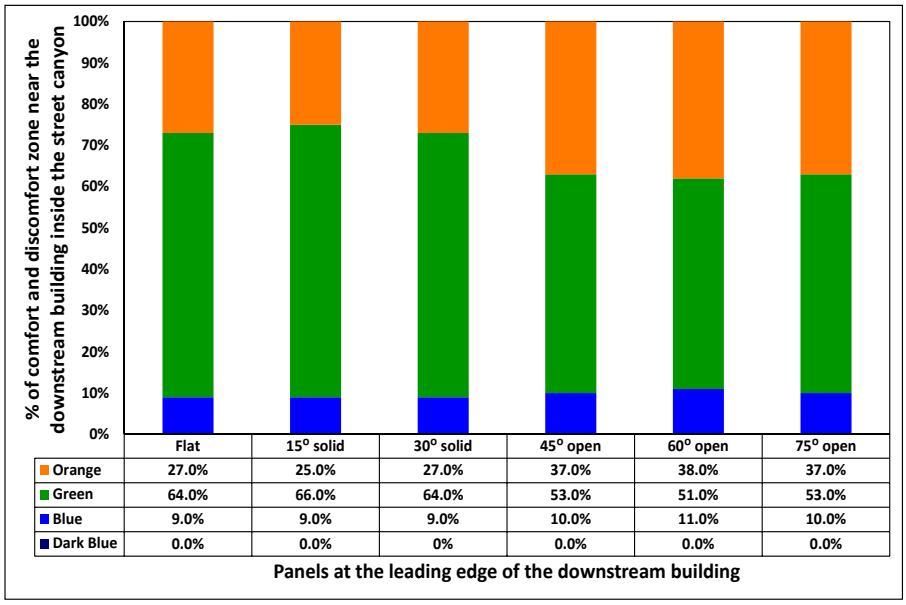

	Flat	15° solid	30° solid	45° open	60° open	75° open
Orange	27.0%	25.0%	27.0%	37.0%	38.0%	37.0%
Green	64.0%	66.0%	64.0%	53.0%	51.0%	53.0%
Blue	9.0%	9.0%	9.0%	10.0%	11.0%	10.0%
Dark Blue	0.0%	0.0%	0%	0.0%	0.0%	0.0%

FIGURE 5.39: Comparison of the increase or decrease of comfort and discomfort zone with panels at the leading edge of the downstream building roof compared to the flat-flat case near the downstream building for 3 m distance in the X-direction and 80 m distance in the Z-direction at $Y = 1.5$ m height using the percentage stack chart. Colours as in Figure 5.4.

5.4 Chapter Summary

In this Chapter, the impact of adding a panel at different angles on the roof of the upstream building and downstream building, on the flow structure and pedestrian comfort has been analysed. For all studied cases, the wind direction was normal to the street canyon. The results of this study, when compared with the flat-flat roof case, indicate that adding a panel at the leading edge and trailing edge of the upstream building roof modifies the flow structure on the roof of the upstream building and inside the canyon and has a strong influence on the pedestrian comfort in the canyon.

The added panel at the leading edge of the upstream building roof at higher angles ($\geq 45°$), delays the flow separation i.e. the flow separates from the top of the panel instead of the leading edge of the upstream building roof. Also, the separated shear layer from the roof of the upstream building reattaches on the roof of the downstream building. This modification of the reattachment of the shear layer on the roof level decreases wind speed in the street canyon at the pedestrian level due to the convection of the low turbulent kinetic energy and hence low wind speed from the roof level inside the canyon. Hence improvement in the wind speed was observed inside the canyon specifically in the case of a panel at an angle of $45°$. Also, with added panels at this place, drastic variation in the pressure coefficient on the front face of the panel and hence increase in the drag force has been observed with increase in the panel angles.

For the cases, when panels were added at the centre plane of the upstream building roof at different angles, earlier reattachment of the separated shear layer from the leading edge of the upstream building was observed compared to the flat-flat case. This shear layer reattachment was seen to be on the front face of the panel and hence created a large negative pressure zone in this region. Hence the corresponding drag on the panel was negative for all studied cases. No significant improvement in the wind speed at the pedestrian level was observed for these cases.

When panels were added at the trailing edge of the upstream building roof, the flow structure up to the roof of the upstream building was similar for all the studied panel angles. However, the added panel at the trailing edge blocks backflow coming from the canyon into the roof region of the upstream building when compared with that of the flat-flat case. For all studied angles with panels at the trailing edge, a large recirculation was observed inside the canyon with the core of recirculation near the downstream building. This recirculation inside the canyon has shown a reduction in the wind speed at the pedestrian level. Adding panels at the trailing edge of the upstream building roof has no significant effect on the drag force on the panel.

For the added panel at the leading edge of the downstream building roof at different angles, there was no modification in the overall flow structure when compared with the flat-flat case. Therefore, improvement in the pedestrian level wind comfort was negligible.

It can be concluded from this study that, adding a panel at the leading edge of the upstream building roof at an angle of 45°, modifies the overall flow structure and improves the pedestrian level wind comfort inside the canyon. Also, adding panels at the trailing edge of the upstream building roof at angles of 45° and 60°, modifies the flow structure inside the street canyon and hence improves wind comfort at the pedestrian height. Also, for these specified panel angles and locations, the drag force on the panels is less. Therefore, these can be considered as the best locations for adding a panel to modify the flow structure to improve the pedestrian level wind comfort.

Questions associated with adding such panels on the roof of the building, outside what the CFD can tell us include:

1. Is it feasible to build panels of 4 m (considered height of the panel in this study) and attach on the roof of the building?

   The answer to this could be yes when we think of trade-off between the cost of building the panel and strengthening the roof to withstand storm force winds on the panel and the effectiveness of using panels to mitigate the effects of wind discomfort.

2. Is adding a roof panel similar to just making the building one storey taller?

   This could be considered as an alternative to adding a panel on the roof. In our studied cases on added panels, the improvement in the wind comfort at the pedestrian level was observed when panels were attached to the roof of the upstream building. So, if we consider making the upstream building higher compared to the downstream building can improve the wind comfort at the pedestrian level. Making

the upstream building high compared to the downstream building is similar to the step-down street canyon. For such step-down street canyon, we have already analysed the flow structure and pedestrian comfort for the street aspect ratio of $S/H = 1$ and 2 in Chapter 3. The obtained result from that study revealed that such step-down canyon configuration can be effective to reduce the wind speed at the pedestrian level. So, this can be considered as an alternative to adding a panel.

However, the panels considered in this study were thought to be the moveable panels. So, it remains closed and attached to the roof of the building for the normal wind events and can be opened at the time of high wind speed cases. Also, cost of building such panels will be definitely less than making the building one story bigger.

3. What happens when the wind reverses or blows from another direction?

   From this study, it was observed that adding a panel at an angle of 45° at the leading edge of the upstream building and for the panels attached at the trailing edge of the upstream building are the best positions to reduce the pedestrian level high winds. Usually in the real urban areas wind can blow from any direction, so if the direction of the wind is exactly opposite to the one we have considered in this study, such panels could be attached on the roof of the downstream building (which would be the upstream building when wind direction is opposite to the considered here).

   Also, panels could be attached to all edges of the roof and different panels, or a different combination of panels could be raised depending on the wind speed and wind direction. However, future work is needed to come up with the optimal arrangements of such panels to prevent extreme wind events.

In this study, only impermeable (flat surface) panels were added at different locations. With adding porosity into the panel may improve the drag force on the panel at the effective panel location (i.e. at the leading edge of the upstream building roof and at $\theta = 45^\circ$). Further investigations are expected to focus on these areas.

Chapter 6

Conclusions

6.1 Thesis summary

Urban areas should be designed to ensure comfort and safety to their inhabitants. For hundreds of years inhabitants in such urban areas have been sheltered from the wind by closely grouped buildings. In the last 100 years, however, this situation has changed completely as new style and techniques have introduced high rise buildings in such urban areas. Pedestrian level wind is regarded as an important part involved in such building designs because uncomfortable wind conditions can prove harmful to the success of such newly constructed buildings. Identifying the importance of wind climate at pedestrian level, many urban authorities nowadays require information at the design stage about the probable wind conditions for large construction projects. The majority of such studies in the past have been conducted with wind tunnel modelling. Recently, Computational Fluid Dynamics (CFD) has become available as an effective tool.

The aim of this thesis was to develop a three-dimensional numerical model of urban street canyons for medium rise buildings inside a thick atmospheric boundary layer, and an analysis of the flow structure and pedestrian level wind categorisation inside such urban areas. The considered wind direction was perpendicular to the street canyon for all studied cases in this thesis. A Computational Fluid Dynamics (CFD) approach using ANSYS Fluent 17.0 has been employed in this study. The aims of this research include:

- Validation of CFD technique to provide a tool to study the aerodynamics around a generic building or a street canyon at high Reynolds number (Re)
- to analyse a near-wall modelling approach to model the wall roughness effect, with a corresponding validation study for the high Re
- To parametrise generic building models, and analysis of flow structure and pedestrian comfort by changing building dimensions and street width
- To assess the impact of varying building roof shapes on the flow structure and pedestrian comfort

- To assess the impact of adding roof panels to improve pedestrian comfort

The first and second aims were achieved in Chapter 2 in which the turbulence models selected and near-wall modelling approach used for CFD were validated for a single building model for two reduced scale models. Note that, it is important to study the performance of steady RANS turbulence models for the Re of interest (which in the cases in this study is of order $10^6 - 10^7$). However, according to best of our knowledge, previous experimental studies analysing the flow structure and pedestrian-level wind speed for generic building configurations have been performed up to Re of order $10^4 - 10^5$. Therefore, before modelling actual street canyon at high Re, the turbulence models and boundary conditions were validated at available range of Re. The results were compared with the published experimental data to ensure that the aerodynamic forces, velocity profiles in the high turbulence region around model buildings (roof of the building and in the wake, especially at the pedestrian height) and the turbulent kinetic energy on the roof of the building were well matched. The comparison between the published wind tunnel data for velocity, pressure and turbulent kinetic energy and ANSYS Fluent CFD results provided an assurance that the CFD data provided a valid basis for comparison within the accuracy reported in Chapter 2.

The third aim was achieved in Chapter 3 by performing a parametric study using CFD to analyse the flow structure and pedestrian comfort inside uniform and non-uniform street canyons for medium rise buildings. Parameters considered in this study include; the street width, building width and building height. The Re involved in this study was 8.1×10^6 based on the height of the building and free stream velocity. For this study, the pedestrian comfort was quantified as the fraction of the street area where the wind speed was less than 3 m/s on the extended "Land Beaufort Scale" at 1.75 m height. The first objective of this study was to analyse the flow structure around and inside the street canyon at high Re and investigate the reattachment of all separated shear layers (from the roof and sides of the upstream building leading edges) when the wind is approaching perpendicular to the street canyon. From the literature review, it was apparent that the reattachment of such shear layers has been considered as an important factor affecting the flow structure inside the street canyon. The second objective was to find the optimum street width where the pedestrian discomfort becomes noticeable inside the street canyon and find the region where it becomes noticeable (defined as a wind speed greater than 3 m/s). The third objective was to find the influence of building width (building dimension perpendicular to the wind direction) on the flow structure and hence on the pedestrian comfort inside the street canyon. The fourth objective was to find non-uniform street canyon configurations that can improve the pedestrian comfort inside the street canyon.

The next aim of finding the impact of changing roof shapes of the buildings generating street canyons on the flow structure and pedestrian comfort was achieved in Chapter 4 of this thesis. Considered roof shapes were: flat, slanted, vaulted, downwind wedge, upwind wedge and trapezoidal. Different cases studied include changing roof shapes of both upstream and

downstream buildings, only the upstream building and only the downstream building. A constant street width to building height ratio S/H of 1 was considered for this analysis. This ratio was chosen to compare the change in the flow structure and pedestrian comfort inside the street canyon with the flat roof of Chapter 3.

The last aim of this study was to identify the impact of adding panels on the roof of the building on the flow structure and hence on the wind comfort improvement at the pedestrian height. The first objective of this study was to find the optimum street width when pedestrian discomfort inside the street canyon becomes noticeable and to find the wind speed at which the pedestrian discomfort inside the street canyon becomes noticeable. After finding the optimum street width with a larger area of the pedestrian level wind discomfort, a parametric study was performed to find the angle of the panel and the location of the panel on the roof which can modify the flow coming into the street canyon from the roof level and hence improve pedestrian comfort. Different panel angles considered in this study were $0°$, $15°$, $30°$, $45°$, $60°$, and $75°$. Considered locations for adding panels were: at the leading edge of the upstream building roof, in the centre plane (perpendicular to the wind direction) of the upstream building roof, at the trailing edge of the upstream building roof and at the leading edge of the downstream building roof. The Re was 1.1×10^7 based on the building height and free stream velocity. In order to find that whether such panels will be capable of withstand in extreme wind events, the drag on panels was measured for all studied cases.

6.2 Conclusions

In this study, a series of questions, based on the literature review were posed and from the obtained results several conclusions were drawn. The answers to the questions follow:

- **Can a steady RANS turbulence model with the near-wall modelling approach be used for the pedestrian level wind assessment study?**

  In this study, the approach used for modelling wall roughness effect is based on the near-wall treatment. In Fluent, the near-wall modelling implies that the walls are smooth (roughness height is zero), which is also the case for the bottom of the computational domain. A smooth bottom surface can lead to a non-horizontal homogeneous boundary layer (as specified in subsection 2.2.3 in Chapter 2) in the simulations, and, hence, stream-wise gradients can occur in the vertical mean wind speed and turbulence quantities. Therefore it was necessary to evaluate the performance of the turbulence models with the near wall modelling approach in the high turbulence region around the building (especially on the roof of the building and in the wake region or at the pedestrian height). The performance of such turbulence models was evaluated at two different Re based on the height of the building and free stream velocity. The validation study was performed in Chapter 2 and comparison of the obtained results for the wind speed increase ratio (the ratio of the local pedestrian level wind speed to the wind speed that would occur at the position without building) at pedestrian height using different turbulence models

was done with the published wind tunnel data. Among all the tested near-wall based turbulence models the transition $k-kl-\omega$ model was found to predict the wind speed at the pedestrian level with an accuracy of around 85% in the region with the high wind speed (the region which is most important in the evaluation of the pedestrian level wind environment) when compared with the previous wind tunnel data. Yoshie et al. (2007) reported that it is difficult to quantitatively describe the prediction accuracy when CFD analysis results are compared with the wind tunnel data in such a high turbulence region near the ground. However, they have specified that this prediction accuracy within approximately 15% using CFD analysis results in a strong wind region (region near the ground or pedestrian height) can be considered a relatively good match. Willemsen et al. (2002) has also reported that wind tunnel experiments can conservatively exhibit a standard error of 20% when measuring the pedestrian level wind. Therefore, it should be noted that the wind tunnel data also include uncertainties, to an extent. Therefore, steady RANS turbulence model with considered near wall modelling approach was found suitable method for analysing the overall flow structure and categorization of the wind speed at the pedestrian head height and chest height for the wind direction perpendicular to the street axis. However, future work could be extended to generalize this statement by considering the different wind directions and studying for complicated cityscapes.

- **Do the building dimensions and street width affects the flow structure and pedestrian comfort inside the urban street canyons?**

  A study by Oke (1988) showed that compactness of the street is good for the pedestrian wind comfort when the wind is approaching perpendicular to the street canyon. However, no CFD study sufficiently detailed for finding the impact of different parameters defining urban street canyons, including street width, building width and building height on the flow structure and pedestrian comfort at high Re has yet been reported. From the performed parametric study in Chapter 3 it was revealed that the flow structure around and inside the street canyon strongly depends on the reattachment of the separated shear layers due to the sharp leading edges of the upstream building, and on the vortex structure in the canyon. This study also showed that for the uniform street canyon cases, pedestrian comfort near the downstream building inside the canyon decreases with increasing street width. Whereas, a decrease in the building width decreases pedestrian comfort inside the street canyon. For the non-uniform cases, a step-up street canyon increases the pedestrian comfort inside the canyon whereas a step-down street canyon decreases the pedestrian comfort relative to a street with equal height buildings on both sides.

- **Does changing the building roof shapes alter the flow structure inside the street canyon, and hence can improve the wind speed at the pedestrian height?**

  The impact of changing the roof shapes of the buildings generating urban street canyons on the flow structure and hence on the pedestrian wind comfort was evaluated in Chapter 4. The results of this

study, when compared with the flat-flat roof case, indicated that roof shapes have a strong influence on the flow field and pedestrian comfort in the street canyon. From the obtained results it was concluded that the best roof shape to improve overall pedestrian comfort inside the street canyon is the upwind wedge shape when it is used for both buildings or only the upstream building or only the downstream building. The worst roof shapes identified from this analysis were the vaulted roof shape and downwind wedge roof shape when they are used for both buildings or only the upstream building.

- **How can we improve the high wind speed regions at the pedestrian height for the flat-flat roof buildings generating the street canyon**?

  This study considered only deflector panels mounted on the roof to improve such a high wind speed regions at the pedestrian height for the flat-flat roof buildings. From the obtained results it was revealed that adding a panel at the leading edge of the upstream building roof at an angle of 45° and at the trailing edge of the upstream building roof at angles of 45° and 60° modifies the flow structure in a way that noticeably improves the wind comfort at a pedestrian height.

6.3 Scope for future work

This study has shown that the steady RANS CFD approach can be used for analysing the flow structure and pedestrian level wind categorisation. However, there exists a broad range of future work that can be undertaken.

In this study, the wind direction considered for all simulations was perpendicular to the street canyon. However, any change in the wind direction will cause variation in the flow structure and pedestrian comfort inside the street canyon. Also, in this study considered street canyons were isolated and no other surrounding buildings were modelled, which might be the cases considered in the future work.

Also, note that provided wind velocity profile at the inlet of the computational domain was given by a logarithmic profile for atmospheric boundary layer (ABL) as given by Equation 1.1 in Chapter 1 with providing roughness length for specific terrain of the type in Australia and New Zealand. The turbulence kinetic energy was also specified using the turbulence intensity at the inlet of the computational domain for all studied cases. In this study, this turbulence intensity at each level from the ground was obtained from the AS/NZS $1170.2 : 2011$ (Structural Design Actions-Part 2: Wind Actions, 2011) standards. However, wind tunnel studies for the scale model or full scale measurements to get exact logarithmic profile specifying terrain type and turbulence profile is desirable.

It has been predicted in this study that vortex shedding occurs inside the canyon and in the wake of the downstream building. Transient flow simulations are required to confirm the predictions and the effect of gusts due to vortex shedding on pedestrian comfort should be considered.

Further, in the study analysing the flow structure and pedestrian comfort with different roof shapes, the roof height was fixed to be 3.4 m for all cases of the different roof shapes. From the literature review, it was observed that changing the roof height also influences the flow structure

inside the street canyon and may cause a change in the wind speed at the pedestrian level. Further investigations are expected to focus on these areas. Also, in this study, an upwind wedge roof shape is favourable but is only shown to work for one wind direction. A future study should consider the best shape for any wind direction.

Appendix A

Calculation of the height of the first cell of inflation layer

The target y^+ value and fluid properties are know priori, so we need to calculate the friction velocity u_τ, which is defined as:

$$u_\tau = \sqrt{\frac{\tau_w}{\rho}}$$

The wall shear stress, τ_w can be calculated from skin friction coefficient C_f, such that:

$$\tau_w = \frac{1}{2} \cdot C_f \cdot \rho \cdot U^2$$

Empirical results for C_f used to estimate this value for external flow:

$$C_f = 0.058 \cdot Re^{-0.2}$$

The definition of the y^+ value is such that:

$$y^+ = \frac{\rho \cdot u_\tau \cdot \triangle y}{\mu}$$

Therefore, First cell height from the wall can be calculated as,

$$\triangle y = \frac{y^+ \cdot \mu}{\rho \cdot u_\tau}$$

Appendix B

UDF for mean wind speed for validation Model A

```
#include "udf.h"
#define VISC 1.7894e-05
#define CMU 0.09
#define yref 0.16
#define Karmannk 0.42
#define yzero 0.00018
#define UstarABL 0.28


DEFINE_PROFILE(inlet_x_velocity,thread,position)
{
real x[ND_ND];
real y,z;
face_t f;
cell_t c;
Thread *tc;
begin_f_loop(f,thread)
{
F_CENTROID(x,f,thread);
y=x[1];
z = x[2];
F_PROFILE(f,thread,position) =
((UstarABL/Karmannk)* log((y+yzero)/yzero));
}
end_f_loop(f,thread)
}
```

Appendix C

UDF for mean wind speed and turbulent profiles for validation Model B

```
#include "udf.h"
#define VISC 1.7894e-05
#define density 1.225
#define CMU 0.09
#define B 1./4.
#define D 1./2.
#define C 3./2.
#define Uref 21.8
#define I 0.132
#define yref 0.24
#define Karmannk 0.42
#define yzero 0.00035
#define UstarABL 1.40

DEFINE_PROFILE(inlet_x_velocity,thread,position)
{
        real x[ND_ND];
        real y,z;
        face_t f;
        cell_t c;
    Thread *tc;

begin_f_loop(f,thread)
{
F_CENTROID(x,f,thread)
y=x[1];
z = x[2];
F_PROFILE(f,thread,position)
=((UstarABL/Karmannk)* log((y+yzero)/yzero));
}
end_f_loop(f,thread)
```

```
}

/*  profile for kinetic energy  */

DEFINE_PROFILE(k_profile,thread,index)
{
        real x[ND_ND];
        face_t f;

begin_f_loop(f,thread)
{

F_CENTROID(x,f,thread);
y=x[1];
z = x[2];
F_PROFILE(f,thread,index) = C*pow((((UstarABL/Karmannk)
* log((y+yzero)/yzero))*I),2);
}
end_f_loop(f,thread)
}

DEFINE_PROFILE(dissip_profile,thread,index)
{
        real x[ND_ND];
        face_t f;
        real y,z;
begin_f_loop(f,thread)
{
F_CENTROID(x,f,thread);
y=x[1];
F_PROFILE(f,thread,index)=
(pow(UstarABL,3))/(Karmannk*(y+yzero));
}
end_f_loop(f,thread)
}

DEFINE_PROFILE(specific_profile,thread,index)
{
        real x[ND_ND];
        face_t f;
        real y,z;
begin_f_loop(f,thread)
{
F_CENTROID(x,f,thread);
y=x[1];
F_PROFILE(f,thread,index) = ((pow(UstarABL,3))
/(Karmannk*(y+yzero)))/(CMU*(C*pow((UMEAN*I),2)));
}
end_f_loop(f,thread)
}
```

Appendix D

UDF for mean wind speed and turbulence profiles for street canyons

```
#include "udf.h"
#define VISC 1.7894e-05
#define CMU 0.09
#define B 1./4.
#define D 1./2.
#define C 3./2.
#define Uref 5.9
#define yref 20
#define Karmannk 0.42
#define I 0.215
#define UMEAN 7.11
#define yzero 0.2
#define UstarABL 0.55
DEFINE_PROFILE(inlet_x_velocity,thread,position)
{
        real x[ND_ND];
        real y,z;
        face_t f;
        cell_t c;
    Thread *tc;
begin_f_loop(f,thread)
{
        F_CENTROID(x,f,thread);
y=x[1];
z = x[2];
F_PROFILE(f,thread,position) =((UstarABL/Karmannk)*
 log((y+yzero)/yzero));
}
end_f_loop(f,thread)
}
/*  profile for kinetic energy  */
```

```
DEFINE_PROFILE(k_profile,thread,index)
{
        real x[ND_ND];
        real y,z;
        face_t f;
        cell_t c;
    Thread *tc;
begin_f_loop(f,thread)
{

F_CENTROID(x,f,thread);
y=x[1];
z = x[2];
F_PROFILE(f,thread,index) = C*pow((((UstarABL/Karmannk)
* log((y+yzero)/yzero))*I),2);
}
end_f_loop(f,thread)
}

DEFINE_PROFILE(dissip_profile,thread,index)
{
        real x[ND_ND];
        face_t f;
        real y,z;
begin_f_loop(f,thread)
{
F_CENTROID(x,f,thread);
y=x[1];
F_PROFILE(f,thread,index)=(pow(UstarABL,3))
/(Karmannk*(y+yzero));
}
end_f_loop(f,thread)
}

DEFINE_PROFILE(specific_profile,thread,index)
{
        real x[ND_ND];
        face_t f;
        real y,z;
begin_f_loop(f,thread)
{
F_CENTROID(x,f,thread);
y=x[1];
F_PROFILE(f,thread,index) = ((pow(UstarABL,3))
/(Karmannk*(y+yzero)))/(CMU*(C*pow((UMEAN*I),2)));
}
end_f_loop(f,thread)
}
```

Appendix E

Calculation of the boundary layer thickness

E.1 Uniform street canyon

According to Counihan et al. (1974), the equation to calculate boundary layer thickness is given as,

$$U(y) = U_g \left[\frac{(y - y_1)}{\delta}\right]^n; \tag{E.1}$$

Here we take, $U_g \approx 17$ m/s is the wind speed outside the boundary layer (as calculated below using the power law wind velocity profile equation E.2). The exponent $n = 0.28$ and y_1 is a zero-plane displacement which is according to Garratt (1992) (chapter-4, page no:86) may be ignored in case of measurement are made over the short grass.

$$\frac{U_{ref}}{U_g} = \left(\frac{y_{ref}}{y_g}\right)^{\alpha}; \tag{E.2}$$

where $U_{ref} = 5.9$ m/s at the reference height or the eave height of the building (which is $y_{ref} = 20$ m for all the studied cases of street canyons) and y_g is the gradient height (above the layer of frictional influence near the surface the air moves purely under the influence of the pressure gradients and attains what is know as *gradient velocity* denoted by U_g and the height above ground at which the gradient velocity is attained is generally defined as *gradient height*, denoted by y_g Davenport (1965)) defined by

$$y_g = \frac{U^*_{ABL}}{6f}; \tag{E.3}$$

where $f = 2\,\omega \sin\phi$ is the Coriolis parameter, ω is the rate of rotation of the earth (72.9×10^{-6} rad/s), and ϕ is the latitude assumed to be $45°$ ((Richards et al., 2015)). As a result $f = 1.03 \times 10^{-4}$ rad/s. U^*_{ABL} can be calculated by a specified velocity U_{ref} at reference height y_{ref} as given by Equation Equation 2.4. Therefore equation E.1 becomes;

$$U(y) = U_g \left[\frac{y}{\delta}\right]^n; \tag{E.4}$$

and calculating δ using equation E.4 gives value of $\delta \approx 900$. So, $\delta/H \approx 45$ in present study.

Appendix F

Calculation for the reference wind speed

According to Blocken et al. (2009b), to assess the wind climate at a particular location requires the combination of (1) statistical meteorological data; (2) aerodynamic information and (3) a comfort criteria.

F.1 Statistical meteorological data

Generally, data are selected from a nearby meteorological station at which the wind climate is considered representative for the building site (Blocken et al., 2009b). An ideal meteorological station according to Blocken et al. (2009b) is the one with aerodynamic roughness length $y_0 = 0.03$ m and gives the mean wind speed at 10 m height. In this study, we have considered the buildings or street canyon belongs to the city area of the country like New Zealand or Australia.

F.2 Aerodynamic information

The aerodynamic information is used to transfer the statistical meteorological data from the meteorological station to the location of interest at the building site (Blocken et al., 2009b). In this study, we have considered the terrain with roughness length $y_0 = 0.2$ m according to Structural Design Actions-Part 2: Wind Actions (2011) (page:19) for the location of our building site. This roughness length and terrain type belong to a woodland forest according to Davenport roughness classification table 4 from Wieringa (1992) and power law wind velocity profiles for surfaces of different roughness Fig. 5 from Davenport (1965). The specified power law exponent for this type of terrain is $\alpha = 0.28$ and gradient height is $y_g = 1300^{'} \approx 900$ m (as given by Equation Equation E.3). The meteorological station or airport station, according to above-mentioned references belongs to flat open country, for which $\alpha = 0.16$.

F.3 Comfort criteria

Most of the wind comfort criteria mentioned in the literature review are the combination of a wind discomfort and danger threshold. We are using extended "Land Beaufort Scale" by Lawson et al. (1975) as a comfort criterion for this study. As we are analysing wind velocity of $U_{1.75\,m} = 3$ m/s at the pedestrian height at the location of interest at the building site. Therefore according to power law wind velocity profile,

$$\frac{U_{ref}}{U_g} = \left(\frac{y_{ref}}{y_g}\right)^{\alpha};$$

and at pedestrian height

$$\frac{U_{1.75\,m}}{U_g} = \left(\frac{y = 1.75\,m}{y_g}\right)^{\alpha};$$

$$\frac{3}{U_g} = \left(\frac{1.75}{900}\right)^{0.28};$$

Which gives,

$$U_g \approx 17\,m/s.$$

So, if we consider, the building height (H) to be $20\,m$, the velocity calculation at building height U_{ref} will be,

$$\frac{U_{ref}}{U_g} = \left(\frac{y = 20\,m}{900}\right)^{0.28}$$

Therefore,

$$U_{ref} = 5.9\,m/s$$

and Reynolds number at this height will be,

$$Re = \frac{\rho \cdot U_{ref} \cdot L}{\mu} = 8.1 \times 10^6.$$

Appendix G

Code to extract wind velocity data from Fluent and do the contour plot using Matlab

```
clc
close all
clear all


A=xlsread('flattrapdownstreamdata.xlsx');
B= round(A,1);
x = B(:,1);
y = B(:,2);
z = B(:,3);
cellsize=0.5;
minx=min(x);
maxx=max(x);
miny=min(y);
maxy=max(y);
%zmax=max(B(:,3));
xi=(minx:cellsize:maxx);
yi=(miny:cellsize:maxy);
[X,Y]=meshgrid(xi,yi);
ZI = griddata(x,y,z,X,Y);


contourf(X,flipud(Y),ZI,'Linestyle','none')
pb = pbaspect;
pbaspect([1 4 1])
ax = gca;
axis off;
ax.YDir = 'reverse';
set(gcf,'units','normalized');
%ax.PaperPosition = [0 0 587 16];
load('myfinalmap','myfinalmap')
```

```
%%%%%%%%%%%%%%%%%%%%%%%%%
% To save modified colormap
% use the command
%mymaplatest = colormap(ax);
%save('mymaplatest','mymaplatest')

%note that every time when colormap is
%modified and if you want to save the
%modification you have to give differnt
% name for example
%next time you can write it as
%mymapmodified = colormap(ax);
%save('mymapmodified','mymapmodified')
%%% When you want  load it load the latest one

%%%%%%%%%%%%%%%%%%%%%%%%%%5
colormap(ax,myfinalmap)
% change myfinalmap to modified
%colormap name every time you make modification
colorbar('Ticks',[[0:0.2:8])
% you can set []  to [0:0.1:8] or [0:0.1:8]
[cmin,cmax] = caxis;
caxis([0,8])
```

Appendix H

Matlab Code to count colour pixels of the Fluent/Matlab contour plot

Code for the color pixel counts for the fluent contour plot

```
clear;
close all;
clc;
contplot = imread('streetdownstreamrcomparisonfluentDWflat.png');
[height, width, dim] = size(contplot);
dbcount=0;
for i=1:height
for j=1:width
if contplot(i,j,1)==0& contplot(i,j,2)==0& contplot(i,j,3)==120
dbcount=dbcount+1;
end
end
end
Percentagedarkblue=(100*dbcount)/(height*width);

bcount=0;
for i=1:height
for j=1:width
if contplot(i,j,1)==0& contplot(i,j,2)==0& contplot(i,j,3)==255
bcount=bcount+1;
end
end
end
Percentageblue=(100*bcount)/(height*width);

orangecount=0;
for i=1:height
for j=1:width
if contplot(i,j,1)==255&contplot(i,j,2)==174&contplot(i,j,3)==0
```

```
orangecount=orangecount+1;
end
end
end
Percentageorange=(100*orangecount)/(height*width);

greencount=0;
for i=1:height
for j=1:width
if contplot(i,j,1)==0&contplot(i,j,2)==195&contplot(i,j,3)==0
greencount=greencount+1;
end
end
end
Percentagegreen=(100*greencount)/(height*width);
whitecount=0;
for i=1:height
for j=1:width
if contplot(i,j,1)==255&contplot(i,j,2)==255&contplot(i,j,3)==255
whitecount=whitecount+1;
end
end
end
Percentagewhite=(100*whitecount)/(height*width);

return;
```

Code for the color pixel counts for the Matlab contour plot

```
clear;
close all;
clc;

contplot = imread('Matlabflattrapdownstream.png');
[height, width, dim] = size(contplot);
dbcount=0;
for i=1:height
for j=1:width
if contplot(i,j,1)==20& contplot(i,j,2)==43& contplot(i,j,3)==140
dbcount=dbcount+1;
end
end
end
Percentagedarkblue=(100*dbcount)/(height*width);
bcount=0;
for i=1:height
for j=1:width
if contplot(i,j,1)==0& contplot(i,j,2)==0& contplot(i,j,3)==255
bcount=bcount+1;
```

```
end
end
end
Percentageblue=(100*bcount)/(height*width);

orangecount=0;
for i=1:height
for j=1:width
if contplot(i,j,1)==222&contplot(i,j,2)==125&contplot(i,j,3)==0
orangecount=orangecount+1;
end
end
end
Percentageorange=(100*orangecount)/(height*width);

greencount=0;
for i=1:height
for j=1:width
if contplot(i,j,1)==0&contplot(i,j,2)==127&contplot(i,j,3)==0
greencount=greencount+1;
end
end
end
Percentagegreen=(100*greencount)/(height*width);
% blackcount=0;
% for i=1:height
% for j=1:width
% if contplot(i,j,1)==0&contplot(i,j,2)==0&contplot(i,j,3)==0
% blackcount=blackcount+1;
% end
% end
% end
% Percentageblack=(100*blackcount)/(height*width);

return;
```

Appendix I

Computational Fluid Dynamics ANSYS Fluent Setup

I.1 Overview

over the course of this research, the setting for geometry, meshing and CFD choices changed and evolved. The settings indicated below are for the simulations run for adding a panel on the roof of the flat-flat building case. All simulations are run on ANSYS Fluent 17.0 and geometric modelling, meshing and set-up were all run through ANSYS workbench 17.0.

I.2 Geometry

Computational domain enclosure co-ordinates (in meter): $(0, 0, -160)$ to $(660, 120, 160)$
Body box 1 co-ordinates (in meter): $(130, 0, -40)$ to $(150, 20, 40)$
Body box 2 co-ordinates (in meter): $(176, 0, -40)$ to $(196, 20, 40)$
Wake box co-ordinates (in meter): $(40, 0, -100)$ to $(320, 70, 100)$

I.3 Mesh

Size function: Curvature
Relevance center: Coarse
Initial size seed: Active Assembly
Smoothing: Medium
Transition: Slow
Curvature normal: $18°$
Inflation:
- Boundary scoping method: Name selection
- Boundary: walls of both buildings and panel and ground
- Inflation option: First layer thickness
- First layer height: 2×10^{-5} m
- Maximum layers: 40
- Growth rate: 1.2
- Inflation algorithm: Pre

Face sizing:

Scoping method: Geometry selection
Geometry: Both building and panel faces
Type: Element size
Element size: 1 m
Behaviour: Soft
Body sizing:
Scoping method: Geometry selection
Geometry: computational domain enclosure
Type: Body of influence
Body of influence: wake box
Element size: 2 m
Number of elements: 7.3 million

I.4 Solver

Number of processor: 16
Pressure based
Velocity formulation: Absolute
Time: Steady
Viscous model: Transition $k - kl - \omega$ (3 eqn)
Reference values:
Area: 226.27 m^2
Density: 1.225 (kg/m^3)
Viscosity: 1.7894×10^{-5} ($kg/m - s$)

I.5 Solution

Solution Method: PISO
Skewness correction: 1
Neighbourhood correction: 0
Gradient: List square cell based
Momentum: Second order upwind
Turbulent kinetic energy: Second order upwind
Laminar kinetic energy: Second order upwind
Specific dissipation rate: Second order upwind
Under relaxation factor: Default
Solution initialize: Standard initialization using velocity Inlet
Run conditions: till the convergence of specified surface monitor points

Bibliography

Abdi, D. and Bitsuamlak, G. T. (2014). "Numerical evaluation of the effect of multiple roughness changes". In: *Wind and Structures* 19.6, pp. 585–601.

ASCE (2003). "Outdoor Human Comfort and its assessment, State of the Art Report". In: *American Society of Civil Engineers, Boston, VA, USA*.

Auckland City (1997). "Auckland City Council, Proposed District Plan 1997: Central Area Section, 6.12". In: *Environmental Wind Control, Auckland*.

Aynsley, R. M. (1989). "Politics of pedestrian level urban wind control". In: *Building and Environment* 24.4, pp. 291–295.

Azad, R. S. (1993). *The atmospheric boundary layer for engineers*. Springer.

Baskaran, A. and Stathopoulos, T. (1989). "Computational evaluation of wind effects on buildings". In: *Building and Environment* 24.4, pp. 325–333.

Baskaran, A. and Stathopoulos, T. (1992). "Influence of computational parameters on the evaluation of wind effects on the building envelope". In: *Building and Environment* 27.1, pp. 39–49.

Baskaran, A. and Kashef, A. (1996). "Investigation of air flow around buildings using computational fluid dynamics techniques". In: *Engineering Structures* 18.11, pp. 861–875.

Blazek, J. (2015). *Computational fluid dynamics: principles and applications*. Butterworth-Heinemann.

Blocken, B. and Carmeliet, J. (2004). "Pedestrian wind environment around buildings: Literature review and practical examples". In: *Journal of Thermal Envelope and Building Science* 28.2, pp. 107–159.

Blocken, B., Carmeliet, J., and Stathopoulos, T. (2007a). "CFD evaluation of wind speed conditions in passages between parallel buildings: effect of wall-function roughness modifications for the atmospheric boundary layer flow". In: *Journal of Wind Engineering and Industrial Aerodynamics* 95.9, pp. 941–962.

Blocken, B., Stathopoulos, T., and Carmeliet, J. (2007b). "CFD simulation of the atmospheric boundary layer: wall function problems". In: *Atmospheric Environment* 41.2, pp. 238–252.

Blocken, B. and Carmeliet, J. (2008a). "Pedestrian wind conditions at outdoor platforms in a high-rise apartment building: generic sub-configuration validation, wind comfort assessment and uncertainty issues". In: *Wind and Structures* 11.1, pp. 51–70.

Blocken, B., Stathopoulos, T., and Carmeliet, J. (2008b). "Wind environmental conditions in passages between two long narrow perpendicular buildings". In: *Journal of Aerospace Engineering* 21.4, pp. 280–287.

Blocken, B., Defraeye, T., Derome, D., and Carmeliet, J. (2009a). "High-resolution CFD simulations for forced convective heat transfer coefficients at the facade of a low-rise building". In: *Building and Environment* 44.12, pp. 2396–2412.

Blocken, B. and Persoon, J. (2009b). "Pedestrian wind comfort around a large football stadium in an urban environment: CFD simulation, validation and application of the new Dutch wind nuisance standard". In: *Journal of Wind Engineering and Industrial Aerodynamics* 97.5, pp. 255–270.

Blocken, B., Stathopoulos, T., Carmeliet, J., and Hensen, J. L. M. (2011). "Application of computational fluid dynamics in building performance simulation for the outdoor environment: an overview". In: *Journal of Building Performance Simulation* 4.2, pp. 157–184.

Blocken, B., Janssen, W. D., and Hooff, T. V. (2012). "CFD simulation for pedestrian wind comfort and wind safety in urban areas: General decision framework and case study for the Eindhoven University campus". In: *Environmental Modelling & Software* 30, pp. 15–34.

Bottema, M. (1992). "Wind climate and urban geometry". In: *Tech. Univ. Eindhoven, Faculteit Bouwkunde, Vakgroep Fago, Rapport* 92.63.

Bottema, M. (2000). "A method for optimisation of wind discomfort criteria". In: *Building and Environment* 35.1, pp. 1–18.

Bottema, M., Leene, J. A., and Wisse, J. A. (1992). "Towards forecasting of wind comfort". In: *Journal of Wind Engineering and Industrial Aerodynamics* 44.1-3, pp. 2365–2376.

Casey, M. and Wintergerste, T. (2000). "Best practice guidelines for industrial computational fluid dynamics of single-phase flows". In: *Lausanne: ERCOFTAC (European Research Community on Flow, Turbulence and Combustion)*.

Castro, I. P. (1981). "Measurements in shear layers separating from surface-mounted bluff bodies". In: *Journal of Wind Engineering and Industrial Aerodynamics* 7.3, pp. 253–272.

Castro, I. P. and Robins, A. G. (1977). "The flow around a surface-mounted cube in uniform and turbulent streams". In: *Journal of Fluid Mechanics* 79.02, pp. 307–335.

Castro, I. P. and Dianat, M. (1983). "Surface flow patterns on rectangular bodies in thick boundary layers". In: *Journal of Wind Engineering and Industrial Aerodynamics* 11.1-3, pp. 107–119.

Cook, N. J. (1985). "The Designer's Guide to Wind Loading on Building Structures. Part I: Background, Damage Survey, Wind Data, and Structural Classification". In: *Building Research Establishment, Watford*.

Council, W. C. (2000). "Design Guide for Wind". In: *Wellington, New Zealand: Wellington City Council*.

Counihan, J., Hunt, J. C. R., and Jackson, P. S. (1974). "Wakes behind two-dimensional surface obstacles in turbulent boundary layers". In: *Journal of Fluid Mechanics* 64.03, pp. 529–564.

Davenport, A. F. (1965). "The relationship of wind structure to wind loading". In: 54.

Dianat, M. and Castro, I. P. (1984). "Fluctuating surface shear stresses on bluff bodies". In: *Journal of Wind Engineering and Industrial Aerodynamics* 17.1, pp. 133–146.

Ekman, V. W. (1905). "On the influence of the earth's rotation on ocean currents". In: *Ark. Mat. Astron. Fys.* 2, pp. 1–53.

Farhadi, M. and Sedighi, K. (2008). "Flow over two tandem wall-mounted cubes using large eddy simulation". In: *Proceedings of the Institution of Mechanical Engineers, Part C: Journal of Mechanical Engineering Science* 222.8, pp. 1465–1475.

Ferreira, A. D., Sousa, A. C. M., and Viegas, D. X. (2002). "Prediction of building interference effects on pedestrian level comfort". In: *Journal of Wind Engineering and Industrial Aerodynamics* 90.4, pp. 305–319.

Flay, R. G. J. (1989). "Wind environment measurements and acceptance criteria developed at the University of Auckland". In: *Proceedings of the Tenth Australasian Fluid Mechanics Conference, University of Melbourne, Melbourne, Australia*, pp. 11–15.

Fluent, A. (2011a). "Ansys fluent theory guide". In: *ANSYS Inc., USA* 15317, pp. 373–374.

Fluent, A. (2011b). "Ansys fluent theory guide". In: *ANSYS Inc., USA* 15317, p. 114.

Fluent, A. (2011c). "Ansys fluent theory guide". In: *ANSYS Inc., USA* 15317, pp. 112–127.

Fluent, A. (2011d). "Ansys fluent theory guide". In: *ANSYS Inc., USA* 15317, p. 108.

Fluent, A. (2013). "Ansys fluent user guide". In: *ANSYS Inc., USA* 15317, pp. 696–702.

Franke, J. and Baklanov, A. (2007). *Best practice guideline for the CFD simulation of flows in the urban environment: COST action 732 quality assurance and improvement of microscale meteorological models*. Meteorological Inst.

Gandemer, J. (1975). "Wind environment around buildings: aerodynamic concepts". In: *Proc., 4th Int. Conf. Wind Effects on Buildings and Structures, Heathrow*, pp. 423–432.

Gandemer, J. (1981). "The aerodynamic characteristics of windbreaks, resulting in empirical design rules". In: *Journal of Wind Engineering and Industrial Aerodynamics* 7.1, pp. 15–36.

Garratt, J. R. et al. (1992). "The atmospheric boundary layer. Cambridge atmospheric and space science series". In: *Cambridge University Press, Cambridge* 416, p. 444.

Havel, B. (2006). *Experimental and numerical investigation of the coherent flow structures around tandem in-line surface-mounted cubes in a thin boundary layer*.

Havel, B., Hangan, H., and Martinuzzi, R. (2001). "Buffeting for 2D and 3D sharp-edged bluff bodies". In: *Journal of Wind Engineering and Industrial Aerodynamics* 89.14, pp. 1369–1381.

Holmes, J. D. (2015). *Wind loading of structures*. CRC press.

Huang, Y., He, W., and Kim, C. (2015). "Impacts of shape and height of upstream roof on airflow and pollutant dispersion inside an urban street canyon". In: *Environmental Science and Pollution Research* 22.3, pp. 2117–2137.

Hunt, J. C. R. and Poulton, E. C. (1972). "Some effects of wind on people". In: *Proceedings of Symposium on external flows*.

Hunt, J. C. R., Poulton, E. C., and Mumford, J. C. (1976). "The effects of wind on people; new criteria based on wind tunnel experiments". In: *Building and Environment* 11.1, pp. 15–28.

Hussein, H. J. and Martinuzzi, R. J. (1996). "Energy balance for turbulent flow around a surface mounted cube placed in a channel". In: *Physics of Fluids (1994-present)* 8.3, pp. 764–780.

Irtaza, H., Beale, R. G., Godley, M. H. R., and Jameel, A. (2013). "Comparison of wind pressure measurements on Silsoe experimental building from full-scale observation, wind-tunnel experiments and various CFD techniques". In: *International Journal of Engineering, Science and Technology* 5.1, pp. 28–41.

Ishizaki, H. and Sung, I. W. (1971). "Influence of adjacent buildings to wind". In: *Proceedings 3rd International Conference on Wind Effects on Buildings and Structures*, pp. 145–152.

Isyumov, N. and Davenport, A. G. (1975a). "Comparison of full-scale and wind tunnel wind speed measurements in the commerce court plaza". In: *Journal of Wind Engineering and Industrial Aerodynamics* 1, pp. 201–212.

Isyumov, N. and Davenport, A. G. (1975b). "The ground level wind environment in built-up areas". In: *Proceedings of the 4th International Conference on Wind Effects on Buildings and Structures,(Heathrow 1975)*, pp. 403–422.

Janssen, W. D., Blocken, B., and Hooff, T. V. (2013). "Pedestrian wind comfort around buildings: Comparison of wind comfort criteria based on whole-flow field data for a complex case study". In: *Building and Environment* 59, pp. 547–562.

Kenworthy, A. T. (1985). "Wind as an influential factor in the orientation of the orthogonal street grid". In: *Building and Environment* 20.1, pp. 33–38.

Kim, K. C., Ji, H. S., and Seong, S. H. (2003). "Flow structure around a 3-D rectangular prism in a turbulent boundary layer". In: *Journal of Wind Engineering and Industrial Aerodynamics* 91.5, pp. 653–669.

Koss, H. H. (2006). "On differences and similarities of applied wind comfort criteria". In: *Journal of Wind Engineering and Industrial Aerodynamics* 94.11, pp. 781–797.

Larousse, A., Martinuzzi, R., and Tropea, C. (1993). "Flow around surface-mounted, three-dimensional obstacles". In: *Turbulent Shear Flows 8*. Springer, pp. 127–139.

Lawson, T. V. (1978). "The wind content of the built environment". In: *Journal of Wind Engineering and Industrial Aerodynamics* 3.2, pp. 93–105.

Lawson, T. V. and Penwarden, A. D. (1975). "The effects of wind on people in the vicinity of buildings". In: *Proceedings 4th International Conference on Wind Effects on Buildings and Structures, Cambridge University Press, Heathrow*, pp. 605–622.

Lim, H. C., Castro, I. P., and Hoxey, R. P. (2007). "Bluff bodies in deep turbulent boundary layers: Reynolds-number issues". In: *Journal of Fluid Mechanics* 571, pp. 97–118.

Lohmeyer, A., Fasslrinner, H., Schmitt, H., and Fehrenbach, K. (1988). "Case study: quantitative determination of the pedestrian comfort near a high-rise building". In: *Energy and Buildings* 11.1-3, pp. 149–156.

Martinuzzi, R. and Tropea, C. (1993). "The flow around surface-mounted, prismatic obstacles placed in a fully developed channel flow (data bank contribution)". In: *Journal of Fluids Engineering* 115.1, pp. 85–92.

Martinuzzi, R. J. and Havel, B. (2000). "Turbulent flow around two interfering surface-mounted cubic obstacles in tandem arrangement". In: *Journal of Fluids Engineering* 122.1, pp. 24–31.

Martinuzzi, R. J. and Havel, B. (2004). "Vortex shedding from two surface-mounted cubes in tandem". In: *International Journal of Heat and Fluid Flow* 25.3, pp. 364–372.

Mathieu, J. and Scott, J. (2000). *An introduction to turbulent flow*. Cambridge University Press.

Meinders, E. R. and Hanjalić, K. (1999). "Vortex structure and heat transfer in turbulent flow over a wall-mounted matrix of cubes". In: *International Journal of Heat and Fluid Flow* 20.3, pp. 255–267.

Melbourne, W. H. (1978). "Criteria for environmental wind conditions". In: *Journal of Wind Engineering and Industrial Aerodynamics* 3.2, pp. 241–249.

Mochida, A., Tominaga, Y., Murakami, S., Yoshie, R., Ishihara, T., and Ooka, R. (2002). "Comparison of various k-ε models and DSM applied to flow around a high-rise building". In: *Wind and Structures* 5.2-4, pp. 227–244.

Moin, P. and Mahesh, K. (1998). "Direct numerical simulation: a tool in turbulence research". In: *Annual Review of Fluid Mechanics* 30.1, pp. 539–578.

Murakami, S. (1990). "Computational wind engineering". In: *Journal of Wind Engineering and Industrial Aerodynamics* 36, pp. 517–538.

Murakami, S. (1993). "Comparison of various turbulence models applied to a bluff body". In: *Journal of Wind Engineering and Industrial Aerodynamics* 46, pp. 21–36.

Murakami, S., Mochida, A., and Hibi, K. (1987). "Three-dimensional numerical simulation of air flow around a cubic model by means of large eddy simulation". In: *Journal of Wind Engineering and Industrial Aerodynamics* 25.3, pp. 291–305.

Murakami, S. and Mochida, A. (1988). "3-D numerical simulation of airflow around a cubic model by means of the k-epsilon model". In: *Journal of Wind Engineering and Industrial Aerodynamics* 31.2-3, pp. 283–303.

Oke, T. R. (1988). "Street design and urban canopy layer climate". In: *Energy and Buildings* 11.1, pp. 103–113.

O'Sullivan, J. P., Archer, R. A., and Flay, R. G. J. (2011). "Consistent boundary conditions for flows within the atmospheric boundary layer". In: *Journal of Wind Engineering and Industrial Aerodynamics* 99.1, pp. 65–77.

Paik, J., Sotiropoulos, F., and Porté-Agel, F. (2009). "Detached eddy simulation of flow around two wall-mounted cubes in tandem". In: *International Journal of Heat and Fluid Flow* 30.2, pp. 286–305.

Paterson, D. A. and Apelt, C. J. (1986). "Computation of wind flows over three-dimensional buildings". In: *Journal of Wind Engineering and Industrial Aerodynamics* 24.3, pp. 193–213.

Penwarden, A. D. (1973). "Acceptable wind speeds in towns". In: *Building Science* 8.3, pp. 259–267.

Penwarden, A. D. and Wise, A. F. E. (1975). *Wind environment around buildings*. HMSO.

Pirooz, A. A. S. and Flay, R. G. J. (2018). "Comparison of Speed-Up Over Hills Derived from Wind-Tunnel Experiments, Wind-Loading Standards, and Numerical Modelling". In: *Boundary-Layer Meteorology*, pp. 1–34.

Poitras, G. J., Brizzi, L., and Gagnon, Y. (2003). "Flow Over Model Buildings With Sloped Roofs". In: *ASME/JSME 2003 4th Joint Fluids Summer Engineering Conference*. American Society of Mechanical Engineers, pp. 191–198.

Quinn, A. D., Wilson, M., Reynolds, A., Couling, S. B., and Hoxey, R. P. (2001). "Modelling the dispersion of aerial pollutants from agricultural buildings: an evaluation of computational fluid dynamics (CFD)". In: *Computers and Electronics in Agriculture* 30.1, pp. 219–235.

Ratnam, G. S. and Vengadesan, S. (2008). "Performance of two equation turbulence models for prediction of flow and heat transfer over a wall mounted cube". In: *International Journal of Heat and Mass Transfer* 51.11, pp. 2834–2846.

Richards, P. J. and Hoxey, R. P. (1993). "Appropriate boundary conditions for computational wind engineering models using the k–ε turbulence model". In: *Journal of Wind Engineering and Industrial Aerodynamics* 46, pp. 145–153.

Richards, P. J., Hoxey, R. P., and Short, L. J. (2001). "Wind pressures on a 6m cube". In: *Journal of Wind Engineering and Industrial Aerodynamics* 89.14, pp. 1553–1564.

Richards, P. J., Mallinson, G. D., McMillan, D., and Li, Y. F. (2002). "Pedestrian level wind speeds in downtown Auckland". In: *Wind and Structures* 5.2_3_4, pp. 151–164.

Richards, P. J., Hoxey, R. P., Connell, B. D., and Lander, D. P. (2007). "Wind-tunnel modelling of the Silsoe Cube". In: *Journal of Wind Engineering and Industrial Aerodynamics* 95.9, pp. 1384–1399.

Richards, P. J. and Norris, S. E. (2011). "Appropriate boundary conditions for computational wind engineering models revisited". In: *Journal of Wind Engineering and Industrial Aerodynamics* 99.4, pp. 257–266.

Richards, P. J. and Norris, S. E. (2015). "Appropriate boundary conditions for a pressure driven boundary layer". In: *Journal of Wind Engineering and Industrial Aerodynamics* 142, pp. 43–52.

Riddle, A., Carruthers, D., Sharpe, A., McHugh, C., and Stocker, J. (2004). "Comparisons between FLUENT and ADMS for atmospheric dispersion modelling". In: *Atmospheric Environment* 38.7, pp. 1029–1038.

Rodi, W. (1997). "Comparison of LES and RANS calculations of the flow around bluff bodies". In: *Journal of Wind Engineering and Industrial Aerodynamics* 69, pp. 55–75.

Sakamoto, H. and Haniu, H. (1988). "Aerodynamic forces acting on two square prisms placed vertically in a turbulent boundary layer". In: *Journal of Wind Engineering and Industrial Aerodynamics* 31.1, pp. 41–66.

Sayma, A. (2009). *Computational fluid dynamics*. Bookboon.

Schofield, W. H. and Logan, E. (1990). "Turbulent shear flow over surface mounted obstacles". In: *Journal of Fluids Engineering* 112.4, pp. 376–385.

Seguro, J. V. and Lambert, T. W. (2000). "Modern estimation of the parameters of the Weibull wind speed distribution for wind energy analysis". In: *Journal of Wind Engineering and Industrial Aerodynamics* 85.1, pp. 75–84.

Shah, K. B. and Ferziger, J. H. (1997). "A fluid mechanicians view of wind engineering: Large eddy simulation of flow past a cubic obstacle". In: *Journal of Wind Engineering and Industrial Aerodynamics* 67, pp. 211–224.

Smirnov, A., Shi, S., and Celik, I. (2001). "Random flow generation technique for large eddy simulations and particle-dynamics modeling". In: *Transactions of the ASME-I-Journal of Fluids Engineering* 123.2, pp. 359–371.

Stathopoulos, T. (2006). "Pedestrian level winds and outdoor human comfort". In: *Journal of Wind Engineering and Industrial Aerodynamics* 94.11, pp. 769–780.

Stathopoulos, T. and Storms, R. (1986). "Wind environmental conditions in passages between buildings". In: *Journal of Wind Engineering and Industrial Aerodynamics* 24.1, pp. 19–31.

Stathopoulos, T. and Baskaran, A. (1990). "Boundary treatment for the computation of three-dimensional wind flow conditions around a building". In: *Journal of Wind Engineering and Industrial Aerodynamics* 35, pp. 177–200.

Stathopoulos, T. and Wu, H. (1995). "Generic models for pedestrian-level winds in built-up regions". In: *Journal of Wind Engineering and Industrial Aerodynamics* 54, pp. 515–525.

Structural Design Actions-Part 2: Wind Actions (2011). "AS/NZS 1170.2:2011 Structural design actions-Part 2: Wind actions". In: *Australian/New Zealand Standard (AS/NZS): Joint Technical Committee BD-006, Australia/New Zealand*.

To, A. P. and Lam, K. M. (1995). "Evaluation of pedestrian-level wind environment around a row of tall buildings using a quartile-level wind speed descripter". In: *Journal of Wind Engineering and Industrial Aerodynamics* 54, pp. 527–541.

Tominaga, Y., Mochida, A., Yoshie, R., Kataoka, H., Nozu, T., Yoshikawa, M., and Shirasawa, T. (2008a). "AIJ guidelines for practical applications of CFD to pedestrian wind environment around buildings". In: *Journal of Wind Engineering and Industrial Aerodynamics* 96.10, pp. 1749–1761.

Tominaga, Y., Mochida, A., Murakami, S., and Sawaki, S. (2008b). "Comparison of various revised k–ε models and LES applied to flow around a high-rise building model with 1: 1: 2 shape placed within the surface boundary layer". In: *Journal of Wind Engineering and Industrial Aerodynamics* 96.4, pp. 389–411.

Vardoulakis, S., Dimitrova, R., Richards, K., Hamlyn, D., Camilleri, G., Weeks, M., Sini, J., Britter, R., Borrego, C., Schatzmann, M., et al. (2011). "Numerical model inter-comparison for wind flow and turbulence around single-block buildings". In: *Environmental Modeling & Assessment* 16.2, pp. 169–181.

Versteeg, H. K. and Malalasekera, W. (2007). *An introduction to computational fluid dynamics: the finite volume method*. Pearson Education.

Wieringa, J. (1992). "Updating the Davenport roughness classification". In: *Journal of Wind Engineering and Industrial Aerodynamics* 41.1, pp. 357–368.

Wilcox, D. C. et al. (1998). *Turbulence modeling for CFD*. Vol. 2. DCW industries La Canada, CA.

Willemsen, E. and Wisse, J. A. (2002). "Accuracy of assessment of wind speed in the built environment". In: *Journal of Wind Engineering and Industrial Aerodynamics* 90.10, pp. 1183–1190.

Williams, C. D. and Wardlaw, R. L. (1992). "Determination of the pedestrian wind environment in the city of Ottawa using wind tunnel and field measurements". In: *Journal of Wind Engineering and Industrial Aerodynamics* 41.1, pp. 255–266.

Williams, C. J., Hunter, M. A., and Waechter, W. F. (1990). "Criteria for assessing the pedestrian wind environment". In: *Journal of Wind Engineering and Industrial Aerodynamics* 36, pp. 811–815.

Wiren, B. G. (1975). "A wind tunnel study of wind velocities in passages between and through buildings". In: *Proceedings of the 4th International Conference on Wind Effects on Buildings and Structures,(Heathrow 1975)*, pp. 465–475.

Wise, A. F. E. (1970). *Wind effects due to groups of buildings*. Vol. 23. Building Research Station, Ministry of Public Building and Works.

Wise, A. F. E., Sexton, D. E., and Lillywhite, M. S. T. (1965). *Studies of air flow around buildings*. Tech. rep. Building Research Station, Watford (England).

Yang, T. (2004). "CFD and field testing of a naturally ventilated full-scale building". PhD thesis. University of Nottingham.

Yassin, M. F. (2011). "Impact of height and shape of building roof on air quality in urban street canyons". In: *Atmospheric Environment* 45.29, pp. 5220–5229.

Yoshie, R., Mochida, A., Tominaga, Y., Kataoka, H., Harimoto, K., Nozu, T., and Shirasawa, T (2007). "Cooperative project for CFD prediction of pedestrian wind environment in the Architectural Institute of Japan". In: *Journal of Wind Engineering and Industrial Aerodynamics* 95.9, pp. 1551–1578.

Zhang, C. X. (1994). "Numerical predictions of turbulent recirculating flows with a $\kappa - \varepsilon$ model". In: *Journal of Wind Engineering and Industrial Aerodynamics* 51.2, pp. 177–201.